Doctoral Dissertation

Ion Pairing Based on Charged Porphyrins

March 2023

Doctoral Program in Advanced Life Sciences
Graduate School of Life Sciences
Ritsumeikan University

TANAKA Hiroki

Doctoral Dissertation Reviewed

by Ritsumeikan University

Ion Pairing Based on Charged Porphyrins

(荷電ポルフィリンを基盤としたイオンペアリング)

March 2023

2023 年 3 月

Doctoral Program in Advanced Life Sciences

Graduate School of Life Sciences

Ritsumeikan University

立命館大学大学院生命科学研究科

生命科学専攻博士課程後期課程

TANAKA Hiroki

田中 宏樹

Supervisor : Professor MAEDA Hiromitsu

研究指導教員：前田 大光 教授

Preface

The studies on the dissertation were conducted under the guidance of Prof. Dr. Hiromitsu Maeda at the College of Life Sciences, Ritsumeikan University during the period from April 2017 to March 2023. The author's main subject was the investigation on ion pairing based on charged porphyrins.

Submitted December 22, 2022
Revised February 9, 2023

Table of Contents

Chapter 1

General Introduction

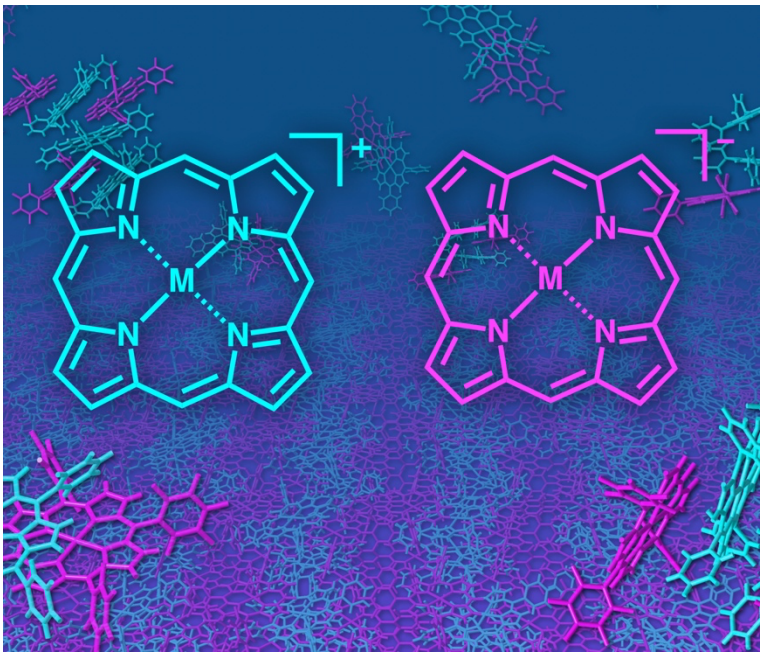

Contents

1–1 Background

Noncovalent interactions are crucial for developing various assembled structures that exhibit characteristic properties.[1] In DNA, complementary hydrogen-bonded base pairs stack via π–π interactions with a distance of 3.4 Å, resulting in double helical structures that carry genetic instructions.[2,3] In a conceptual sense, interactions such as hydrogen-bonding and π–π interactions consist of several intermolecular forces. Fundamental intermolecular forces include electrostatic, induction, and dispersion forces, which are long-range interactions based on Coulombic force. Exchange-repulsion and charge-transfer forces are short-range interactions attributed to interorbital interactions (Figure 1–1). The total interaction energy (E_{tot}) between molecules can be represented by the summation of the intermolecular forces ($E_{tot} = E_{es} + E_{ind} + E_{disp} + E_{ex} + E_{ct}$). Contributions by these intermolecular forces are dependent on the geometries and electronic structures of the constituent molecules.[4] Especially, electrostatic force acts as attraction between oppositely charged species and repulsion between identically charged species, so that charged species (ions) can form ordered structures. In 1828, an ion pair consisting of $[Pt(NH_3)_4]^{2+}$ and $[PtCl_4]^{2-}$ with planar geometries was reported as Magnus' green salt.[5,6] The single-crystal X-ray analysis revealed that the cation and anion were stacked alternately by electrostatic forces, forming a one-dimensional chain structure with electrical conductivity (Figure 1–2).[7] It clearly showed that the shape of the constituent ions affect the assembled structure and the resulting properties. On the other hand, π–π interactions, which are attractive interactions between π-electronic systems arising chiefly from dispersion (London dispersion), are essential for the assembly of π-electronic systems.[8–12] The contribution of dispersion forces is significant and predominant in most π–π stacking structures, although weak electrostatic forces are present even for electronically neutral π-electronic systems. The stacking orientations of π-electronic systems are controlled by minimizing electrostatic repulsion between the π-electrons and maximizing attraction between the π-electrons and positively charged σ-frameworks.[2,8,9,13] Recent advanced studies regarding π–π interactions have created opportunities for the development of various electronic materials and devices such as semiconductors.[14]

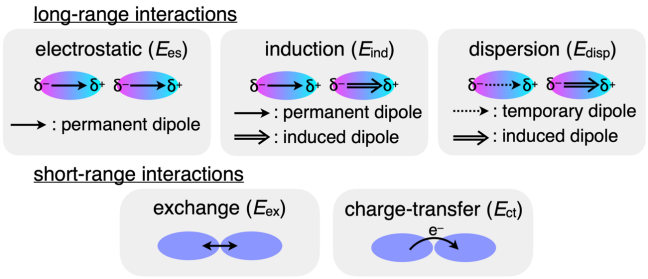

Figure 1–1 Fundamental intermolecular forces in noncovalent interactions.

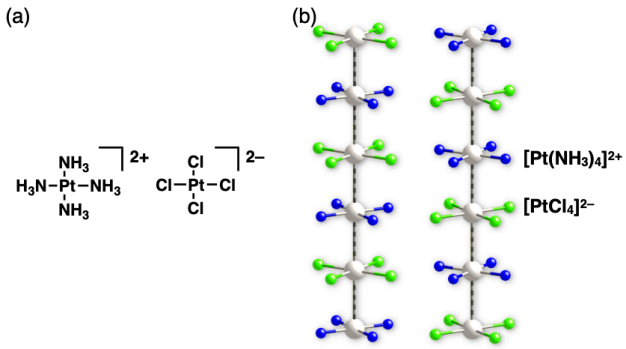

Figure 1–2 Magnus' green salt: (a) structure formula and (b) packing structure. Atom color code: in (b): blue, green, and gray refer to nitrogen, chlorine, and platinum, respectively.

1–2 π-Electronic Ions

The introduction of charge into π-electronic systems leads to highly ordered assemblies due to the elevated contribution of electrostatic interaction. Ion-pairing assemblies can be classified as charge-by-charge and charge-segregated assemblies, according to their alternately and identically stacking arrangements of ion pairs, respectively (Figure 1–3). In addition, charged π-electron systems (π-electronic ions) have a variety of combinations of cations and anions, which are the constituent units of assemblies. Therefore, specific functions can be demonstrated by selecting and assembling π-electronic ions with appropriate shape and electronic state. Here, π-electronic ions are defined as π-electronic systems with a charged core unit rather than a species with an electronically neutral core bearing ionic side chains. The charged π-cores are more advantageous for the following reasons: (i) freedom from bulky moieties (peripheral charged substituents) and availability of various uncharged substituents for controlling the electronic states of core parts, (ii) possibility of producing (partially) unsubstituted species, without a change in total charge, for efficient stacking, (iii) utilization of both the charged cores for stacking between ions to exhibit ion-pairing assembly and resulting properties derived from this direct

contact, and (iv) possession of charge at the core unit without requiring multiple charges introduced by peripheral substituents.

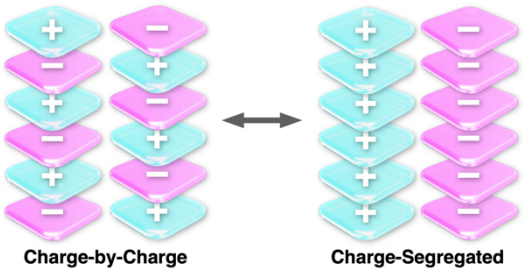

Figure 1–3 Conceptual diagram of ion-pairing arrangement, including charge-by-charge and charge-segregated assembling modes.

1–3 Ion-Pairing Assemblies of π-Electronic Ions

π-Electronic ions are highly reactive, and it is essential to establish stabilization strategies for their utilization as building units in assemblies and functional materials. One stabilization strategy is the use of aromatic cyclic compounds; Hückel aromaticity is attributed to the (4*n*+2) π-electron cyclic conjugation system, which tends to retain a specific number of π-electrons and generally acquires stability.

By Müllen et al., nanostructures and liquid crystals of charged polycyclic aromatic hydrocarbons (PAHs) were reported.[15–19] They synthesized positively charged 9-phenylbenzo[1,2]quinolizino[3,4,5,6-*fed*]phenenthridinylium cations (PQP^+) by dehydrogenation of 1-aryl-2,4,6-triphenylpyridinium cations under photoirradiation. In addition, various ion pairs based on PQP^+ were prepared by ion exchange from BF_4^- ion pair **1** and the sodium salts of various sulfonic acids (Figure 1–4a).[18] The solid-state ion-pairing assembly of **2** as an ion pair of PQP^+ in combination with sulfonate anion was fabricated, and the structure was revealed by single-crystal analysis (Figure 1–4b). Ion pair **2** presented a charge-segregated assembly mode, wherein the stacking distances between PQP^+ were 3.38, 3.40, and 3.42 Å. Furthermore, sulfonate anions with long alkyl chains and PQP^+ ion pairs **3** and **4** were identified by polarized optical microscopy (POM) as **3** existing as needle-like crystals and **4** as liquid crystals (Figure 1–4c). In 2D wide-angle X-ray scattering (WAXS) measurements of **3** and **4**, clear signals were observed at 0.35 nm, corresponding to the stacking distance between two PQP^+, and at 0.70 nm, corresponding to twice the stacking distance (Figure 1–4d). These results indicated that **3** and **4** in the bulk state were charge-segregated assemblies based on a columnar structure of stacked PQP^+

as well as the packing structure in the single crystal of **2**. PQP^+ with long alkyl chains were synthesized, and the morphologies of the assemblies were controlled depending on the counteranions (Figure 1–5).[15] Transmission electron microscopy (TEM) of MeOH solutions of Cl^- ion pair **5** and BF_4^- ion pair **6** revealed nanoribbons and nanotubes, respectively. WAXS measurements found that **5** formed a face-to-face stacking and **6** formed a slipped stacking structure, influenced by the size of the anions.

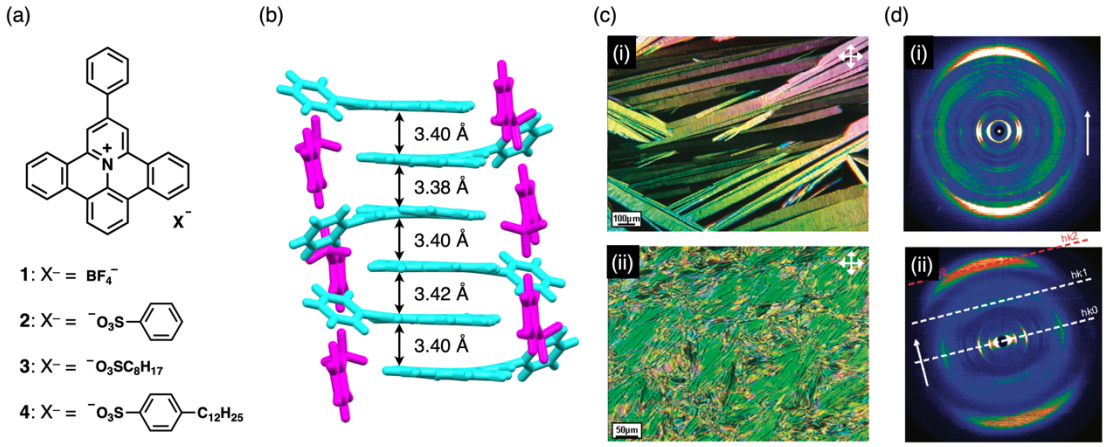

Figure 1–4 (a) Structures of PQP^+ ion pairs **1**–**4**, (b) crystal structure of **2**, (c) POM images, and (d) 2D WAXS patterns of (i) **3** and (ii) **4** at 30 °C (cooling from Iso).

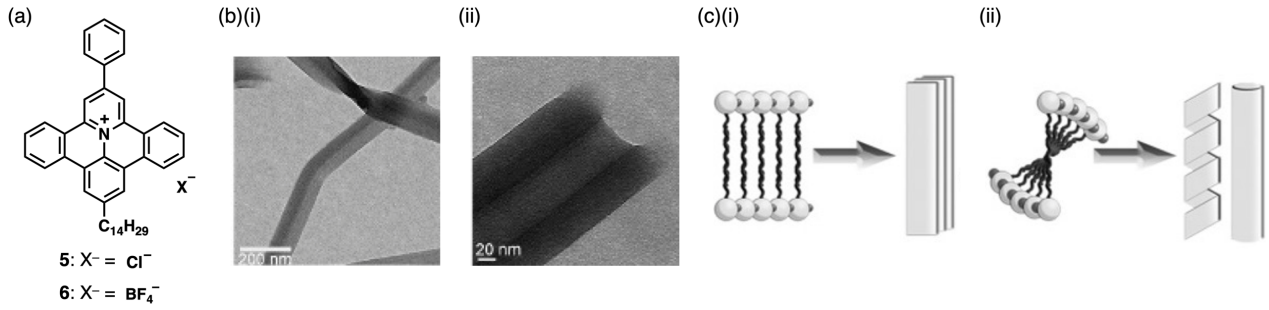

Figure 1–5 (a) PQP^+ ion pairs **5**,**6** and (b) TEM images in MeOH and (c) assembled modes of (i) **5** and (ii) **6**.

Trioxatriangulenium ($TOTA^+$) and triazatriangulenium ($TATA^+$) cations were synthesized by Laursen et al.[20,21] The PF_6^- ion pair **7** and Cl^- ion pair **8** of the decyl-substituted derivatives of $TOTA^+$ formed nanostructures under 10% CH_3CN/water solvent conditions (Figure 1–6).[22] As shown in the results of cryo-TEM, **7** formed 60–100 nm wide nanoribbons and 150 nm nanorods, and **8** constructed 29 nm wide nanotubes. The lipophilic moieties of decyl substituted $TOTA^+$ aggregate through hydrophobic interactions to form a bilayer structure. Compared to PF_6^-, whose negative charge is delocalized to fluorine, Cl^-, which is classified as a

point charge, is more solvated with water molecules. In **7**, the entire molecular system was hydrophobic, so the bilayer structure was further stacked to form aggregates, resulting in nanoribbons. In contrast, **8** could maintain the bilayer structure of $TOTA^+$ due to the solvation of Cl^-, thus stabilizing the nanotube structure.

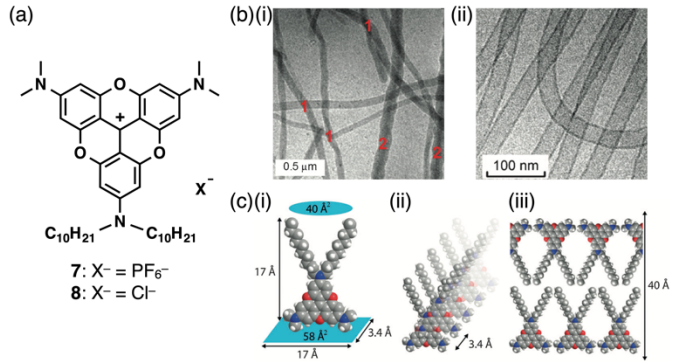

Figure 1–6 (a) Structures of **7** and **8**, (b) cryo-TEM micrograph of nanostructures of (i) **7** and (ii) **8** formed in 10% CH_3CN/water: nanoribbons and twisted nanorods refer to red colored 1 and 2, respectively, in (b), and (c) models of $TOTA^+$ with (i) the monomer, (ii) the columnar structure, and (iii) the cross-section of the bilayer. Atom color code in (c): gray, white, blue, and red refer to carbon, hydrogen, nitrogen, and oxygen, respectively.

Maeda et al. reported the formation of dimension-controlled assemblies by introducing dipyrrolyldiketone boron complexes[23] as effective anion receptors **9**–**11** with appropriate substituents to Cl^- ion pair of $TATA^+$ (**12**$^+$-Cl^-) (Figure 1–7).[24,25] Ion pair **12**$^+$-**9**·Cl^- provided a supramolecular gel from *n*-octane (10 mg mL^{-1}), and optical microscopy (OM), scanning electron microscopy (SEM), and atomic force microscopy (AFM) of the xerogel showed that it formed fibrous aggregates 0.1–2 μm wide (Figure 1–8). The XRD showed that a Col_h structure with the *c* value of 0.73 nm was constructed in the fiber, which suggests the formation of a charge-by-charge assembly of supramolecular gels with stacking between **12**$^+$ and **9**·Cl^-. Furthermore, POM and differential scanning calorimetry (DSC) measurements revealed that **12**$^+$-**9**–**11**·Cl^- afforded mesophases (Figure 1–9). Their XRD measurements showed the formation of assemblies based on charge-by-charge type for **12**$^+$-**9**·Cl^- and charge-segregated type for **12**$^+$-**9**,**10**·Cl^-. In particular, the ion pairs **12**$^+$-**9**,**10**·Cl^- were found to exhibit bipolar charge transport ability due to the charge-segregated arrangements.

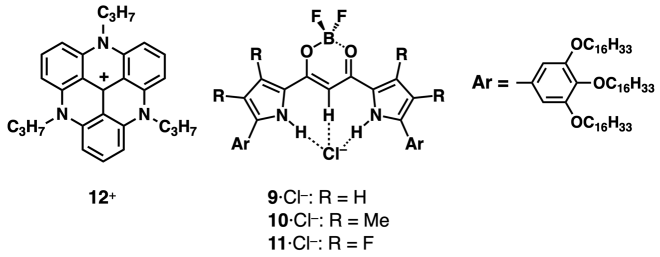

Figure 1–7 Chemical structures of TATA$^+$ cation **12**$^+$ and receptor–anion complexes **9**–**11**·Cl$^-$.

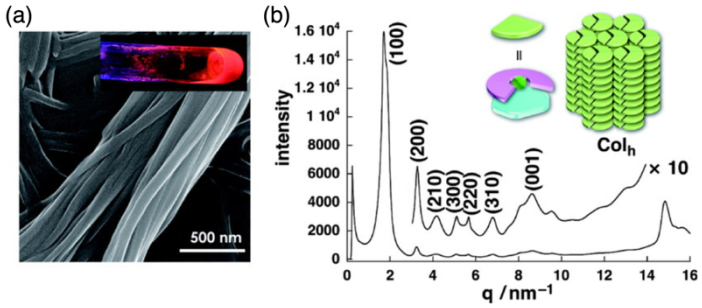

Figure 1–8 (a) SEM image (inset: photograph of the supramolecular gel irradiated under a UV_{365} light) and (b) the XRD pattern and the proposed assembling models of **12**$^+$-**9**·Cl$^-$ as the xerogel.

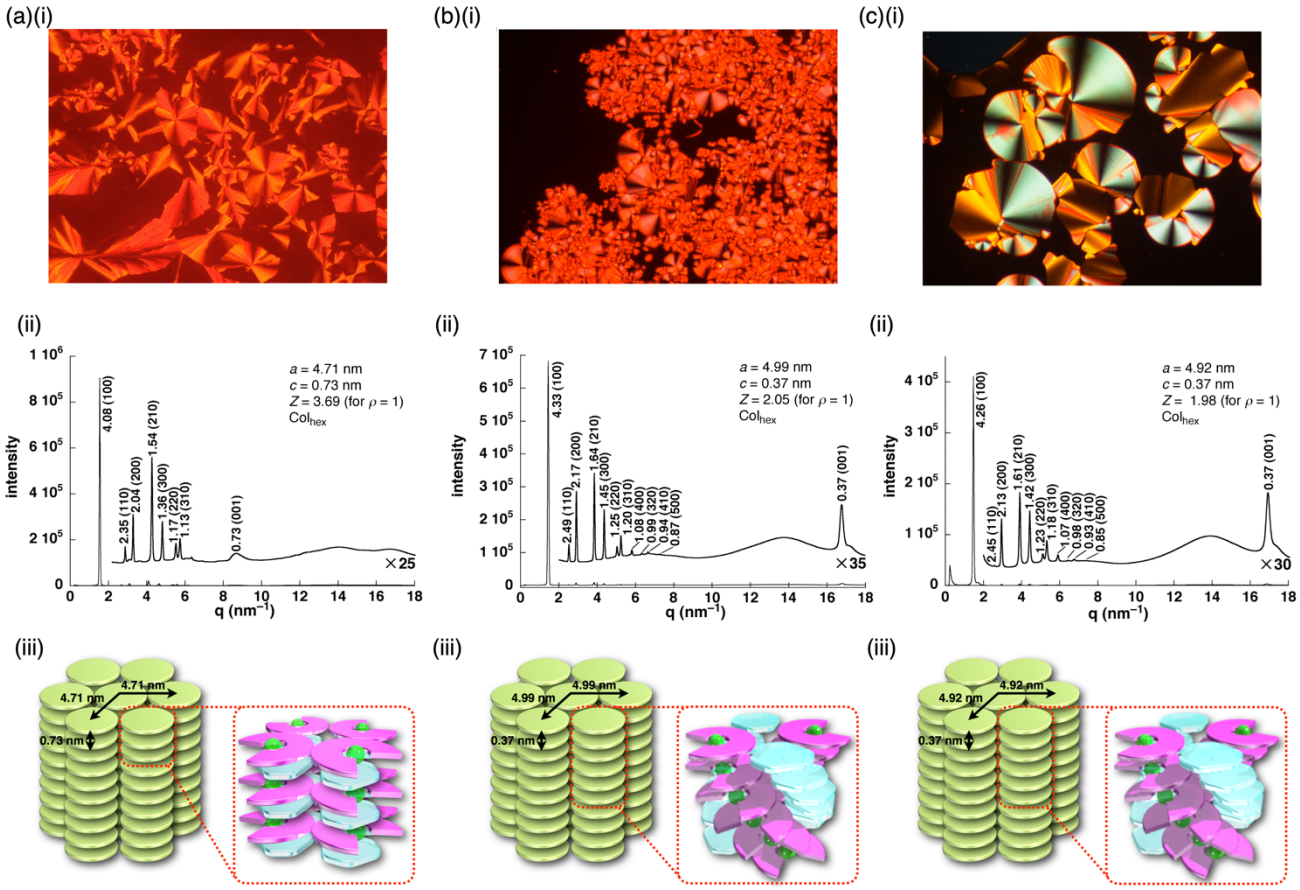

Figure 1–9 Liquid crystal properties of (a) **12**$^+$-**9**·Cl$^-$, (b) **12**$^+$-**10**·Cl$^-$, and (c) **12**$^+$-**11**·Cl$^-$: (i) POM images, (ii) XRD patterns, and (iii) the proposed assembled structures.

π-Electronic anions are difficult to synthesize due to their high reactivity resulting from the electron-rich systems. Hence, even fewer examples have been deployed as ion-pairing assemblies. However, pentacyanocyclopentadienide ($PCCp^-$), reported by Webster,[26] can be used as a constituent unit of ion-pairing assemblies because it is stabilized by the electron-withdrawing effect of the cyano group in addition to the stabilization based on the six π-electron system. Since $PCCp^-$ can be obtained as a Na^+ ion pair,[27] the desired ion pair can be synthesized by mixing it with the Cl^- ion pair of the desired cation under appropriate conditions. For example, Maeda et al. found by single-crystal X-ray structure analysis that π-electronic ion pairs with **13**$^+$ and **12**$^+$ formed charge-by-charge assemblies (Figure 1–10).[28] On the other hand, the introduction of tetraalkylammonium as a countercation of $PCCp^-$ showed charge-segregated assemblies in crystals and liquid crystals.

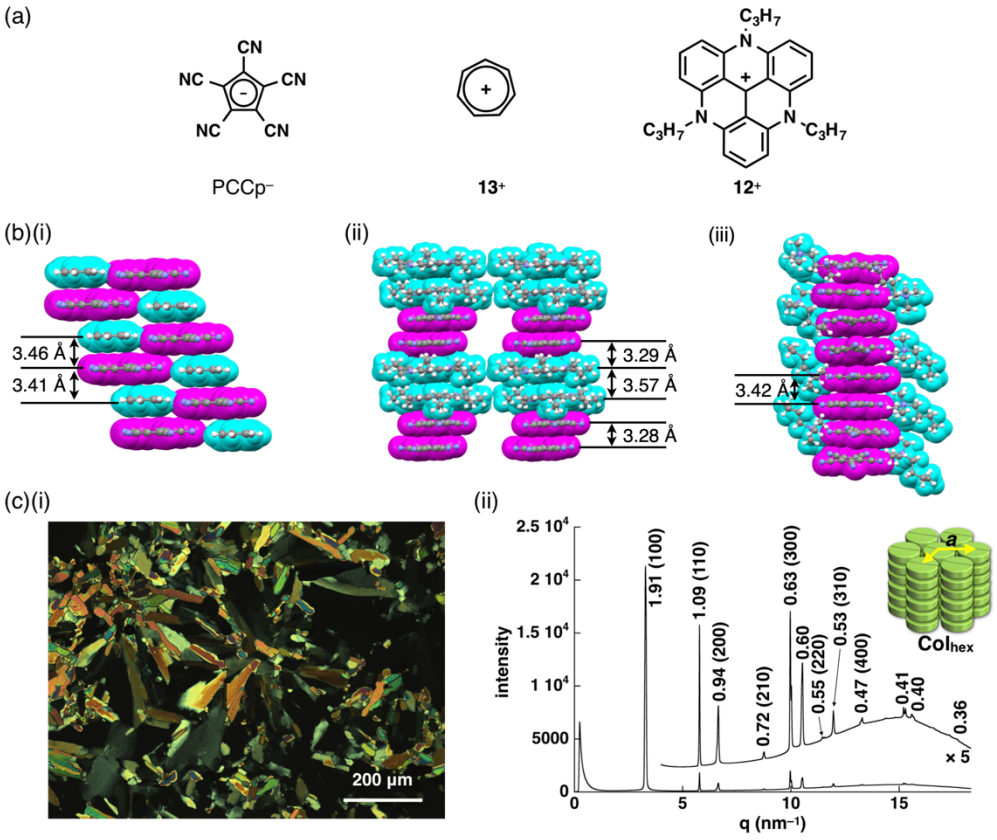

Figure 1–10 (a) Structures of $PCCp^-$, **13**$^+$, and **12**$^+$, (b) single-crystal X-ray structures of (i) **13**$^+$-$PCCp^-$, (ii) **12**$^+$-$PCCp^-$, and (iii) $BuMe_3N^+$-$PCCp^-$ as their space-filling models in side views, and (c)(i) POM image and (ii) XRD pattern of $(C_{12}H_{25})_3MeN^+$-$PCCp^-$ at 70 °C cooling from Iso. Color code in (b): cyan and magenta represent cations and anions, respectively.

1–4 Charged Porphyrins

Porphyrin is the basic skeleton of biological pigments such as chlorophyll and heme and is one of the most well-known functional π-electronic systems.[29,30] In addition, porphyrins, planar tetradentate dianionic ligands for metal complexation, can compensate all or part of the charges of introduced metal ions, affording π-electronic cations for the latter. However, porphyrin metal complexes with high valent metals, such as tricationic metals, require an axial ligand in most cases, making it difficult to form stacking assemblies. For example, in the Cl^- ion pair of the triisoproplysilyloxy-substituted porphyrin Fe^{III} complex **14**$^+$, Cl^- was coordinated to Fe^{III}, and the charge of Fe^{III} porphyrin was compensated.[31] Similarly, boron complexes of subporphyrins, such as **15**$^+$, lose charge because ligands such as OH^- and MeO^- coordinate to B^{III} (Figure 1–11).[32,33] Both **14**$^+$ and **15**$^+$ functioned as cations when the counteranions were noncoordinating anions, but their use as cations was limited. On the other hand, porphyrins with metal ions in d^8 electronic configuration can function as charged π-electronic systems because they require no axial ligand coordination. On the basis of the synthesis strategy of charged π-electronic systems, porphyrin–Au^{III} complexes were expected to act as π-electronic cations for ion-pairing assemblies. The synthesis of porphyrin–Au^{III} complexes was reported by Fleischer et al. in 1969.[34] They have been used as acceptors in electron transfer systems[35–37] and intercalators to nucleobase sites in DNA.[38] In 2019, Maeda et al. found Au^{III} complexes of *meso*-tetraphenylporphyrin derivatives to function as cationic building units of π-electronic ion pairs, which form crystal states and dimension-controlled assemblies such as supramolecular gels and thermotropic liquid crystals (Figure 1–12).[39] In particular, ion pairs **16**$^+$-$PCCp^-$ and **17**$^+$-$PCCp^-$ formed ordered arrangements with the contributions of charge-by-charge assemblies.

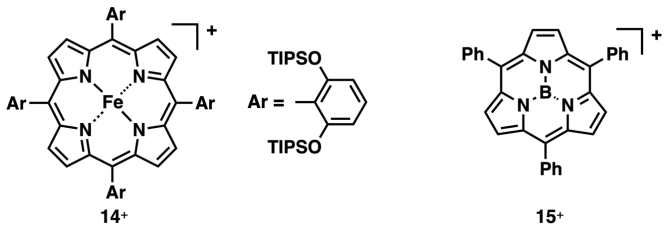

Figure 1–11 Positively charged porphyrin **14**$^+$ and subporphyrin **15**$^+$.

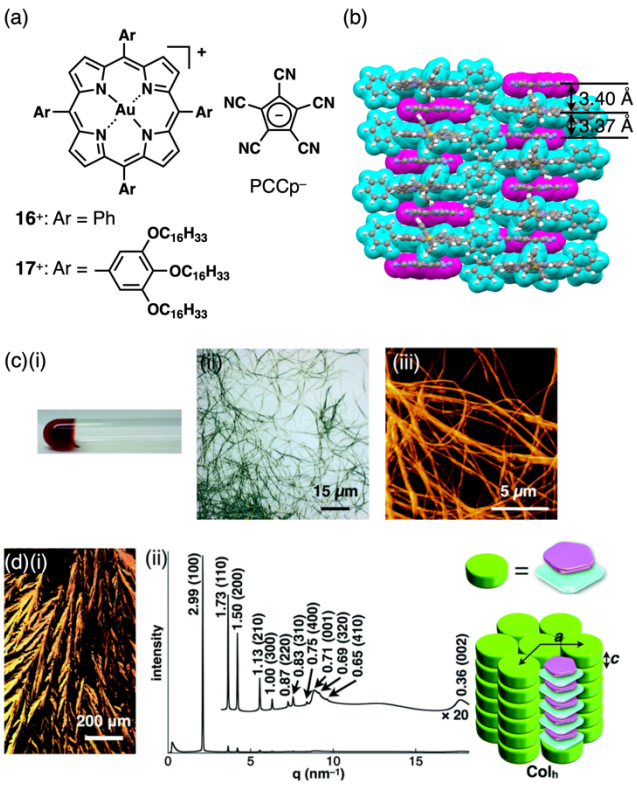

Figure 1–12 (a) Structures of **16**$^{+}$-PCCp^{-} and **17**$^{+}$-PCCp^{-}, (b) single-crystal structure of **16**$^{+}$-PCCp^{-}, (c)(i) photograph of the supramolecular gel, (ii) OM image, and (iii) STM image of **17**$^{+}$-PCCp^{-}, and (d)(i) POM image and (ii) XRD pattern and a proposed assembling model of **17**$^{+}$-PCCp^{-} at 280 °C upon cooling from Iso.

π-Electronic anions were prepared by the deprotonation of an acid unit introduced into π-electronic systems.[40–42] The delocalization of negative charges in porphyrin core, is essential for stabilizing the deprotonated anions. *meso*-Hydroxy-substituted porphyrins (MHPs), which are the intermediates of heme degradation[43,44] and can form radical species via oxidation,[45–53] were the candidate precursors of π-electronic anions. By Maeda et al., the Ni^{II} complexes of deprotonated MHPs **18**–**20**$^{-}$ as stable anions were reported to form solid-state charge-by-charge assemblies with aliphatic tetrabutylammonium (TBA^{+}) cation and **16**$^{+}$ (Figure 1–13).[39,54,55] The electronic states of porphyrin-based π-electronic anions can be tuned by varying the central metal species and peripheral modifications, which additionally affects the packing states of ion-pairing assemblies.

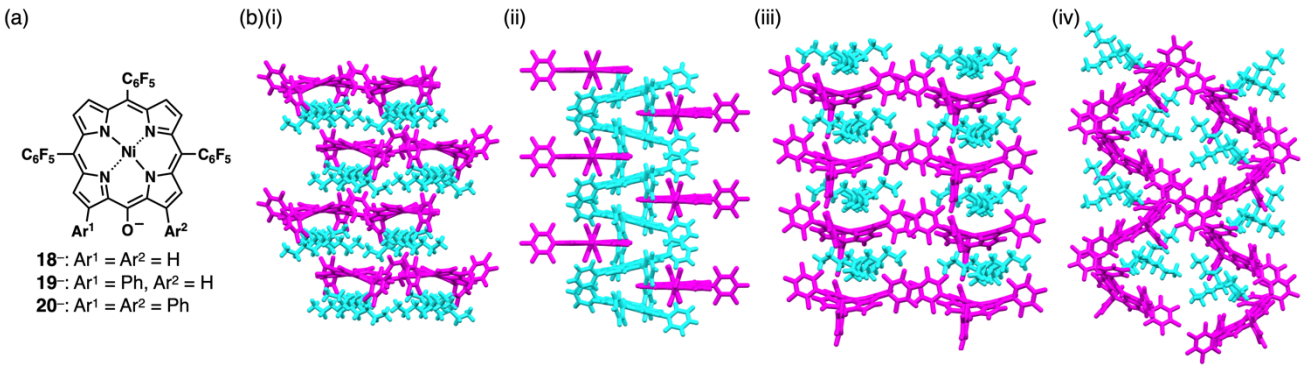

Figure 1–13 (a) Structures of **18**–**20**$^-$ and (b) single-crystal packing structures of (i) TBA$^+$-**18**$^-$, (ii) **16**$^+$-**18**$^-$, (iii) TBA$^+$-**19**$^-$, and (iv) TBA$^+$-**20**$^-$.

1–5 Overview of This Dissertation

As mentioned above, ion-pairing assemblies can be formed in a variety of combinations of charged species. Despite numerous studies on ion-pairing assemblies, the characteristics of interactions between π-electronic ions in the solid state are not well understood. The author has attempted to systematize the interactions and resulting physical properties of charged π-electronic systems using charged porphyrins, which are capable of a variety of peripheral modifications. In Chapter 2, the author describes the synthesis of porphyrin–Au^{III} complexes, which are partially or totally modified with C_6F_5 at the *meso* positions and their ion-pairing assemblies with characteristics dependent on the number and substitution pattern of the C_6F_5 units and the geometries of the anions.[56] Chapters 3 and 4 summarize ion-pairing assemblies of porphyrin–Au^{III} complexes in combination with receptor–anion complexes that can behave as pseudo-π-electronic anions.[57,58] The details of the stacking structures in the assemblies are verified by theoretical calculations. In Chapter 5, the author attempts a detailed discussion of the interactions between charged π-electronic systems and proposes $^i\pi$–$^i\pi$ interactions as a new interaction.[59] Solid-state ion-pairing assemblies are constructed for negatively charged porphyrin derivatives in combination with a bulky cation and a π-electronic cation and their photophysical properties are evaluated. In Chapters 6 and 7, porphyrin ion pairs are synthesized by combining the porphyrin cations in Chapters 2–4 and the porphyrin anions in Chapter 5.[60,61] The electronic states of the porphyrin ions are controlled by the peripheral electron-donating and electron-withdrawing groups and the electron transfer by external stimuli such as light and solvents is observed.

Chapter 2

Substitution-Pattern- and Counteranion-Depending Ion-Pairing Assemblies Based on Electron-Deficient Porphyrin–Au^{III} Complexes

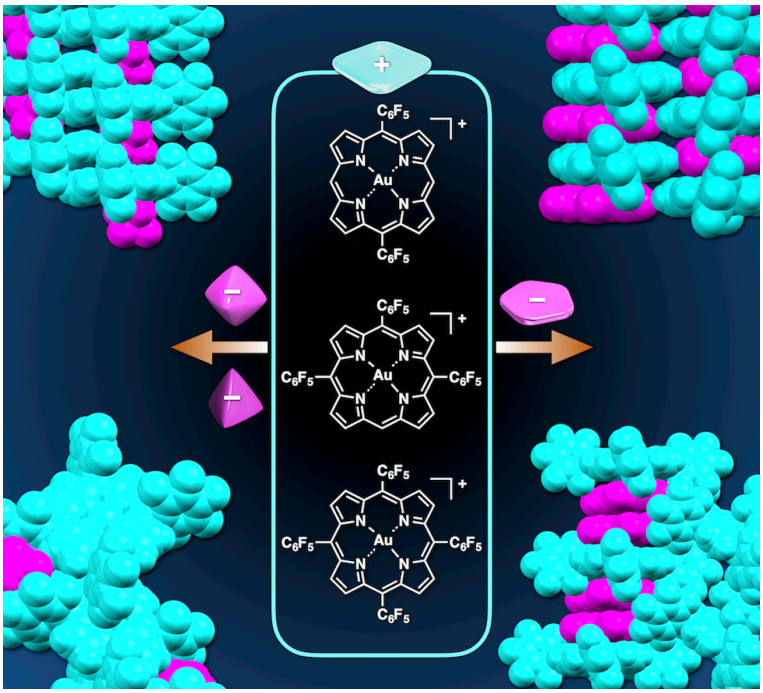

Contents

2–1 Introduction

Modifications at the peripheries of porphyrins would enable the preparation of various fascinating π-electronic ion pairs and their associated functional ion-pairing assemblies and materials. In particular, highly electron-withdrawing substituents induce electron-deficient states and Lewis acid properties. These effects would influence the electronic properties of ion-pairing assemblies. Furthermore, partially modified porphyrins are effective for stacking of π-electronic systems, affording functional ion-pairing assemblies and electronic materials. Polarization of π-electronic systems as an important factor for stacking can be induced by appropriate substituting patterns. Fine-tuning of assembling modes can also be achieved by the combination with counteranions. However, the relationship between the geometries and electronic states of ion pairs and their assembling modes have not been investigated based on porphyrin–Au^{III} complexes. In this chapter, the synthesis and assembly behavior of porphyrin–Au^{III} complexes, partially or totally bearing *meso*-C_6F_5 modifications, are discussed.

2–2 Synthesis of Porphyrin–Au^{III} Complexes with Electron-Withdrawing Substituents

5,15-Bis(pentafluorophenyl)porphyrin **21** and the corresponding 5,10,15-trisubstituted **22** and 5,10,15,20-tetrasubstituted **23**, prepared according to literature procedures,[62–64] were converted to Au^{III} complexes as OTf^- ion pairs, $\mathbf{21}^+$-OTf^-, $\mathbf{22}^+$-OTf^-, and $\mathbf{23}^+$-OTf^-, by treatment with $HAuCl_4 \cdot 4H_2O$ in the presence of AgOTf and NaOAc.[65] The OTf^- ion pairs, which were purified by column chromatography with silica gel and recrystallization, were converted to Cl^- ion pairs with ion-exchange resin (Amberlite), followed by the purification procedures similar to the OTf^- ion pairs (Figure 2–1). The obtained OTf^- and Cl^- ion pairs were identified by spectroscopic and elemental analyses.

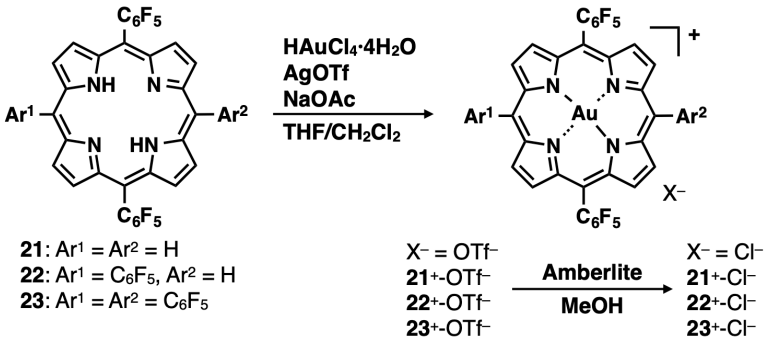

Figure 2–1 Synthetic route for porphyrin–Au^{III} complexes $\mathbf{21}^+$–$\mathbf{23}^+$ as OTf^- and Cl^- ion pairs.

Partial substitution of the *meso* positions can be useful for the examination of electronic states based on the chemical shifts of *meso*-CH. The ^{1}H NMR spectrum of $\mathbf{21}^+$ as a Cl^- ion pair ($\mathbf{21}^+$-Cl^-) in DMSO-d_6 showed downfield shifts of the *meso*-CH and β-CH signals at 11.63 and 10.33/9.99 ppm, respectively, compared to those of **21** at 10.78 and 9.80/9.42 ppm, respectively, suggesting the formation of a positive charge in $\mathbf{21}^+$. Similar behaviors were also observed in $\mathbf{22}^+$-Cl^- with *meso*-CH and β-CH signals at 11.66 and 10.35–9.99 ppm, respectively, which were shifted downfield compared to those of **22** (10.83 and 9.83–9.38 ppm, respectively) (Figure 2–2). Furthermore, the β-CH signal of $\mathbf{23}^+$-Cl^- was observed at 10.01 ppm, which was shifted downfield compared to that of $\mathbf{16}^+$-Cl^- at 9.32 ppm, suggesting that the electron deficiency of the porphyrin core increased with the introduction of C_6F_5 units (Figure 2–3). The electrostatic potentials (ESP) of $\mathbf{21}^+$, $\mathbf{22}^+$, and $\mathbf{23}^+$, calculated at B3LYP/6-31+G(d,p) with LanL2DZ for Au based on the optimized structures (B3LYP/6-31G(d,p) with LanL2DZ for Au), were different from that of $\mathbf{16}^+$, supporting the results of the ^{1}H NMR analysis. Furthermore, theoretical calculation at the same level revealed that 5,10,15-trisubstituted $\mathbf{22}^+$ has a dipole moment of 6.02 Debye due to the lack of one C_6F_5 unit, whereas $\mathbf{21}^+$ and $\mathbf{23}^+$ showed negligible dipole moments (Figure 2–4,5).[66]

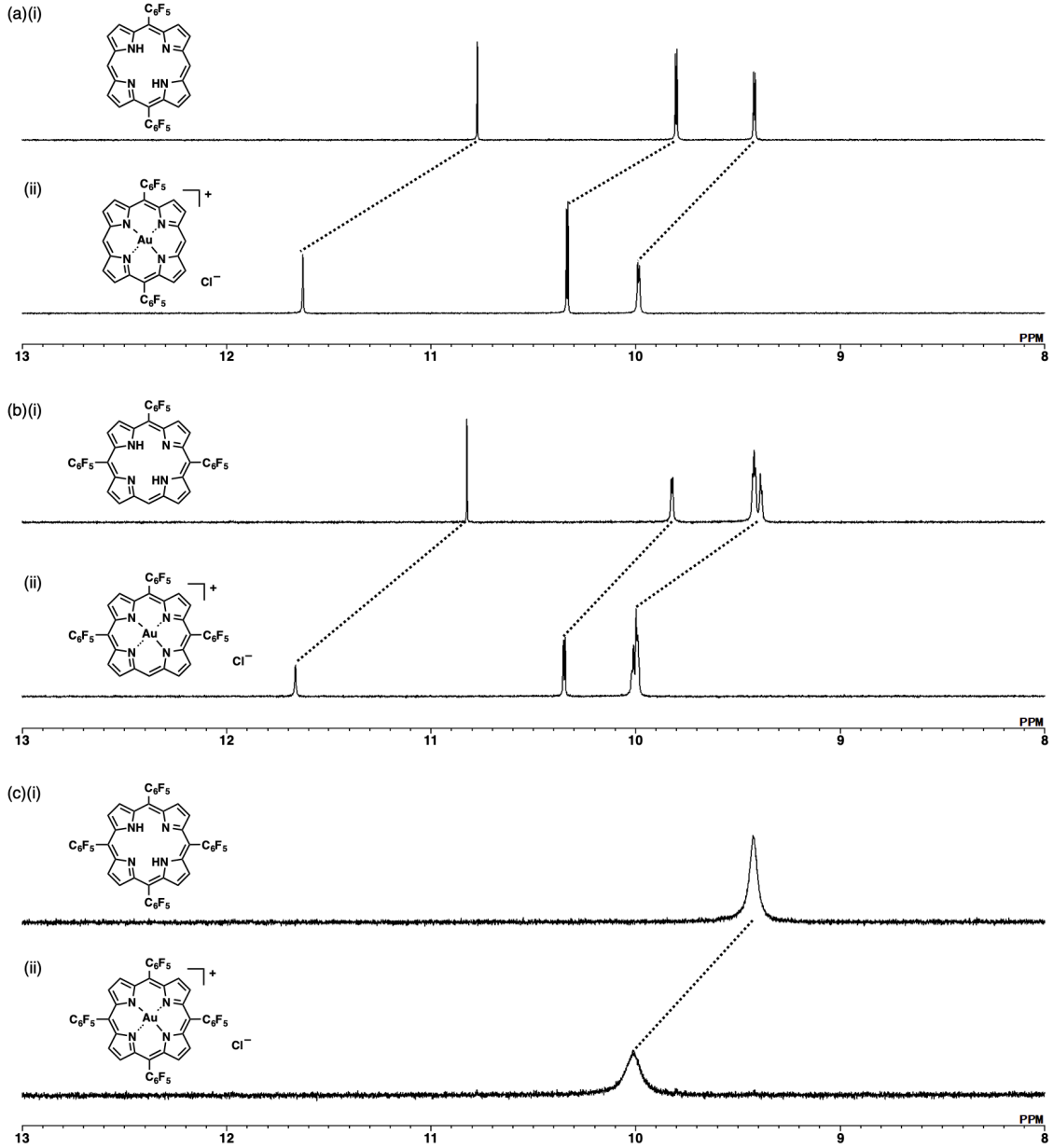

Figure 2–2 Summarized ^{1}H NMR of (a)(i) **21** and (ii) **21**$^{+}$-Cl^{-}, (b)(i) **22** and (ii) **22**$^{+}$-Cl^{-}, and (c)(i) **23** and (ii) **23**$^{+}$-Cl^{-} in DMSO-d_6 at 20 °C (1.0×10^{-3} M).

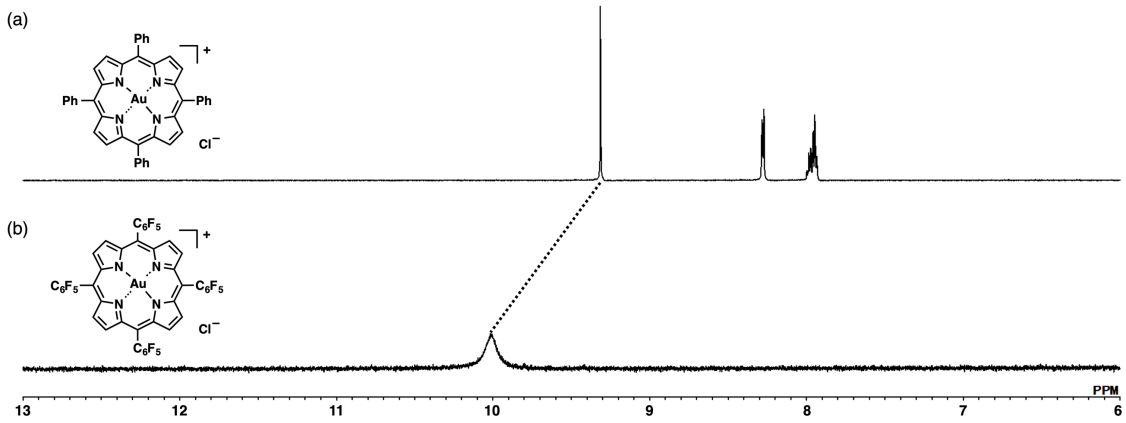

Figure 2–3 Summarized ^{1}H NMR of (a) **16**$^{+}$-Cl^{-} and (b) **23**$^{+}$-Cl^{-} in DMSO-d_6 at 20 °C (1.0×10^{-3} M).

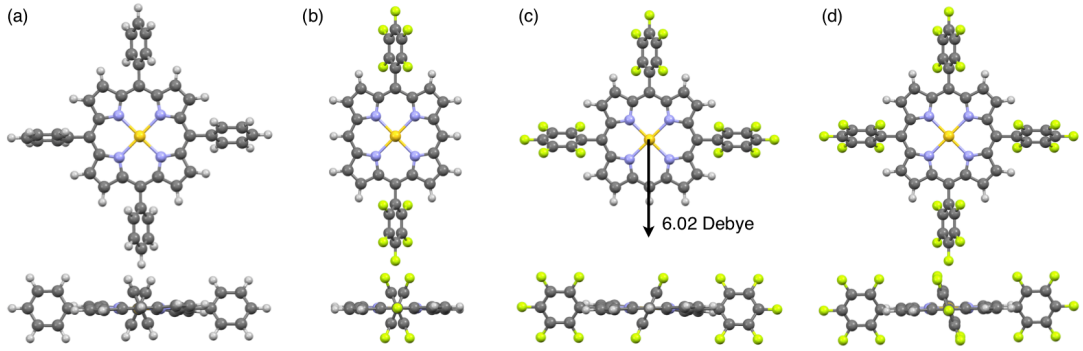

Figure 2–4 Optimized structures (top and side views) of (a) **16**$^{+}$, (b) **21**$^{+}$, (c) **22**$^{+}$, and (d) **23**$^{+}$ at B3LYP/6-31G(d,p) for C, H, N, and F and B3LYP/LanL2DZ for Au. LanL2DZ basis set was used for Au atom due to the limited calculation resource. Dipole moment of **22**$^{+}$ was estimated as 6.02 Debye.

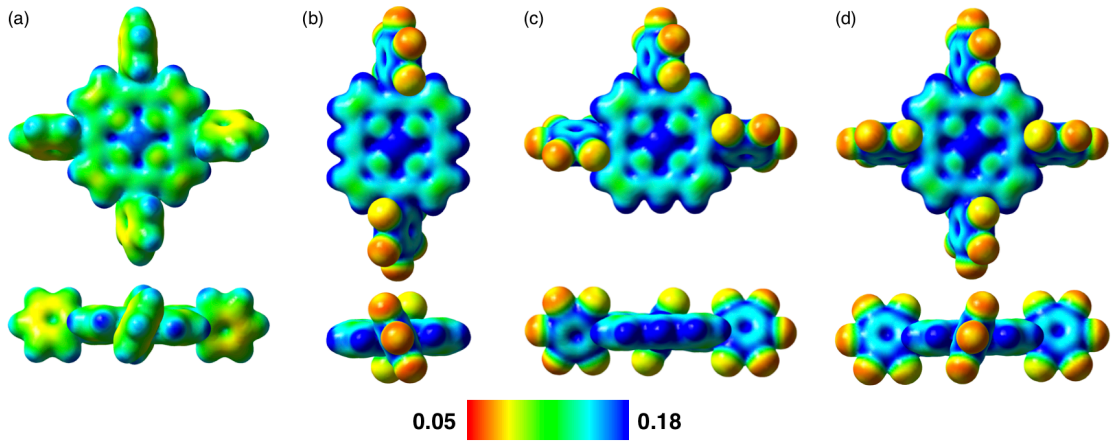

Figure 2–5 Electron density diagrams (top and side views) of (a) **16**$^{+}$, (b) **21**$^{+}$, (c) **22**$^{+}$, and (d) **23**$^{+}$. ESPs were mapped onto the electron density isosurface (δ = 0.01) calculated at B3LYP/6-31+G(d,p) for C, H, N, and F and B3LYP/LanL2DZ for Au.

The polarities of the ion pairs depend on the delocalization of the negative charges of the constituent anions.[39] Cl^- ion pair **23**$^+$-Cl^- significantly enhanced the polarity with an R_f value of 0.14, with 10% MeOH/CH_2Cl_2 as an eluent, compared to free base **23** (R_f = 0.89) (Figure 2–6a). The TLC analysis of **16**,**21**–**23** showed R_f values of 0.05, 0.13, 0.19, and 0.31, respectively, with 25% CH_2Cl_2/*n*-hexane as an eluent, whereas the ion pairs **16**,**21**–**23**$^+$-Cl^- showed R_f values of 0.18, 0.10, 0.10, and 0.14, respectively, with 10% MeOH/CH_2Cl_2 as an eluent (Figure 2–6b,c). Interestingly, the tendency in the polarities of **16**/**16**$^+$ and the other species were reversed by Au^{III} complexation, suggesting that the electronic state can be controlled by the substituents (C_6H_5 and C_6F_5) in different ways for electronically neutral species and cationic species.

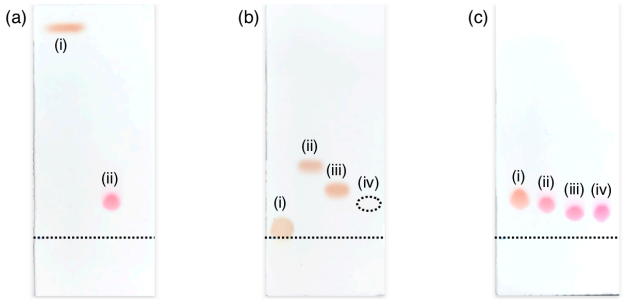

Figure 2–6 TLC analysis for (a)(i) **23** and (ii) **23**$^+$-Cl^-, (b)(i) **16**, (ii) **23**, (iii) **22**, and (iv) **21**, and (c)(i) **16**$^+$-Cl^-, (ii) **23**$^+$-Cl^-, (iii) **22**$^+$-Cl^-, and (iv) **21**$^+$-Cl^-, using 10% MeOH/CH_2Cl_2, 25% CH_2Cl_2/*n*-hexane, and 10% MeOH/CH_2Cl_2, respectively, as eluents. A dotted circle in (b) indicates the spot of **21**, which was observed under a UV_{365} light due to poor solubility.

The UV/vis absorption spectra of **21**$^+$-Cl^-, **22**$^+$-Cl^-, and **23**$^+$-Cl^- showed Soret bands at 393, 397, and 401 nm, respectively, in CH_2Cl_2 (6.0×10^{-6} M) (Figure 2–7). The absorption maximum of **23**$^+$-Cl^- is blue-shifted compared to that of **16**$^+$-Cl^- (409 nm)[39] due to the electron-withdrawing effect of C_6F_5 units. Interestingly, the transitions at 401 nm in the UV/vis absorption spectrum of **23**$^+$ can be assigned as intramolecular charge-transfer (CT) excitations: the theoretically estimated excitations at 400.0, 405.7, and 405.9 nm include the respective major transitions from HOMO–7, HOMO–2, and HOMO–2, localized at the electron-withdrawing *meso*-aryl rings, to LUMO, LUMO+2, and LUMO+1, respectively, localized at the positively charged core macrocycle (Figure 2–10,13).[66] Likewise, **21**$^+$ and **22**$^+$ showed similar CT-oriented excitations from aryl rings to porphyrin cores. This is characteristic to the electronic excitation behaviors of positively charged π-electronic systems (Figure 2–8,9,11,12).

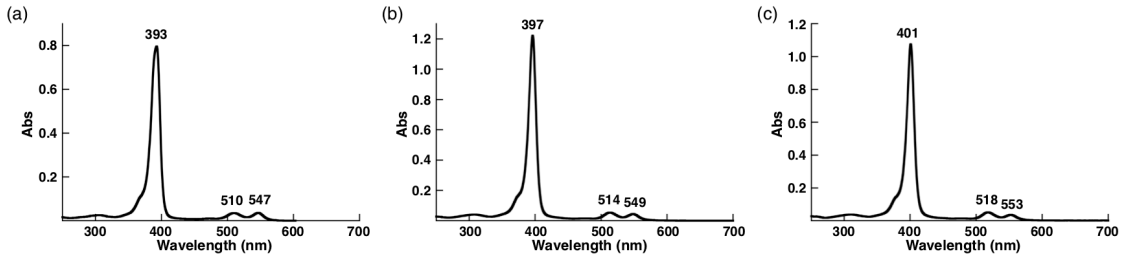

Figure 2–7 UV/vis absorption spectra of (a) $\mathbf{21}^{+}$-Cl^{-}, (b) $\mathbf{22}^{+}$-Cl^{-}, and (c) $\mathbf{23}^{+}$-Cl^{-} in CH_2Cl_2 (3.0×10^{-6} M, 20 °C).

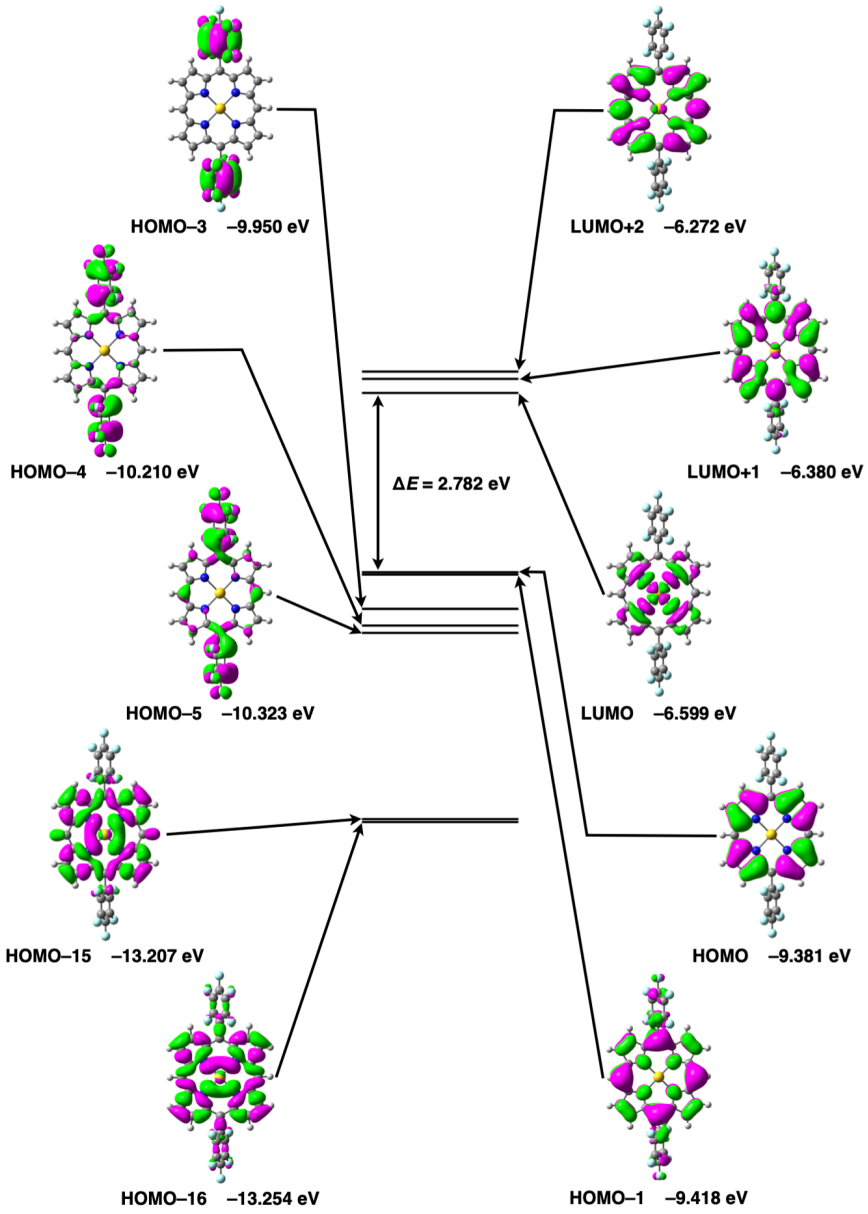

Figure 2–8 Molecular orbitals (HOMO/LUMO) of $\mathbf{21}^{+}$ estimated at B3LYP/6-31+G(d,p) for C, H, N, and F and B3LYP/LanL2DZ for Au.

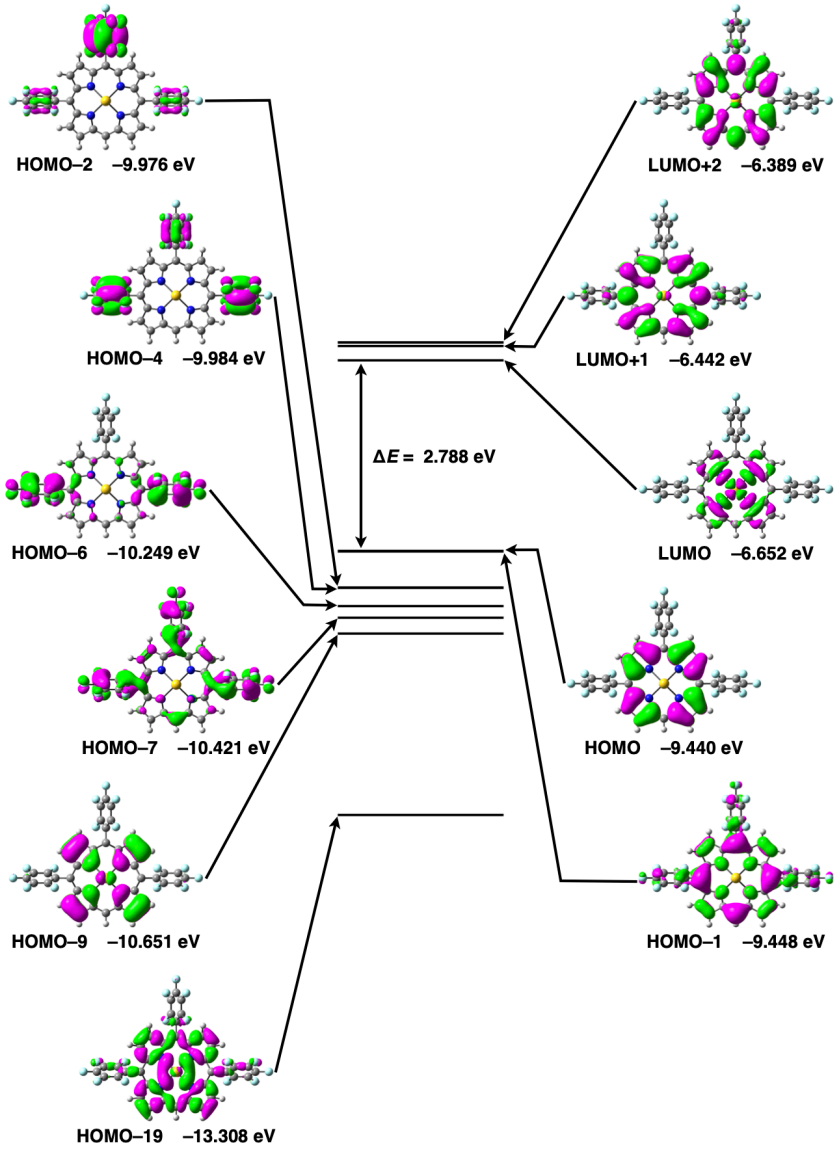

Figure 2–9 Molecular orbitals (HOMO/LUMO) of **22**$^{+}$ estimated at B3LYP/6-31+G(d,p) for C, H, N, and F and B3LYP/LanL2DZ for Au.

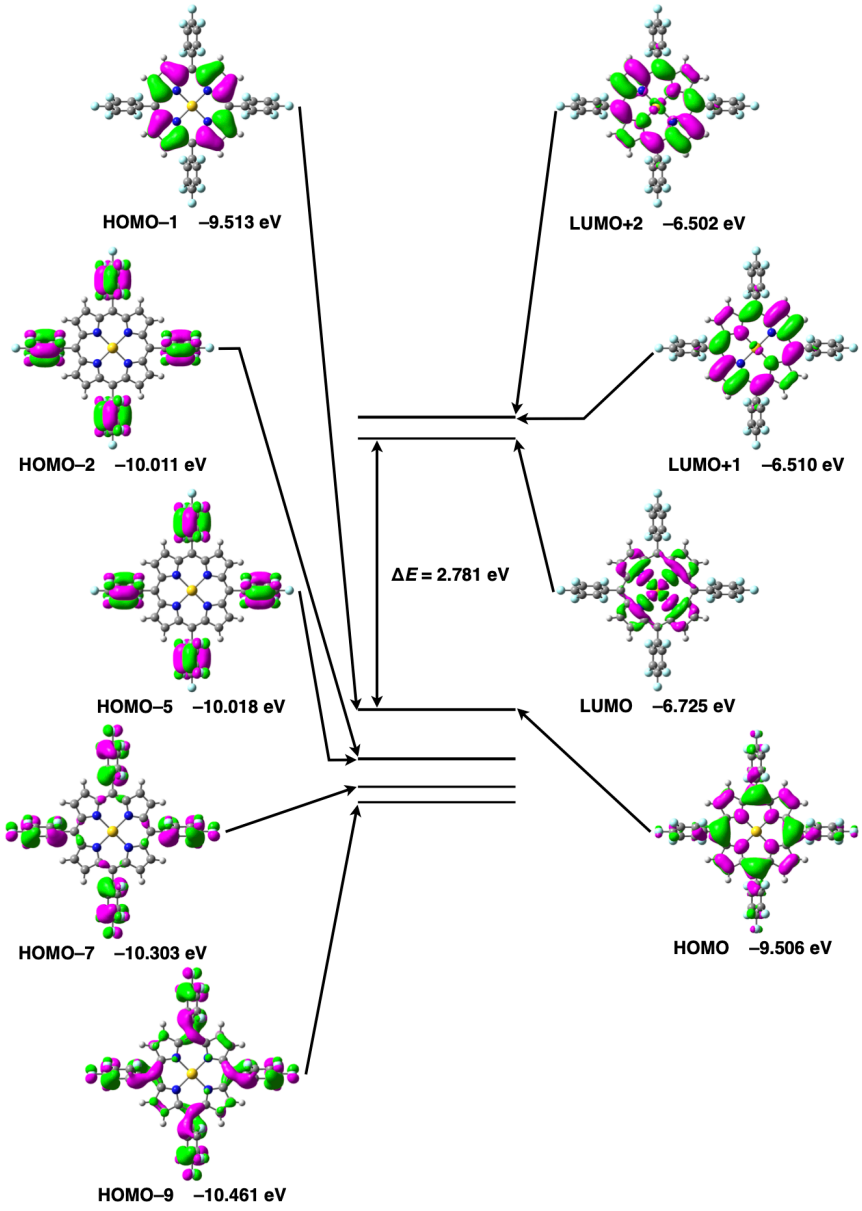

Figure 2–10 Molecular orbitals (HOMO/LUMO) of **23**$^{+}$ estimated at B3LYP/6-31+G(d,p) for C, H, N, and F and B3LYP/LanL2DZ for Au.

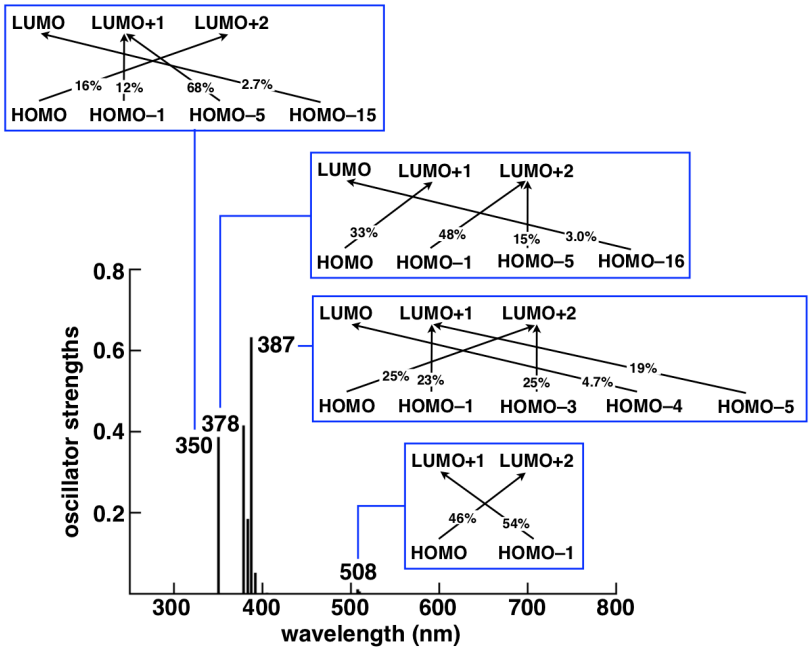

Figure 2–11 TD-DFT-based UV/vis absorption stick spectrum of **21**$^{+}$ with the transitions correlated with molecular orbitals estimated at B3LYP/6-31+G(d,p) for C, H, N, and F and B3LYP/LanL2DZ for Au.

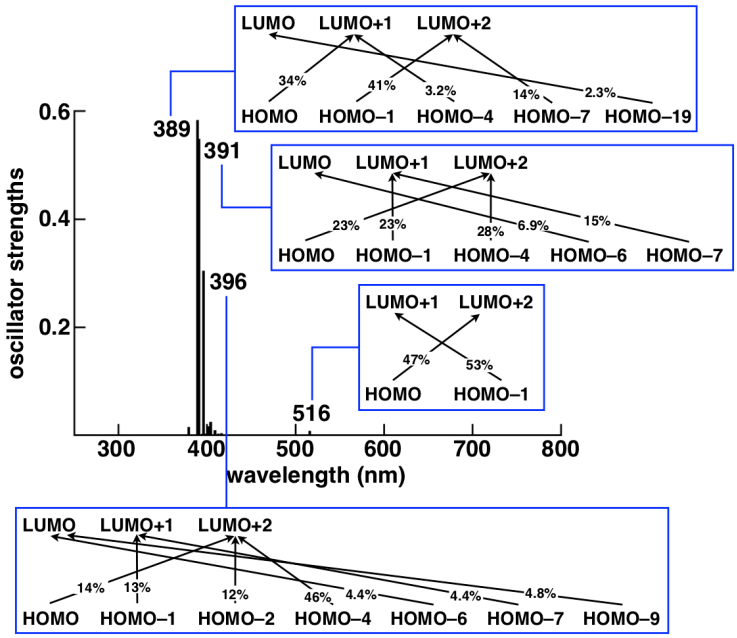

Figure 2–12 TD-DFT-based UV/vis absorption stick spectrum of **22**$^{+}$ with the transitions correlated with molecular orbitals estimated at B3LYP/6-31+G(d,p) for C, H, N, and F and B3LYP/LanL2DZ for Au.

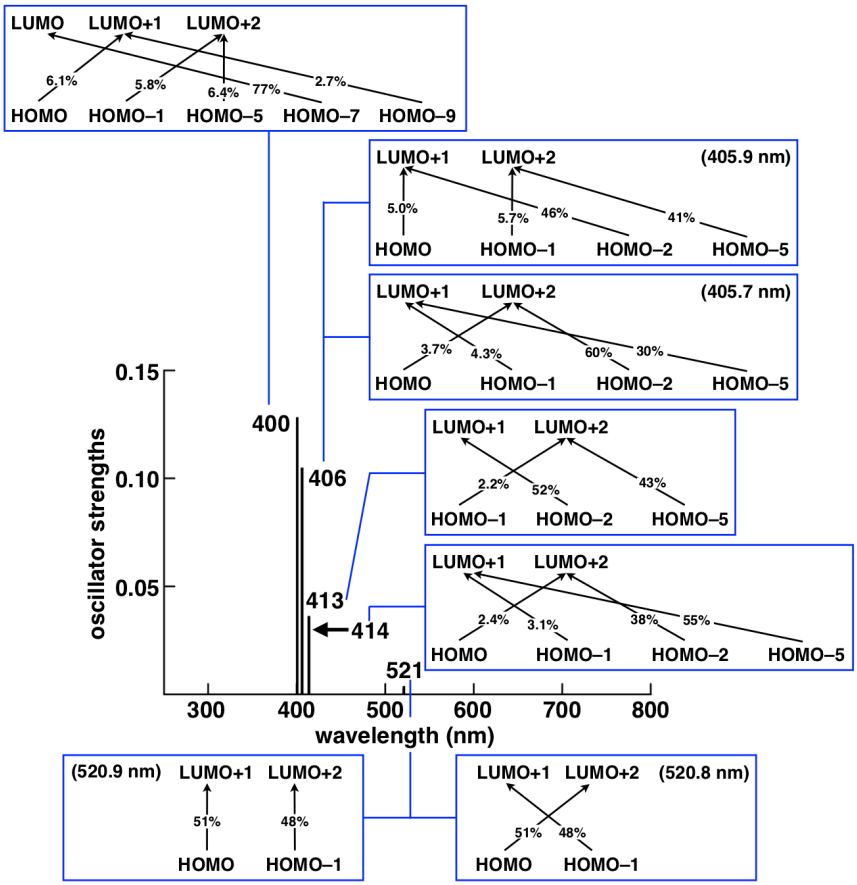

Figure 2–13 TD-DFT-based UV/vis absorption stick spectrum of **23**$^{+}$ with the transitions correlated with molecular orbitals estimated at B3LYP/6-31+G(d,p) for C, H, N, and F and B3LYP/LanL2DZ for Au.

2–3 Solid-State Assemblies of Cl^- Ion Pairs

The solid-state structure of the ion pair **22**$^+$-Cl^- was elucidated by X-ray analysis of single crystals prepared by vapor diffusion of CH_2Cl_2/*n*-hexane (Figure 2–14a).[67,68] Due to the partial substitution pattern, a columnar structure exhibiting stacked **22**$^+$ was observed in the crystal of **22**$^+$-Cl^- with stacking distances of 3.35 and 3.44 Å between the dipyrrin planes (core 11 atoms) and an Au···Au distance of 4.93 Å (Figure 2–14a i,ii). Stacking dimers of **22**$^+$ are formed in the arrangement to cancel their dipole moments. The Cl^- counteranion formed intermolecular hydrogen bonding with the CH of **22**$^+$ with C(–H)···Cl distances of 3.53 and 3.61 Å (Figure 5a iii). It is noteworthy that the proximal Au···Cl^- distance is 3.00 Å, which is comparable to the sum of the ionic radii of Au^{3+} and Cl^- (3.18 Å), suggesting an absence of a coordinating bond between them. Furthermore, the line passing through both Au and Cl has an angle of 81.1°, not 90°, to the mean plane of **22**$^+$ (core 25 atoms including Au). Therefore, Cl^- is not coordinated to the core Au but proximally located around **22**$^+$ via electrostatic interaction.

The exact solid-state structure and ion-pairing assembly of **23**$^+$-Cl^- were also elucidated by X-ray analysis of a single crystal, prepared by vapor diffusion of CH_2Cl_2/$CHCl_3$ (Figure 2–14b).[67,68] In the packing diagram, a columnar structure based on a charge-by-charge assembly was observed for **23**$^+$ and Cl^- associated with four co-crystalized $CHCl_3$ molecules with a distance of 6.57 Å between two **23**$^+$ planes (Figure 2–14b i,ii). The Au···Cl^- distance of 7.08 Å indicated no coordination between Cl^- and Au. The Cl^- counteranion exhibited intermolecular hydrogen bonding with *meso*-CH of **4**$^+$ and $CHCl_3$ with the C(–H)···Cl distances of 3.53 and 3.65 Å (Figure 2–14b iii). The porphyrin core was distorted, as indicated by the mean-plane deviation of the 25-atom plane of **23**$^+$ at 0.244 Å. Furthermore, ESP diagrams for **22**$^+$-Cl^- and **23**$^+$-Cl^- revealed that the electron density in the porphyrin–Au^{III} complexes is slightly larger at the sites proximal to the counteranions (Figure 2–14a,b iv).

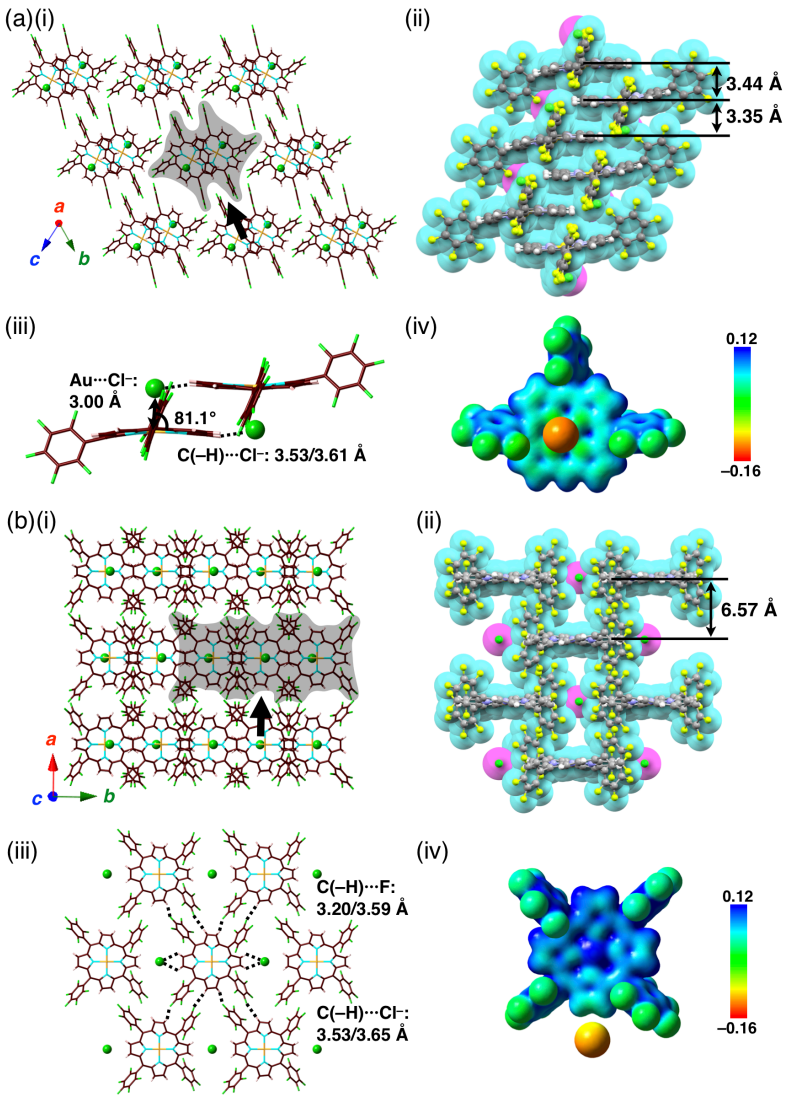

Figure 2–14 Single-crystal X-ray structures of (a) $\mathbf{22}^{+}$-Cl^{-} and (b) $\mathbf{23}^{+}$-Cl^{-}: (i) representative packing modes as top views, (ii) space-filling packing models as side views from arrows in (i), (iii) enlarged view of the packing structures in (i), and (iv) ESP mapped onto the electron density isosurface (δ = 0.01) for the ion pair calculated at B3LYP/6-31+G(d,p) for C, H, N, F, and Cl and LanL2DZ for Au based on the crystal structure. Solvent molecules are omitted for clarity. Atom color code in (i) and (iii): brown, pink, blue, green, green (sphere), and orange refer to carbon, hydrogen, nitrogen, fluorine, chlorine, and gold, respectively. Color code in (ii): cyan and magenta represent cations and anions, respectively.

2–4 Anion Exchange Providing a Variety of Ion-Pairing Assemblies

The Cl^{-} ion pairs were suitable for further anion exchange because of the high affinity of Cl^{-} for inorganic cations. In fact, Au^{III} complexes as Cl^{-} ion pairs were converted to a variety of ion pairs utilizing BF_4^{-}, PF_6^{-}, and $PCCp^{-}$,[26–28] by treatment with 3 equiv of Ag^{+} (BF_4^{-} and PF_6^{-}) or Na^{+} ($PCCp^{-}$) ion pairs, followed by the

removal of metal chlorides, column chromatography with silica gel and recrystallization (Figure 2–15). The ion pairs synthesized in this study, which were identified by spectroscopic and elemental analyses, showed no significant interactions between cationic Au^{III} complexes and coexisting anions in ^1H NMR at 20 °C.

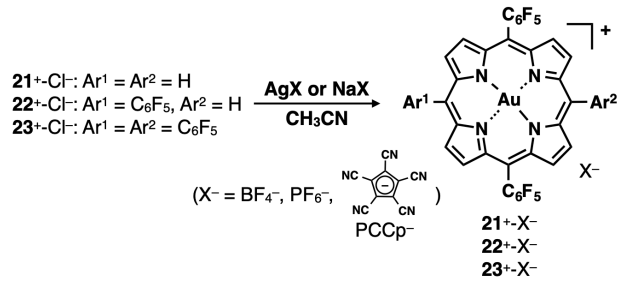

Figure 2–15 Synthetic route for ion pairs by anion exchange.

Counteranion exchange is an effective way to modify the assembly modes of ion pairs. BF_4^- and PF_6^- are common non-coordinating bulky anions. The exact structure of **23**$^+$-BF_4^-, which was prepared by vapor diffusion of cyclohexane into CH_2ClCH_2Cl, was revealed using single-crystal X-ray analysis (Figure 2–16a).[67,68] The C(–H)···F and F···π distances in the column are 3.06–3.24 and 2.92/3.08 Å, respectively, suggesting that the charge-segregated assembly is stabilized by hydrogen-bonding and F–π[69–71] interactions (Figure 2–16a iii). The ESP of **23**$^+$-BF_4^-, calculated at B3LYP/6-31+G(d,p) with LanL2DZ for Au based on the crystal structure,[66] revealed a larger negative charge in the C_6F_5 unit that forms F–π interaction with BF_4^- than the other C_6F_5 units in **23**$^+$ (Figure 2–16a iv). The single crystal of **21**$^+$-PF_6^- was obtained via the vapor diffusion of *n*-hexane into CH_2ClCH_2Cl and investigated via single-crystal X-ray analysis (Figure 2–17a). A two-by-two charge-by-charge structure was revealed, exhibiting a repeating arrangement of pairs of **21**$^+$-PF_6^- ion pairs and the stacking of **21**$^+$ planes with a distance of 3.64 Å (Figure 2–17a ii). The C(–H)···F distances in the column are 3.04–3.30 Å, suggesting a contribution from intermolecular hydrogen-bonding interactions (Figure 2–17a iii). Similar to **22**$^+$-Cl^-, **22**$^+$-PF_6^- formed a columnar assembly of **22**$^+$ with the distances of 3.50 and 3.84 Å between dipyrrin units (core 11 atoms) (Figure 2–17b). Dimeric structure is formed in the reversed orientations of two **22**$^+$ to cancel their dipole moments. Compared to the columnar structure of **22**$^+$-Cl, that of **22**$^+$-PF_6^- was formed more vertically by 17.6° due to the bulky PF_6^- counteranion relieving the steric hindrance of the C_6F_5 units (Figure 2–17b iii).

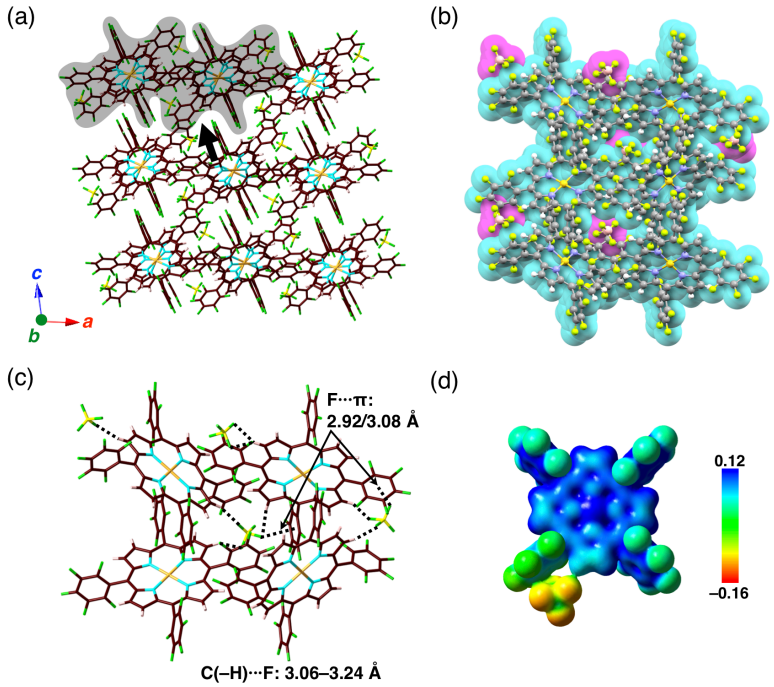

Figure 2–16 Single-crystal X-ray structure of **23**$^{+}$-BF_4^{-}: (a) representative packing mode as a top view, (b) space-filling packing model as a side view from arrow in (a), (c) enlarged view of the packing structure in (a), and (d) ESP mapped onto the electron density isosurface (δ = 0.01) for the ion pair calculated at B3LYP/6-31+G(d,p) for C, H, B, N, and F, and LanL2DZ for Au based on the crystal structure. Solvent molecules are omitted for clarity. Atom color code in (a) and (c): brown, pink, yellow, blue, green, and orange refer to carbon, hydrogen, boron, nitrogen, fluorine, and gold, respectively. Color code in (b): cyan and magenta represent cations and anions, respectively.

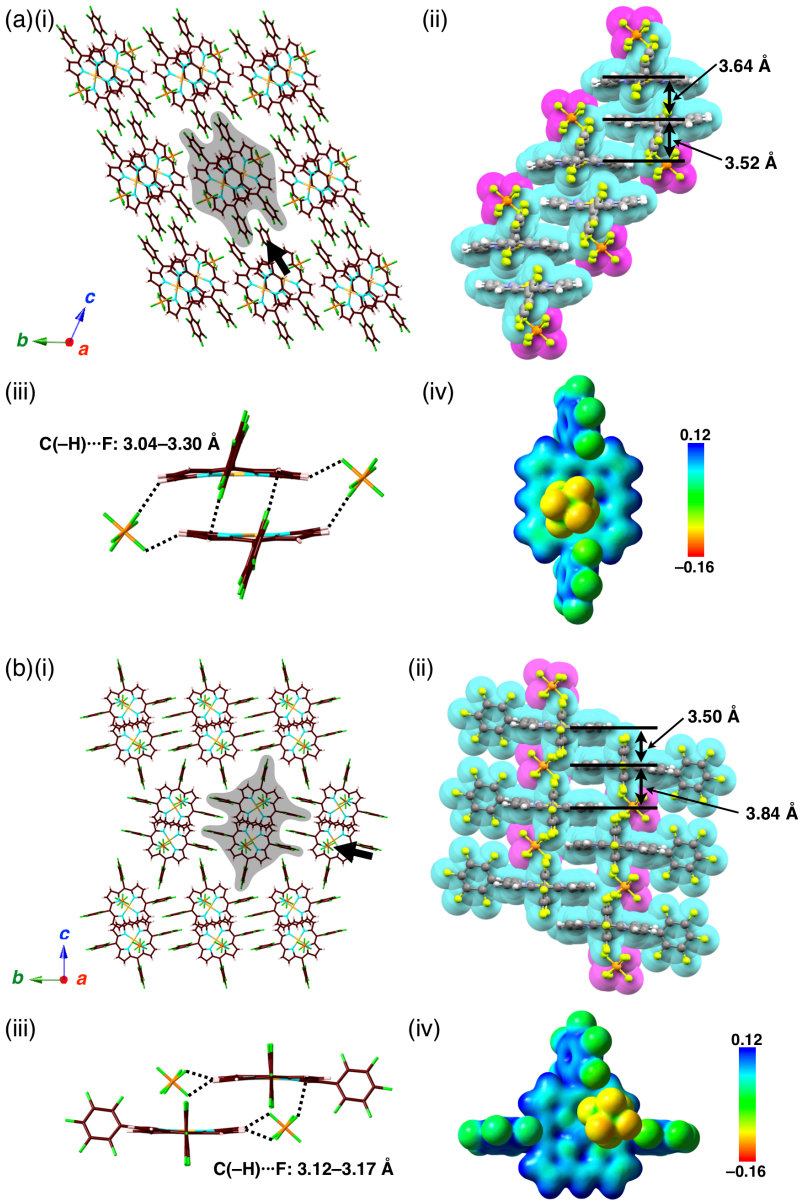

Figure 2–17 Single-crystal X-ray structures of (a) **21**$^{+}$-PF_6^{-} and (b) **22**$^{+}$-PF_6^{-}: (i) representative packing modes as top views, (ii) space-filling packing models as side views from arrows in (i), (iii) enlarged view of the packing structures in (i), and (iv) ESP mapped onto the electron density isosurface (δ = 0.01) for the ion pair calculated at B3LYP/6-31+G(d,p) for C, H, N, F, and P, and LanL2DZ for Au based on the crystal structure. Solvent molecules are omitted for clarity. Atom color code in (i) and (iii): brown, pink, blue, green, tangerine, and orange refer to carbon, hydrogen, nitrogen, fluorine, phosphorus, and gold, respectively. Color code in (ii): cyan and magenta represent cations and anions, respectively.

$PCCp^-$ is a stable six π-electron aromatic anionic species with a planar geometry and is an important building block for the alignment of π-electronic charged species.[28] A charge-by-charge assembly was observed in the single crystal of **21**$^+$-$PCCp^-$, which was prepared by vapor diffusion of THF/*n*-hexane (Figure 2–18a). A columnar structure comprising alternately stacked **21**$^+$ and $PCCp^-$ was observed with stacking distances of 3.34 and 3.40 Å between the porphyrin mean plane (core 25 atoms) and $PCCp^-$ (Figure 2–18b).[67,68] **21**$^+$-$PCCp^-$ formed two types of packing structures. Through hydrogen bonding between β-CH of **21**$^+$ and N of $PCCp^-$ with the C(–H)···N distances of 3.22–3.86 Å (Figure 2–18c), a perpendicularly stacking structure was formed (Figure 2–18b i). Via the formation of hydrogen bonding between β-CH and C–F of **21**$^+$ with C(–H)···F distances of 3.03 and 3.37 Å, **21**$^+$-$PCCp^-$ formed another columnar structure, wherein the neighboring planes were distorted with a dihedral angle of 149.7° (Figure 2–18b ii).

The single-crystal X-ray analysis of the ion pair **23**$^+$-$PCCp^-$ showed its solid-state ion-pairing assembly.[67,68] The single crystal of **23**$^+$-$PCCp^-$ was prepared by the vapor diffusion of CH_2Cl_2/*n*-hexane (Figure 2–19). In the solid state, **23**$^+$-$PCCp^-$ formed intermolecular hydrogen bonding between β-CH of **23**$^+$ and N of $PCCp^-$ with C(–H)···N distances of 3.10–3.88 Å (Figure 2–19b,c). Ion pair **23**$^+$-$PCCp^-$ showed the formation of a charge-by-charge assembly of **23**$^+$ and $PCCp^-$ (1:2) along with a columnar assembly of **23**$^+$. The $PCCp^-$ dimers with stacking distances of 3.28 and 3.31 Å were stabilized by hydrogen-bonding and π–π interactions (Figure 2–19). Formation of charge-by-charge stacking assemblies is consistent with the hard and soft acids and bases (HSAB) theory; soft anions such as $PCCp^-$ tend to interact with soft cations such as π-electronic cations. Furthermore, stabilized stacking of oppositely charged π-electronic system is suggested by ESP diagrams, wherein the positive charge in porphyrin–Au^{III} complexes is delocalized by stacking with $PCCp^-$, calculated at B3LYP/6-31+G(d,p) for C, H, N, and F and LanL2DZ for Au based on the crystal structures of **21**$^+$-$PCCp^-$ and **23**$^+$-$PCCp^-$ (Figure 2–18,19d).[66]

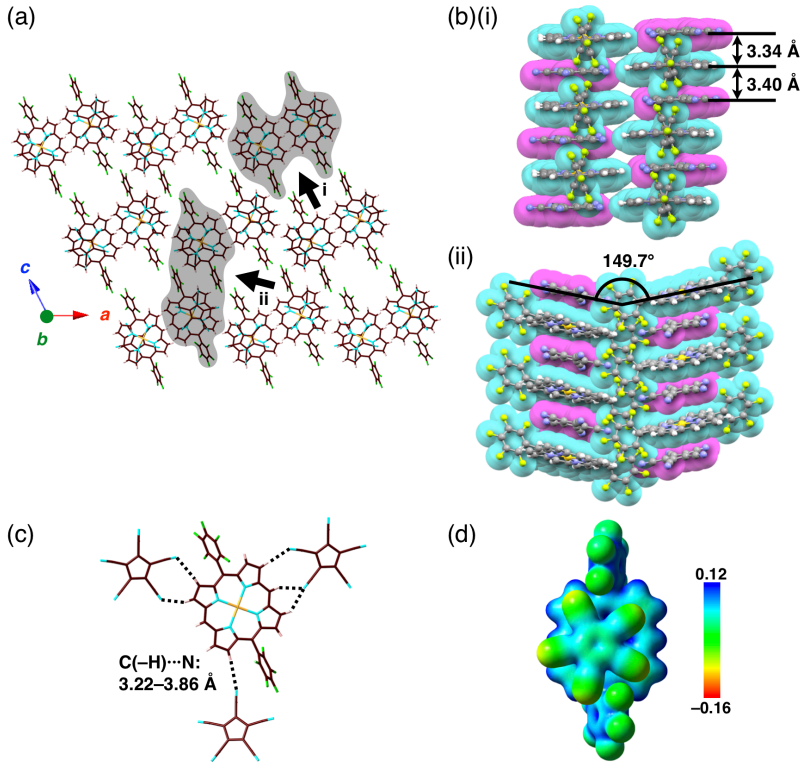

Figure 2–18 Single-crystal X-ray structures of **21**$^{+}$-PCCp^{-}: (a) representative packing modes as top views, (b) space-filling packing models as side views from arrows in (a), and (c) enlarged view of the packing structures in (a), and (d) ESP mapped onto the electron density isosurface (δ = 0.01) for the ion pair calculated at B3LYP/6-31+G(d,p) for C, H, N, and F and LanL2DZ for Au based on the crystal structures. Solvent molecules are omitted for clarity. Atom color code in (a) and (c): brown, pink, blue, and orange refer to carbon, hydrogen, nitrogen, fluorine, and gold, respectively. Color code in (b): cyan and magenta represent cations and anions, respectively.

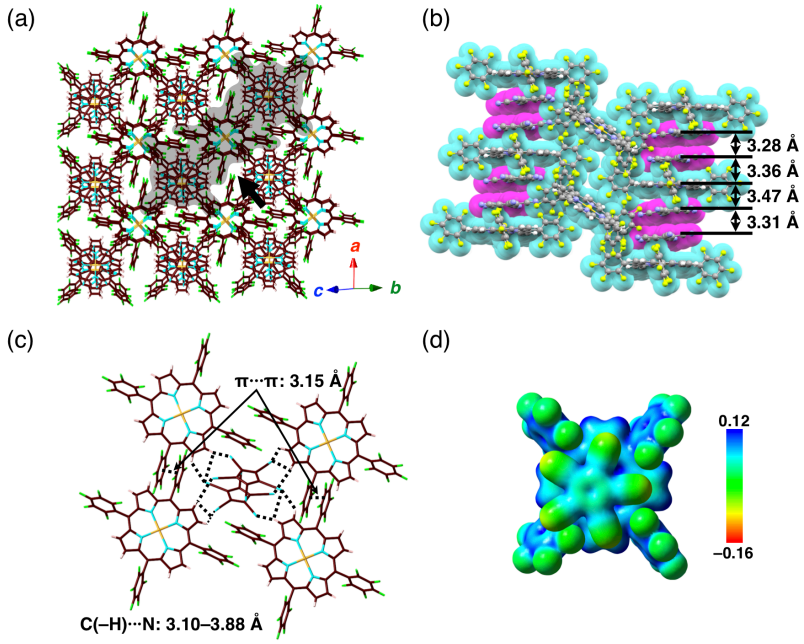

Figure 2–19 Single-crystal X-ray structures of **23**$^{+}$-PCCp^{-}: (a) representative packing modes as top views, (b) space-filling packing models as side views from arrows in (a), and (c) enlarged view of the packing structures in (a), and (d) ESP mapped onto the electron density isosurface (δ = 0.01) for the ion pair calculated at B3LYP/6-31+G(d,p) for C, H, N, and F and LanL2DZ for Au based on the crystal structures. Solvent molecules are omitted for clarity. Atom color code in (a) and (c): brown, pink, blue, and orange refer to carbon, hydrogen, nitrogen, fluorine, and gold, respectively. Color code in (b): cyan and magenta represent cations and anions, respectively.

2–5 Summary of Chapter 2

Partial or total peripheral modifications of π-electronic cations were realized based on C_6F_5-substituted porphyrin–Au^{III} complexes. Porphyrin–Au^{III}-based ion pairs formed charge-by-charge and charge-segregated assemblies in single crystals, depending on the substitution patterns of the C_6F_5 units and the geometries of the anionic species. Importantly, hydrogen-bonding donor properties of β-CH of the porphyrin core were observed in the packing structures, due to the electron-withdrawing effects of the C_6F_5 units. Combination with π-electronic anion induced the delocalization of the positive charge in π-electronic cations, resulting in charge-by-charge stacking assemblies.

Chapter 3

Ion-Pairing Assemblies of Porphyrin–Au^{III} Complexes in Combination with π-Electronic Receptor–Anion Complexes

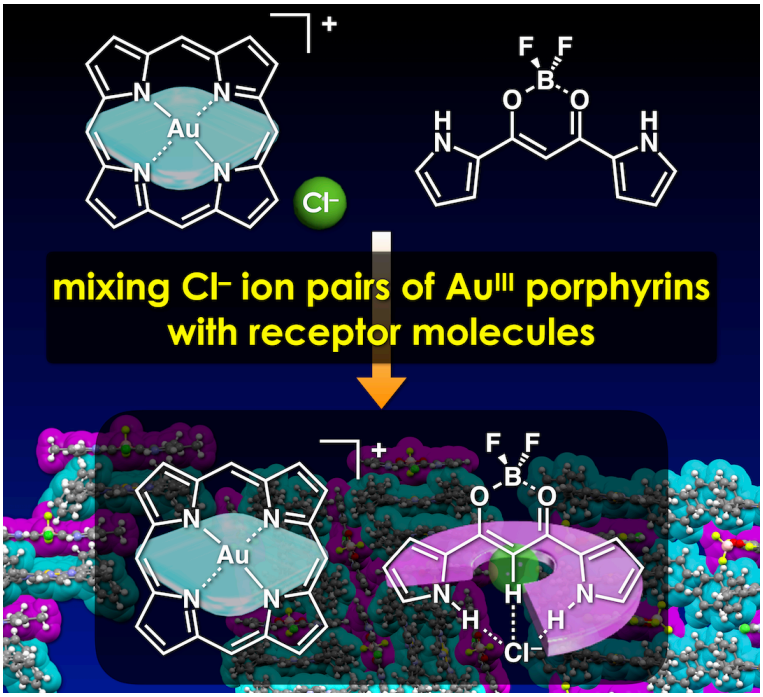

Contents

3–1 Introduction

It is challenging to synthesize π-electronic anions since their excess electrons induce electrophilic reactions. Negatively charged π-electronic systems can be constructed effectively by complexing inorganic anions by electronically neutral π-electronic molecules.[1] Using this strategy, various pseudo π-electronic anions can be formed by combining host π-electronic molecules (receptors) and guest anions. Dipyrrolyldiketone BF_2 complexes (e.g., **24**–**27**, Figure 3–1) are useful receptor molecules that make planar complexes with halide anions[23,72–74] and ion-pairing assemblies in the solid and soft material states.[24,75,76] As a result of anion binding, hard guest anions are transformed into soft anions. Because the anion forms complexes by association with π-electronic systems, properties of the anion complexes can be controlled by the π-electronic receptor molecules. $TATA^+$ cations $\mathbf{12}^+$ [20,21] have been used as π-electronic countercations for the receptor–anion complexes, due to their appropriate geometries.[24,74,76,77] Similarly, the receptor–anion complexes can also be included in cationic porphyrin–Au^{III} complex ion pairs. Herein, this chapter includes their solid-state ion-pairing assemblies and related theoretical studies.

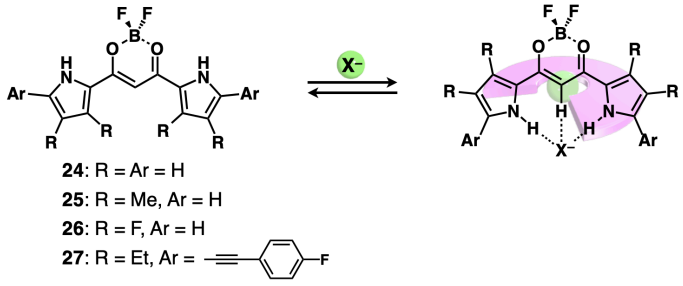

Figure 3–1 π-Electronic anion receptors **24**–**27** and their anion-binding mode.

3–2 Solution- and Solid-State Properties of Ion Pairs Comprising Porphyrin–Au^{III} Complex and Unsubstituted Receptor–Anion Complexes

The formation of ion pairs comprising receptor–anion complexes requires positively charged Au^{III} complex ion pairs of halide anions, such as Cl^-, which is efficiently bound by dipyrrolyldiketone BF_2 complexes. Upon the addition of Cl^- as a $\mathbf{16}^+$ ion pair, ^1H NMR signals of the pyrrole NH and bridged CH of **24** in CD_2Cl_2 (1.0×10^{-3} M) at 20 °C were shifted downfield from 9.61 and 6.58 ppm to 11.52 and 7.56 ppm, respectively, as a result of anion binding (Figure 3–2). The chemical shifts of $\mathbf{24}\cdot Cl^-$ were influenced by shielding effects upon the tightly bound ion pairing with $\mathbf{16}^+$, which exhibits characteristic upfield shifts compared to the ion-unpairing

states of the TBA^+ ion pair of **24**·Cl^- in CD_2Cl_2 and $CDCl_3$ (1.0×10^{-3} M) at 20 °C. Solution-state equilibria for ion pairs comprising receptor–anion complexes and countercations are difficult to assess. Thus, solid-state packing structures, which lack equilibrium processes, are more suitable for evaluating association behaviors and interactions between the constituent ionic species.

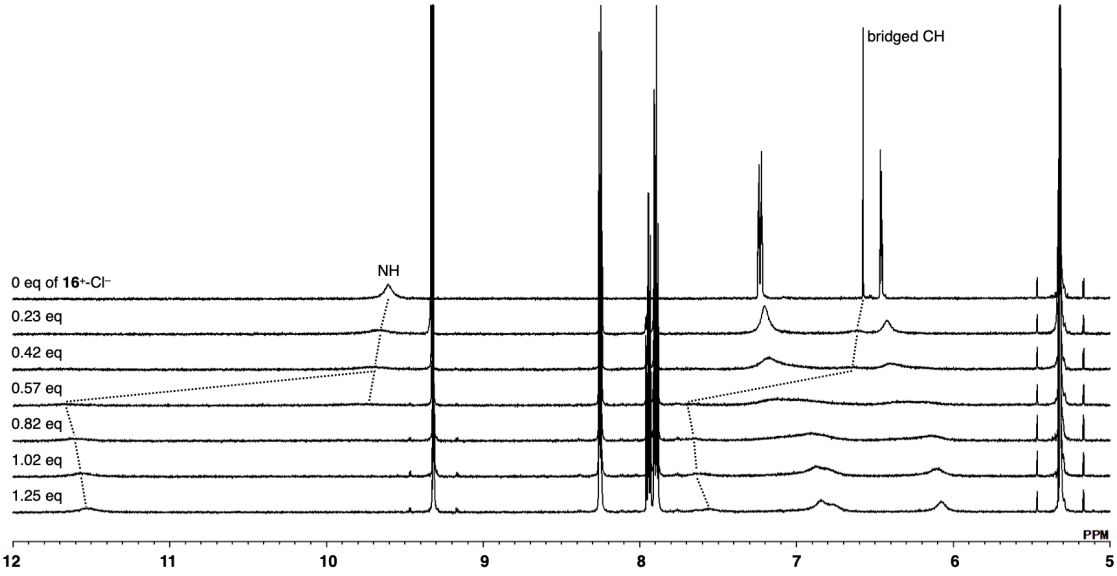

Figure 3–2 ^{1}H NMR spectral changes of **24** (1.0×10^{-3} M) upon the addition of Cl^- (0–1.25 equiv) added as a $\mathbf{16}^+$ ion pair in CD_2Cl_2 at 20 °C.

A mixture of $\mathbf{16}^+$·Cl^- and anion receptors produces receptor–Cl^- complexes accompanied with $\mathbf{16}^+$, which form ion pairs and their assemblies after the appropriate purifications. The X-ray structure of $\mathbf{16}^+$-**24**·Cl^- was determined from a single crystal obtained by vapor diffusion of *n*-hexane into a CH_2Cl_2 solution of containing a 1:1 mixture of $\mathbf{16}^+$·Cl^- and the parent **24**.[67,68] The ion pair showed a [1+1]-type Cl^- complex **24**·Cl^-; it is noteworthy that this is the first example of a [1+1]-type Cl^- complex of **24** in the solid state. Ion pairs with TBA^+ and $\mathbf{12}^+$ formed Cl^--bridged 1D chain structures with a single pyrrole inversion[23] and a planar [2+1]-type complex,[77] respectively. The geometry of **24**·Cl^- is suitable to stack with $\mathbf{16}^+$ at the core plane (Figure 3–3). In this ion pair, two pyrrole NH and bridged CH of **24** and a *meso*-phenyl-*o*-CH of $\mathbf{16}^+$ interact with Cl^-, giving rise to N(–H)···Cl^-, C(–H)···Cl^-, and Ph-C(–H)···Cl^- distances of 3.30/3.32, 3.47, and 3.68 Å, respectively (Figure 3–3a). In the packing diagram, a tetrameric stacking assembly comprising two $\mathbf{16}^+$ and two **24**·Cl^-, located at the tetramer ends, is packed almost perpendicularly to the neighboring tetramer with β-C(–H)···F and Ph-C(–H)···Cl^- distances of 3.11/3.39 and 3.43/3.51 Å, respectively (Figure 3–3b,c), suggesting that the almost orthogonal structure forms by hydrogen-bonding interactions between the β-CH of $\mathbf{16}^+$ and the BF_2 unit of

24·Cl^- and between Ph-CH of $\mathbf{16}^+$ and Cl^- of **24**·Cl^-, respectively. These tetramers exhibit stacking either two $\mathbf{16}^+$ units or one $\mathbf{16}^+$ and one **24**·Cl^- with distances of 3.54 and 3.68 Å, respectively, estimated as the distance between two porphyrin mean planes (defined hereafter as a core of 25 atoms, including Au) and the average distance between the porphyrin mean planes and the dipyrrolydiketone units (hereafter defined as 15 atoms), respectively (Figure 3–3d). The dimeric structure of $\mathbf{16}^+$ is also observed in the crystal packing of $\mathbf{16}^+$-Cl^- with a co-crystallized $CHCl_3$ molecule.[39]

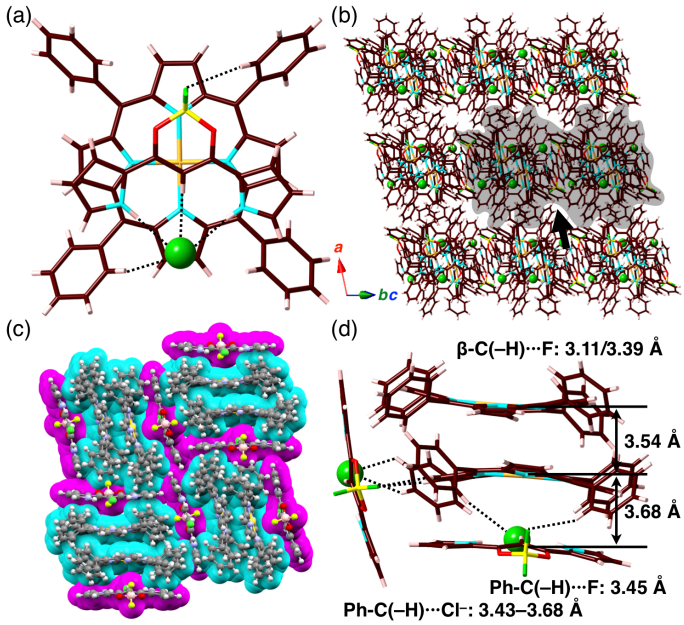

Figure 3–3 Single-crystal X-ray structure of $\mathbf{16}^+$-**24**·Cl^-: (a) one ion pair showing the hydrogen-bonding interaction (black broken lines), (b) representative packing structure mode as the top view, (c) space-filling packing model as the side view from the arrow in (b), and (d) enlarged view of the packing structure in (c). Solvent molecules are omitted for clarity. Color code in (c): cyan and magenta represent cations and anions, respectively. Atom color code in (a),(b),(d): brown, pink, yellow, blue, red, green, green (sphere), and orange refer to carbon, hydrogen, boron, nitrogen, oxygen, fluorine, chlorine, and gold, respectively.

3–3 Modulation of Ion-Pairing Assemblies by Modifications of Receptor Molecules

Various ion-pairing assemblies were constructed by modifying receptor molecules such as the introduction of β-substituents. The exact solid-state structures and ion-pairing assemblies of **16**$^+$-**25**,**26**·Cl^- were elucidated by X-ray analysis of single crystals,[67,68] which were prepared from 1:1 mixtures of **16**$^+$·Cl^- and **25**,**26** in solution by vapor diffusion of $CHCl_3$/*n*-hexane and CH_2Cl_2/*n*-hexane, respectively. In ion pairs with **16**$^+$, **25**·Cl^- and **26**·Cl^- exist as [1+1]-type Cl^- complexes with N/C(–H)···Cl^- average distances of 3.30/3.46 and 3.22/3.36 Å, respectively (Figure 3–4a,5a). The **16**$^+$-**26**·Cl^- pair exhibits a [1+1]-type Cl^- complex similar to that of the $TATA^+$ ion pair,[77] but in contrast to the Cl^--bridged 1D chain structure without pyrrole inversions of the TBA^+ ion pair.[73] Interestingly, **16**$^+$-**25**·Cl^- demonstrates the first solid-state structure of anion complexes of **25**. In contrast to **16**$^+$-**5**·Cl^-, the β-modified **16**$^+$-**25**,**26**·Cl^- displayed columnar assemblies comprising alternately stacked **16**$^+$ and receptor–Cl^- complexes **25**,**26**·Cl^- (Figure 3–4,5b,c), with distances of 3.56/3.66 and 3.50/3.75 Å, respectively, estimated from the average distances between the porphyrin mean planes and the dipyrrolyldiketone units. Steric hindrance between the *meso*-phenyl units of **16**$^+$ and the methyl moieties of **25**·Cl^- produced the **16**$^+$-**25**·Cl^- packing structure with alternately offset stacked ion pairs at 3.66 Å. The lines through two Au atoms to the corresponding porphyrin core were estimated at 44.5° and 49.0°. In the solid state, **16**$^+$-**25**·Cl^- forms hydrogen bonding of the CH of **16**$^+$ with Cl^- and BF_2 unit in **25**·Cl^- with distances of 3.78/3.83 and 3.35–3.48 Å, respectively (Figure 3–4d). On the other hand, **16**$^+$-**26**·Cl^- forms a columnar structure arranged more vertically by 25.9° than that of **16**$^+$-**25**·Cl^- with hydrogen bonding between the phenyl-CH of **16**$^+$ and the β-F of **26** having C(–H)···F distances of 3.35–3.82 Å. The Au···Au distance (7.44 Å) was almost equal to the sum of the two stacking distances for **16**$^+$ and **26**·Cl^-, suggesting almost completely perpendicular stacking (Figure 3–5d).

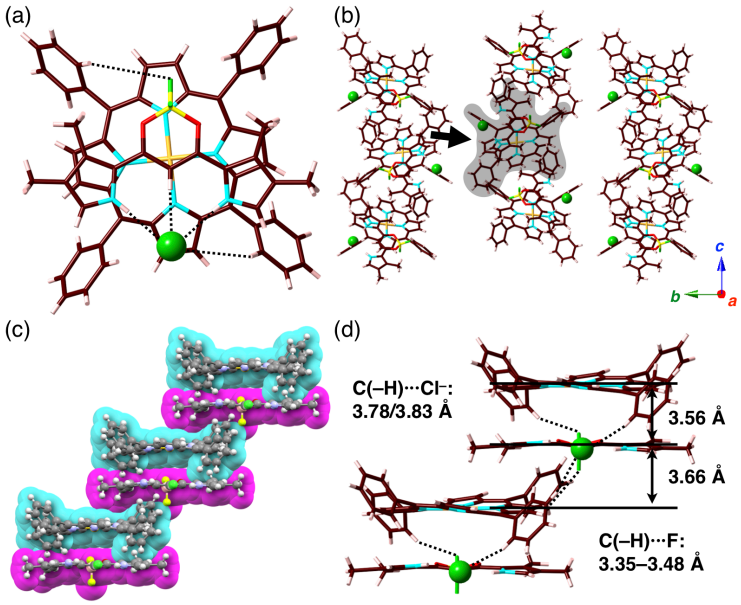

Figure 3–4 Single-crystal X-ray structure of **16**$^{+}$-**25**·Cl^{-}: (a) one ion pair showing the hydrogen-bonding interaction (black broken lines), (b) representative packing structure mode as the top view, (c) space-filling packing model as the side view from the arrow in (b), and (d) enlarged view of the packing structure in (c). Solvent molecules are omitted for clarity. Color code in (c): cyan and magenta represent cations and anions, respectively. Atom color code in (a),(b),(d): brown, pink, yellow, blue, red, green, green (sphere), and orange refer to carbon, hydrogen, boron, nitrogen, oxygen, fluorine, chlorine, and gold, respectively.

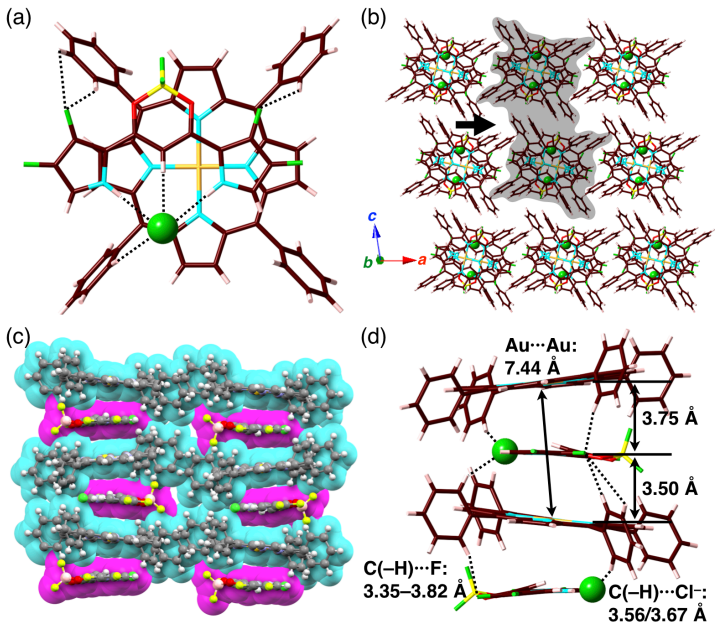

Figure 3–5 Single-crystal X-ray structure of **16**$^+$-**26**·Cl$^-$: (a) one ion pair showing the hydrogen-bonding interaction (black broken lines), (b) representative packing structure mode as the top view, (c) space-filling packing model as the side view from the arrow in (b), and (d) enlarged view of the packing structure in (c). Solvent molecules are omitted for clarity. Color code in (c): cyan and magenta represent cations and anions, respectively. Atom color code in (a),(b),(d): brown, pink, yellow, blue, red, green, green (sphere), and orange refer to carbon, hydrogen, boron, nitrogen, oxygen, fluorine, chlorine, and gold, respectively.

One key route to provide diverse π-electronic systems is to modify the α-positions of anion receptors. Arylethynyl-substituted receptors (e.g., **27**) exhibit various anion-binding modes, planar [1+1]-type and interlocked [2+1]-type complexes, and resulting ion-pairing assemblies.[74] Vapor diffusion of *n*-hexane into a 1:1 mixture of **16**$^+$-Cl$^-$ and **27** in CH_2Cl_2 produced a single crystal of the [1+1]-type Cl$^-$ complex **27**·Cl$^-$ with **16**$^+$ for X-ray analysis.[67,68] The inverted pyrrole NH and bridged CH of **27** are associated with a Cl$^-$ ion with N/C(–H)···Cl$^-$ average distances of 3.25 and 3.41 Å, respectively (Figure 3–6a). Similar to **16**$^+$-**25**·Cl$^-$, **16**$^+$-**27**·Cl$^-$ exhibited the offset stacking, due to the bulky β-ethyl and α-arylethynyl substituents, with a line passing through the two Au atoms to the mean plane of **16**$^+$ estimated at 47.9° (Figure 3–6b,c). The C(–H)···F distance in the column is 3.03 Å, suggesting hydrogen-bonding interactions between the β-CH of **16**$^+$ and the BF_2 unit of **27**·Cl$^-$ (Figure 3–6d).

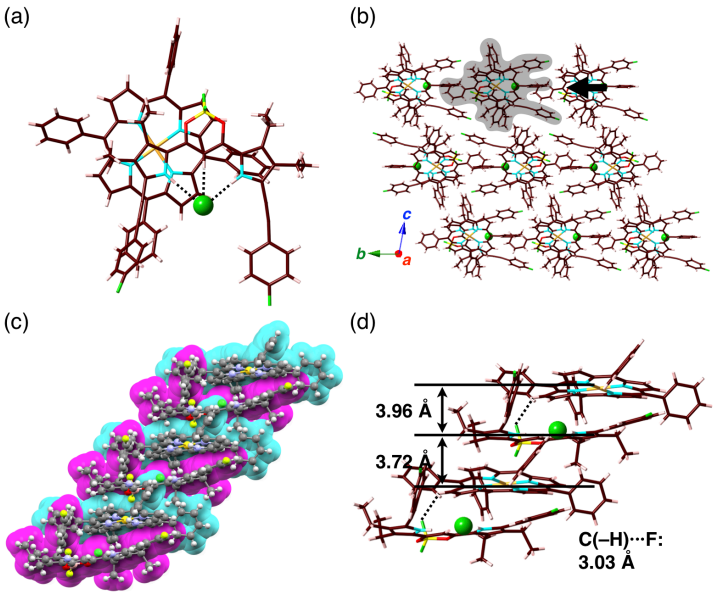

Figure 3–6 Single-crystal X-ray structure of **16**$^+$-**27**·Cl^-: (a) one ion pair showing the hydrogen-bonding interaction (black broken lines), (b) representative packing structure mode as the top view, (c) space-filling packing model as the side view from the arrow in (b), and (d) enlarged view of the packing structure in (c). Solvent molecules are omitted for clarity. Color code in (c): cyan and magenta represent cations and anions, respectively. Atom color code in (a),(b),(d): brown, pink, yellow, blue, red, green, green (sphere), and orange refer to carbon, hydrogen, boron, nitrogen, oxygen, fluorine, chlorine, and gold, respectively.

3–4 Evaluation of Stacked Structures by Theoretical Calculations

ESP diagrams of the stacked ion pairs **16**$^+$-**24**–**27**·Cl^- demonstrated the compensation of the positive and negative charges in **16**$^+$ and **24**–**27**·Cl^-, respectively, in contrast to those of their unpairing states, calculated at B3LYP/6-31+G(d,p) with LanL2DZ for Au based on the corresponding crystal structures (Figure 3–7).[66] These results suggest that electrostatic interactions between **16**$^+$ and **24**–**27**·Cl^- are essential for stabilizing stacking in the oppositely charged π-electronic systems. In the ion pair **16**$^+$-Cl^-, obtained as two crystal pseudo-polymorphs with one and four $CHCl_3$ molecules around the Cl^-, Cl^- was not coordinated to the core Au^{III} but located proximal to the Au^{III} by electrostatic interaction, with Au···Cl^- distances of 3.00 and 3.12 Å, and the lines passing through both Au and Cl^- to the porphyrin (**16**$^+$) mean plane measuring 76.9° and 80.2°, respectively.[39] Despite the negative charge distribution of Cl^- observed in ESP diagrams, Cl^- of **16**$^+$-**24**–**26**·Cl^- was located above the edge of the porphyrin–Au^{III} core plane with Au···Cl^- distances of 4.67, 5.14, and 4.40 Å, respectively, and Cl–Au–**16**$^+$ angles of 42.0°, 41.9°, and 48.1°, respectively, since the geometries of **24**–**26**·Cl^- fit well with the core plane of **16**$^+$. Furthermore, **16**$^+$-**27**·Cl^- showed that Cl^- was arranged out of the core plane of **16**$^+$ with Au···Cl^- distance of 5.72 Å and Cl–Au–**16**$^+$ angle of 39.1°,

resulting in the offset stacking of **16**$^+$ and **27**·Cl$^-$ (Figure 3–8). Hirshfeld surface analysis of **16**$^+$ mapped over shape-index and curvedness properties indicates that the packing structures of **16**$^+$-**24**–**27**·Cl$^-$ are also stabilized by the interactions between **16**$^+$ and **24**–**27**·Cl$^-$ (Figure 3–9).[78–80] In particular, the surfaces of **16**$^+$-**24**·Cl$^-$ show the red and blue triangles arranged in bow-tie shapes on the shape-index surface and a flat region on the curvedness surface, indicating the characteristic mapping pattern for stacking structures of receptor–anion complexes and the core part of **16**$^+$.[79,81]

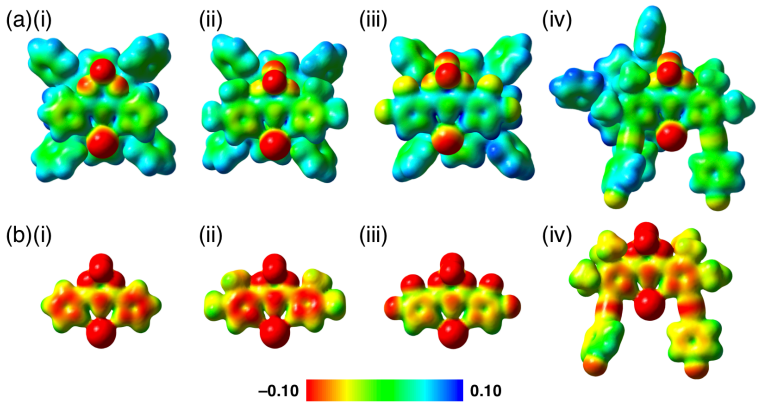

Figure 3–7 ESP mapped onto the electron density isosurface (δ = 0.01) for (a) stacked ion pairs and (b) receptor–anion complexes calculated at B3LYP/6-31+G(d,p) for C, H, B, N, O, F, and Cl and LanL2DZ for Au based on the crystal structures of (i) **16**$^+$-**24**·Cl$^-$, (ii) **16**$^+$-**25**·Cl$^-$, (iii) **16**$^+$-**26**·Cl$^-$, and (iv) **16**$^+$-**27**·Cl$^-$.

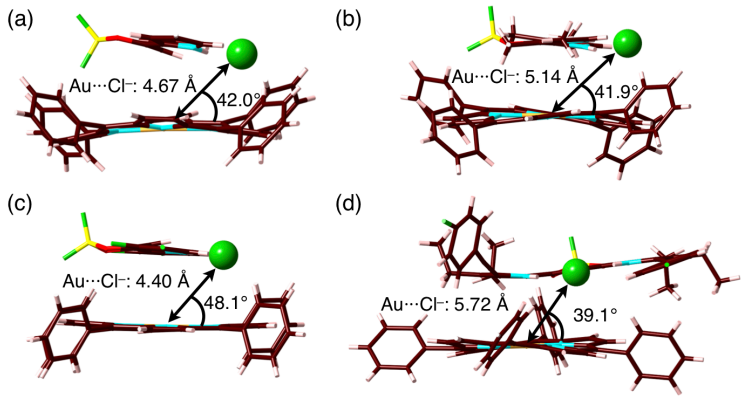

Figure 3–8 Summarized crystal structures (side views) of (a) **16**$^+$-**24**·Cl$^-$, (b) **16**$^+$-**25**·Cl$^-$, (c) **16**$^+$-**26**·Cl$^-$, and (d) **16**$^+$-**27**·Cl$^-$. Atom color code: brown, pink, yellow, blue, red, green, green (sphere), and orange refer to carbon, hydrogen, boron, nitrogen, oxygen, fluorine, chlorine, and gold, respectively.

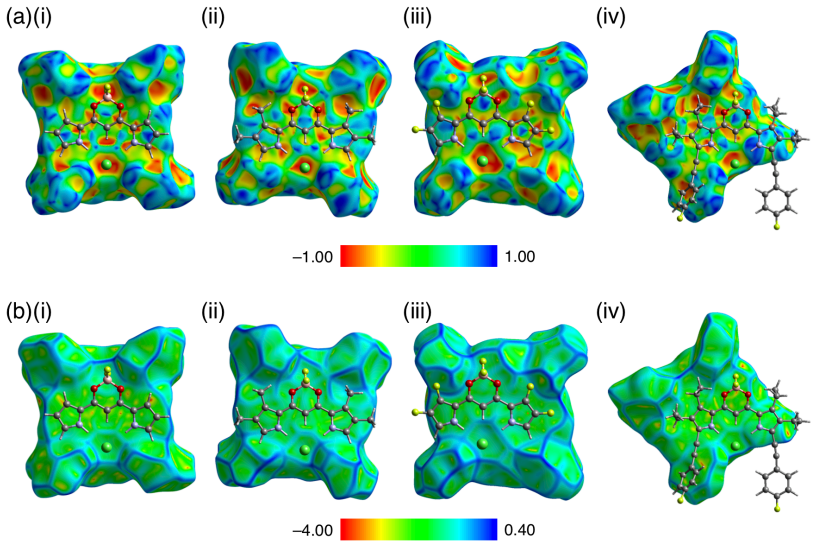

Figure 3–9 Hirshfeld surface of $\mathbf{16}^+$ mapped over (a) shape-index property and (b) curvedness property in the crystal structure of (i) $\mathbf{16}^+$-**24**·Cl^-, (ii) $\mathbf{16}^+$-**25**·Cl^-, (iii) $\mathbf{16}^+$-**26**·Cl^-, and (iv) $\mathbf{16}^+$-**27**·Cl^-. Atom color code: gray, white, pink, blue, red, yellow, and green refer to carbon, hydrogen, boron, nitrogen, oxygen, fluorine, and chlorine, respectively.

3–5 Modulation of Assembly by Introduction of Partially *meso*-Substituted Porphyrin–Au^{III} Complex

The *meso*-substituents of porphyrin–Au^{III} complexes are also important for controlling the ion-pairing assembled structures. According to Chapter 2, porphyrin–Au^{III} complexes that are partially substituted with *meso*-pentafluorophenyl units, including 5,10,15-trisubstituted $\mathbf{22}^+$, display the electron-deficient properties and solid-state columnar structures, depending on substitution patterns. Single-crystal X-ray analysis of the ion pair $\mathbf{22}^+$-**26**·Cl^- reveals a solid-state ion-pairing assembly.[67,68] The single crystal of $\mathbf{22}^+$-**26**·Cl^- was prepared by vapor diffusion of 1,4-dioxane into a 1:1 mixture of $\mathbf{22}^+$·Cl^- and **26** in CH_2ClCH_2Cl. In contrast to the other ion pairs discussed in this report, the ion pair $\mathbf{22}^+$-**26**·Cl^- in the solid state exhibited a [2+2]-type Cl^- complex $\mathbf{26}_2$·Cl^-_2, whose pyrrole NH and bridged CH of **26**, and *meso*- and β-CH of $\mathbf{22}^+$ interact with Cl^- with N(–H)···Cl^-, C(–H)···Cl^-, and *meso*- and β-C(–H)···Cl^- distances of 3.04/3.04, 3.73, 3.44, and 3.55 Å, respectively (Figure 3–10a). Comparison of the ion pairs of **26**·Cl^- with $\mathbf{16}^+$ and $\mathbf{22}^+$ indicates that the geometries and electronic structures of coexisting cations modulate the solid-state anion-binding modes. A two-by-two charge-by-charge columnar structure is observed (Figure 3–10b,c), in which dimeric stacking of $\mathbf{22}^+$ has a stacking distance of 3.25 Å between the porphyrin mean planes (Figure 3–10d). This dimeric structure is also observed in the solid states of $\mathbf{22}^+$-Cl^- and $\mathbf{22}^+$-PF_6^-, wherein two $\mathbf{22}^+$ are stacked in reversed orientation, cancelling the dipole moments. The Cl^-···Cl^- distance in the column is 3.98 Å (Figure 3–

10a), suggesting that the electrostatic repulsion between two Cl^- can be overcome by hydrogen-bonding and electrostatic interactions between $\mathbf{26}_2 \cdot Cl^-_2$ with two $\mathbf{22}^+$, as revealed by the ESP diagram calculated at B3LYP/6-31+G(d,p) with LanL2DZ for Au based on the crystal structure (Figure 3–11).[66] The electron-withdrawing effects of C_6F_5 units in $\mathbf{22}^+$ enhance the hydrogen-bonding donor ability of the *meso*- and β-CH of the porphyrin core. Thus, electron-deficient porphyrin–Au^{III} complexes can stabilize negative charges on $\mathbf{26}_2 \cdot Cl^-_2$, resulting in closely arranged identically charged species.

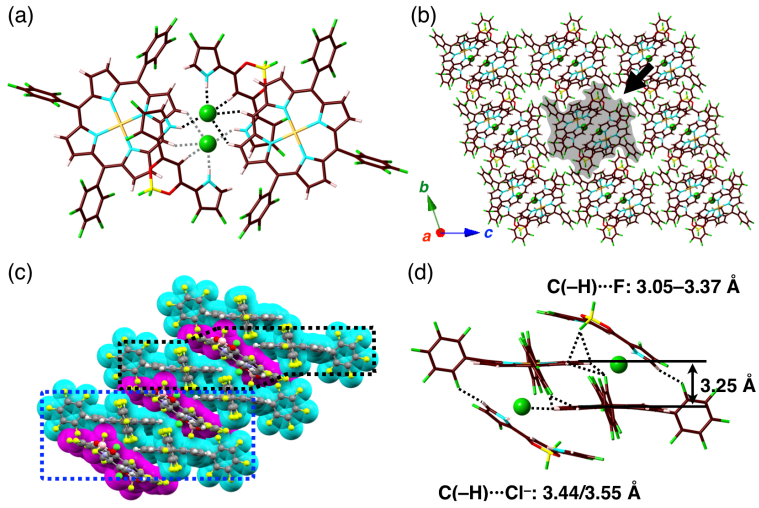

Figure 3–10 Single-crystal X-ray structure of $\mathbf{22}^+$-$\mathbf{26} \cdot Cl^-$: (a) two ion pairs showing the hydrogen-bonding interaction (black broken lines), as indicated blue-dashed area in (c), (b) representative packing structure as the top view, (c) space-filling packing model as the side view from the arrow in (b), and (d) enlarged view of the packing structure, as indicated by black dashed area in (c). Color code in (c): cyan and magenta represent cations and anions, respectively. Atom color code in (a),(b),(d): brown, pink, yellow, blue, red, green, green (sphere), and orange refer to carbon, hydrogen, boron, nitrogen, oxygen, fluorine, chlorine, and gold, respectively.

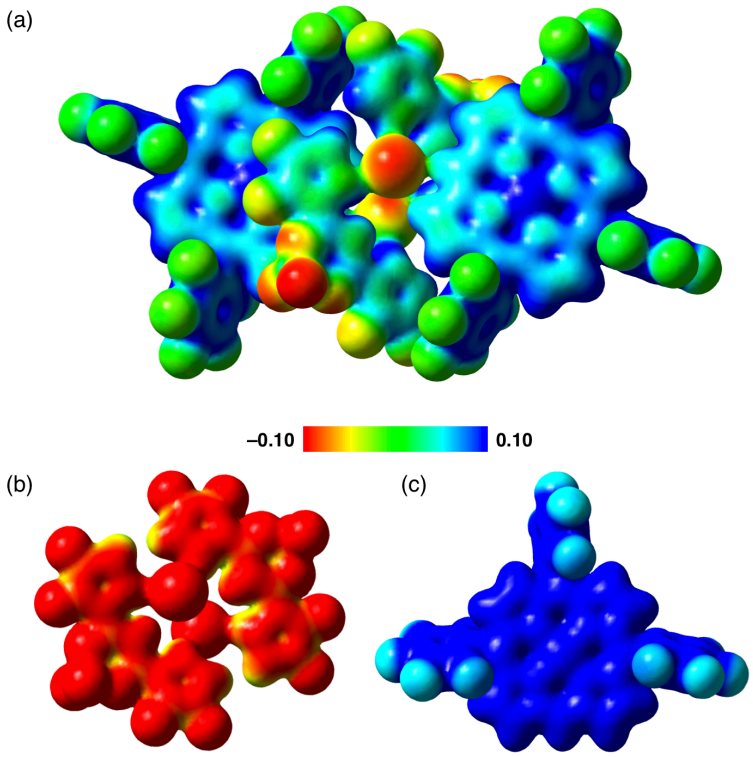

Figure 3–11 Electron density diagrams (top and side views) of (a) two sets of **22**$^{+}$-**26**·Cl^{-}, (b) two sets of **26**·Cl^{-} (**26**$_2$·Cl^{-}_2), and (c) **22**$^{+}$ in the crystal structure of **22**$^{+}$-**26**·Cl^{-}. ESP were mapped onto the electron density isosurface (δ = 0.01) calculated at B3LYP/6-31+G(d,p) for C, H, B, N, O, F, and Cl, and B3LYP/LanL2DZ for Au.

3–6 Summary of Chapter 3

π-Electronic ion-pairing assemblies of porphyrin–Au^{III} complexes and diverse receptor–anion complexes were constructed in the solid state. The combination of ions controls the properties of assembled structures. In particular, ordered assembled structures were formed readily due to the large π-systems of cationic porphyrins and anion complexes. The use of π-electronic ions that can be peripherally modified is very effective for the preparation of various interesting ion pairs and their resulting functional materials. Ion pairs of positively charged porphyrins and negatively charged receptor–anion complexes are suitable for fabricating a library of charge-based assemblies.

Chapter 4

Ion-Pairing Assemblies Comprising Porphyrin–Au^{III} Complexes and Helical π-System–Anion Complexes

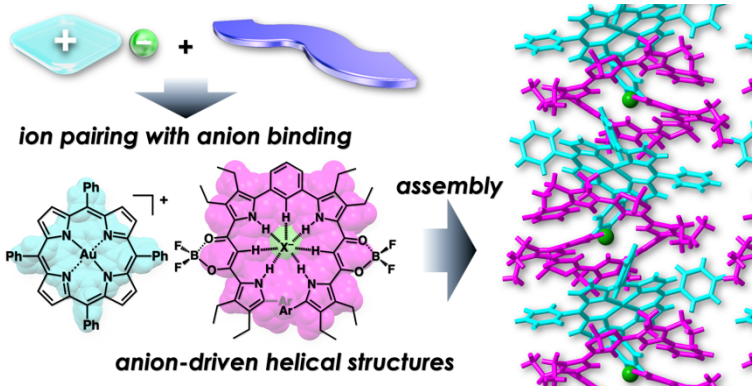

Contents

4–1 Introduction

As shown in Chapter 3, dipyrrolyldiketone boron complexes, which associate anions with pyrrole inversions, provide functionalities through various peripheral modifications.[82–84] *Meta*-phenylene-bridged dimer derivatives (e.g., **28** and **29**; Figure 4–1) form anion-driven helical structures,[85–100] which enable the induction of chirality[99] and hydrostatic pressure control[100] via anion recognition and ion-pair formation with chiral countercations. Furthermore, the anion complexes of **28** and **29** can be used as pseudo-π-electronic anions because the dimers show high anion-binding constants (5.9×10^7 and 1.2×10^7 M^{-1}, respectively) in titration experiments of tetrabutylammonium chloride (TBACl) in CH_2Cl_2.[98] This chapter introduces the π-electronic ion pairs of porphyrin–Au^{III} complexes with helical π-electronic receptor–anion complexes and their ion-pairing assemblies.

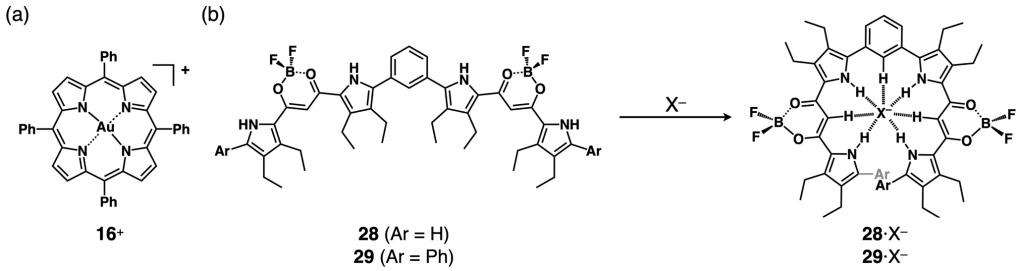

Figure 4–1 (a) Tetraphenylporphyrin Au^{III} complex (**16**$^+$) and (b) π-electronic anion receptors **28** and **29** with their helical anion complexes.

4–2 Single-Crystal Preparation and Evaluation of Helical Structures

Single crystals of **16**$^+$-**28**·$Cl^–$ and **16**$^+$-**29**·$Cl^–$ were obtained as racemic crystals by vapor diffusion of *n*-hexane into CH_2ClCH_2Cl solutions containing 1:1 mixtures of receptors **28** and **29**, respectively, and **16**$^+$-$Cl^–$ (Figure 4–2). The exact solid-state structures and ion-pairing assemblies of **16**$^+$-**28**·$Cl^–$ and **16**$^+$-**29**·$Cl^–$ were determined using single-crystal X-ray analysis. The ion pair **16**$^+$-**28**·$Cl^–$ was crystalized in the monoclinic $P2_1/c$ system, yielding a [1+1]-type $Cl^–$ complex **28**·$Cl^–$ (Figure 4–3a). Four pyrrole NH, two bridged CH and *m*-phenylene CH of **28** associate with $Cl^–$, giving rise to N/C(–H)···Cl average distances of 3.46, 3.61, and 3.73 Å, respectively. α-CH sites of the terminal pyrrole with the C···C distance of 3.44 Å marginally overlap to form a single helix. The mean-plane deviation (the plane based on pyrrole, phenyl, and 1,3-diketone–boron complex units) of the helical structure of **28**·$Cl^–$ was 0.624 Å and the dihedral angle between the terminal pyrroles was 12.4°. In the tetrapropylammonium ion pair TPA^+-**28**·$Cl^–$, the anion complex also formed a single helix, in which the distances between terminal α-C(–H) were 3.51 and 3.63 Å and the mean-plane deviations

were 0.850 and 0.877 Å.[99] The helical structure of the $\mathbf{16}^+$ ion pair is more planar than that of the TPA^+ ion pair due to the stacking structure at the core plane of $\mathbf{16}^+$. On the other hand, in the solid state, the ion pair $\mathbf{16}^+$-**29**·Cl^- crystalized in the monoclinic $P2_1/c$ system exhibited a single-helical structure based on a [1+1]-type Cl^- complex **29**·Cl^-, having pyrrole NH, bridged CH, *m*-phenylene CH, and terminal phenyl CH of $\mathbf{16}^+$ interacting with Cl^- with N/C(–H)···Cl^- average distances of 3.43, 3.44, 3.60, and 3.87 Å, respectively (Figure 4–3b). The mean-plane deviation (the plane based on pyrrole, phenyl, and 1,3-diketone–boron complex units) of **29**·Cl^- was estimated to be 1.41 Å and the dihedral angle between the planes of the terminal phenyl pyrrole units was 15.9°. Interestingly, the Cl^- in the helical structure of **29**·Cl^- was disordered, suggesting that Cl^- shuttles between two dipyrrolyldiketone units, as previously observed in solution-state double helical structures.[101] This is because the sterically bulky terminal phenyl groups allowed each of the two dipyrrolyldiketone units of **29** to function as an association site. As seen in Maeda's research, the ion pair with TPA^+ provided a double helical structure in the form of a [2+2]-type Cl^- complex.[99] Notably, different helical structures can be formed from a single anion receptor depending on the pairing countercations.

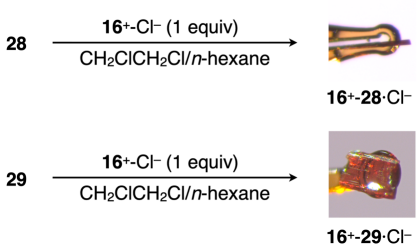

Figure 4–2 Preparation of $\mathbf{16}^+$-**28**·Cl^- and $\mathbf{16}^+$-**29**·Cl^- in the single crystals and their photographs.

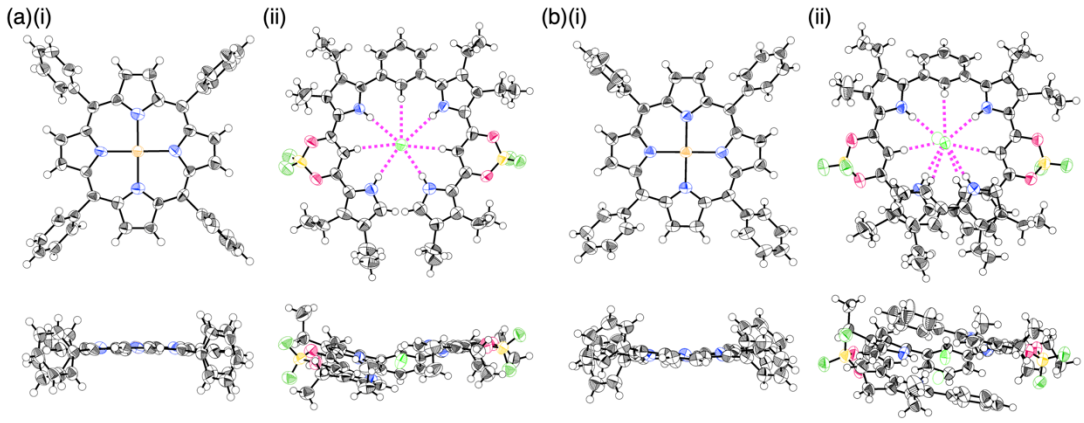

Figure 4–3 Ortep drawings of single-crystal X-ray structures (top and side views) of (a) **16**$^+$-**28**·Cl^- and (b) **16**$^+$-**29**·Cl^-: (i) **16**$^+$ and (ii) *M* helices of receptor–anion complexes. Thermal ellipsoids are scaled to a 50% probability level. In (b)(ii), the Cl^- disorder is in a ratio of 85:15 with the major (equatorial octant) and minor (hollow) parts. Solvent molecules and disordered atoms of anion receptors are omitted for clarity. Atom color code: black, white (sphere), yellow, blue, red, green, light green, and orange refer to carbon, hydrogen, boron, nitrogen, oxygen, fluorine, chlorine, and gold, respectively. In (ii), magenta dashed lines are hydrogen bonding for Cl^- by pyrrole NH, bridging CH, and *m*-phenylene-bridged CH in anion receptors.

4–3 Evaluation of Packing Structures

In the packing structure, **16**$^+$-**28**·Cl^- showed a charge-by-charge assembly of **16**$^+$ with the *P* strand of **28**·Cl^- along with that with the *M* strand via stacking of **16**$^+$ and **28**·Cl^- planes with a distance of 3.49 Å (Figure 4–4a). In contrast, **16**$^+$-**29**·Cl^- formed a charge-by-charge assembly comprising both *P* and *M* helices of **29**·Cl^-, which were alternately stacked with **16**$^+$ (Figure 4–4b). In the columnar structures of **16**$^+$-**28**·Cl^- and **16**$^+$-**29**·Cl^-, the Au···Cl distances were 5.05/7.46 and 5.60/5.80 Å, respectively, the Au···Au distances were 12.07 and 11.16 Å, respectively, and the line passing through both Au and Cl has angles of 38.3°/47.8° and 41.8°/52.9° to the mean plane of **16**$^+$ (core 25 atoms including Au). These results indicated that **16**$^+$-**28**·Cl^- formed a packing structure with a more sliped stacking structure than **16**$^+$-**29**·Cl^-. Hirshfeld surface analysis[78–80] of **16**$^+$-**28**·Cl^- showed that the **16**$^+$ surface had a bow-tie arrangement of red and blue triangles in the shape-index property and flat regions in the curvedness property (Figure 4–5a). These are the characteristic mapping patterns for close stacking between the receptor–anion complex **28**·Cl^- and the **16**$^+$ core. On the other hand, these patterns were not observed clearly on the **16**$^+$ surface in **16**$^+$-**29**·Cl^-, suggesting that the bulkiness of the terminal phenyl groups makes forming closely stacked structures difficult (Figure 4–5b). In the ESP diagrams calculated at the B3LYP/6-31+G(d,p) level with LanL2DZ for Au based on the crystal structures of **16**$^+$-**28**·Cl^- and **16**$^+$-**29**·Cl^-,

the electron density of the Cl^- in **29**·Cl^- was smaller than that in **28**·Cl^-.[102] This suggests that the terminal phenyl groups of **29** more effectively delocalize the negative charge (Figure 4–6).

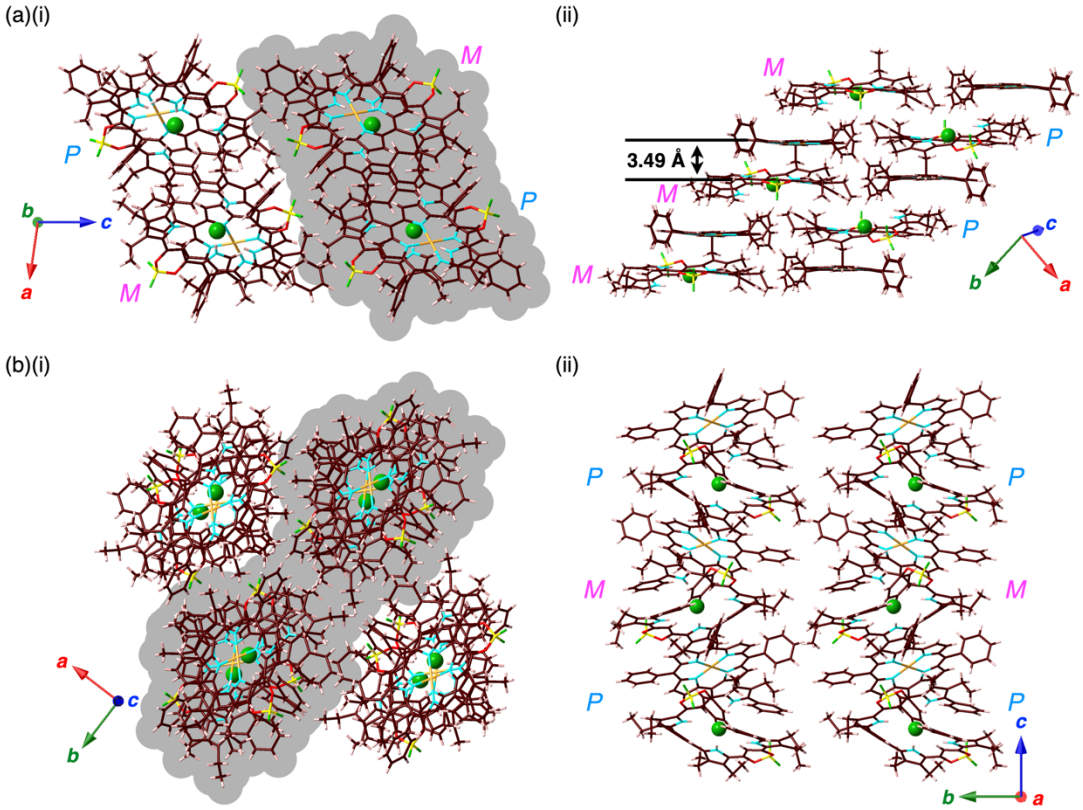

Figure 4–4 Packing diagrams of (a) **16**$^+$-**28**·Cl^- and (b) **16**$^+$-**29**·Cl^- as (i) top views and (ii) side views of the shaded parts in (i). Atom color code: brown, pink, yellow, cyan, red, green, green (sphere), and orange refer to carbon, hydrogen, boron, nitrogen, oxygen, fluorine, chlorine, and gold, respectively.

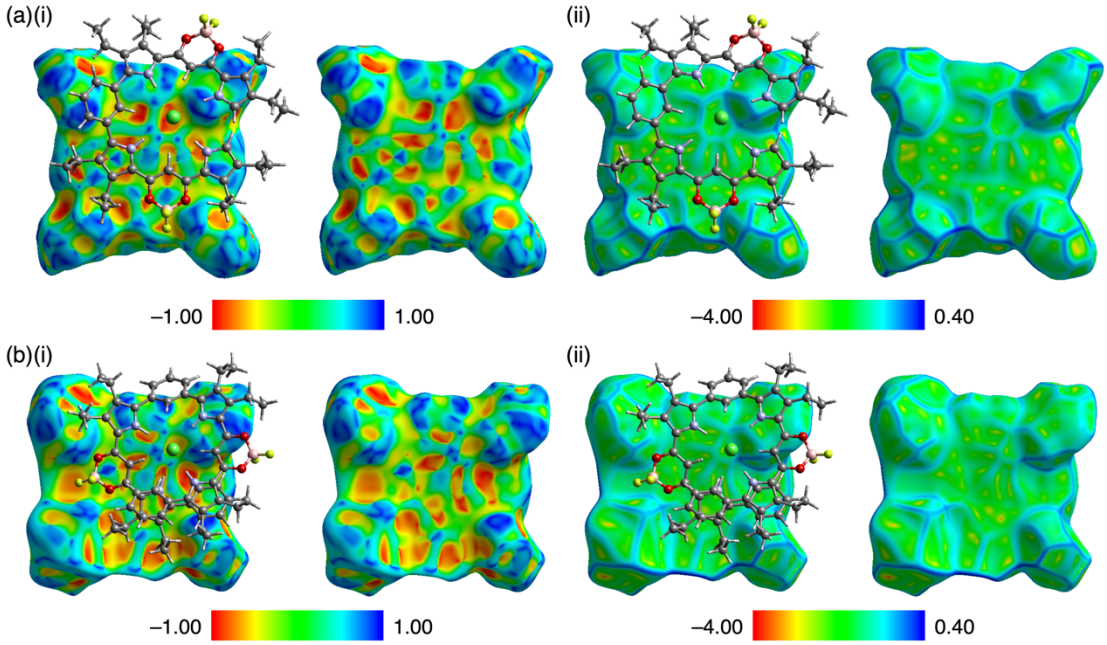

Figure 4–5 Hirshfeld surfaces of **16**$^{+}$ in the crystal structures of (a) **16**$^{+}$-**28**·Cl^{-} and (b) **16**$^{+}$-**29**·Cl^{-} mapped over (i) shape-index and (ii) curvedness properties: surfaces with the ball-and-stick model of the neighboring receptor–anion complexes (left) and only surfaces (right). Atom color code: gray, white, pink, blue, red, yellow green, and green refer to carbon, hydrogen, boron, nitrogen, oxygen, fluorine, and chlorine, respectively.

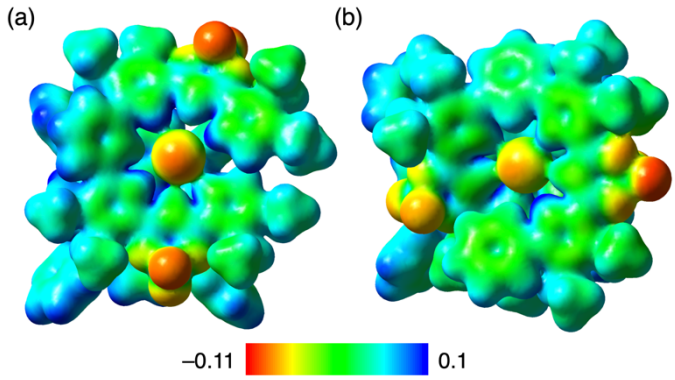

Figure 4–6 ESP mapping (δ = 0.01) of (a) **16**$^{+}$-**28**·Cl^{-} and (b) **16**$^{+}$-**29**·Cl^{-} based on the crystal structures at B3LYP/6-31+G(d,p) for C, H, B, N, O, F, and Cl and B3LYP/LanL2DZ for Au.

To elucidate the intermolecular interactions between ions with planar and helical structures, energy decomposition analysis (EDA)[103] based on the fragment molecular orbital (FMO) method FMO2-MP2 was performed. The mixed basis sets consisted of NOSeC-V-TZP with model core potential (MCP) for Au and NOSeC-V-DZP with MCP for other atoms.[104,105] The EDA calculations output electrostatic (E_{es}), dispersion (E_{disp}), charge transfer (E_{ct}), and exchange-repulsion (E_{ex}) interaction energies along with the total interaction

energy (E_{tot}). The EDA calculation for the solid-state assembly of **16**$^{+}$-**28**·Cl^{-} revealed characteristic interaction energy contributions (Figure 4–7a). E_{tot} values of the stacked ion pair of **16**$^{+}$ and **28**·Cl^{-} were –164.42 (c3-a4) and –255.37 (c3-a2) kcal/mol. The large E_{tot} values mainly consist of electrostatic and dispersion forces, especially with the E_{es} and E_{disp} values for c3-a2, which were –62.87 and –213.25 kcal/mol, respectively. Similarly, EDA calculations for **16**$^{+}$-**29**·Cl^{-} showed large E_{tot} values for the stacked ion pairs of **16**$^{+}$ and **29**·Cl^{-} (–251.12 and –259.72 kcal/mol for c2-a2 and c3-a2, respectively) (Figure 4–7b). Electrostatic and dispersion interactions between **16**$^{+}$ and **29**·Cl^{-} were stabilized in stacked ion pairs c2-a2 (E_{es}: –59.81 kcal/mol, E_{disp}: –209.15 kcal/mol) and c3-a2 (E_{es}: –61.23 kcal/mol, E_{disp}: –221.09 kcal/mol).

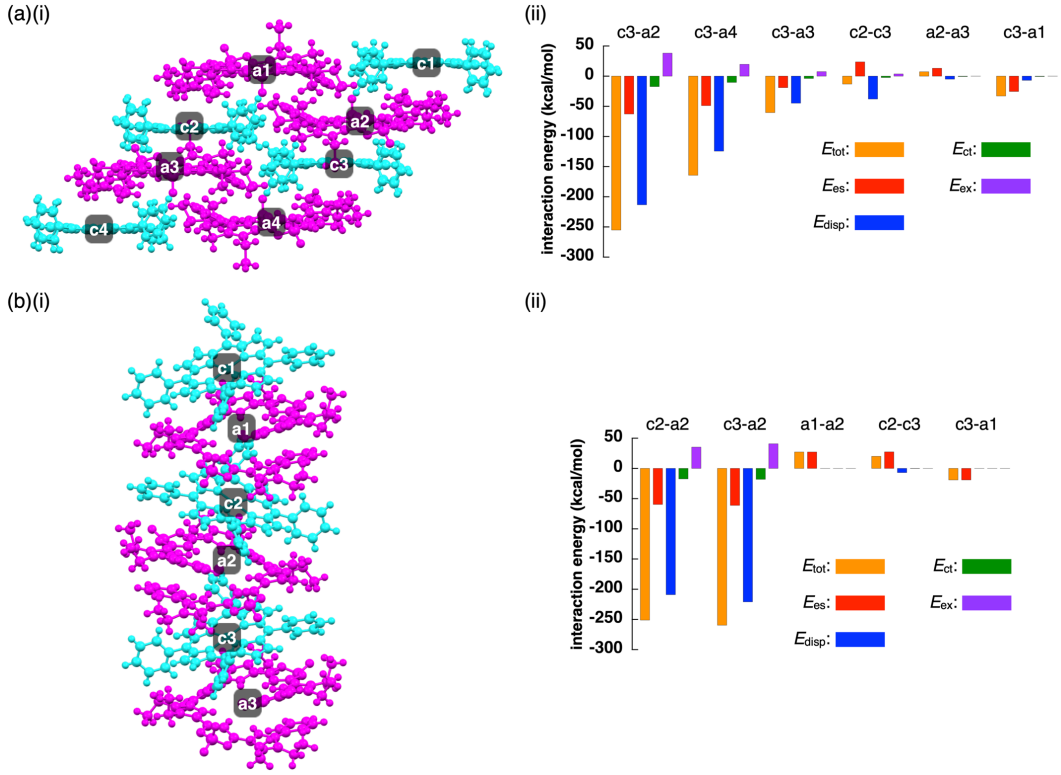

Figure 4–7 EDA of (a) **16**$^{+}$-**28**·Cl^{-} and (b) **16**$^{+}$-**29**·Cl^{-}: (i) single-crystal X-ray structures and (ii) intermolecular interaction energies (kcal/mol) between selected ions estimated at the FMO2-MP2 method using mixed basis sets including NOSeC-V-TZP with MCP for and Au and NOSeC-V-DZP with MCP for the other atoms. Color code in (i): cyan and magenta refer to cation and anion parts, respectively.

4–4 Summary of Chapter 4

In this chapter, the ion pairs of tetraphenylporphyrin–Au^{III} complex combined with helical π-system–anion complexes were obtained in the form of single crystals. Single-crystal X-ray analysis revealed that the ion pairs formed charge-by-charge assemblies containing *P* and *M* strands of [1+1]-type Cl^- complexes. Although both ion pairs showed stacking structures between cations and anions, Hirshfeld surface analysis indicated that the stacking behavior depended on the substituents of the anion receptors. Via EDA calculations, mainly electrostatic and dispersion forces were found to be the effective intermolecular interactions between cations and anions.

Chapter 5

Ion-Pairing π-Electronic Systems: Ordered Arrangement and Noncovalent Interactions of Negatively Charged Porphyrins

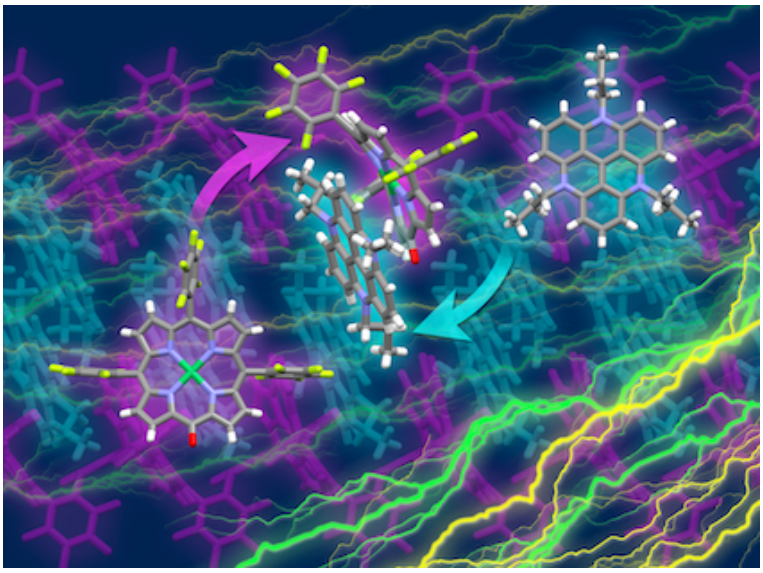

Contents

5–1 Introduction

Similar to many reported π–π interactions (Figure 5–1a i), detailed discussions of the properties for charged π-electronic systems require a newly proposed conceptual interaction: ^{i}π–^{i}π interactions (Figure 5–1a ii), wherein ^{i}π represents π-electronic ions and charged π-electronic systems. The major contributive interionic forces in the ^{i}π–^{i}π interactions are electrostatic and dispersion forces. As shown in Chapter 1, based on the ^{i}π–^{i}π interactions, two distinct assembly modes of π-electronic ions can be considered for charge-by-charge assemblies, namely alternately stacking anions and cations (Figure 5–1b left), and charge-segregated assemblies, wherein identically charged species stack.[82,83] These two modes are represented in the perfectly ordered arrangements of constituent π-electronic ions for easily understanding what ion-pairing assemblies are. The assemblies that are obtained in forms such as crystals and liquid crystals are constructed with contributions of both the charge-by-charge and charge-segregated modes (Figure 5–1b right).

Despite numerous studies on assembling modes, the characteristics of ^{i}π–^{i}π interactions that exist between π-electronic ions in the solid state are not well understood. The under-exploration of ^{i}π–^{i}π interactions is partially attributed to the lack of appropriate ion-pairing systems. In particular, the preparation of π-electronic anions is challenging because anionic species are readily converted to other species due to their electron-rich states. Furthermore, for the development of electronic devices based on crystal engineering,[106,107] it is crucial to understand the interactions within the complete crystal systems and not only those of constituent stacked ion pairs. This chapter focuses on the characteristic interactions operative in ion-pairing assemblies comprising π-electronic anions in combination with two different counter species: aliphatic (bulky) and π-electronic (planar) cations. The solid-state properties, including UV/vis absorption and photo-induced electron transfer correlated with the assembling modes, have also been elucidated.

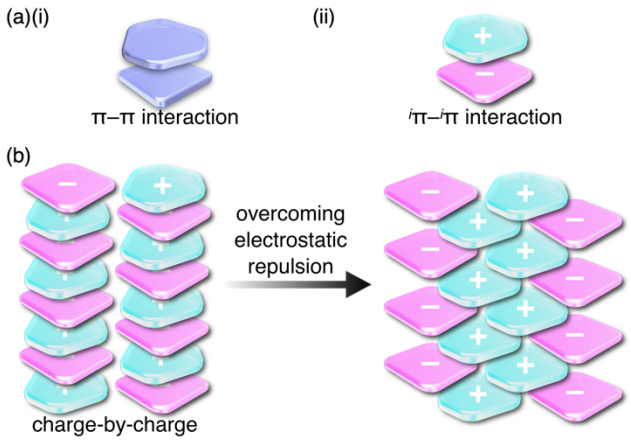

Figure 5–1 (a) Representative model structures based on (i) π–π and (ii) ^{i}π–^{i}π interactions and (b) charge-by-charge assembly (left) and an actually observed assembly mode (right).

5–2 ^{i}π–^{i}π Interactions in the PCCp^{-}-TATA^{+} Ion-Pairing Assembly

As an example of ion-pairing assemblies of π-electronic ion pairs, a two-by-two charge-by-charge assembly was observed in a single crystal of the ion pair of PCCp^{-} and TATA^{+} cation **12**$^{+}$ by Maeda et al. (Figure 5–2a).[28] In the crystal structure, the stacking distances between PCCp^{-} and **12**$^{+}$ were 3.28 and 3.29 Å, which were within the typical π–π stacking range. The pairs of oppositely charged π-electronic ions can be observed in the stacking charge-by-charge columns as well as in the neighboring columns. Thus, π-electronic ions compensate their charges not only with stacking counterions but also with laterally located ions. To reveal the interaction energies between the ion pairs, EDA[103] based on the FMO method (FMO2-MP2) using the NOSeC-V-DZP basis set with MCP[104,105,108,109] was performed for the packing structure of PCCp^{-}-**12**$^{+}$ (Figure 5–2b). It is to be noted that the calculated packing structures for EDA were surrounded by point charges to simplify the calculation systems.[66] The EDA calculations output E_{es}, E_{disp}, E_{ct}, and E_{ex} along with E_{tot}. It is to be noted that the induction energy was considered to be due to the polarization effects. In FMO calculations, the fragment monomer wavefunctions were optimized with the presence of classical electrostatic potentials of other fragment monomers; hence, the converged fragment monomers were polarized. Therefore, induction energy is included in all the energy values obtained by using EDA. E_{tot} of representative stacked ion pairs, a1-c1 and a2-c2, of PCCp^{-}-**12**$^{+}$ were –141.34 and –140.62 kcal/mol, respectively, which were larger than those of laterally located ion pairs a3-c1 and a4-c2 (–54.55 and –34.36 kcal/mol, respectively). The large E_{tot} of stacked ion pairs were attributed to the characteristic E_{es} and E_{disp} values. In particular, the E_{disp} of the stacked ion pairs were –95.54 and –95.44 kcal/mol for a1-c1 and a2-c2, respectively, which were larger than those of the lateral

pairs (a3-c1 and a4-c2 for –15.53 and –6.81 kcal/mol, respectively), indicating that E_{disp} is a crucial contributive interaction of stacked ion pairs. Favorable E_{es} and E_{disp} for stacked ion pairs indicated effective $^{i}\pi$–$^{i}\pi$ interactions. Interestingly, energetically disfavored E_{es} were observed for the stacking of identically charged a3-a4 and c1-c2 (43.21 and 35.01 kcal/mol), whereas favored E_{disp} of –43.92 and –133.40 kcal/mol were observed for the stacking structures of $PCCp^{-}$ and $\mathbf{12}^{+}$, respectively. π-Electronic anions with larger π-planes would show ion-pairing assemblies based on the $^{i}\pi$–$^{i}\pi$ interaction.

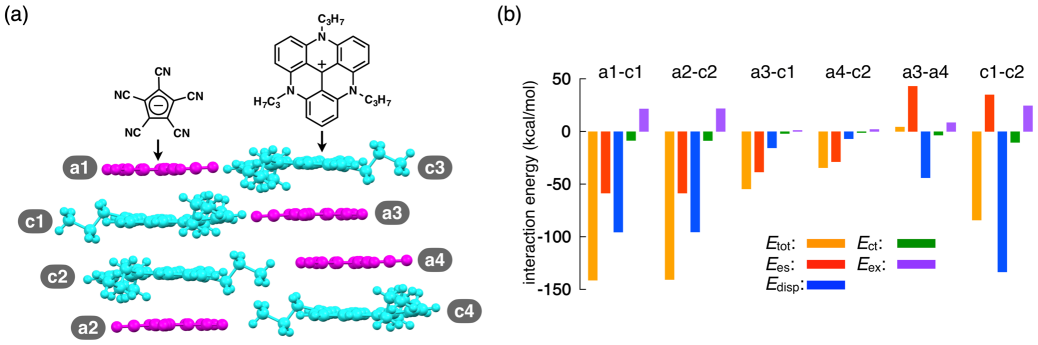

Figure 5–2 (a) Solid-state packing structure of $\mathbf{12}^{+}$-$PCCp^{-}$ and (b) selected oppositely and identically charged ion pairs and their estimated interaction energies (kcal/mol) according to EDA based on the FMO2-MP2 method using the NOSeC-V-DZP basis set with MCP (calculated packing structures for EDA were surrounded by point charges to simplify the calculation systems). Color code in (a): magenta and cyan refer to anion and cation parts, respectively.

5–3 Preparation of Ion Pairs

The solid-state ion-pairing assemblies of π-electronic anions $\mathbf{30}^{-}$, $\mathbf{18}^{-}$, $\mathbf{31}^{-}$, $\mathbf{32}^{-}$, and $\mathbf{33}^{-}$ [110] were fabricated in combination with cations, and their structures were revealed by single-crystal X-ray analysis. Two methods were evaluated for the preparation of ion pairs (Figure 5–3): (a) mixing CH_2Cl_2 solutions of MHPs and 1 equiv of hydroxide ion pairs such as tetrabutylammonium hydroxide (TBAOH), followed by the removal of water, and (b) mixing Na^{+} ion pairs of porphyrin anions, prepared from the CH_2Cl_2 solutions of MHPs with aqueous NaOH, and 1 equiv of Cl^{-} ion pairs of the desired organic cations including $\mathbf{12}^{+}$, followed by the removal of NaCl by washing with water.[39] In both the methods, deprotonated porphyrin anions and organic cations were soluble as ion pairs in the CH_2Cl_2 phase. Following CH_2Cl_2 evaporation, the solid-state ion-pairing assemblies were formed by appropriate purification techniques, such as recrystallization.

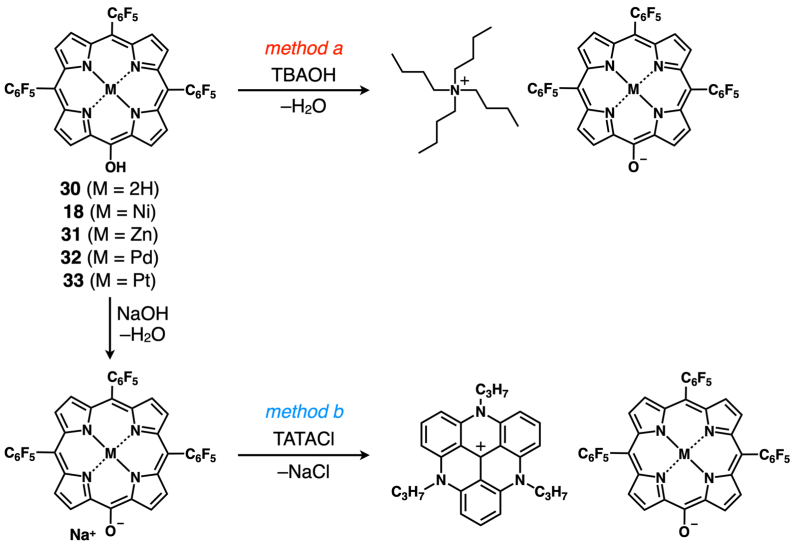

Figure 5–3 Methods for preparing single crystals of ion pairs.

5–4 Interactions of Stacked Ion Pairs

Assembled ion pair behavior in the solid state is influenced by the geometries and electronic states of constituent ions. In the packing structures of **30**$^-$-**12**$^+$, **18**$^-$-**12**$^+$, and **31**$^-$-**12**$^+$, the Hirshfeld surface analysis[78–81] of porphyrin anions mapped over shape-index and curvedness properties indicated that a close interplanar contact and a flat region, respectively, resembling a characteristic mapping pattern for the $^i\pi$–$^i\pi$ stacking of π-electronic ion pairs (Figure 5–4).[79,81] These results suggested that the packing structures of **30**$^-$-**12**$^+$, **18**$^-$-**12**$^+$, and **31**$^-$-**12**$^+$ were stabilized by the $^i\pi$–$^i\pi$ interactions. In contrast, the surfaces of porphyrin anions when paired with TBA$^+$ ion pairs (**18**$^-$-TBA$^+$,[54] **31**$^-$-TBA$^+$, **32**$^-$-TBA$^+$, and **33**$^-$-TBA$^+$) mapped over the shape-index property exhibited depressions above the anionic π-planes, suggesting that the stacking structures were stabilized by the CH–π interactions (Figure 5–4). Interestingly, in the ESP diagrams at the B3LYP/6-31+G(d,p) with LanL2DZ for Ni and Pd based on the corresponding crystal structures, the electron densities of the π-planes in **18**$^-$ and **32**$^-$ of **12**$^+$ ion pairs were larger than those of TBA$^+$ ion pairs (**18**$^-$-TBA$^+$ [54] and **32**$^-$-TBA$^+$) (Figure 5–5).[66] In the X-ray structures of **18**$^-$ and **32**$^-$, the C–O distances of **18**$^-$-TBA$^+$ and **32**$^-$-TBA$^+$ were shorter than those of the corresponding **12**$^+$ ion pairs. These results indicated that the C=O double-bond characters of **18**$^-$ and **32**$^-$ as TBA$^+$ ion pairs increased due to the enhanced delocalization of electrons (negative charge) of the anionic oxygen into the porphyrin framework, which occurs due to the lowering of the electron density of the anion core decreased by the positive charge of TBA$^+$. Furthermore, the interionic charge delocalization between the oppositely charged species in the **12**$^+$ ion pairs occurred to a lesser extent than that in the TBA$^+$ ion pairs because

12^{+} can more efficiently delocalize the positive charge by itself more efficiently than TBA^{+}. Therefore, the ion pairs comprising π-electronic anions and cations can effectively form assembled structures via electrostatic interactions.

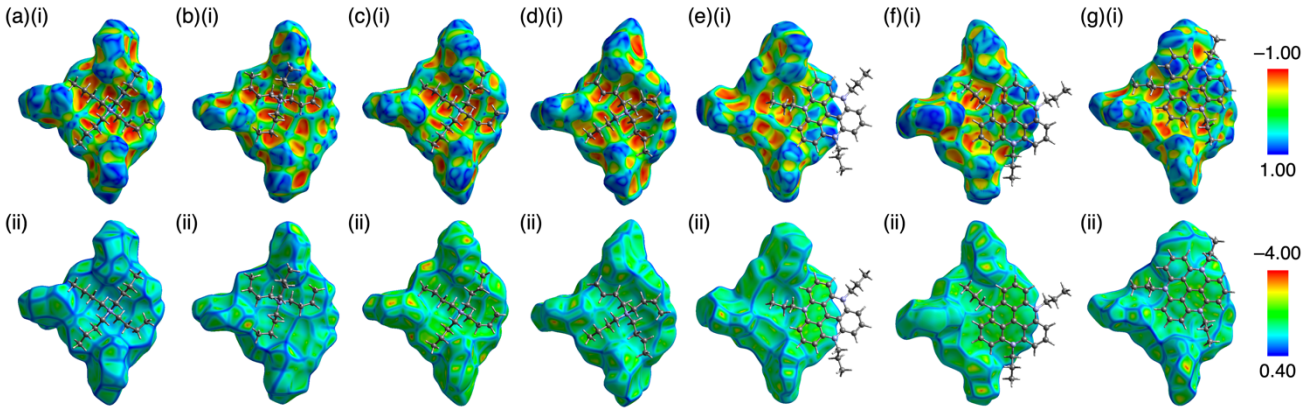

Figure 5–4 Hirshfeld surfaces of representative anions in the crystal structures of (a) **18**$^{-}$-TBA^{+}, (b) **31**$^{-}$-TBA^{+}, (c) **32**$^{-}$-TBA^{+}, (d) **33**$^{-}$-TBA^{+}, (e) **30**$^{-}$-**12**$^{+}$, (f) **18**$^{-}$-**12**$^{+}$, and (g) **31**$^{-}$-**12**$^{+}$ mapped over (i) shape-index and (ii) curvedness properties with ball-and-stick models of the neighboring cations. Atom color code: gray, white, and blue refer to carbon, hydrogen, and nitrogen, respectively.

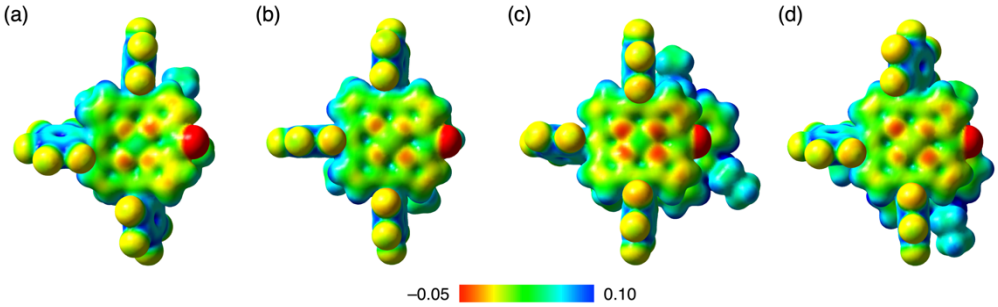

Figure 5–5 ESP mappings of (a) **18**$^{-}$-TBA^{+}, (b) **32**$^{-}$-TBA^{+}, (c) **18**$^{-}$-**12**$^{+}$, and (d) **32**$^{-}$-**12**$^{+}$ (δ = 0.01), calculated at B3LYP/6-31+G(d,p) for C, H, N, O, and F with LanL2DZ for Ni and Pd, for the single-crystal X-ray structures.

To investigate the contributions of interactions between π-electronic ions in the ion-pairing assemblies of single crystals, the interactions between the components of ion-pairing assemblies were estimated using EDA[103] based on FMO2-MP2 using mixed basis sets including NOSeC-V-TZP with MCP for Ni and NOSeC-V-DZP with MCP for the other atoms (Figure 5–6).[104,105,108,109] In the packing structure of **18**$^{-}$-TBA^{+}, the E_{tot} values of –169.00 and –129.07 kcal/mol were observed for the charge-by-charge stacked ion pairs of a5-c2 and a5-c5, respectively, with the values of E_{es}/E_{disp} being –68.34/–111.09 and –68.08/–67.66 kcal/mol, respectively (Figure

5–6a ii). Moreover, E_{tot} of –83.34 and –23.77 kcal/mol were observed for a5-c4 and a5-c6 ion pairs, respectively, indicating lower attractive interaction energies than those of charge-by-charge stacked ion pairs (a5-c2 and a5-c5). Decreased E_{disp} values were observed for ion pairs with longer interionic distances, whereas E_{es} were relatively effective even in these cases. Identically charged ions, such as those in the c1-c2 pair, were in energetically disfavored states and its dominant contributor is electrostatic repulsion. Furthermore, the identically charged pair a4-a5 yielded a favorable E_{tot} value, arising chiefly due to a contribution from dispersion forces.

The EDA calculation for the packing structure of **18**$^-$-**12**$^+$ revealed characteristic energy contributions (Figure 5–6b). E_{tot} of the oppositely charged stacked ion pair a2-c2 was –196.17 kcal/mol, whose absolute value was larger than that of the ion pair located at the lateral positions (–63.42 kcal/mol for a2-c4). The main contributions to the attractive forces in **18**$^-$-**12**$^+$ are E_{es} and E_{disp}, with values of –69.72 and –141.89 kcal/mol, respectively, for the a2-c2 ion pair. The E_{es} values were comparable to the values observed in the charge-by-charge stacked ion pairs of **18**$^-$-TBA$^+$. On the other hand, characteristic large negative E_{disp} values can be attributed to the overlap of the π-planes. The E_{disp} values of a2-c1 (–63.30 kcal/mol) and a2-c4 (–21.14 kcal/mol) are lower in absolute values than that of a2-c2 due to the diminished or absent overlapping of core π-planes. Similarly, the stacking of **12**$^+$ in **18**$^-$-**12**$^+$ (c1-c4) is stabilized chiefly by the contribution of dispersion forces. These results strongly support that dispersion forces are important for controlling the locations of identically charged species. Favored E_{disp} values for the stacking structures of **12**$^+$ are also observed in PCCp$^-$-**12**$^+$. On the basis of the favorable contribution by dispersion forces in the stacking of π-planes, E_{tot} of charge-by-charge stacked ion pairs in the ion-pairing assembly of **18**$^-$-**12**$^+$ are larger than those of **18**$^-$-TBA$^+$. Furthermore, the E_{tot} value of **18**$^-$-**12**$^+$ is larger than that of PCCp$^-$-**12**$^+$, particularly for E_{disp}, suggesting that larger π-electronic ions exhibit more effective ^{i}π–^{i}π interactions. These results clearly demonstrate that effective electrostatic and dispersion forces as attractive forces are characteristic in the ^{i}π–^{i}π stacking charge-by-charge structures comprising π-electronic ions.

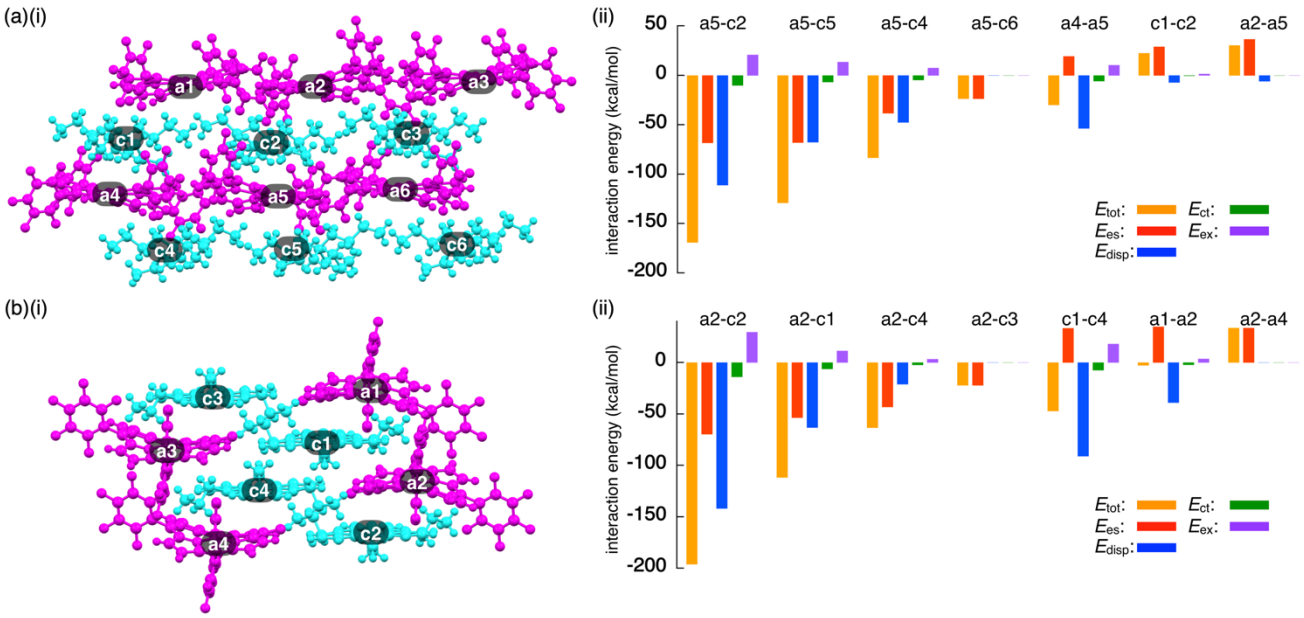

Figure 5–6 Decomposition of the total intermolecular interaction energy (E_{tot}) of (a) **18**$^{-}$-TBA^{+} and (b) **18**$^{-}$-**12**$^{+}$ for (i) single-crystal X-ray structures and (ii) selected ion pairs and their estimated interaction energies (kcal/mol) according to EDA based on the FMO2-MP2 method using mixed basis sets including NOSeC-V-TZP with MCP for Ni and NOSeC-V-DZP with MCP for the other atoms (calculated packing structures for EDA were surrounded by the point charges to simplify calculation systems). Color code in (i): magenta and cyan refer to anion and cation parts, respectively.

For evaluating the results of EDA calculations without considering the effect of packing structures, monomeric ion pairs obtained from the crystal structures and their optimized structures were examined. Ion-pair monomers in the crystal state exhibited energy contributions analogous to those of the packing structures (Figure 5–7 and Table 5–1). The importance of electrostatic forces in $^{i}\pi$–$^{i}\pi$ interactions was clearly supported by the analysis of the model structure as an electronically neutral pair **18-34** based on **18**$^{-}$-**12**$^{+}$ in the crystal form (Figure 5–8). Model structure of **18-34** was prepared based on the crystal structure of monomeric **18**$^{-}$-**12**$^{+}$ (Figure 5–7b i), wherein the oxygen of **18**$^{-}$ was protonated and the central carbon of **12**$^{+}$ was substituted to boron. The EDA calculation of **18-34** revealed decreased electrostatic forces due to the absence of charges (Table 5–2). Meanwhile, the electronically neutral pair exhibited an E_{disp} value similar to that of the ion pair **18**$^{-}$-**12**$^{+}$, suggesting a distinction between the π–π and $^{i}\pi$–$^{i}\pi$ interactions and higher total interaction energies for the latter. On the other hand, optimized monomer ion pairs that were based on the crystal structures exhibited larger E_{tot} because of a closer ion-pairing arrangement than that in the crystal structures (Table 5–1). It is to be noted that the EDA calculations of packing states and monomer ion pairs indicated that the E_{es} of **18**$^{-}$-**12**$^{+}$ is

comparable with that of **18**$^{-}$-TBA^{+}, although ESP calculations of ion pairs suggested significant interionic charge delocalization in **18**$^{-}$-TBA^{+}. The enhanced dispersion forces of **18**$^{-}$-**12**$^{+}$ compared to that of **18**$^{-}$-TBA^{+} can be attributed to the effective delocalization of negative and positive charges in **18**$^{-}$ and **12**$^{+}$, respectively. Therefore, the critical intermolecular forces for the $^{i}\pi$–$^{i}\pi$ interactions are electrostatic and dispersion forces.

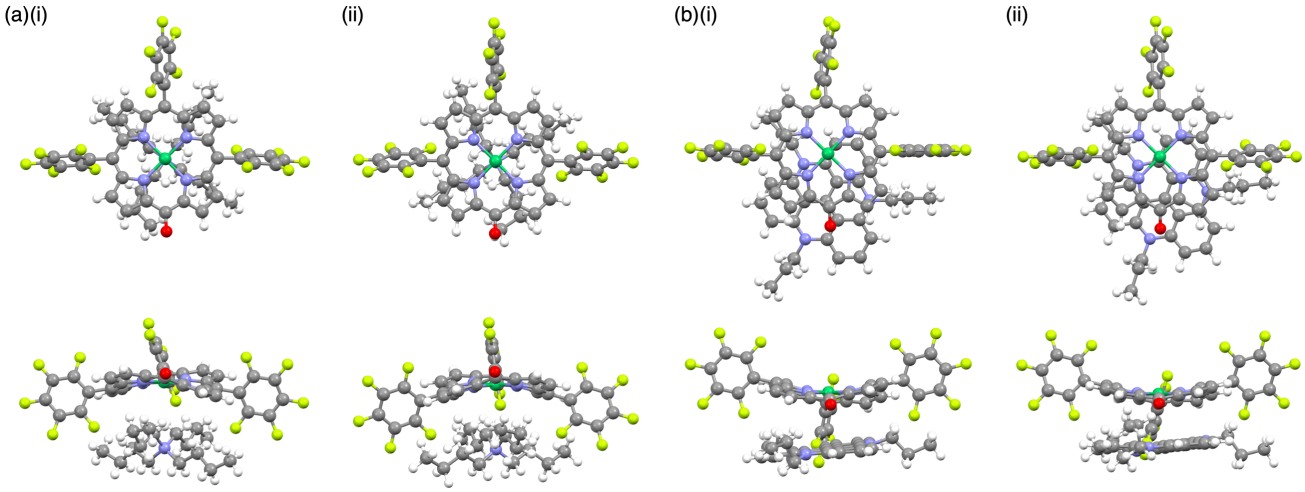

Figure 5–7 Monomeric ion pairs (a) **18**$^{-}$-TBA^{+} and (b) **18**$^{-}$-**12**$^{+}$ for EDA calculations: (i) crystal and (ii) optimized structures. Optimized structures were calculated at B3LYP-GD3BJ/6-31+G(d,p) for C, H, N, O, and F and B3LYP-GD3BJ/LanL2DZ for Ni.

Table 5–1 Energies between anion and cation as crystal and optimized structures **18**$^{-}$-TBA^{+} and **18**$^{-}$-**12**$^{+}$ estimated by EDA calculation based on an FMO2-MP2 using mixed basis sets including NOSeC-V-TZP with MCP for Ni and NOSeC-V-DZP with MCP for the other atoms.

fragments	total interaction energy (kcal/mol)	electrostatic interaction energy (E_{es}) (kcal/mol)	dispersion interaction energy (E_{disp}) (kcal/mol)	exchange repulsion interaction energy (E_{ex}) (kcal/mol)	charge-transfer interaction energy (E_{ct+mix}) (kcal/mol)
18^{-}-TBA^{+} (crystal)	–175.081	–74.176	–111.175	20.558	–10.289
18^{-}-**12**$^{+}$ (crystal)	–196.473	–70.294	–141.749	29.058	–13.489
18^{-}-TBA^{+} (optimized)	–204.804	–90.129	–149.250	52.871	–18.296
18^{-}-**12**$^{+}$ (optimized)	–229.567	–88.573	–181.323	62.514	–22.185

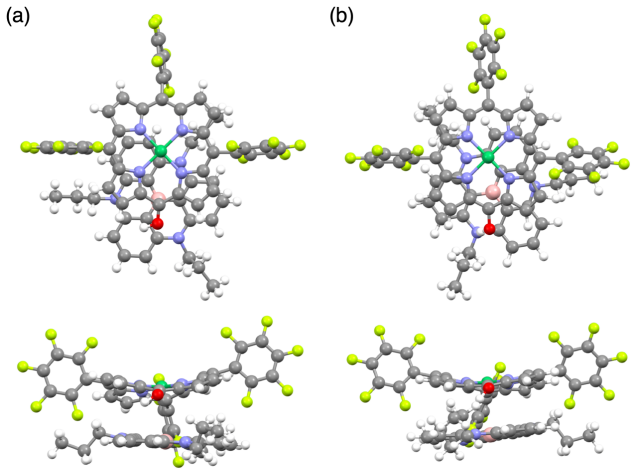

Figure 5–8 18-34 as a model of electronically neutral species for $\mathbf{18}^{-}$-$\mathbf{12}^{+}$ for EDA calculation: (a) unoptimized and (b) optimized structures. In (a), the position of the proton at oxygen was optimized using B3LYP/6-31G(d) with the fixed coordination for the other atoms, whereas, in (b), the structure was optimized using B3LYP/6-31G(d,p).

Table 5–2 Energies between **18** and **34** as unoptimized and optimized structures estimated by EDA calculation based on an FMO2-MP2 using mixed basis sets including NOSeC-V-TZP with MCP for Ni and NOSeC-V-DZP with MCP for the other atoms.

fragments	total interaction energy (kcal/mol)	electrostatic interaction energy (E_{es}) (kcal/mol)	dispersion interaction energy (E_{disp}) (kcal/mol)	exchange repulsion interaction energy (E_{ex}) (kcal/mol)	charge-transfer interaction energy (E_{ct+mix}) (kcal/mol)
18-34 (unoptimized)	–149.135	–24.975	–144.099	38.969	–19.030
18-34 (optimized)	–168.533	–29.679	–175.519	59.887	–23.222

5–5 Solid-State Absorption and Photoinduced Electron Transfer

The charge-by-charge and charge-segregated modes in the crystal states of ion-pairing assembles can modulate the electronic properties based on the arrangement of the π-electronic systems, as evidenced from the UV/vis absorption spectra. The UV/vis absorption spectra of the assemblies can provide valuable information on the arrangement of the π-electronic ions based on exciton coupling. It is noteworthy that Maeda's study revealed the existence of weak exciton coupling between stacking oppositely charged species owing to the significantly different MO levels of the cations and anions. This was also corroborated by the faint spectral changes (Figire 5–9).[39] This property is in contrast to those of the stacking electronically neutral π-electronic systems. Thus, the crystal-state absorption spectra of the ion pairs were acquired by optical microscopy for spectroscopically examining the assembling modes of the ion-pairing assemblies.

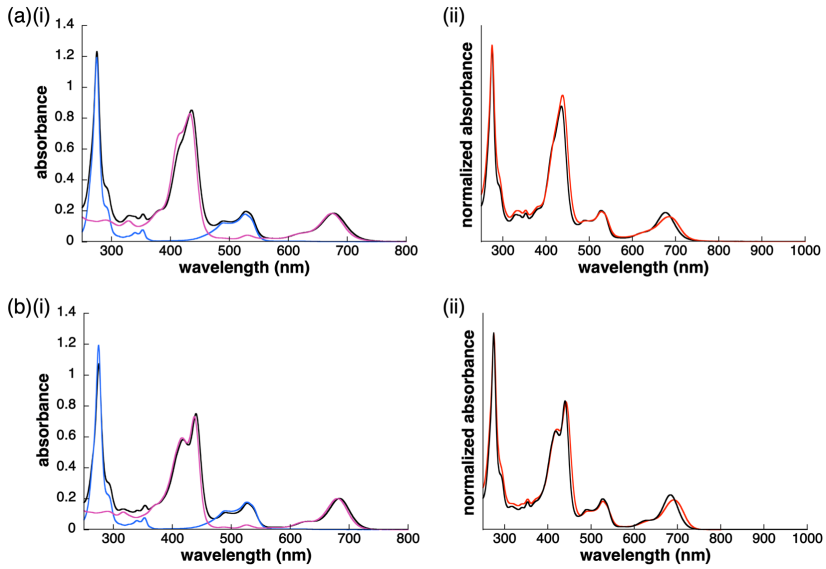

Figure 5–9 UV/vis absorption spectra of (a)(i) **18**$^{-}$-**12**$^{+}$ (black), **12**$^{+}$-Cl^{-} (cyan), and **18**$^{-}$-TBA^{+} (magenta) with the concentrations of 1×10^{-5} M and (ii) **18**$^{-}$-**12**$^{+}$ with concentrations of 1×10^{-5} M (black) and 1×10^{-3} M (red) and (b)(i) **32**$^{-}$-**12**$^{+}$ (black), **12**$^{+}$-Cl^{-} (cyan), and **32**$^{-}$-TBA^{+} (magenta) with the concentrations of 1×10^{-5} M and (ii) **32**$^{-}$-**12**$^{+}$ with concentrations of 1×10^{-5} M (black) and 1×10^{-3} M (red) in CH_2Cl_2 at 25 °C.

The UV/vis absorption spectrum of the single crystal of **18**$^{-}$-**12**$^{+}$, which included the contribution of the charge-segregated assembly, showed significantly broad bands with λ_{max} at 539 and 580 nm and a shoulder at 650 nm (Figure 5–10b,11b). These bands in the solid state were considerably distinct from the UV/vis absorption bands of **18**$^{-}$ and **12**$^{+}$ in solution. The shoulder at 650 nm was blue-shifted with respect to the band at 680 nm, which corresponded to monomeric **18**$^{-}$ (1×10^{-5} M **18**$^{-}$-TBA^{+} in CH_2Cl_2). In contrast, the bands at 539 and 580 nm were red-shifted with respect to those at 490 and 527 nm, which corresponded to monomeric **12**$^{+}$ (1×10^{-5} M **12**$^{+}$-Cl^{-} in CH_2Cl_2). Therefore, the shift in the broad absorption bands of solid-state **18**$^{-}$-**12**$^{+}$ with respect to those of the monomeric states can be considered to originate from the exciton coupling of the proximally located identically charged π-electronic systems.[111] The arrangement of the charged π-electronic systems is more clearly discussed on the basis of their transition dipole moments, which were estimated by the TD-DFT calculations at the B3LYP/6-31+G(d,p) level (Figure 5–12). The **18**$^{-}$ units, with the side-by-side-arrangement in solid-state **18**$^{-}$-**12**$^{+}$, showed parallel transition dipole moments, resulting in the blue-shifted absorption band. On the other hand, **12**$^{+}$ formed slipped-stacking dimeric structures with the head-to-tail-arranged transition dipole moments, resulting in the red-shifted absorption bands. In contrast to **18**$^{-}$-**12**$^{+}$, the crystal-state absorption spectrum of **32**$^{-}$-**12**$^{+}$ showed bands corresponding to the sum of the bands of monomeric **32**$^{-}$ and **12**$^{+}$ owing their arrangement in the charge-by-charge assembly (Figure 5–11d,13). Similarly, the absorption bands

of the charge-by-charge assemblies of **18**$^{-}$-TBA^{+} [54] and **32**$^{-}$-TBA^{+} were correlated with the arrangement of monomeric **18**$^{-}$ and **32**$^{-}$, respectively (Figure 5–10a,c,11a,c,14,15). The excitonic interactions between identically charged species were less effective in the charge-by-charge assemblies due to the long distances. The arrangement of π-electronic ions through $^{i}\pi$–$^{i}\pi$ interactions enabled the modulation of the bulk-state electronic properties. It should be emphasized that the correlation between the modes of the solid-state assemblies and their absorption spectra was established in the constructed ion-pairing assemblies. To the best of our knowledge, this feature for assemblies comprising π-electronic cations and anions has not been demonstrated thus far.

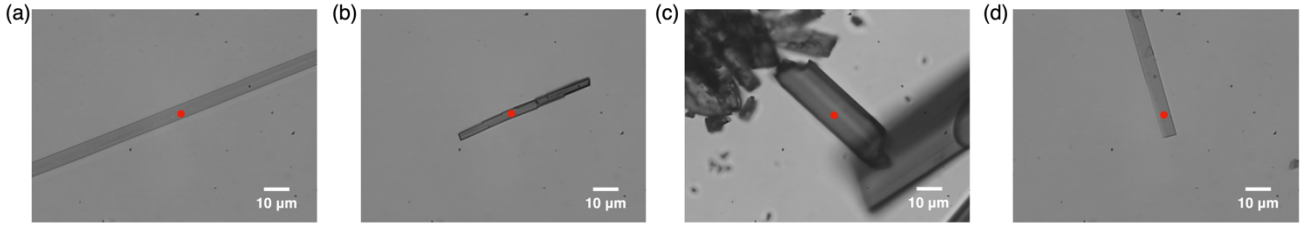

Figure 5–10 Optical microscopic images of single crystals of (a) **18**$^{-}$-TBA^{+}, (b) **18**$^{-}$-**12**$^{+}$, (c) **32**$^{-}$-TBA^{+}, and (d) **32**$^{-}$-**12**$^{+}$. Red spots indicate the position where the UV/vis absorption measurements were conducted (Figure 5–11).

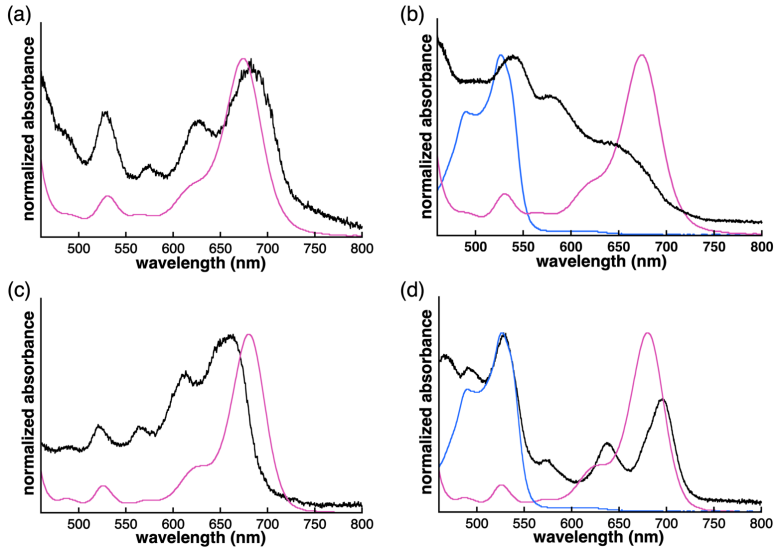

Figure 5–11 UV/vis absorption spectra of (a) **18**$^{-}$-TBA^{+} in the form of a single crystal (black) and in CH_2Cl_2 (1×10^{-5} M) (magenta), (b) **18**$^{-}$-**12**$^{+}$ in the form of a single crystal (black) and **18**$^{-}$-TBA^{+} (magenta) and **12**$^{+}$-Cl^{-} (cyan) in CH_2Cl_2 (1×10^{-5} M), (c) **32**$^{-}$-TBA^{+} in the form of a single crystal (black) and in CH_2Cl_2 (1×10^{-5} M) (magenta), and (d) **32**$^{-}$-**12**$^{+}$ in the form of single crystals (black) and **32**$^{-}$-TBA^{+} (magenta) and **12**$^{+}$-Cl^{-} (cyan) in CH_2Cl_2 (1×10^{-5} M).

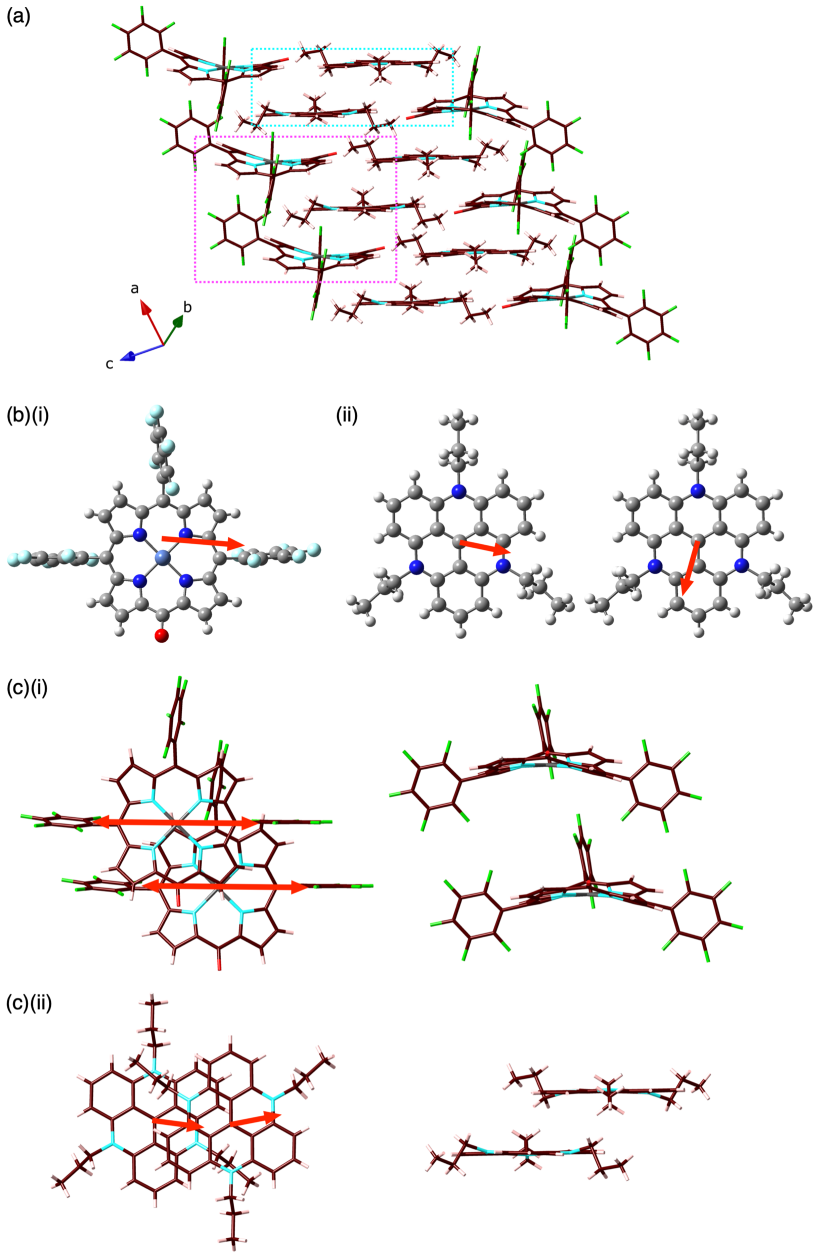

Figure 5–12 Evaluation of the transition dipole moments for the solid-state **18**$^{-}$-**12**$^{+}$: (a) packing structure of **18**$^{-}$-**12**$^{+}$, (b) ground-to-excited-state transition dipole moments of (i) **18**$^{-}$ for 662 nm (HOMO–1-to-LUMO+1 and HOMO-to-LUMO transition with the strength of 4.80 Debye) and (ii) **12**$^{+}$ for 472 and 462 nm (state 1 and 2 for HOMO-to-LUMO and HOMO–1-to-LUMO transitions with the strengths of 2.79 and 3.10 Debye, respectively) estimated by TD-DFT calculation at B3LYP/6-31+G(d,p) of the crystal structure, and (c)(i) side-by-side-arranged two **18**$^{-}$ and (ii) slipped-stacking dimeric structure of **12**$^{+}$ extracted from the cyan boxed area in (a).

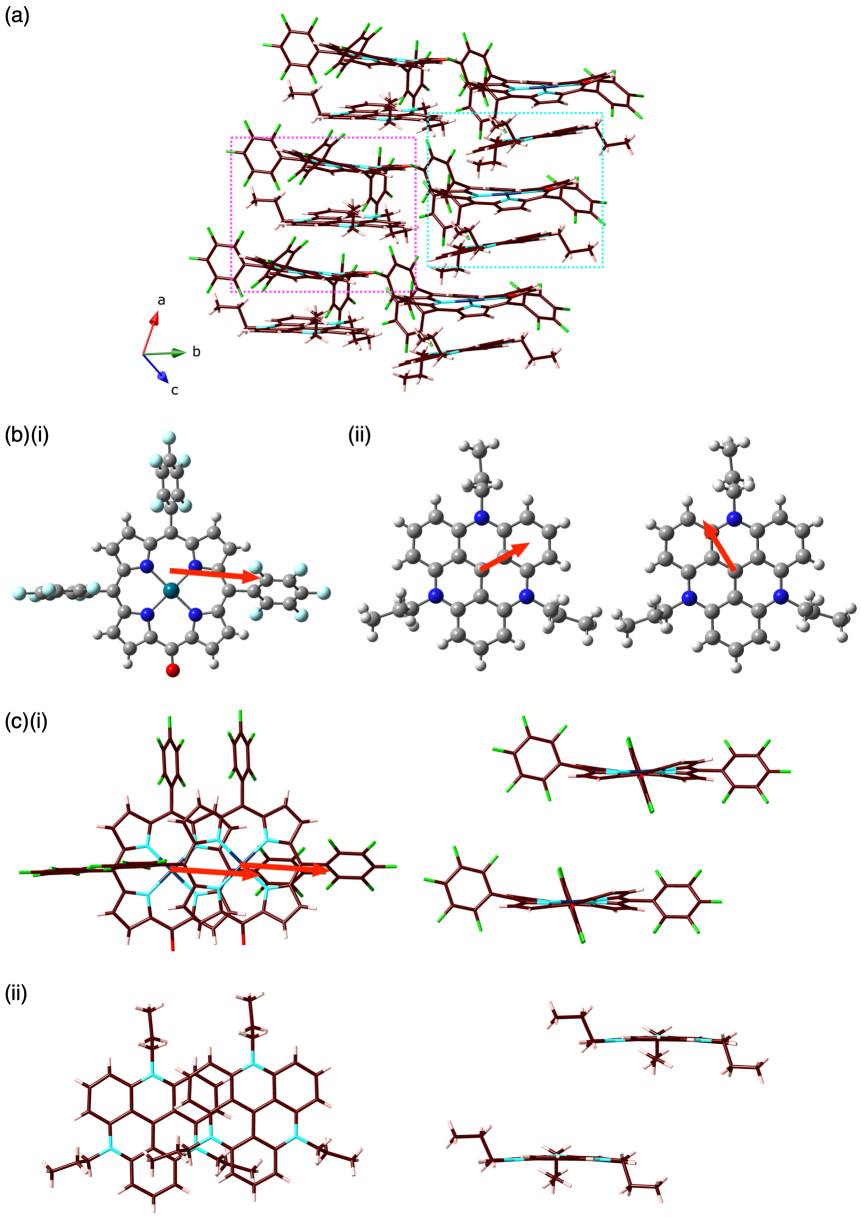

Figure 5–13 Evaluation of the transition dipole moments for the solid-state **32**$^{-}$-**12**$^{+}$: (a) packing structure of **32**$^{-}$-**12**$^{+}$, (b) ground-to-excited-state transition dipole moments of (i) **32**$^{-}$ for 678 nm (HOMO-to-LUMO transition with the strength of 5.15 Debye) and (ii) **12**$^{+}$ for 455 and 448 nm (state 1 (left) and 2 (right) for HOMO-to-LUMO and HOMO–1-to-LUMO transitions with the strengths of 2.81 and 3.06 Debye, respectively) estimated by TD-DFT calculation at B3LYP/6-31+G(d,p) of the crystal structure, and (c)(i) side-by-side-arranged two **32**$^{-}$ and (ii) slipped-stacking dimeric structure of **12**$^{+}$ extracted from the magenta and cyan boxed areas, respectively, in (a).

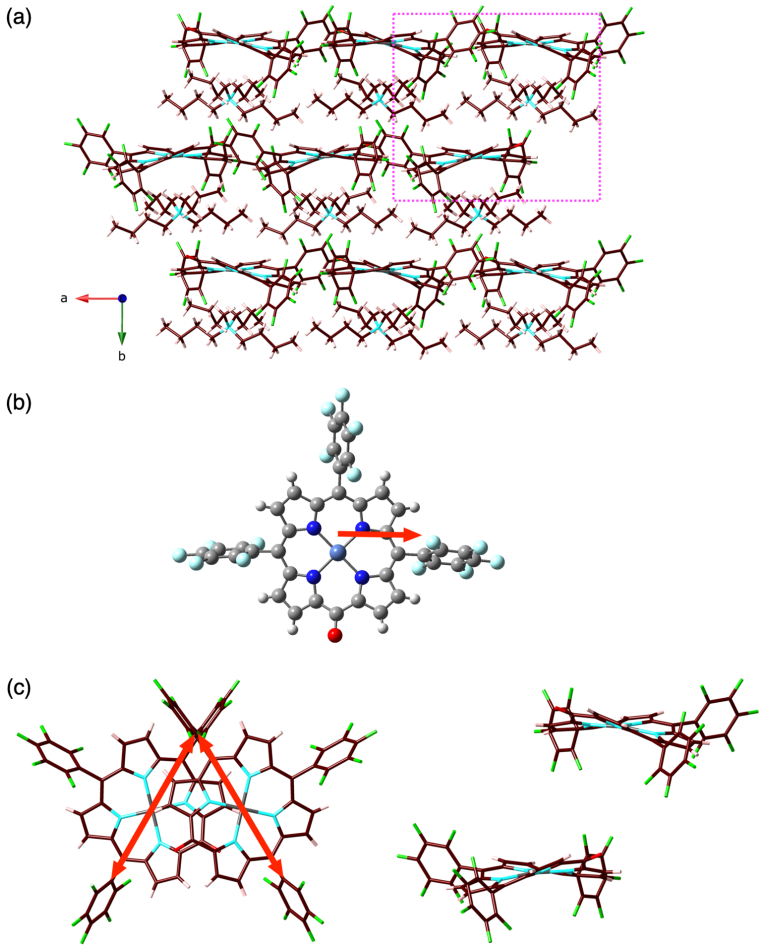

Figure 5–14 Evaluation of the transition dipole moments for the solid-state **18**$^{-}$-TBA^{+}: (a) packing structure of **18**$^{-}$-TBA^{+}, (b) ground-to-excited-state transition dipole moments of **18**$^{-}$ for 650 nm (HOMO–1-to-LUMO+1 and HOMO-to-LUMO transition with the strength of 4.62 Debye) estimated by TD-DFT calculation at B3LYP/6-31+G(d,p) of the crystal structure, and (c) oblique-arranged two **18**$^{-}$ extracted from the magenta boxed area in (a).

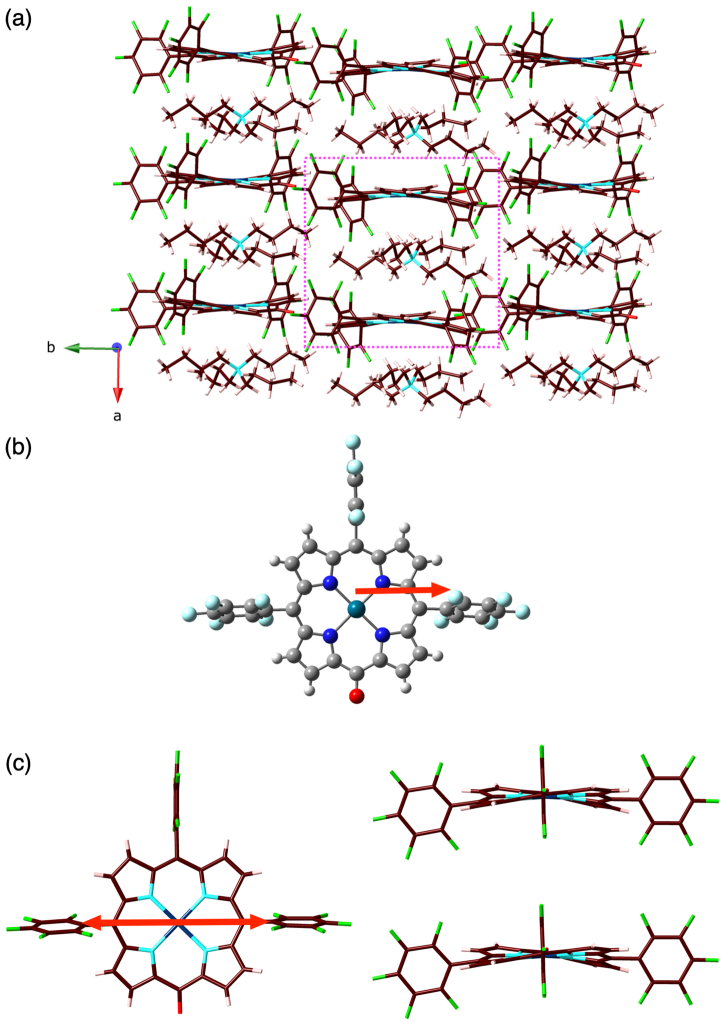

Figure 5–15 Evaluation of the transition dipole moments for the solid-state **32**$^{-}$-TBA^{+}: (a) packing structure of **32**$^{-}$-TBA^{+}, (b) ground-to-excited-state transition dipole moments of **32**$^{-}$ for 654 nm (HOMO-to-LUMO transition with the strength of 5.01 Debye) estimated by TD-DFT calculation at B3LYP/6-31+G(d,p) of the crystal structure, and (c) side-by-side-arranged two **32**$^{-}$ extracted from the magenta boxed area in (a).

π-Electronic anion and cation in an ordered arrangement can behave as electron donor and acceptor, respectively, thus inducing effective electron transfer in their ion-pairing assemblies.[112,113] To investigate the electron transfer process, visible transient absorption spectroscopy of the single crystals of **18**$^{-}$-TBA^{+} and **18**$^{-}$-**12**$^{+}$ under a microscopy was performed using a 650-nm excitation pulse. A pulse of this wavelength can selectively excite **18**$^{-}$ because its countercations do not absorb at 650 nm. The obtained transient absorption spectra were globally analyzed using three- or four-state sequential decay kinetic models convolved with a Gaussian pulse using the Glotaran program.[114] The evolution-associated difference spectra (EADS) thus ob-

tained present the transient absorption spectra resolved into each component of the kinetic models. Time evolution of the transient absorption spectra of **18**$^{-}$-TBA^{+} (Figure 5–16a) showed several sharp absorption bands at ~475, 555, and 731 nm instantaneously after excitation. The intense negative signals in the range 625–675 nm originate due to the scattering of the excitation pulse, although the ground-state bleach signal is also superposed in this region. The peak at 731 nm was slightly shifted to shorter wavelengths and the broad absorption band at ~475 nm was gradually resolved into two peaks at 456 and 505 nm with a lifetime of 760 fs. After the slight shifts in the bands, all the signals gradually decayed with lifetimes of 60 and 680 ps. The spectral shape and time evolution were similar to those in CH_2Cl_2, although the decay of the excited state in solution is much faster than those in the crystal, i.e., 700 fs and 8.6 ps. The accelerated excited state dynamics of **18**$^{-}$-TBA^{+} in solution relative to that in crystal is most probably due to the restricted nonradiative relaxation in the crystal. Therefore, the transient absorption spectrum of the single crystal of **18**$^{-}$-TBA^{+} indicates that **18**$^{-}$ is electronically well isolated due to the charge-by-charge assembly with the aliphatic cation.

The single crystal of **18**$^{-}$-**12**$^{+}$ shows additional transient absorption band at 780 nm immediately after the excitation (Figure 5–16b, 0.15 ps), in addition to the transient absorption bands which are similar to those of **18**$^{-}$-TBA^{+} and are slightly broadened probably due to the π-stacking of **18**$^{-}$. It is noteworthy that the simultaneous two-photon absorption can be neglected, because the excitation occurs at an exposure of less than 100 μJ/cm^2, indicating that some electron transfer occurs through the excitation of **18**$^{-}$. Moreover, spectroelectrochemical measurements in CH_3CN suggest the oxidation of **18**$^{-}$; the radicals resulted in a very similar absorption band at ~790 nm, where no absorption bands were observed upon the reduction of **18**$^{-}$ and oxidation of **12**$^{+}$ (Figure 5–17,18). This strongly suggests that the ultrafast electron transfer occurs within the instrumental response function in the single crystal of **18**$^{-}$-**12**$^{+}$. This solid-state electron transfer process in π-electronic ion-pairing assemblies has not been achieved thus far.

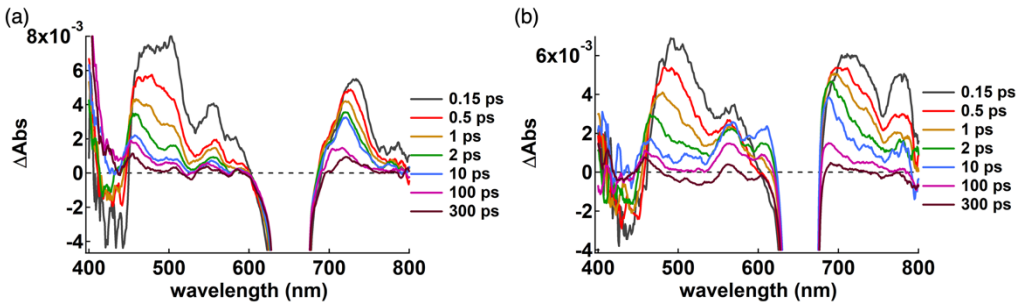

Figure 5–16 Transient absorption spectra of single crystals of (a) **18**$^{-}$-TBA^{+} and (b) **18**$^{-}$-**12**$^{+}$ excited at 650 nm (<100 μJ/cm^{2}) with delay time spanning from 0.15 ps to 300 ps. A negative signal ranges from 625–675 nm contains the scattering of the excitation beam in addition to the ground-state bleach signal.

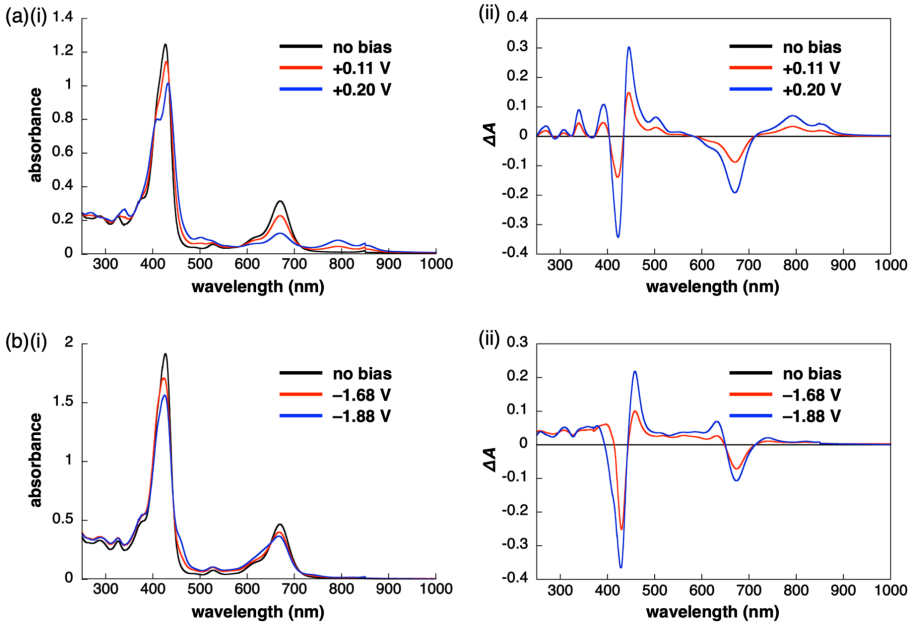

Figure 5–17 Spectroelectrochemical analysis of **18**$^{-}$-TBA^{+} in (a) the oxidation states at +0.11 V (red) and +0.20 V (blue) and (b) the reduction states at –1.68 V (red) and –1.88 V (blue) in CH_3CN (1.2×10^{-4} M in (a) and 1.8×10^{-4} M in (b)) containing of 0.1 M $TBAPF_6$ as an electrolyte under Ar atmosphere: (i) UV/vis absorption spectral changes and (ii) difference spectra between no bias and applied bias.

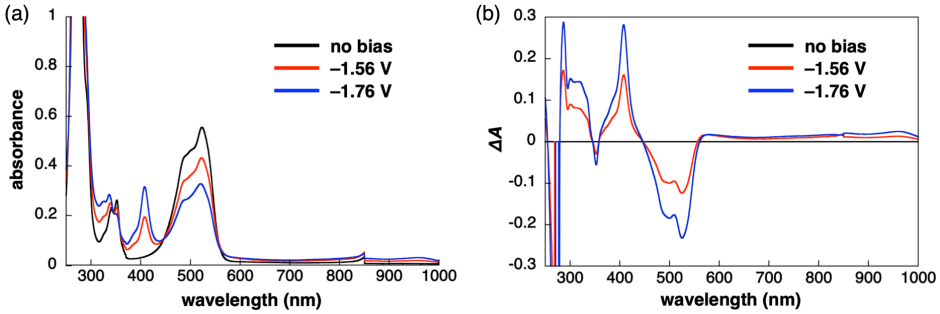

Figure 5–18 Spectroelectrochemical analysis of $\mathbf{12}^{+}$-Cl^{-} in the reduction states at –1.56 V (red) and –1.76 V (blue) in CH_3CN (3.0×10^{-4} M) containing of 0.1 M $TBAPF_6$ as an electrolyte under Ar atmosphere: (a) UV/vis absorption spectral changes and (b) difference spectra between no bias and applied bias.

5–6 Summary of Chapter 5

In this chapter, the detailed analysis of interaction energies in the ion-pairing packing structures revealed that the stacking pairs of π-electronic ions exhibited the ${}^{i}\pi$–${}^{i}\pi$ interactions, resulting predominantly from synergistically operating electrostatic and dispersion forces. Furthermore, the correlations between the solid-state ion-pairing assembling modes based on the ${}^{i}\pi$–${}^{i}\pi$ interactions and their absorption spectra were clearly observed. Electron transfer from the π-electronic anion was also observed in the crystal with contribution of the charge-segregated assembly.

Chapter 6

π-Stacked Ion Pairs: Tightly Associated Charged Porphyrins in Ordered Arrangement Enabling Radical-Pair Formation

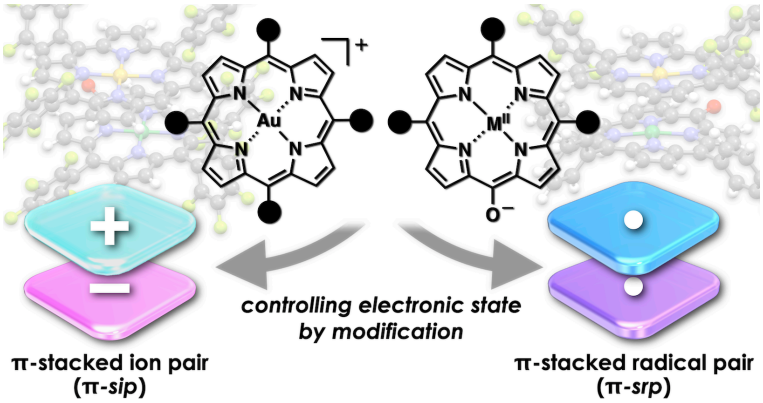

Contents

6–1 Introduction

Interactions between cations and anions form various states resulting from ion pairing (Figure 6–1a). For example, in solution, the arrangement of ions can be defined as contact, solvent-shared, and solvent-separated ion pairs, and the influence of ion-pairing formation on physical properties has been examined.[115] According to the combination of ions, charge-transfer complexes appear as new absorption bands distinct from those of constituent cations and anions, and their photoexcited states have been studied.[116,117] Moreover, ion pairs of carbocations and carbanions,[118–120] including hydrocarbon ion pairs,[121] exist in equilibrium with radicals and covalent species. Thus, investigating the properties of ion pairs as discrete chemical species is crucial for developing functional materials. As shown in Chapter 5, π-electronic ion pairs are of interest for fabricating electronic materials that use intermolecular interactions based on electrostatic and dispersion forces, defined as $^{i}\pi$–$^{i}\pi$ interactions, to provide dimension-controlled assemblies. The $^{i}\pi$–$^{i}\pi$ interactions induce stacking between cations and anions, forming contact ion pairs as π-stacked ion pairs (*π-sips*). Controlling the electronic states can provide π-stacked radical pairs (*π-srps*) (Figure 6–1b). *π-Sips* and *π-srps*, which exhibit attractive properties for potential applications, have not been investigated in detail owing to the difficulties in their preparation and structure determination in the solution state.

As shown in the previous chapters, porphyrin–Au^{III} complexes and divalent metal complexes of oxophlorins (deprotonation states of MHPs) act as π-electronic cations and anions, respectively, for ion-pairing assemblies (Figure 6–1c). Porphyrin ion pairs can be obtained from various derivatives through peripheral modifications of the charged porphyrin skeletons, resulting in interesting electronic properties and functional materials. This study describes the synthesis and solid-state assemblies of charged porphyrins and the solution-state *π-sips*. Controlling the electronic states of the charged π-electronic systems resulted in electron transfer between them in the steady and excited states according to solvent polarity and photoexcitation, thereby producing *π-srps*.

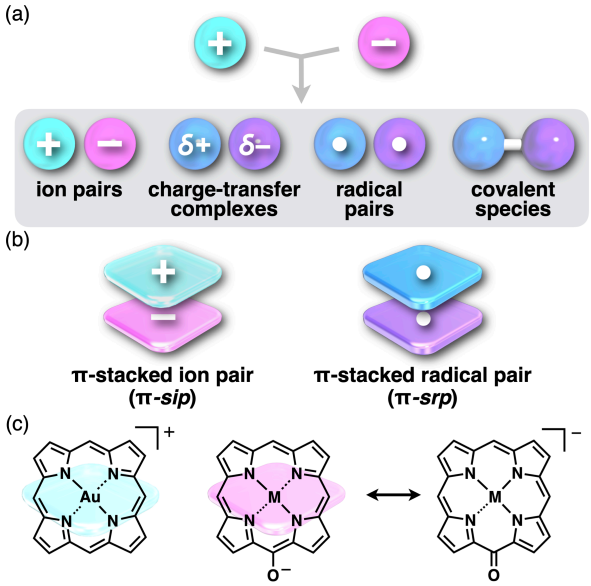

Figure 6–1 (a) Various states resulting from ion pairing, (b) π-stacked ion pair (*π-sip*) and π-stacked radical pair (*π-srp*) induced by stacking of charged π-electronic systems, and (c) constituents of porphyrin ion pairs.

6–2 Synthesis and Characterization

Following the previously reported synthetic procedures for the porphyrin ion pair **16**$^{+}$-**18**$^{-}$,[39] Na^{+} ion pairs of porphyrin anions were prepared by adding solid NaOH or the aqueous solution to the CH_2Cl_2 solutions of MHPs. To the solutions including the Na^{+} ion pairs of porphyrin anions, equivalent amounts of porphyrin–Au^{III} complexes as Cl^{-} ion pairs were added, followed by washing the mixture solutions with water to remove NaCl (Figure 6–2). Via the ion-pair metathesis based on hard and soft acids and bases (HSAB) theory, ion pairs **16**$^{+}$-**19**,**35**$^{-}$ and **22**$^{+}$-**18**,**19**,**35**$^{-}$ were synthesized in 59–85% yields. **22**$^{+}$ was selected as an electron-deficient cation because the tetrasubstituted cation would be less suitable for the formation of *π-sip* due to the bulky C_6F_5 groups. These ion pairs were characterized by ^{1}H, ^{13}C, and ^{19}F NMR and HR-ESI-TOF-MS.

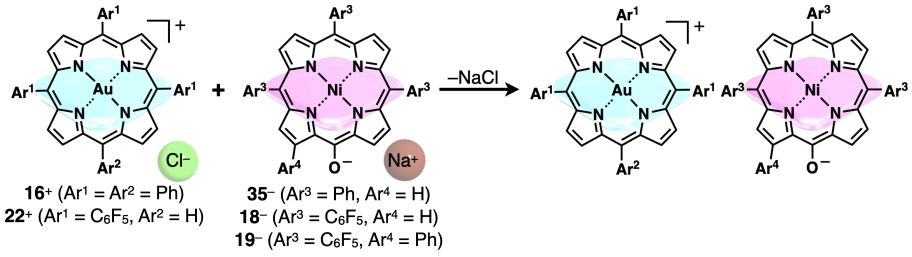

Figure 6–2 Synthesis of porphyrin ion pairs via the ion-pair metathesis based on HSAB theory.

6–3 Interactions of *π-Sips* in the Solid State

Single crystals of ion pairs **16**$^+$-**35**$^-$ and **22**$^+$-**18**,**19**,**35**$^-$ were obtained using the vapor diffusion technique according to the solvent-dependent solubilities. The exact structures and solid-state assemblies of these ion pairs were elucidated by single-crystal X-ray analysis.[67,68] In the solid state, **16**$^+$-**35**$^-$ exhibited *π-sip*-based charge-by-charge assembly modes, wherein the distances between porphyrin cations and anions were 3.67 and 3.91 Å (Figure 6–3a). Compared to a charge-by-charge assembly arranged in a zigzag pattern of **16**$^+$-**18**$^-$,[39] that of **16**$^+$-**35**$^-$ induced $^i\pi$–$^i\pi$ interaction between porphyrin ions due to the relaxed steric hindrance of the porphyrin anion. On the other hand, **22**$^+$-**35**$^-$ exhibited the contribution from charge-segregated mode, containing four benzene molecules for each ion pair (Figure 6–3b). In the packing diagram, the ion pair **22**$^+$-**18**$^-$ with a stacking distance of 3.57 Å formed a 1D-chain structure of *π-sip* connected in a four-fold helical symmetry (Figure 6–3c). The C(–H)···F distances in the column were 2.98–3.55 Å, suggesting the stacking stabilized by hydrogen-bonding interactions. Interestingly, in the single crystal of the ion pair **22**$^+$-**19**$^-$, the space group was triclinic *P*1, which induced polarization caused by inhomogeneous stacking in *π-sip*, with stacking distances of 3.38 and 3.63 Å, due to the curved anion structure (Figure 6–3d).

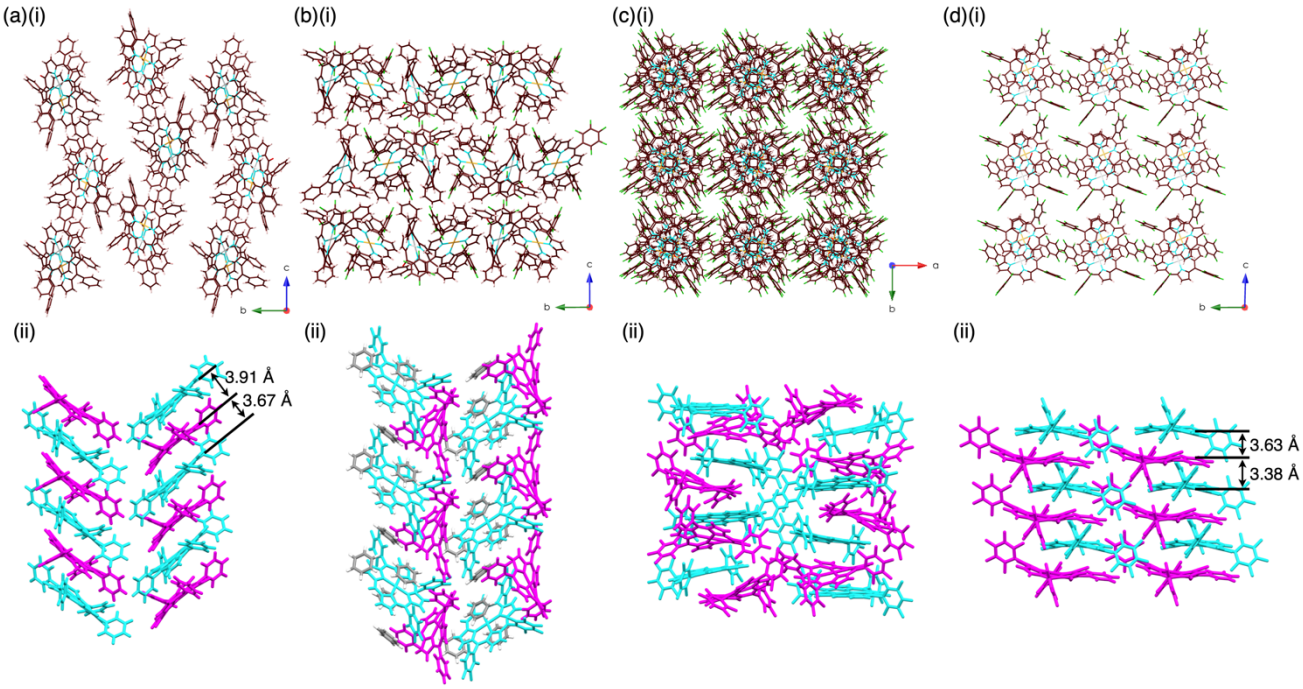

Figure 6–3 Ion-pairing assembled structures of (a) **16**$^+$-**35**$^-$, (b) **22**$^+$-**35**$^-$, (c) **22**$^+$-**18**$^-$, and (d) **22**$^+$-**19**$^-$ as (i) top and (ii) side views in the crystal state. Atom color code in (i): brown, pink, cyan, red, yellow green, gray, and orange refer to carbon, hydrogen, nitrogen, oxygen, fluorine, nickel, and gold, respectively. Color code in (ii): cyan and magenta refer to cation and anion species, respectively, and gray parts in (b) represent benzene molecules.

Hirshfeld surface analysis of **16**$^{+}$-**35**$^{-}$, **22**$^{+}$-**18**$^{-}$, and **22**$^{+}$-**19**$^{-}$ showed characteristic mapping patterns for $^{i}\pi$–$^{i}\pi$ interactions in shape-index and curvedness evaluations, revealing close stacking *π-sip* structures between the porphyrin cations and anions (Figure 6–4).[78–80] The packing structures depend on intermolecular interactions based on $^{i}\pi$–$^{i}\pi$ interaction influenced by the electronic states and shapes of the porphyrin ions. For evaluating the roles of intermolecular interactions, EDA[103] was performed via the FMO method using mixed basis sets including NOSeC-V-TZP for Ni and Au and NOSeC-V-DZP for the other atoms with MCP (Figure 6–5).[104,105,108,109] In the *π-sips* of **16**$^{+}$-**35**$^{-}$, **22**$^{+}$-**18**$^{-}$, and **22**$^{+}$-**19**$^{-}$ in the solid state, the main contributions of $^{i}\pi$–$^{i}\pi$ interactions between cations and anions were electrostatic (E_{es} = –76.69, –85.37, and, –99.31 kcal/mol, respectively) and dispersion forces (E_{disp} = –185.95, –150.76, and –183.39 kcal/mol, respectively). The introduction of electron-deficient **22**$^{+}$ effectively enhanced electrostatic attraction. On the other hand, ion pair **16**$^{+}$-**35**$^{-}$ with reduced steric hindrance stabilized *π-sip* through effective dispersion forces. The correlations were observed between the cation–anion offset distances (Figure 6–6) and the EDA, showing the largest total interaction energy for **22**$^{+}$-**19**$^{-}$ with the shortest offset distance.

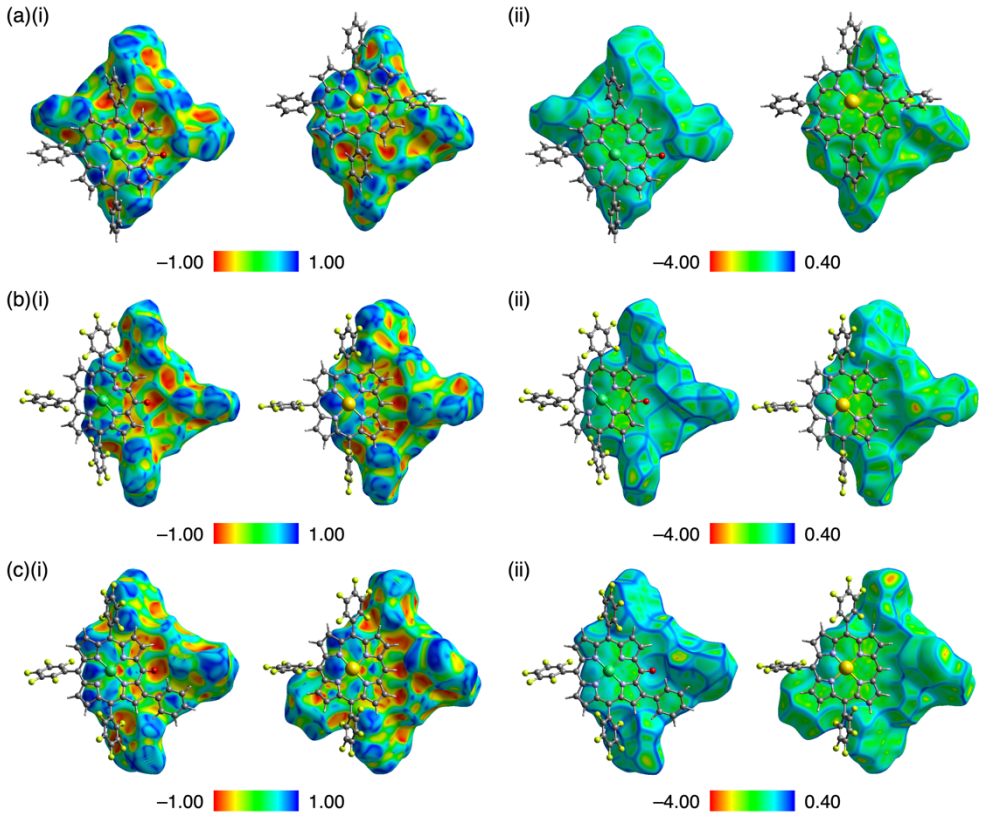

Figure 6–4 Hirshfeld surfaces of cations (left) and anions (right) in the crystal structure of (a) **16**$^{+}$-**35**$^{-}$, (b) **22**$^{+}$-**18**$^{-}$, and (c) **22**$^{+}$-**19**$^{-}$ mapped over (i) shape-index property and (ii) curvedness property: surfaces with a ball-and-stick model of the neighboring counterion (left) and only surfaces (right). Atom color code: gray, white, blue, red, yellow green, green, and orange refer to carbon, hydrogen, nitrogen, oxygen, fluorine, nickel, and gold, respectively.

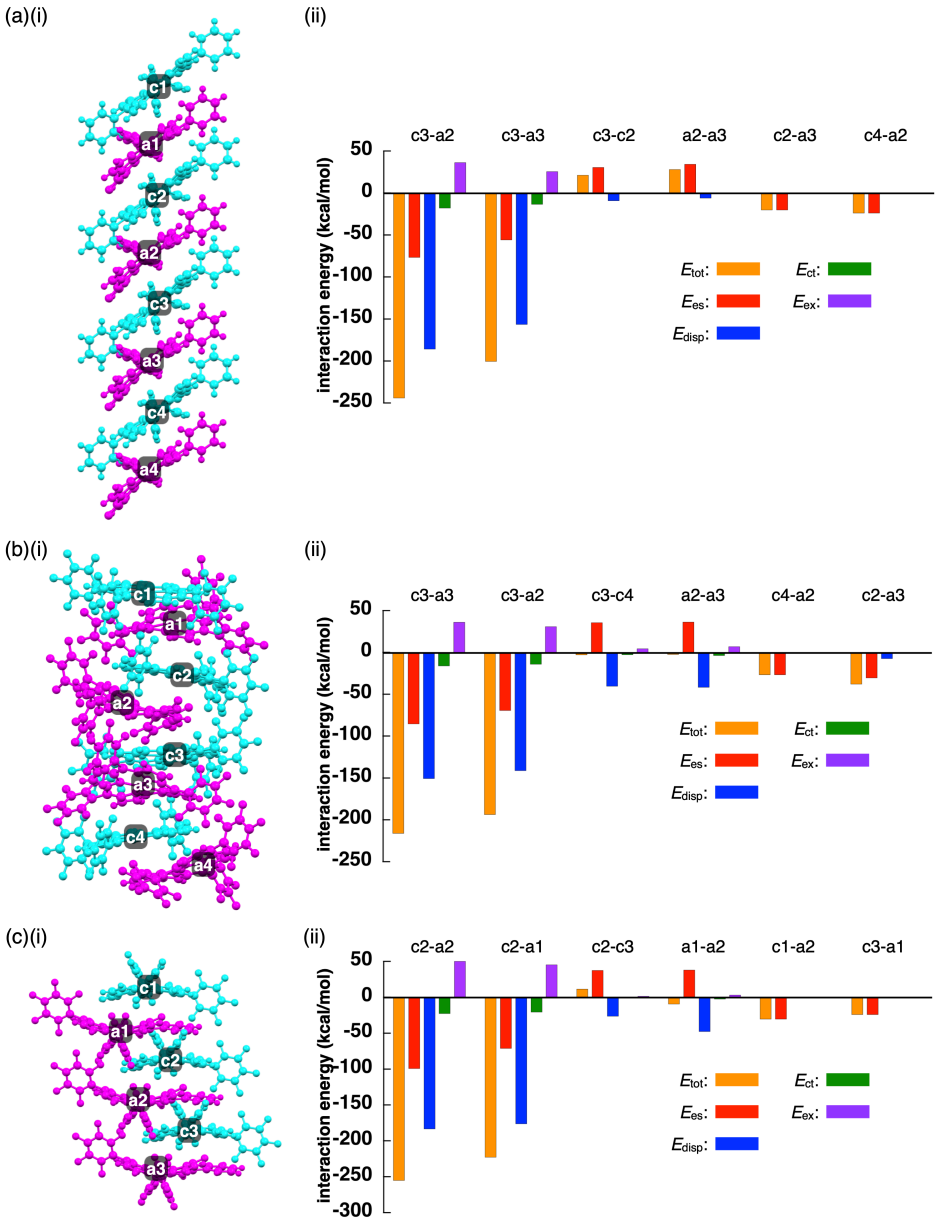

Figure 6–5 EDA of (a) **16**$^{+}$-**35**$^{-}$, (b) **22**$^{+}$-**18**$^{-}$, and (c) **22**$^{+}$-**19**$^{-}$: (i) single-crystal X-ray structure and (ii) intermolecular interaction energies (kcal/mol) between selected ions estimated at the FMO2-MP2 method using mixed basis sets including NOSeC-V-TZP with MCP for Ni and Au and NOSeC-V-DZP with MCP for the other atoms. Color code in (i): cyan and magenta refer to cation and anion parts, respectively.

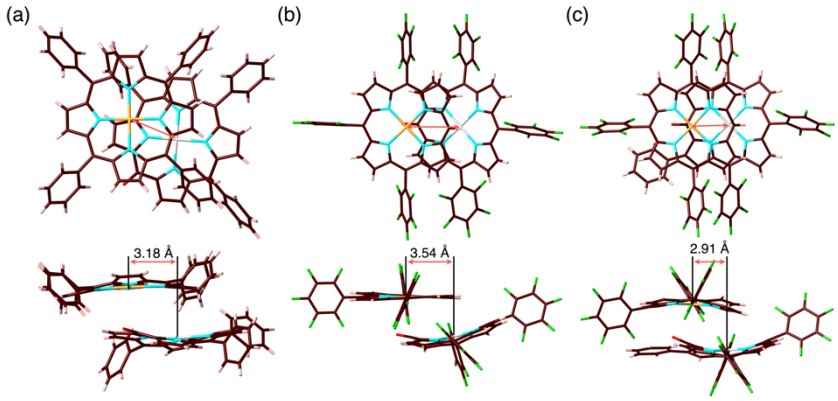

Figure 6–6 Offset distances between representative cations and anions in the crystal structures of (a) **16**$^{+}$-**35**$^{-}$, (b) **22**$^{+}$-**18**$^{-}$, and (c) **22**$^{+}$-**19**$^{-}$. The offset distances were estimated as the average of the distance between the perpendicular point from the Au center to the anion plane and the Ni center and that between the perpendicular point from the Ni center to the cation plane and the Au center. Atom color code: brown, pink, cyan, red, yellow green, gray, and orange refer to carbon, hydrogen, nitrogen, oxygen, fluorine, nickel, and gold, respectively.

6–4 Solution-State *π-Sip* Behaviors

Single-crystal X-ray analysis clearly showed the 1:1 combinations of cations and anions, allowing us to evaluate the behaviors of ion pairs in the solution state. The **22**$^{+}$-**18**$^{-}$ ion pair exhibited characteristic ^{1}H NMR signal shifts due to the formation of *π-sip* in the solution state (Figure 6–7a). In CD_2Cl_2 at 20 °C (1.0 mM), the ^{1}H NMR signals of **22**$^{+}$ in **22**$^{+}$-**18**$^{-}$ were observed at 9.42, 9.34, 9.11, 8.54, and 7.72 ppm and those of **18**$^{-}$ appeared at 8.04, 8.02, 6.76, and 6.02 ppm. The signals of **22**$^{+}$ were shifted upfield compared to those of **22**$^{+}$-PF_6^{-}, which were shown at 11.41, 10.13, 9.58, 9.56, and 9.54 ppm, respectively. In contrast to **22**$^{+}$, the signals of **18**$^{-}$ were shifted upfield and downfield compared to those of TBA^{+} ion pair of **18**$^{-}$ (8.68, 7.93, 7.75, and 7.70 ppm). This tendency could be explained by the stacking positions of **22**$^{+}$ and **18**$^{-}$, as shown in the optimized structure of **22**$^{+}$-**18**$^{-}$ at the GD3BJ-B3LYP/6-31G(d,p) for C, H, N, O, and F and GD3BJ-B3LYP/LanL2DZ for Ni and Au based on its crystal structure (Figure 6–7b).[66] The H^{e} and H^{f} of **18**$^{-}$, β-CH close to the anionic oxygen, were located on the porphyrin plane of **22**$^{+}$, resulting in the shielding effects. In contrast, H^{g} of **18**$^{-}$, the other β-CH, were located out of the porphyrin plane of **22**$^{+}$, inducing deshielding effect. Furthermore, the ion-pairing process of **22**$^{+}$-**18**$^{-}$ was examined by concentration-dependent ^{1}H NMR in CD_2Cl_2 (Figure 6–8a). The ^{1}H NMR signals of H^{a}, H^{b}, and H^{c} of **22**$^{+}$ and H^{e} and H^{f} of **18**$^{-}$ were shifted upfield with increasing concentrations, suggesting the *π-sip* formation. The concentration-dependent ^{1}H NMR signal shifts of **22**$^{+}$-**18**$^{-}$ gave rise to the estimation of the hetero-dimerization constant (K_{dim}) of 2.8×10^{5} M^{-1} in CD_2Cl_2 at 20 °C (Figure 6–

8b) by curve-fitting of the chemical shifts relative to the concentrations equation (1):

$$\sigma_{obs} = \sigma_{mono} + \frac{1 + 2K_aC - \sqrt{1 + 4K_aC}}{2K_aC}(\sigma_{dim} - \sigma_{mono}) \qquad (1)$$

for the equilibrium between the monomer and the hetero dimer showing their averaged signals (δ_{obs}: observed chemical shifts, δ_{mono}: ideal monomer chemical shift, δ_{dim}: ideal hetero dimer chemical shift, K_a: hetero dimerization constant, C: total concentrations of the ion pair). To the best of our knowledge, the hetero-dimerization constants of charged π-systems have not been estimated using concentration-dependent spectral changes. The formation of higher-order aggregates could be excluded by the hetero-dimerization model analysis and no observation of further chemical shift changes under high concentration conditions. *π-Sip* formation was observed even in CD_3CN, as a more polar solvent, with an estimated K_{dim} of 190 M^{-1} (Figure 6–9).

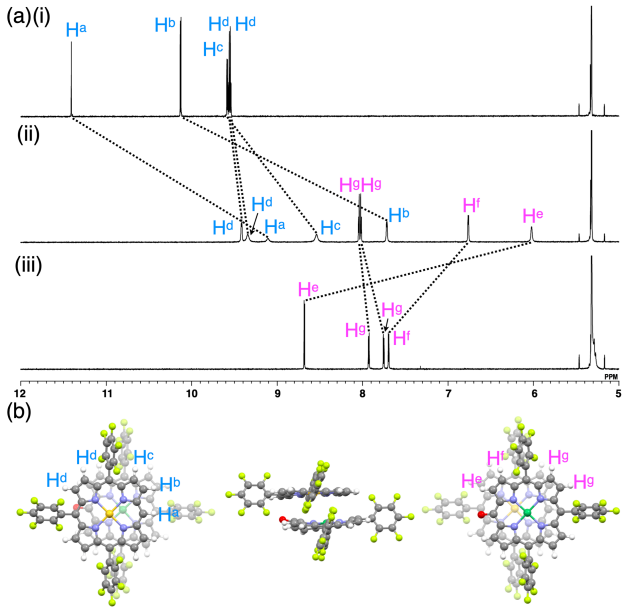

Figure 6–7 (a) ^{1}H NMR spectra of (i) **22**$^+$-PF_6^-, (ii) **22**$^+$-**18**$^-$, and (iii) TBA$^+$-**18**$^-$ in CD_2Cl_2 (1.0 mM, 20 °C), (b) optimized structure of **22**$^+$-**18**$^-$ as top views from the planes of **22**$^+$ (left) and **18**$^-$ (right) and side view (middle).

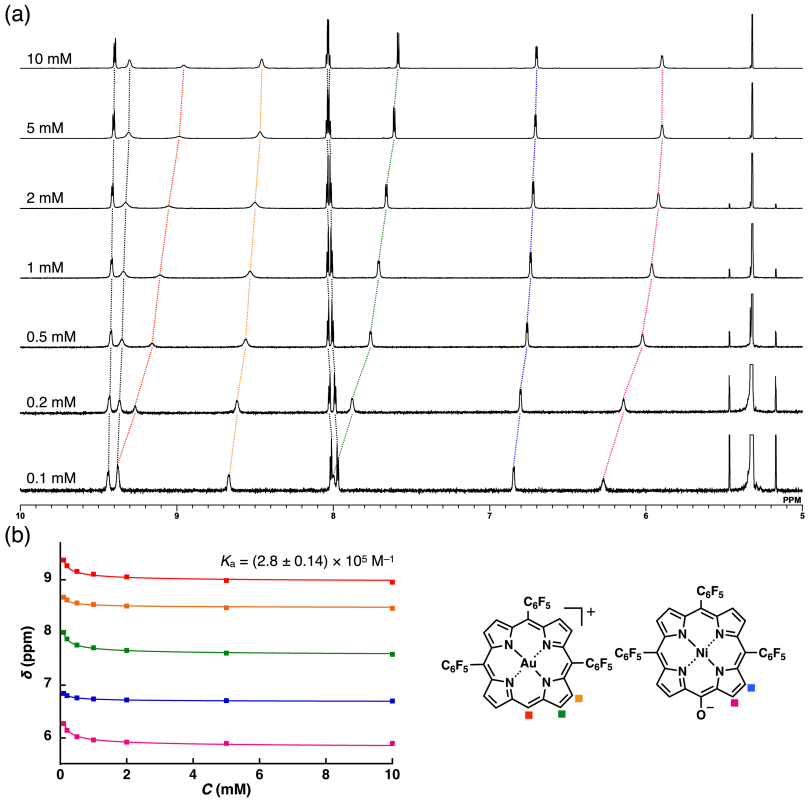

Figure 6–8 (a) ^{1}H NMR spectral changes at various concentrations and (b) concentration-dependent plots and fitting curves of **22**$^+$-**18**$^-$ in CD_2Cl_2.

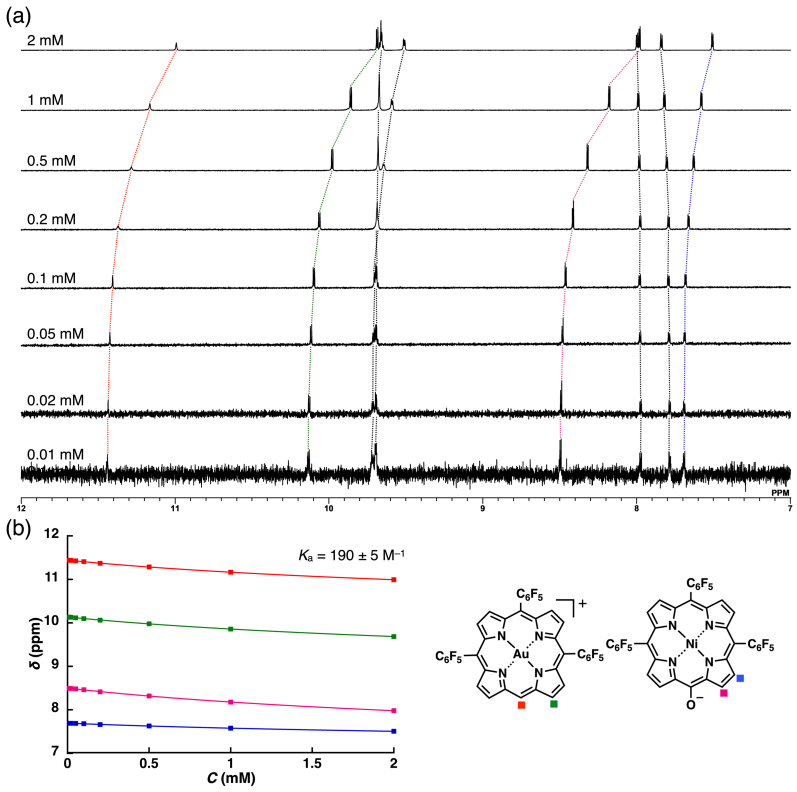

Figure 6–9 (a) ^{1}H NMR spectral changes at various concentrations and (b) concentration-dependent plots and fitting curves of **22**$^+$-**18**$^-$ in CD_3CN.

π-Electronic ion pairs such as **16**$^+$-**18**$^-$ show negligible exciton coupling between oppositely charged species due to their quite different MO levels.[39] Similarly, the UV/vis absorption spectra of **16**$^+$-**35**$^-$, **16**$^+$-**19**$^-$, **22**$^+$-**18**$^-$, and **22**$^+$-**19**$^-$ showed the sums of the absorption bands of the constituents (Figure 6–10). However, the ion pair of electron-poor cation **22**$^+$ and electron-rich anion **35**$^-$ in toluene exhibited a different absorption spectrum from the respective spectra (Figure 6–11a). Given the possibility of the anion-to-cation electron transfer, the corresponding radicals **22**$^\bullet$ and **35**$^\bullet$ (Figure 6–11b) were prepared by reduction of **22**$^+$ and oxidation of **35**$^-$, respectively, following the previously reported synthetic procedures for porphyrin–Au^{II} complexes[122] and porphyrin *meso*-oxy radicals[50–52] for further examinations. The X-ray analysis of **35**$^\bullet$, whose single crystal was obtained by the vapor diffusion of *n*-hexane into a CH_2Cl_2 solution, revealed the stacking assembly with distances of 3.32 and 3.63 Å between the radical species (Figure 6–12). A modest agreement was seen between the sum of absorption spectra of the obtained radical species **22**$^\bullet$ and **35**$^\bullet$ and that of "the ion pair **22**$^+$-**35**$^-$" (Figure 6–11a). The difference from other systems was due to the activation of charged π-electron systems, resulting in electron transfer and the radical pair **22**$^\bullet$-**35**$^\bullet$ derived from **22**$^+$-**35**$^-$. The electron transfer depended on the solvent polarity as seen in the ion pair of **22**$^+$-**35**$^-$ in polar solvents and increased radical pairs in less polar solvents (Figure 6–13). Furthermore, the radical pair **22**$^\bullet$-**35**$^\bullet$ formed in nonpolar solvents can be converted to the ion pair in polar solvents, and vice-versa.

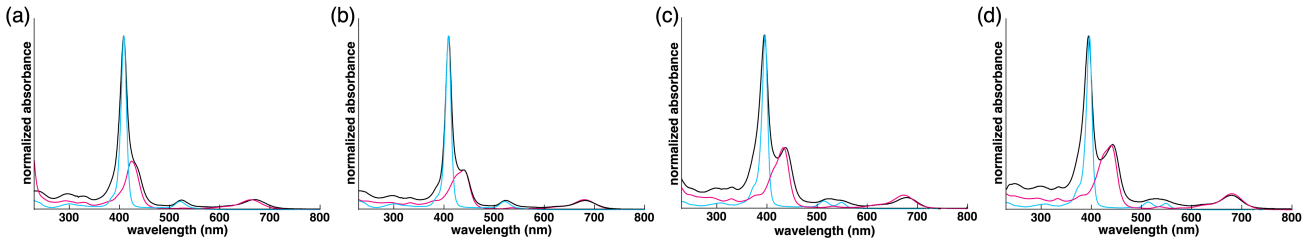

Figure 6–10 UV/vis absorption spectra in CH_2Cl_2: (a) **16**$^+$-**35**$^-$ (black, 3.0×10^{-4} M), **16**$^+$-PF_6^- (cyan, 4.0×10^{-6} M), and TBA$^+$-**35**$^-$ (magenta, 5.3×10^{-6} M), (b) **16**$^+$-**19**$^-$ (black, 3.0×10^{-4} M), **16**$^+$-PF_6^- (cyan, 4.0×10^{-6} M), and TBA$^+$-**19**$^-$ (magenta, 1.0×10^{-5} M), (c) **22**$^+$-**18**$^-$ (black, 3.0×10^{-4} M), **22**$^+$-PF_6^- (cyan, 3.0×10^{-6} M), and TBA$^+$-**18**$^-$ (magenta, 7.6×10^{-6} M), and (d) **22**$^+$-**19**$^-$ (black, 3.0×10^{-4} M), **22**$^+$-PF_6^- (cyan, 3.0×10^{-6} M), and TBA$^+$-**19**$^-$ (magenta, 1.0×10^{-5} M).

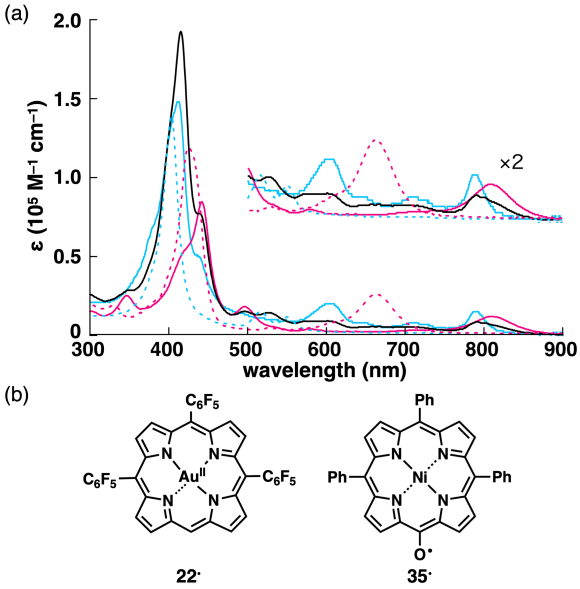

Figure 6–11 (a) UV/vis absorption spectra of "**22**$^{+}$-**35**$^{-}$" (black, 2.8 × 10^{-6} M), **22**$^{\bullet}$ (cyan, 1.0 × 10^{-6} M), **35**$^{\bullet}$ (magenta, 3.0 × 10^{-6} M), **22**$^{+}$-PF_6^{-} (dotted cyan, 3.0 × 10^{-6} M), and TBA^{+}-**35**$^{-}$ (dotted magenta, 3.0 × 10^{-6} M) in toluene and (b) porphyrin-based radical species **22**$^{\bullet}$ and **35**$^{\bullet}$.

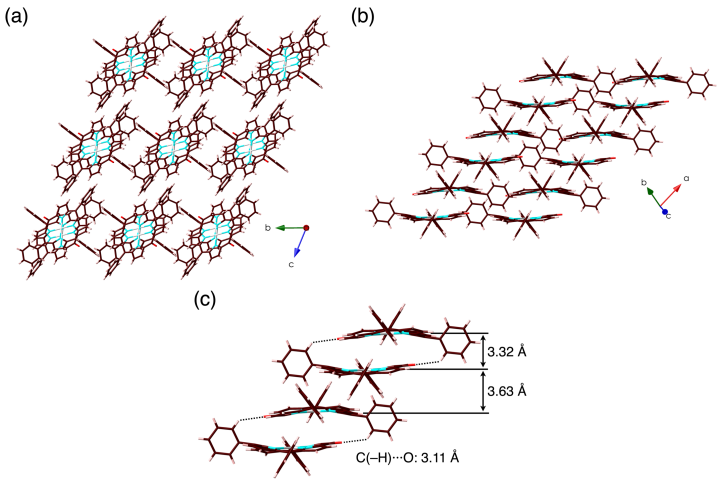

Figure 6–12 Packing diagrams of **35**$^{\bullet}$: packing structures as (a) top and (b) side views and (c) enlarged view of the packing structure in (b). Atom color code: brown, pink, cyan, red, and gray refer to carbon, hydrogen, nitrogen, oxygen, and nickel, respectively.

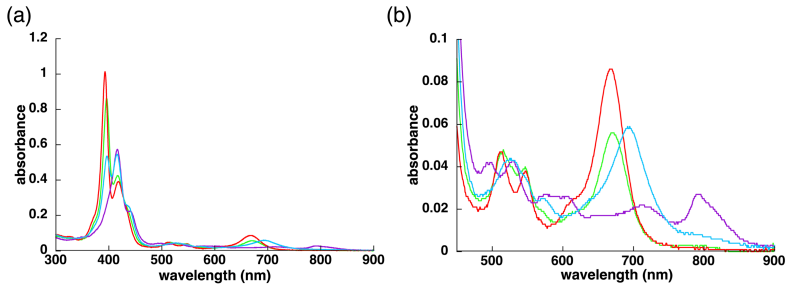

Figure 6–13 (a) UV/vis absorption spectra with (b) enlarged version for **22**$^+$-**35**$^-$ (2.8×10^{-6} M) in toluene (purple), THF (light blue), CH_2Cl_2 (light green), and CH_3CN (red).

The redox behaviors of **16**$^+$-PF_6^-, **22**$^+$-PF_6^-, TBA$^+$-**35**$^-$, and TBA$^+$-**18**$^-$ were studied by cyclic voltammetry (CV) in CH_2Cl_2 containing 0.1 M $TBAPF_6$ as an electrolyte (Figure 6–14). To properly evaluate the electrochemical properties, the electrolyte ions were consistent with the counterions of charged porphyrins. The first reduction potentials (vs Ag^+/Ag) of **16**$^+$ and **22**$^+$ were estimated to be –0.86 and –0.55 V, respectively, suggesting that **22**$^+$ is more likely to be reduced by 0.31 V than **16**$^+$. On the other hand, the first oxidation potentials of **35**$^-$ and **18**$^-$ at –0.14 and 0.19 V, respectively, showed easier oxidation for **35**$^-$ by 0.33 V than for **18**$^-$. Theoretically estimated HOMO/LUMO energy levels of the charged porphyrins showed a trend similar to CVs. In addition, the calculations incorporating solvent effects suggested that **22**$^+$ and **35**$^-$ would be more activated in toluene than in CH_2Cl_2 (Figure 6–15).[66,123] These results are consistent with the fact that an electron transfer in **22**$^+$-**35**$^-$ proceeds in less polar solvents.

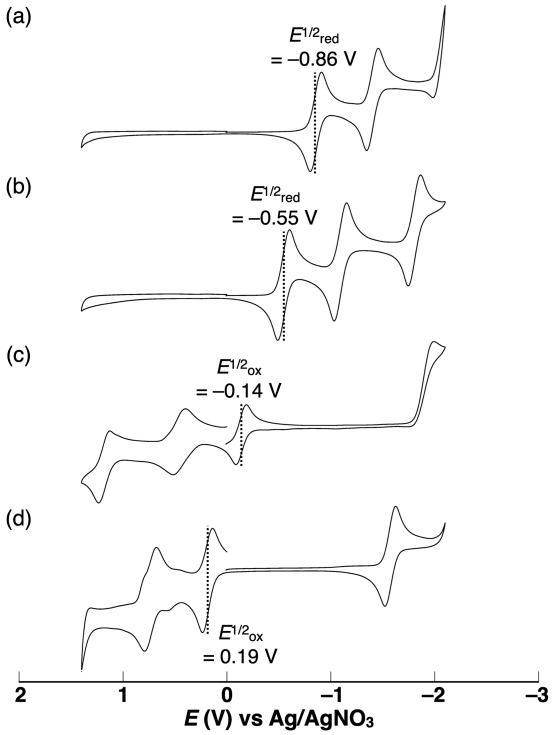

Figure 6–14 CVs of (a) **16**$^+$-PF_6^-, (b) **22**$^+$-PF_6^-, (c) TBA$^+$-**35**$^-$, and (d) TBA$^+$-**18**$^-$ in CH_2Cl_2 (1.0 mM) containing $TBAPF_6$ (0.1 M) as an electrolyte under Ar atmosphere at a scan rate of 100 mV/s.

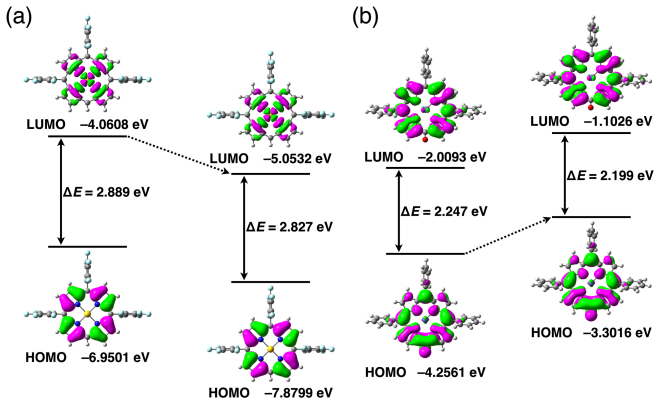

Figure 6–15 Molecular orbitals of (a) **22**$^+$ and (b) **35**$^-$ with solvent effect (left: CH_2Cl_2, right: toluene). These were estimated at PCM-B3LYP/6-31+G(d,p) for C, H, N, O, and F and PCM-B3LYP/LanL2DZ for Ni and Au.

The magnetic properties of the radical pair **22**$^{\bullet}$-**35**$^{\bullet}$, derived from **22**$^+$-**35**$^-$, and constituent radicals **22**$^{\bullet}$ and **35**$^{\bullet}$ were revealed by electron spin resonance (ESR) spectroscopy in frozen toluene at 10 K. The ESR signals of **22**$^{\bullet}$ and **35**$^{\bullet}$ were shown to be the Au^{II} complex (g_{Au} = 2.037, 2.012, 1.942; A_{Au} = 102.0, 40.0, 90.0 MHz) and the *meso*-oxy radical **35**$_{oxy}^{\bullet}$ with a spin localized on the oxygen atom (g_{oxy} = 2.006, 2.002, 1.9985), respectively (Figure 6–16). On the other hand, the ESR of the radical pair **22**$^{\bullet}$-**35**$^{\bullet}$ was significantly different from those of

22$^{\bullet}$ and **35**$^{\bullet}$. This spectrum was reproduced by simulation[124] using the *g* values and the hyperfine coupling constant of **22**$^{\bullet}$ and assuming the production of the Ni^{III} complex $\mathbf{35}_{Ni}^{\bullet}$ (g_{Ni} = 2.722, 2.922, 1.890) with the magnetic dipole interaction (|*D*| = 3575 MHz, |*E*| = 150 MHz (zero-field splitting parameters *D* and *E* for axial and transversal components, respectively) (Figure 6–17a i). Using a point-dipole approximation from the *D* value, the spin–spin distance was estimated to be 3.02 Å, suggesting the *π-srp* formation. These results indicated that the change in the *g* values of Ni complex was due to the spin shift from the oxygen atom to the Ni center by the neighboring Au^{II} complex (Figure 6–17b). In addition, the shift of *g* values was observed upon increasing the temperature to 140 K (Figure 6–18a). The ESR signal of **22**$^{\bullet}$-**35**$^{\bullet}$ at 140 K was well-simulated as the Au^{II} complex **22**$^{\bullet}$ and *meso*-oxy radical $\mathbf{35}_{oxy}^{\bullet}$ (g_{oxy} = 2.150, 2.150, 2.000) with the magnetic dipole interaction (|*D*| = 1325 MHz, |*E*| = 441 MHz) (Figure 6–17a ii). The spin–spin distance derived from the *D* value was estimated to be 3.93 Å, which was augmented from the distance at 10 K, also suggesting a change in the spin distribution of **35**$^{\bullet}$ from the Ni center to mainly the oxygen atom (Figure 6–17b bottom). Furthermore, the relationship between the ESR signal intensities at 10 and 140 K should be consistent with the antiferromagnetic interaction between **22**$^{\bullet}$ and **35**$^{\bullet}$ (Figure 6–18b). To our knowledge, the systems with a spin distribution change by the interaction with the counterspecies have not been achieved thus far. The radical pair **22**$^{\bullet}$-**35**$^{\bullet}$ had been expected to dissociate because of the lower contribution of electrostatic interaction than the ion pair. However, in fact, it maintained a closely stacked structure of **22**$^{\bullet}$ and **35**$^{\bullet}$ by the antiferromagnetic dipolar interactions in frozen toluene. Such a stacked structure is ascribable to the precursory stacking structure (*π-sip*) formed by electrostatic and dispersion forces, as well as to the spin–spin interactions between the two kinds of species. The antiparallel electron spins in the tightly stacked structure can be considered as the intermediate state between covalent and noncovalent bonding, providing a new insight into chemical bonding.

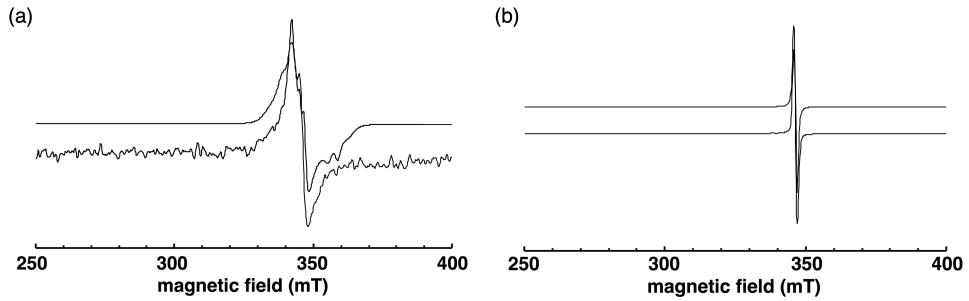

Figure 6–16 ESR spectra of (a) **22**• and (b) **35**• in toluene at 10 K (bottom) and the simulated spectrum (top).

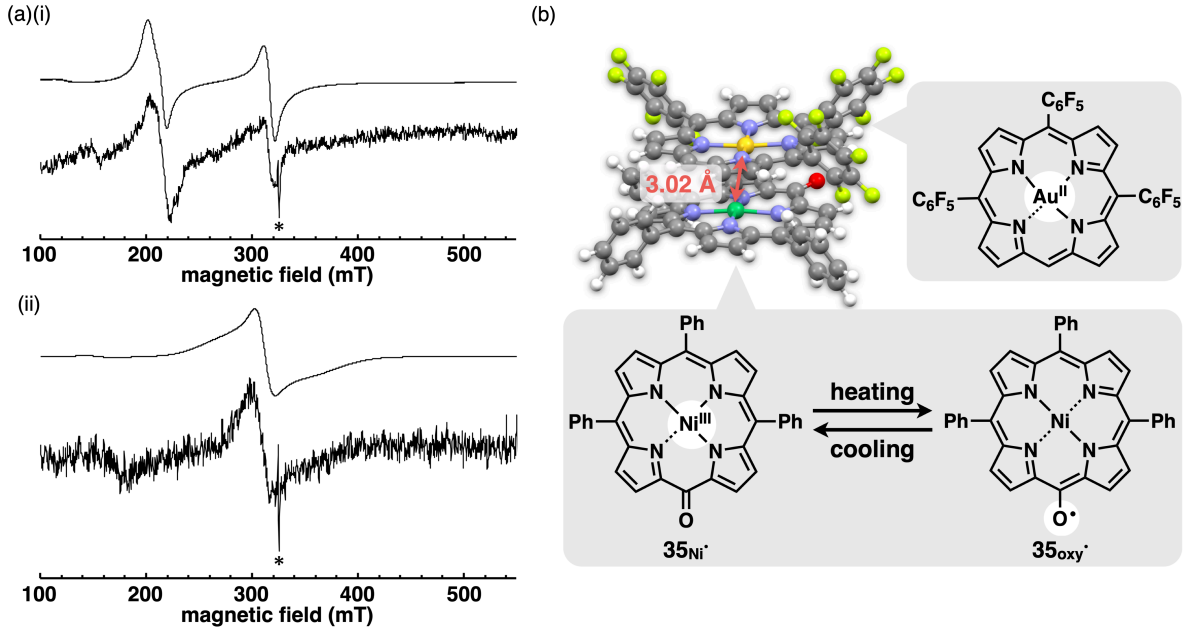

Figure 6–17 (a) Simulated (top) and observed (bottom) ESR spectra of $\mathbf{22}^{+}$-$\mathbf{35}^{-}$ in toluene at (i) 10 K and (ii) 140 K and (b) closely stacked structure (*π-srp*) of **22**• and **35**• with the spin–spin distance and the change in spin distribution of **35**• ($\mathbf{35}_{Ni}$• and $\mathbf{35}_{oxy}$•) as a result of temperature change. Signals marked with * in (a) are ascribable to a trace amount of the dissociated **35**•, whereas white circles in (b) represent spin distributions.

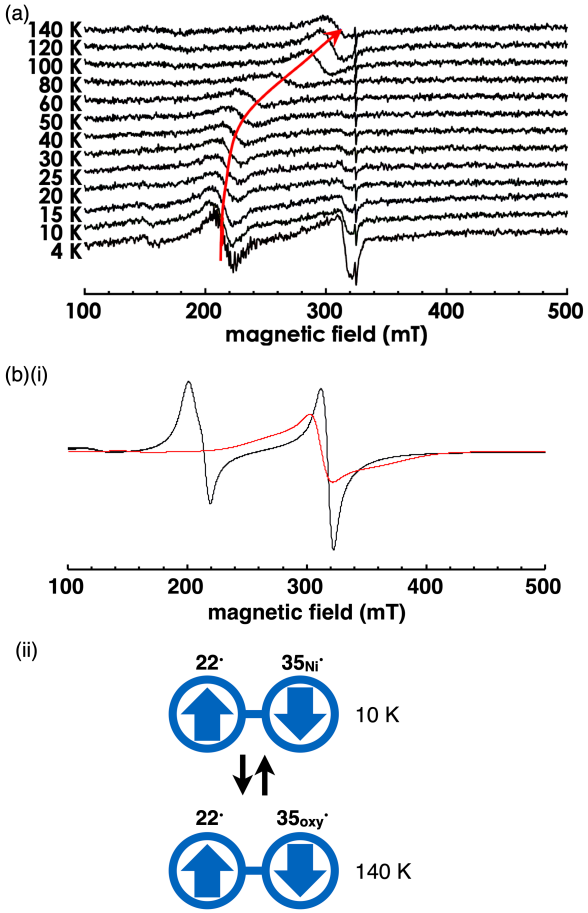

Figure 6–18 (a) ESR spectral changes of radical pair **22**$^{\bullet}$-**35**$^{\bullet}$, derived from **22**$^{+}$-**35**$^{-}$, in toluene at various temperatures (4–140 K) and (b)(i) simulated spectra with antiferromagnetic interactions ($J = -7 \times 10^5$ MHz) at 10 (black) and 140 K (red) and (ii) the relationship between antiferromagnetic interactions at 10 and 140 K.

6–5 Transient Absorption Measurements and Photo-Induced Electron Transfer of Porphyrin Ion Pairs

The fact that electron transfer occurs in the ground state depending on the solvent polarity indicates that the energy difference between the ion-pair and radical-pair states is small. For such a pair of ions or radicals, electron transfer would proceed in the excited state even in solvents where the ion pair is stable in the ground state (Figure 6–19). In addition, porphyrin–Au^{III} complexes are ideal for ion-pairing photoinduced electron transfer because they function as electron acceptors by connecting with uncharged π-electronic systems.[35–37] To investigate the hypothesis, the transient absorption spectra of **22**$^{+}$-**35**$^{-}$, containing the state of the radial pair **22**$^{\bullet}$-**35**$^{\bullet}$, were measured in different solvents with a 680-nm laser pulse selectively exciting **35**$^{-}$ (Figure 6–20). In the transient absorption spectra of **22**$^{+}$-**35**$^{-}$ in CH_3CN excited at 680 nm, a positive sharp signal and a broad

signal were observed at 710 and <600 nm, respectively, instantaneously after the excitation, while a negative signal was observed at 670 nm due to the ground-state bleach (Figure 6–20a). The transient absorption spectra evolve with time and decay within hundreds of picoseconds. The spectral shape and the time evolution are very similar to those of TBA^+-**18**$^-$ in CH_2Cl_2 excited at 680 nm, where no photoinduced electron transfer occurs in the ion pair. This result indicates that no photoinduced electron transfer occurs in **22**$^+$-**35**$^-$ in CH_3CN due to the dissociation of *π-sip* and the photogenerated excited state of **35**$^-$ quickly reverts to the ground state.

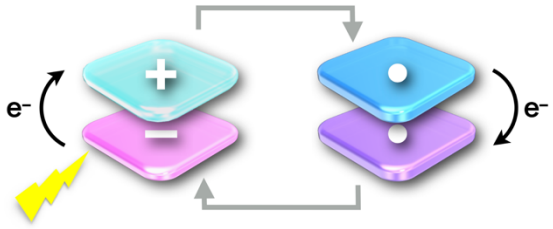

Figure 6–19 Photo-induced electron transfer of charged π-electronic systems.

In the transient absorption spectra of **22**$^+$-**35**$^-$ in THF excited at 680 nm, the additional transient absorption bands are clearly observed at 590, 790, and 830 nm instantaneously after the excitation (Figure 6–20c). The relative amplitude of the transient absorption bands to that of the bleach signal at 690 nm is larger in toluene (Figure 6–20d) than that of THF, while is smaller in CH_2Cl_2 (Figure 6–20b). It indicates that the transient absorption bands of **22**$^•$ and **35**$^•$ increase with the decrease in the relative dielectric constants of the media, i.e., *π-sip* is easily dissociated in polar solvents. These results show that ultrafast photoinduced electron transfer occurs in **22**$^+$-**35**$^-$ in THF within instrumental response function. The obtained transient absorption spectra were globally analyzed using the four-state sequential decay kinetic models convolved with a Gaussian pulse using the Glotaran program.[114] The lifetimes of the obtained EADS, which present the transient absorption spectra resolved into each component of the kinetic models, were 4 fs, 330 fs, 3.0 ps, and 31 ps. The first EADS (4 fs) was safely assigned to the scattering of the incident excitation pulse and nonlinear solvent responses because the lifetime is too short to assign the electronic excited state. The second and third EADS (330 fs and 3.0 ps) have the absorption band ascribable to **35**$^•$, while the transient absorption band is much smaller in the fourth EADS (31 ps). The amplitude of the signal at 790 nm of the fourth EADS is ~20% as compared to that of the first EADS. This indicates that ~80% of the generated **35**$^•$ decays rapidly with a time constant of 3.0 ps, and the residual signal decays with a time constant of 31 ps. The formation of **22**$^•$ and **35**$^•$ is clearly demonstrated via photo-induced electron transfer in the *π-sips*. The phenomena in *π-sips* are quite

different from those of noncharged donor–acceptor systems, as observed in the production of noncharged radical pairs from *π-sips*.

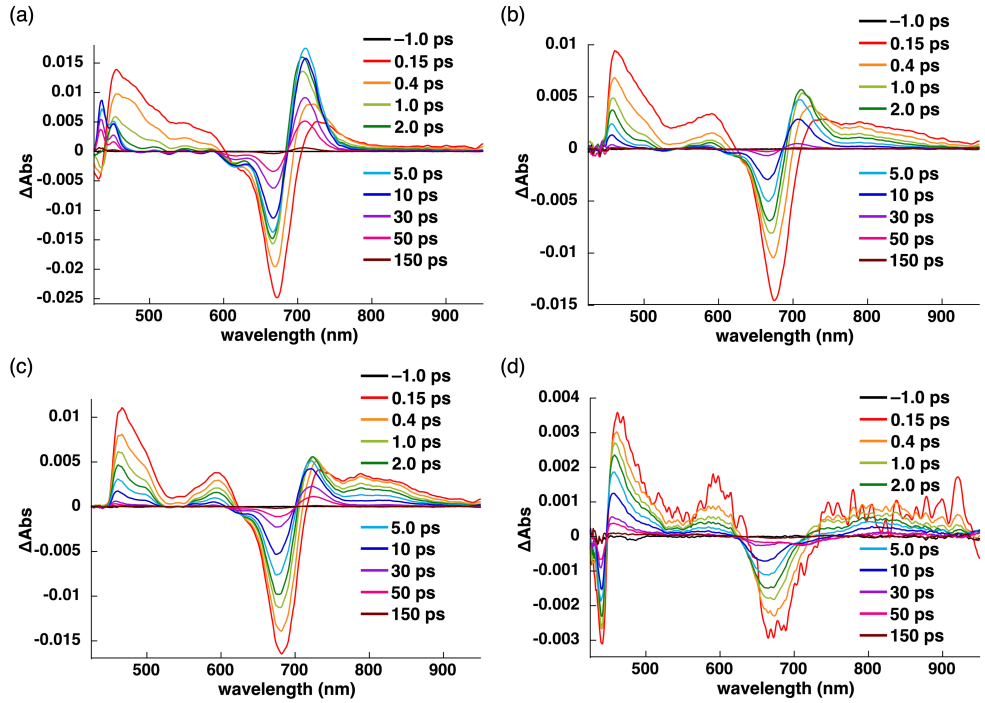

Figure 6–20 Transient absorption spectra of **22**$^{+}$-**35**$^{-}$ in (a) CH_3CN, (b) CH_2Cl_2, (c) THF, and (d) toluene excited at 680 nm (60 nJ/pulse) with delay time spanning from –1.0 to 150 ps.

6–6 Summary of Chapter 6

In this chapter, various porphyrin ion pairs have been synthesized through ion-pair metathesis based on HSAB theory. Single-crystal X-ray analysis, Hirshfeld surface analysis, and EDA calculations revealed the solid-state ion-pairing assemblies based on the $^{i}\pi$–$^{i}\pi$ interactions of *π-sips*. In solution, *π-sip* formation has been clearly shown with the estimation of hetero-dimerization constants. π-Electronic cations and anions can be activated by introducing electron-withdrawing and electron-donating groups, respectively, resulting in the formation of a radical pair via electron transfer in steady and excited states due to solvent polarity and photoexcitation, respectively. The ESR in frozen toluene reveals the *π-srp* formation with a close stacking distance of 3.02 Å, suggesting a tightly stacked "condensed conjugation" structure. Furthermore, this chapter has demonstrated temperature-dependent spin distribution changes due to the antiferromagnetic spin–spin interactions between the constituent distinct radicals in *π-srp*. The spin–spin interactions are influenced by the stacking structure of the hetero π-electronic systems and the Au–Ni distance, which are characteristic to the *π-srp* derived from the *π-sip*. Interactions between the spins in different moieties associated with noncovalent interactions are rare but efficiently achieved by the ion-pairing strategy.

Chapter 7

Substituent-Dependent Photoexcitation Processes of π-Stacked Ion Pairs

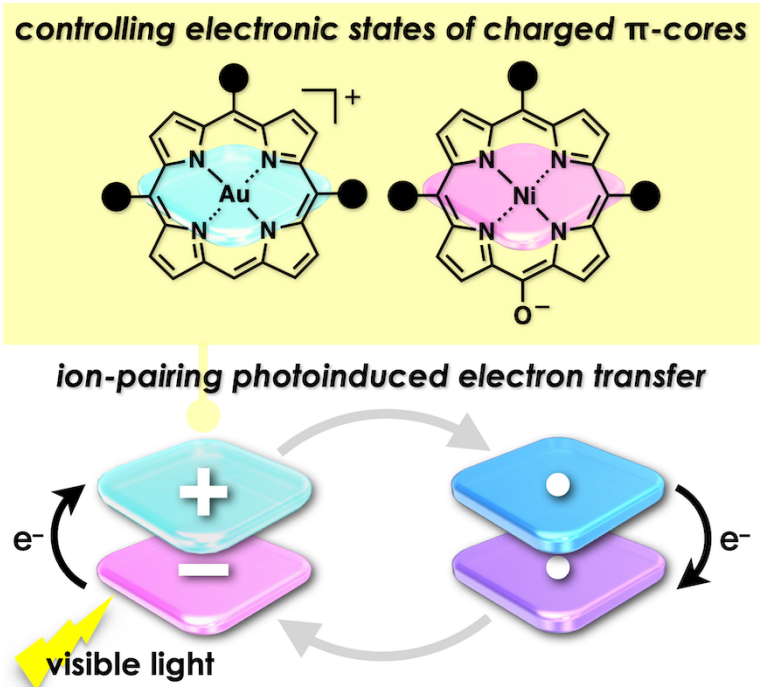

Contents

7–1 Introduction

The smallest ion-pairing components in charge-by-charge assemblies are π-stacked ion pairs (*π-sips*), which comprise stacked oppositely charged π-electronic systems. Examination of the photophysical properties and behavior of *π-sips* in the excited state is essential for producing functional materials in the bulk state. Charged porphyrins, with charge in the core units, are suitable components of *π-sips*. Various ion pairs have been formed from the charged porphyrins as *π-sips* in solution and solid-state assemblies (Figure 7–1a). As shown in Chapter 6, the ion pair comprising cation **22**$^+$ and anion **35**$^-$, activated by electron-withdrawing and electron-donating substituents, respectively, underwent electron transfer in the ground state to form the corresponding π-stacked radical pair (*π-srp*). On the other hand, porphyrin radical pairs were also produced from **22**$^+$-**35**$^-$ and **22**$^+$-**18**$^-$ by photoexcitation of the activated and less activated *π-sips* via electron transfer (Figure 7–1b). However, the details of the effects of substituents on the excited-state behavior of *π-sips* have not been fully elucidated. In this chapter, the substituent effects on the photoexcitation response are investigated.

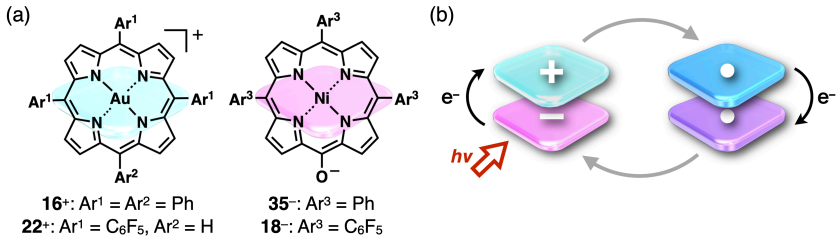

Figure 7–1 (a) Charged species forming porphyrin ion pairs and (b) expected photoexcitation process in charged π-electronic systems.

7–2 Synthesis and Characterization of Triphenyl-Substituted Porphyrin Cation

To achieve efficient stacking like **22**$^+$, the 5,10,15-triphenyl-substituted porphyrin Au^{III} complex **36**$^+$ was selected as the π-electronic cation, which is a component of *π-sips*. **36**$^+$ as a OTf^- ion pair was prepared by the treatment of 5,10,15-triphenylporphyrin[125] with $[Au(tht)_2]OTf$ (tht: tetrahydrothiophene) and 2,6-lutidine in refluxing $CHCl_3$ (Figure 7–2).[126] Thereafter, the crude OTf^- ion pair was converted to the Cl^- ion pair **36**$^+$-Cl^- using an ion-exchange resin (Amberlite), followed by purification through a silica-gel column and recrystallization. Since Cl^- has a high affinity for inorganic cations such as Ag^+, **36**$^+$-Cl^- is suitable for further anion exchange. The treatment of **36**$^+$-Cl^- with 3 equiv of $AgPF_6$ provided the PF_6^- ion pair **36**$^+$-PF_6^- after purification via silica gel column chromatography and recrystallization after the removal of AgCl. The obtained **36**$^+$-

Cl^- and **36**$^+$-PF_6^- were identified using ^1H and ^{13}C NMR and HR-ESI-TOF-MS.

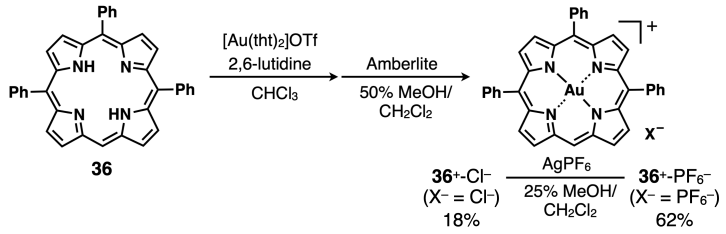

Figure 7–2 Synthesis of 5,10,15-triphenyl-substituted porphyrin–Au^{III} complex as ion pairs **36**$^+$-X^- (X^- = Cl^- and PF_6^-).

The exact structures of **36**$^+$-Cl^- and **36**$^+$-PF_6^- were revealed by X-ray analysis using single crystals prepared by the vapor diffusion of *n*-hexane into CH_2ClCH_2Cl solutions (Figure 7–3).[127] These ion pairs formed charge-segregated assemblies, with the stacking of identically charged species. The distances between **36**$^+$ were 3.50/3.74 and 3.46 Å in the single crystals of **36**$^+$-Cl^- and **36**$^+$-PF_6^-, respectively. Compared to the previously reported stacking distances of 3.75 and 3.87/3.89 Å for **16**$^+$ in single crystals of **16**$^+$-Cl^- and **16**$^+$-PF_6^-,[39] the stacking distances of **36**$^+$ were closer for both cases, indicating that **36**$^+$ with three phenyl substituents more readily forms stacked structures.

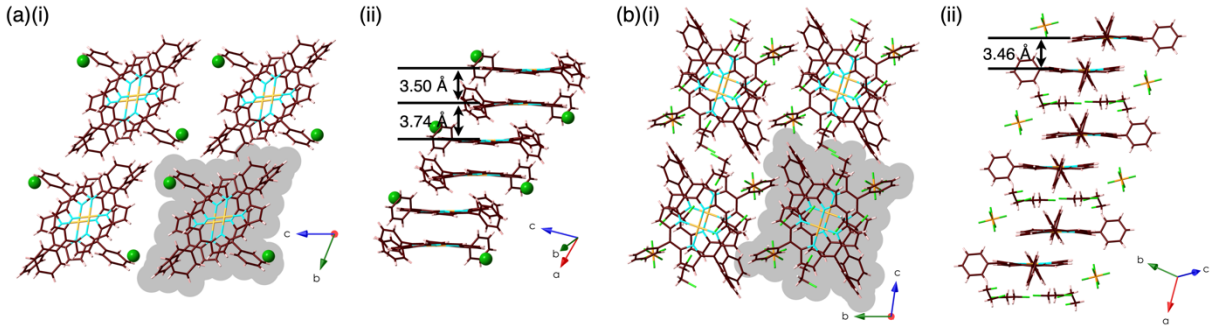

Figure 7–3 Single-crystal X-ray structures of (a) **36**$^+$-Cl^- and (b) **36**$^+$-PF_6^- showing (i) top and (ii) side views of packing structures.

The electrochemical properties of **36**$^+$-PF_6^- were examined by CV in CH_2Cl_2 containing 0.1 M $TBAPF_6$ as an electrolyte (Figure 7–4). The first reduction potential (versus Ag^+/Ag) of **36**$^+$ was estimated to be –0.86 V. This value is comparable to that of **16**$^+$ ($E^{1/2}_{red}$ = –0.86 V) and far from the oxidation potentials of **35**$^-$ and **18**$^-$ ($E^{1/2}_{ox}$ = –0.14 and 0.19 V, respectively), suggesting that **36**$^+$ is stable in the ionic state in combination with these

anions.[123] These results prompted us to form porphyrin ion pairs of **36**$^+$, which is a stable cation suitable for *π-sip* formation.

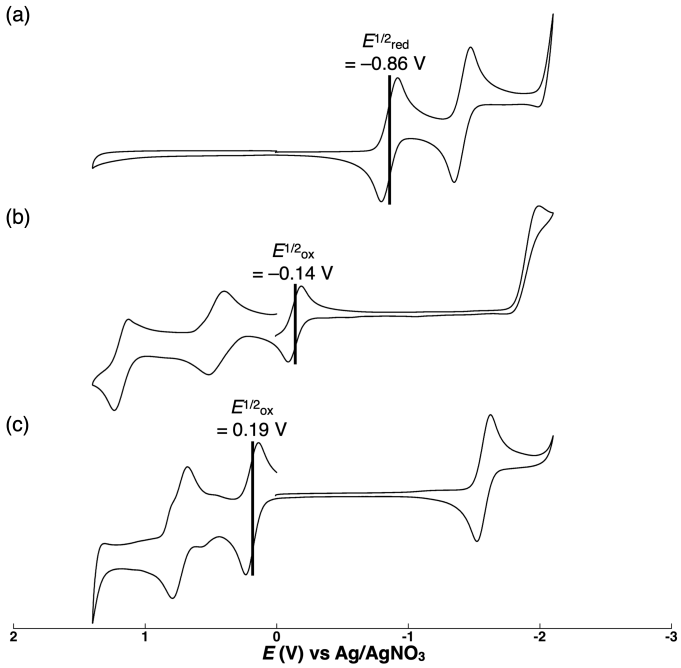

Figure 7–4 CVs of (a) **36**$^+$-PF_6^-, (b) TBA$^+$-**35**$^-$, and (c) TBA$^+$-**18**$^-$ in CH_2Cl_2 (1.0 mM) containing $TBAPF_6$ (0.1 M) as an electrolyte under an Ar atmosphere at a scan rate of 100 mV/s.

7–3 Ion Pairing of Charged Porphyrins

Following a literature method for the preparation of porphyrin ion pairs based on the hard and soft acids and bases (HSAB) theory (Figure 7–5),[128] **36**$^+$-Cl^- was added to CH_2Cl_2 solutions containing equal amounts of porphyrin anion Na^+ ion pairs, Na^+-**35**$^-$ and Na^+-**18**$^-$. The mixed solutions were washed with water to remove NaCl, affording the porphyrin ion pairs **36**$^+$-**35**$^-$ and **36**$^+$-**18**$^-$ in 88% and 87% yields, respectively, after purification by recrystallization in CH_2Cl_2/CH_3CN and CH_2Cl_2/*n*-hexane, respectively. The ion pairs were identified using ^1H, ^{13}C, and ^{19}F NMR and HR-ESI-TOF-MS.

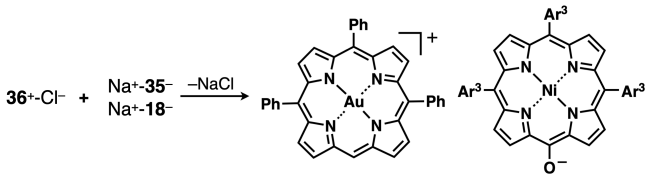

Figure 7–5 Preparation of porphyrin ion pairs based on HSAB theory.

The UV/vis absorption spectra of **36**$^+$-**35**$^-$ (0.3 mM) and **36**$^+$-**18**$^-$ (0.3 mM) in CH_2Cl_2 showed the sum of the absorption bands of the PF_6^- ion pair of **36**$^+$ and TBA ion pairs of **35**$^-$ and **18**$^-$, respectively (Figure 7–6). These results suggest weak exciton coupling between the oppositely charged porphyrins with completely different MO energy levels. Therefore, the stability of the *π-sips* was evaluated using NMR, as the ^{1}H NMR spectrum of **36**$^+$-**18**$^-$ in CD_2Cl_2 showed chemical shifts characteristic of *π-sips* as shown in Chapter 6 (Figure 7–7). The β-CH signals of **36**$^+$ in **36**$^+$-**18**$^-$ were observed at 9.76, 9.24, 9.16, 8.81, and 8.54 ppm, whereas those of **18**$^-$ appeared at 6.80 and 6.35 ppm with the two signals overlapping with those of the phenyl groups. The signals of **36**$^+$ were shifted upfield compared to those of **36**$^+$-PF_6^- (11.08, 9.52, 9.87, 9.41, and 9.39 ppm, respectively). Similar to **36**$^+$, the signals of **18**$^-$ were also shifted upfield compared to those of TBA$^+$-**18**$^-$, shown at 8.68 and 7.70 ppm. These differences are attributed to the stacking positions of **36**$^+$ and **18**$^-$ in the model structure of **36**$^+$-**18**$^-$ (Figure 7–7b). H^a, H^b, and H^c in **36**$^+$ and H^e and H^f in **18**$^-$ were located on the planes of the counter porphyrin ions, suggesting that the upfield shifts of the ^{1}H NMR signals arose from shielding effects due to *π-sip* formation. The upfield shifts with increasing concentration also supported the formation of *π-sip* (Figure 7–7c). Using concentration-dependent ^{1}H NMR in CD_2Cl_2, exhibiting upfield shifts of the protons on the stacked counterion plane due to the shielding effects under higher concentrations, the heterodimerization constant (K_{dim}) was estimated to be 3.5×10^4 M^{-1} by curve-fitting of the chemical shifts relative to the concentration equation (1) in Chapter 6. This value is one order of magnitude smaller than the K_{dim} of **22**$^+$-**18**$^-$ (2.8×10^5 M^{-1}), suggesting that the substituents on the cations are essential for *π-sip* formation. The formation of *π-sips* was also suggested for **36**$^+$-**35**$^-$, although the low solubility and broad NMR signals of **35**$^-$ precluded evaluation of the association constant.

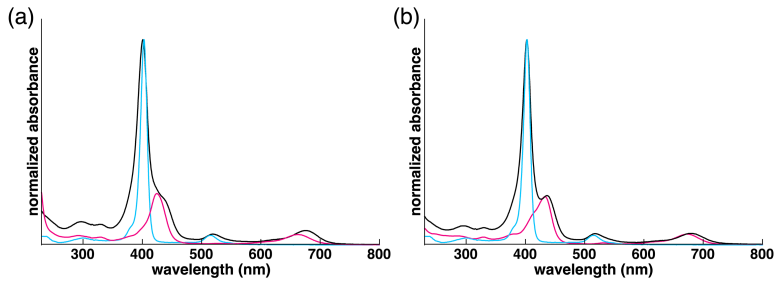

Figure 7–6 UV/vis absorption spectra in CH_2Cl_2: (a) **36**$^+$-**35**$^-$ (black, 3.0×10^{-4} M), **36**$^+$-PF_6^- (cyan, 3.0×10^{-6} M), and TBA$^+$-**35**$^-$ (magenta, 5.3×10^{-6} M) and (b) **36**$^+$-**18**$^-$ (black, 3.0×10^{-4} M), **36**$^+$-PF_6^- (cyan, 3.0×10^{-6} M), and TBA$^+$-**18**$^-$ (magenta, 7.6×10^{-6} M).

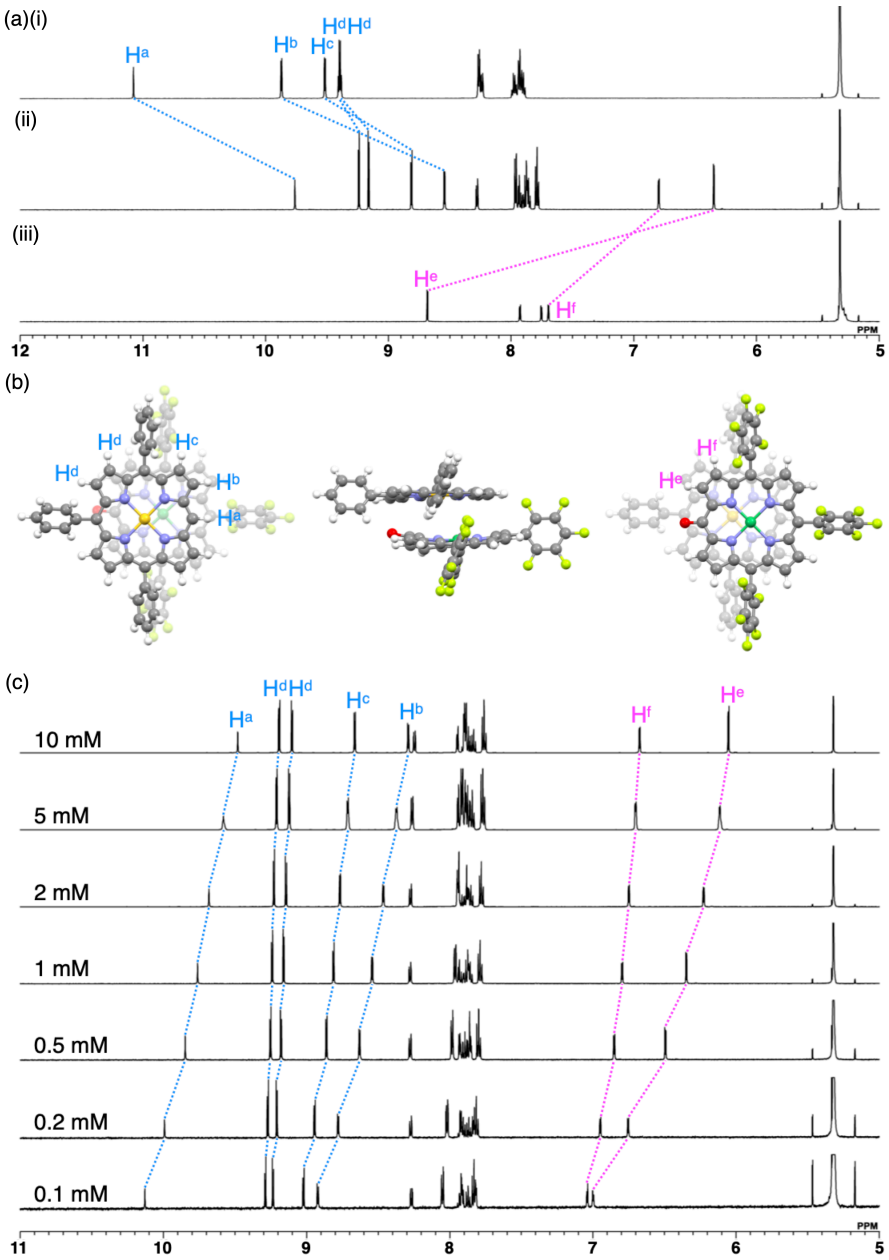

Figure 7–7 (a) ^{1}H NMR spectra of (i) **36**$^{+}$-PF_6^{-}, (ii) **36**$^{+}$-**18**$^{-}$, and (iii) TBA^{+}-**18**$^{-}$ in CD_2Cl_2 (1.0 mM, 20 °C), (b) model structure of **36**$^{+}$-**18**$^{-}$ in top views from the planes of **36**$^{+}$ (left) and **18**$^{-}$ (right) and side view (middle), and (c) concentration-dependent ^{1}H NMR (0.1–10 mM) of **36**$^{+}$-**18**$^{-}$ at 20 °C in CD_2Cl_2.

7–4 Photoexcitation Processes of Porphyrin Ion Pairs

The electronic properties of the ion pairs, depending on the constituent ionic species and their distinct potential levels, can be observed by monitoring the photoinduced electron transfer processes. Therefore, transient absorption spectra of the ion pairs **36**$^{+}$-**35**$^{-}$ and **36**$^{+}$-**18**$^{-}$ were acquired to investigate the photoinduced electron transfer processes in detail by comparison with the previously reported data for **22**$^{+}$-**35**$^{-}$ and **22**$^{+}$-**18**$^{-}$.[60]

In the transient absorption spectra of **36**$^+$-**35**$^-$ in CH_2Cl_2 excited at 680 nm, which selectively excited the anion moiety, positive and negative signals instantaneously appear after the excitation (Figure 7–8a). The transient absorption spectra were almost identical to those of **22**$^+$-**35**$^-$ and **22**$^+$-**18**$^-$ in CH_2Cl_2 and THF.[60] In a previous study, the positive transient absorption bands at >750 nm were ascribed to radicals derived from **35**$^-$ and **18**$^-$, whereas the locally excited states of **35**$^-$ and **18**$^-$ in less polar solvents did not exhibit any transient absorptions in this region. Thus, ultrafast photoinduced electron transfer occurred in **36**$^+$-**35**$^-$ in CH_2Cl_2 within instrumental response function, and a radical pair was instantaneously produced.

The relative amplitude of the transient absorption bands of **36**$^+$-**18**$^-$ in CH_2Cl_2 at >750 nm compared to that of the bleach signal at 690 nm was much smaller than that of **36**$^+$-**35**$^-$ in CH_2Cl_2 (Figure 7–8b). The decrease in the amplitude of the absorption band of the formed radical pair is attributed to the Marcus normal region, as explained below. Since both the HOMO and LUMO of **18**$^-$ are lower than those of **35**$^-$, the energy difference between the LUMOs of the anion and cation, which corresponds to the energy gap for forward electron transfer, becomes small. The small energy gap results in a decrease in the rate constant for forward electron transfer in the Marcus normal region, resulting in a decrease in production of the radical pair.

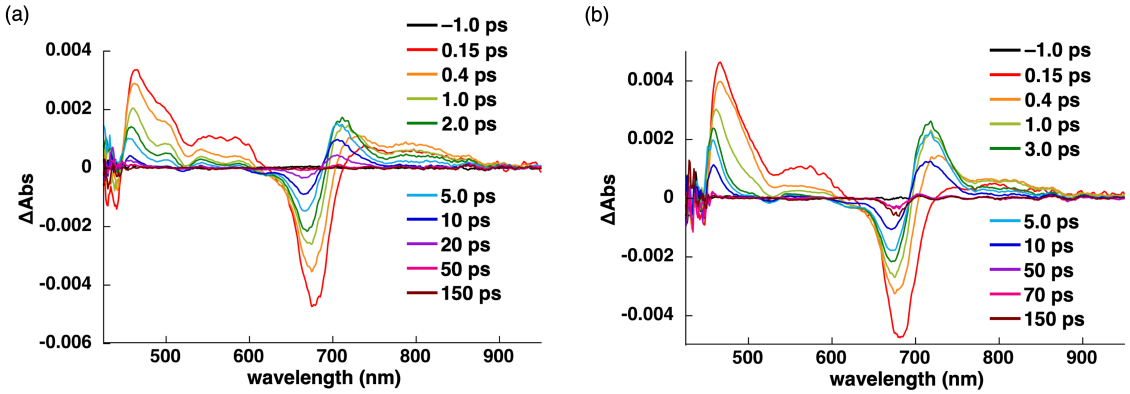

Figure 7–8 Transient absorption spectra of (a) **36**$^+$-**35**$^-$ and (b) **36**$^+$-**18**$^-$ in CH_2Cl_2 excited at 680 nm (80 nJ/pulse) with the delay time spanning from –1.0 to 150 ps.

The obtained transient absorption spectra for **36**$^+$-**35**$^-$ and **36**$^+$-**18**$^-$ were globally analyzed using three- or four-state sequential decay kinetic models convolved with a Gaussian pulse using the Glotaran program.[114] The lifetimes determined from the obtained EADS, which present the transient absorption spectra resolved into each component of the kinetic models, were 180 fs, 1.2 ps, and 11 ps in **36**$^+$-**35**$^-$ and 100 fs, 700 fs, and 11 ps in **36**$^+$-**18**$^-$. The first EADS (180 and 100 fs) was assigned to the Franck-Condon state of the S_1 states of **35**$^-$ and

18^{-}, respectively, because the transient absorption bands associated with radicals were missing and relaxation to the lowest S_1 state takes hundreds of femtoseconds. The second and third EADS (1.2 and 11 ps in **36**$^{+}$-**35**$^{-}$ and 700 fs and 11 ps in **36**$^{+}$-**18**$^{-}$) showed absorption bands ascribed to radicals derived from **35**$^{-}$ and **18**$^{-}$, although the transient absorption band at 790 nm was much smaller in the third EADS (11 ps). Moreover, the positive absorption band at ~700 nm gradually increased in the second and third EADS, indicating that the second and third EADS reflect the geometrical relaxation of **18**$^{-}$ to the lowest S_1 state and decay of the generated radical pair.

The time constants for the forward electron transfer were estimated to be 180 and 100 fs for **36**$^{+}$-**35**$^{-}$ and **36**$^{+}$-**18**$^{-}$ in CH_2Cl_2. Quantitative analysis of these time constants is difficult as the signals include a nonlinear solvent response. On the other hand, the time constants for back electron transfer showed a clear dependence on the energy gaps. The energy gaps for back electron transfer can be roughly estimated by the energy differences between the LUMO of the cations and the HOMO of the anions under the simple assumption that the energy shift by the forward electron transfer is negligible. Under this assumption, the energy gaps for back electron transfer, estimated from CV, were 0.41, 0.74, 0.72, and 1.05 V for **22**$^{+}$-**35**$^{-}$, **22**$^{+}$-**18**$^{-}$, **36**$^{+}$-**35**$^{-}$, and **36**$^{+}$-**18**$^{-}$, respectively (Table 7–1). Decay of the radical pairs appeared across multiple EADS components. Therefore, the amplitudes of each time constant were obtained by comparing the sum of the signals at 765–940 nm of each EADS, thereby yielding amplitude-averaged time constants of 3.4, 5.4, 4.1, and 6.2 ps for **22**$^{+}$-**35**$^{-}$, **22**$^{+}$-**18**$^{-}$, **36**$^{+}$-**35**$^{-}$, and **36**$^{+}$-**18**$^{-}$, respectively (Table 7–1). The results qualitatively indicate that back electron transfer becomes slower with an increase in the energy gaps as observed in the Marcus inverted region. Therefore, these time-resolved experiments strongly suggest that photoinduced electron transfer in the ion pairs to form radical pairs occurs in the Marcus normal region, whereas back electron transfer to regenerate the ion pair occurs in the Marcus inverted region similar to photoinduced electron transfer in the uncharged states.

Table 7–1 Energy gaps (E_{gap}) between LUMOs of the cations and HOMOs of anions in **22**$^{+}$-**35**$^{-}$,[60] **22**$^{+}$-**18**$^{-}$,[60] **36**$^{+}$-**35**$^{-}$, and **36**$^{+}$-**18**$^{-}$ estimated from CVs and amplitude-averaged time constants (τ) from EADS of the corresponding radical pairs.

	22^{+}-**35**$^{-}$	**22**$^{+}$-**18**$^{-}$	**36**$^{+}$-**35**$^{-}$	**36**$^{+}$-**18**$^{-}$
E_{gap} (V)	0.41	0.74	0.72	1.05
τ (ps)	3.4	5.4	4.1	6.2

7–5 Summary of Chapter 7

In this chapter, aryl substituents on cationic and anionic porphyrins in ion pairs have clear effects on photoinduced electron transfer processes and solid- and solution-state ion-pairing behaviors. Specifically, excited-state radical pair formation depends on the electron-donating properties of the anions, as revealed by the transient absorption spectra. New porphyrin ion pairs comprising the triphenyl-substituted Au^{III} complex exhibit potential in the chemistry of *π-sips*. Photoexcitation of the controlled electronic states of the constituent π-electronic ions in *π-sips* after the structural modifications generates transient radical species with the potential for future applications in photocatalysis.

Chapter 8

Summary of This Dissertation

In this dissertation, the author described the scrupulous examination of various π-electronic ion pairs, achieved through synthesis and ion pairing of charged porphyrins, illuminating their structures and functions in solid and solution states. Solid-state ion-pairing assemblies based on the charged porphyrins, with the contributions of the charge-by-charge and charge-segregated modes, were observed according to the constituent charged building units and ${}^{i}\pi$–${}^{j}\pi$ interaction. The crystal-state absorption spectra of the ion pairs were correlated with the assembling modes. In solution, the formation of π-stacked ion pairs has been clearly shown with the estimation of hetero-dimerization constants. π-Electronic cations and anions can be activated by introducing electron-withdrawing and electron-donating groups, respectively, resulting in the formation of a radical pair via electron transfer in steady state according to solvent polarity. The ESR in frozen toluene reveals the formation of π-stacked radical pair with a close stacking distance of 3.02 Å, suggesting a tightly stacked "condensed conjugation" structure. Photoexcitation of the controlled electronic states of the constituent π-electronic ions in π-stacked ion pairs generated transient radical species.

The ion pairs based on charged porphyrins were synthesized by the following methods: (i) ion-pair metathesis based on the HSAB theory and (ii) ion binding of electronically neutral π-electronic receptors. These ion-pairing methods can be applied to ionic species synthesized inside and outside the research group, and the author has developed a wide variety of ion-pairing assemblies as collaborative works (Figure 8–1). In the case of method (i), $PCCp^{-}$ was utilized as a counteranion with heteroporphyrin-based cations **37**$^{+}$–**40**$^{+}$ [129,130] and BN-incorporated polycyclic aromatic cation **41**$^{+}$ [131] to generate a diverse array of assemblies. In addition, the ion-pair formation of dipyrrolylnitrophenoxide derivatives **42**$^{-}$–**44**$^{-}$ and porphyrin–Au^{III} complexes was successfully achieved, indicating the formation of charge-by-charge assemblies.[42] On the other hand, in synthetic method (ii), anion complexes (pseudo π-electronic anions) **45**–**47**·Cl^{-} of a dipyrrolyldiketone boron complex with triazole units introduced by the click reaction[132] and dipyrrolyldiketone Pt^{II} complexes[133] formed ion-pairing assemblies as counteranions of porphyrin–Au^{III} complexes. The creation of a repository of crystal structures for

charged π-electronic systems has facilitated a greater comprehension of the ${}^{i}\pi$–${}^{i}\pi$ interactions between these ionic species and has also been instrumental in the formation of desired assembled structures.

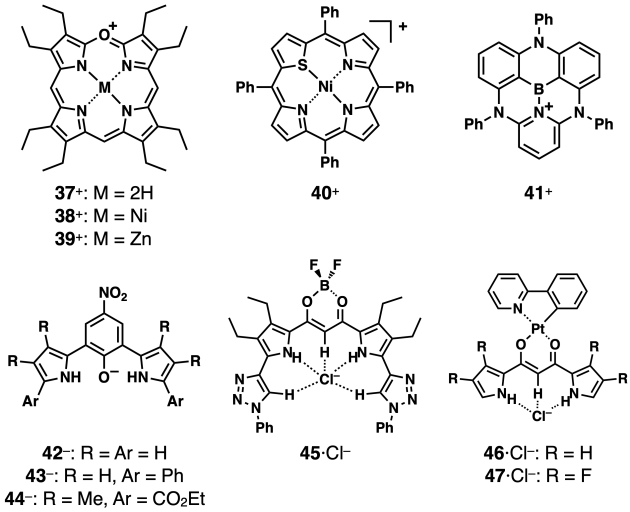

Figure 8–1 Heteroporphyrin-based cations **37**$^{+}$–**40**$^{+}$, cationic BN-embedded polycyclic aromatic hydrocarbon **41**$^{+}$, dipyrrolylnitrophenoxide derivatives **42**$^{–}$–**44**$^{–}$, and receptor–anion complexes **45**–**47**·Cl$^{–}$.

Fascinating results initially observed in well-designed systems, charged porphyrins in this dissertation, will be gradually observed in other related π-electronic systems. New findings can be derived from suitable molecular systems and, subsequently, the observed behavior can be seen to be widespread. The author posits that π-electronic ions can be developed into functional materials in the fields of nanomagnetism, catalytic reactions, and ferroelectrics through a more comprehensive examination of the electronic correlations between oppositely charged π-electronic systems.

Experimental Section

General methods: Starting materials were purchased from FUJIFILM Wako Pure Chemical Corp., Nacalai Tesque Inc., Sigma-Aldrich Co., and Tanaka Kikinzoku Kogyo K.K. and used without further purification unless otherwise stated. NMR spectra used in the characterization of products were recorded on a JEOL ECA-600 600 MHz spectrometer and a Bruker AVANCE III 600 MHz spectrometer equipped with a Prodigy cryoprobe head, with the help of Dr. Ryosuke Miyake, Ochanomizu University. ^{1}H and ^{13}C NMR spectra were referenced to solvent and ^{19}F NMR spectrum was referenced to hexafluorobenzene as an external standard. Solvent-dependent ^{19}F values of hexafluorobenzene were obtained from the report by Togni et al.[134] UV-visible absorption spectra were recorded on a Hitachi U-3500 spectrometer. Electrospray ionization time-of-flight mass spectrometric studies (ESI-TOF-MS) were conducted using a Bruker microTOF. Matrix-assisted laser desorption ionization time-of-flight mass spectrometries (MALDI-TOF-MS) were recorded on a Shimadzu Axima-CFRplus. Elemental analyses were performed on a Yanaco CHN Corders (MT-5, and MT-6) and JSL JM-10 and JM-11 for carbon, hydrogen, and nitrogen and on Mitsubishi Chemical Analytech AQF-100 and AQF-2100H, Dionex ICS-1500, and ThermoFisher ICS-1600 instruments for chlorine, fluorine, and sulfur at the Laboratory for Organic Elemental Microanalysis, Kyoto University. TLC analyses were carried out on aluminum sheets coated with silica gel 60 (Merck 5554). Column chromatography was performed on Wakogel C-300.

5,15-Bis(pentafluorophenyl)porphyrin Au^{III} complex as a OTf$^-$ ion pair, 21$^+$-OTf$^-$. According to the literature procedure,[65] a solution of 5,15-bis(pentafluorophenyl)porphyrin **21** [62] (61.5 mg, 95.8 μmol) and NaOAc (125.8 mg, 1.53 mmol) in CH_2Cl_2 (39 mL) was heated to 40 °C for 10 min. A solution of $HAuCl_4 \cdot 4H_2O$ (157.8 mg, 0.383 mmol) and AgOTf (393.9 mg, 1.53 mmol) in THF (20 mL) was added dropwise. The mixture was stirred under 40 °C for 2 h. After the removal of solvent by vacuum, the residue was then chromatographed over a silica gel column (Wakogel C-300, eluent: 10% MeOH/CH_2Cl_2) and was recrystallized from CH_2Cl_2/*n*-hexane to give **21**$^+$-OTf$^-$ (28.4 mg, 28.8 μmol, 30%) as a red solid. R_f = 0.33 (10% MeOH/CH_2Cl_2). ^{1}H NMR (600 MHz, CD_3CN, 20 °C): δ (ppm) 11.41 (s, 2H, *meso*-CH), 10.12 (d, J = 4.2 Hz, 4H, β-CH), 9.72 (d, J = 4.8 Hz, 4H, β-CH). ^{13}C{^{1}H} NMR (151 MHz, CD_3CN, 20 °C): δ (ppm) 147.64 (dm, J_{C-F} = 244 Hz), 144.23 (dm, J_{C-F} = 255 Hz), 139.36 (dm, J_{C-F} = 252 Hz), 138.04, 137.16, 135.35, 132.65, 122.02 (d, J_{C-F} = 322 Hz), 114.53 (m), 111.08, 106.29. ^{19}F NMR (564 MHz, CD_3CN, 20 °C): δ (ppm) –79.39 (s, 3F, OTf$^-$), –139.56 (dd, J =

21.4 and 8.5 Hz, 4F, Ar-F), 153.42 (t, J = 21.4 Hz, 2F, Ar-F), –162.97 (m, 4F, Ar-F). UV/vis (CH_2Cl_2, λ_{max}[nm] (ε, 10^5 $M^{-1}cm^{-1}$)): 393 (2.6). MALDI-TOF-MS: *m/z* (% intensity): 837.0 (100), 838.0 (49), 839.0 (12). Calcd for $C_{32}H_{10}AuF_{10}N_4$ ([M – OTf]$^+$): 837.04. OTf^- (calcd: 148.95) was also detected as *m/z* = 149.0 (100) in the negative mode. Elemental analysis: C 40.00, H 1.10, N 5.45, S 3.07. Calcd (%) for $C_{33}H_{10}AuF_{13}N_4O_3S$: C 40.18, H 1.02, Au 19.97, F 25.04, N 5.68, O 4.87, S 3.25.

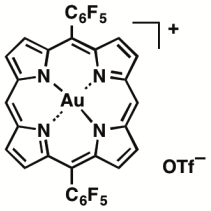

5,15-Bis(pentafluorophenyl)porphyrin Au^{III} complex as a Cl$^-$ ion pair, 21$^+$-Cl$^-$. A solution of **21**$^+$-OTf^- was chromatographed over ion-exchanged resin (Amberlite IRA402BL, eluent: MeOH) and silica gel column (Wakogel C-300, eluent: 10% MeOH/CH_2Cl_2) and the eluted product was recrystallized from CH_2Cl_2/*n*-hexane to give **21**$^+$-Cl^- (23.2 mg, 26.6 μmol, 92%) as a red solid. R_f = 0.10 (10% MeOH/CH_2Cl_2). ^{1}H NMR (600 MHz, CD_3CN, 20 °C): δ (ppm) 11.42 (s, 2H, *meso*-CH), 10.13 (d, J = 4.8 Hz, 4H, β-CH), 9.72 (d, J = 4.8 Hz, 4H, β-CH). $^{13}C\{^1H\}$ NMR (151 MHz, CD_3OD, 20 °C): δ (ppm) 148.21 (dm, J_{C-F} = 246 Hz), 144.81 (dm, J_{C-F} = 262 Hz), 139.72 (dm, J_{C-F} = 262 Hz), 138.87, 138.03, 135.61, 132.84, 114.23 (m), 111.06, 106.76. ^{19}F NMR (564 MHz, CD_3CN, 20 °C): δ (ppm) –139.56 (d, J = 22.0 Hz, 4F, Ar-F), –153.42 (t, J = 17.5 Hz, 2F, Ar-F), –162.97 (t, J = 21.4 Hz, 4F, Ar-F). UV/vis (CH_2Cl_2, λ_{max}[nm] (ε, 10^5 $M^{-1}cm^{-1}$)): 393 (2.7). MALDI-TOF-MS: *m/z* (% intensity): 837.0 (100), 838.0 (39), 839.0 (8). Calcd for $C_{32}H_{10}AuF_{10}N_4$ ([M – Cl]$^+$): 837.04. Cl^- (calcd: 34.97) was also detected as *m/z* = 35.0 (100), 37.0 (33) in the negative mode. Elemental analysis: C 43.34, H 1.48, Cl 4.96, N 6.24. Calcd (%) for $C_{32}H_{10}AuClF_{10}N_4 \cdot 0.7H_2O \cdot 0.13CH_2Cl_2 \cdot 0.06C_6H_{14}$: C 43.28, H 1.40, Au 21.84, Cl 4.95, F 21.07, N 6.21, O 1.24.

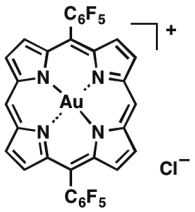

5,10,15-Tris(pentafluorophenyl)porphyrin Au^{III} complex as a OTf$^-$ ion pair, 22$^+$-OTf$^-$. According to the literature procedure,[65] a solution of 5,10,15-tris(pentafluorophenyl)porphyrin **22** [63] (39.6 mg, 49.0 μmol) and NaOAc (26.2 mg, 0.319 mmol) in CH_2Cl_2 (1 mL) was heated to 35 °C for 10 min. A solution of $HAuCl_4 \cdot 4H_2O$

(81.0 g, 0.197 mmol) and AgOTf (202 mg, 0.786 mmol) in THF (10.2 mL) was added dropwise. The mixture was stirred under 35 °C for 2 h. After the removal of solvent by vacuum, the residue was then chromatographed over a silica gel column (Wakogel C-300, eluent: 10% MeOH/CH_2Cl_2) and was recrystallized from CH_2Cl_2/*n*-hexane to give **22**$^+$-OTf^- (41.8 mg, 36.3 μmol, 74%) as a red solid. R_f = 0.50 (10% MeOH/CH_2Cl_2). ^{1}H NMR (600 MHz, CD_3CN, 20 °C): δ (ppm) 11.44 (s, 1H, *meso*-CH), 10.13 (d, J = 4.8 Hz, 2H, β-CH), 9.72 (d, J = 5.4 Hz, 2H, β-CH), 9.70 (m, 4H, β-CH). ^{13}C{^{1}H} NMR (151 MHz, CD_3CN, 20 °C): δ (ppm) 147.70 (dm, $J_{C–F}$ = 246 Hz), 144.38 (dm, $J_{C–F}$ = 255 Hz), 139.42 (dm, $J_{C–F}$ = 250 Hz), 138.64, 137.99, 137.94, 137.85, 136.09, 133.73, 133.49, 133.16, 122.09 (d, $J_{C–F}$ = 322 Hz), 113.41 (m), 112.19, 107.63, 107.55. ^{19}F NMR (564 MHz, CD_3CN, 20 °C): δ (ppm) –79.45 (s, 3F, OTf^-), –139.49 (d, J = 13.0 Hz, 6F, Ar-F), –153.32 (m, 3F, Ar-F), –162.89 (m, 6F, Ar-F). UV/vis (CH_2Cl_2, λ_{max}[nm] (ε, 10^5 $M^{-1}cm^{-1}$)): 396 (3.4). MALDI-TOF-MS: *m*/*z* (% intensity): 1003.0 (100), 1004.0 (45), 1005.0 (8). Calcd for $C_{38}H_9AuF_{15}N_4$ ([M – OTf]$^+$): 1003.02. OTf^- (calcd: 148.95) was also detected as *m/z* = 149.0 (100) in the negative mode. Elemental analysis: C 40.37, H 0.70, N 4.91, S 2.69. Calcd (%) for $C_{39}H_9AuF_{18}N_4O_3S$: C 40.64, H 0.79, Au 17.09, F 29.67, N 4.86, O 4.16, S 2.78.

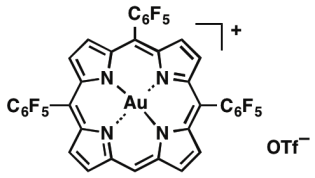

5,10,15-Tris(pentafluorophenyl)porphyrin Au^{III} complex as a Cl^- ion pair, 22$^+$-Cl^-. A solution of **22**$^+$-OTf^- was chromatographed over ion-exchanged resin (Amberlite IRA402BL, eluent: MeOH) and silica gel column (Wakogel C-300, eluent: 10% MeOH/CH_2Cl_2) and the eluted product was recrystallized from CH_2Cl_2/*n*-hexane to give **22**$^+$-Cl^- (115.5 mg, 111.2 μmol, 82%) as a red solid. R_f = 0.10 (10% MeOH/CH_2Cl_2). ^{1}H NMR (600 MHz, CD_3CN, 20 °C): δ (ppm) 11.46 (s, 1H, *meso*-CH), 10.14 (d, J = 5.4 Hz, 2H, β-CH), 9.72 (d, J = 5.4 Hz, 2H, β-CH), 9.71 (d, J = 4.8 Hz, 2H, β-CH), 9.69 (d, J = 4.8 Hz, 2H, β-CH). ^{13}C{^{1}H} NMR (151 MHz, CD_3CN, 20 °C): δ (ppm) 147.72 (dm, $J_{C–F}$ = 247 Hz), 144.33 (dm, $J_{C–F}$ = 256 Hz), 139.40 (dm, $J_{C–F}$ = 247 Hz), 138.57, 137.97, 137.84, 137.79, 136.00, 133.69, 133.44, 132.96, 113.49 (m), 112.30, 107.48, 107.38. ^{19}F NMR (564 MHz, CD_3CN, 20 °C): δ (ppm) –139.43 (d, J = 13.0 Hz, 6F, Ar-F), –153.33 (m, 3F, Ar-F), –162.88 (m, 6F, Ar-F). UV/vis (CH_2Cl_2, λ_{max}[nm] (ε, 10^5 $M^{-1}cm^{-1}$)): 397 (4.1). MALDI-TOF-MS: *m*/*z* (% intensity): 1003.0 (100), 1004.0 (49), 1005.0 (12). Calcd for $C_{38}H_9AuF_{15}N_4$ ([M – Cl]$^+$): 1003.02. Cl^- (calcd: 34.97) was also

detected as *m/z* = 35.0 (100), 37.0 (31) in the negative mode. Elemental analysis: C 42.07, H 1.22, Cl 3.21, N 5.42. Calcd (%) for $C_{38}H_9AuClF_{15}N_4 \cdot 2.8H_2O \cdot 0.2CH_3CN$: C 42.02, H 1.30, Au 18.17, Cl 3.27, F 26.29, N 5.17, O 3.69. This compound was further characterized by single-crystal X-ray diffraction analysis.

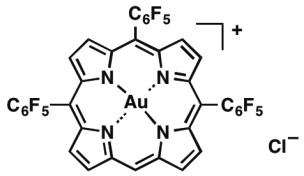

General preparation protocol for anion exchanges from Cl^- to other anions. A solution of Ag^+ or Na^+ ion pair of anions (3 equiv) in CH_3CN was added to a solution of Cl^- ion pairs of porphyrin–Au^{III} complexes in CH_3CN or CH_3CN/MeOH and stirred for a few minutes. The products were filtered and the solvent was evaporated. The residue was then chromatographed over a silica gel column and recrystallized from suitable solvents afforded ion pairs as solid materials. The obtained ion pairs were characterized by ^1H, ^{19}F, and ^{13}C NMR. The details for each ion pair are described as below.

21^+ as a BF_4^- ion pair, 21^+-BF_4^-. $AgBF_4$ was used for anion exchange. After the workup, the residue was purified by chromatography over a silica gel column (Wakogel C-300, eluent: 10% MeOH/CH_2Cl_2) and was recrystallized from CH_2Cl_2/*n*-hexane to give **21**$^+$-BF_4^- (30.5 mg, 33.0 μmol, 85%) as a red solid. R_f = 0.32 (10% MeOH/CH_2Cl_2). ^1H NMR (600 MHz, CD_3CN, 20 °C): δ(ppm) 11.42 (s, 2H, *meso*-CH), 10.12 (d, J = 4.8 Hz, 4H, β-CH), 9.72 (d, J = 5.4 Hz, 2H, β-CH). $^{13}C\{^1H\}$ NMR (151 MHz, CD_3CN, 20 °C): δ(ppm) 147.63 (dm, J_{C-F} = 248 Hz), 144.22 (dm, J_{C-F} = 255 Hz), 139.36 (dm, J_{C-F} = 250 Hz), 138.02, 137.15, 135.35, 132.64, 113.52 (m), 111.06, 106.27. ^{19}F NMR (564 MHz, CD_3CN, 20 °C): δ(ppm) –139.57 (dd, J = 25.9 and 9.0 Hz, 4F, Ar-F), –151.81 (s, $^{10}BF_4^-$), –151.87 (s, $^{11}BF_4^-$), –153.42 (t, J = 21.0 Hz, 2F, Ar-F), –162.98 (m, 4F, Ar-F). UV/vis (CH_2Cl_2, λ_{max}[nm] (ε, 10^5 $M^{-1}cm^{-1}$)): 393 (3.0). MALDI-TOF-MS: *m/z* (% intensity): 837.0 (100), 838.0 (21), 839.0 (13). Calcd for $C_{32}H_{10}AuF_{10}N_4$ ($[M - BF_4]^+$): 837.04. BF_4^- (calcd: 87.00) was also detected as *m/z* = 87.0 (100), 86.0 (28) in the negative mode. Elemental analysis: C 41.49, H 1.26, N 6.16. Calcd (%) for $C_{32}H_{10}AuBF_{14}N_4$: C 41.59, H 1.09, Au 21.31, B 1.17, F 28.78, N 6.06.

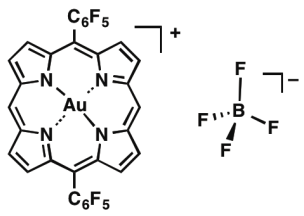

21^+ as a PF_6^- ion pair, 21^+-PF_6^-. $AgPF_6$ was used for anion exchange. After the workup, the residue was purified by chromatography over a silica gel column (Wakogel C-300, eluent: 10% MeOH/CH_2Cl_2) and was recrystallized from CH_2Cl_2/*n*-hexane to give **21^+**-PF_6^- (33.6 mg, 34.2 μmol, 92%) as a red solid. R_f = 0.51 (10% MeOH/CH_2Cl_2). ^{1}H NMR (600 MHz, CD_3CN, 20 °C): δ (ppm) 11.41 (s, 2H, *meso*-CH), 10.12 (d, J = 4.8 Hz, 4H, β-CH), 9.72 (d, J = 5.4 Hz, 2H, β-CH). ^{13}C{^{1}H} NMR (151 MHz, CD_3CN, 20 °C): δ (ppm) 147.63 (dm, $J_{C–F}$ = 248 Hz), 144.23 (dm, $J_{C–F}$ = 252 Hz), 139.36 (dm, $J_{C–F}$ = 252 Hz), 138.02, 137.15, 135.35, 132.64, 113.52 (m), 111.06, 106.27. ^{19}F NMR (564 MHz, CD_3CN, 20 °C): δ (ppm) –72.97 (d, J = 704.4 Hz, 6F, PF_6^-), –139.56 (m, 4F, Ar-F), –153.41 (t, J = 20.9 Hz, 2F, Ar-F), –162.97 (m, 4F, Ar-F). UV/vis (CH_2Cl_2, λ_{max}[nm] (ε, 10^5 $M^{-1}cm^{-1}$)): 393 (2.5). MALDI-TOF-MS: *m/z* (% intensity): 837.0 (100), 838.0 (56), 839.0 (17). Calcd for $C_{32}H_{10}AuF_{10}N_4$ ([M – PF_6]$^+$): 837.04. PF_6^- (calcd: 144.96) was also detected as *m/z* = 145.0 (100) in the negative mode. Elemental analysis: C 39.08, H 1.15, N 5.72, F 30.85. Calcd (%) for $C_{32}H_{10}AuF_{16}N_4P$: C 39.12, H 1.03, Au 20.05, F 30.94, N 5.70, P 3.15. This compound was further characterized by single-crystal X-ray diffraction analysis.

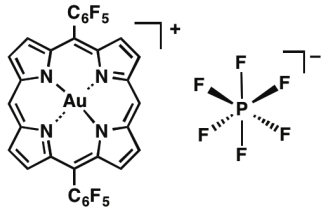

21^+ as a $PCCp^-$ ion pair, 21^+-$PCCp^-$. NaPCCp was used for anion exchange. After the workup, the residue was purified by chromatography over a silica gel column (Wakogel C-300, eluent: 10% MeOH/CH_2Cl_2) and was recrystallized from CH_2Cl_2/*n*-hexane to give **21^+**-$PCCp^-$ (4.42 mg, 4.30 μmol, 97%) as a pink solid. R_f = 0.58 (10% MeOH/CH_2Cl_2). ^{1}H NMR (600 MHz, CD_3CN, 20 °C): δ (ppm) 11.41 (s, 2H, *meso*-CH), 10.12 (d, J = 4.8 Hz, 4H, β-CH), 9.72 (d, J = 5.4 Hz, 4H, β-CH). ^{13}C{^{1}H} NMR (151 MHz, CD_3CN, 20 °C): δ (ppm) 147.64 (dm, $J_{C–F}$ = 249 Hz), 144.23 (dm, $J_{C–F}$ = 255 Hz), 139.34 (dm, $J_{C–F}$ = 253 Hz), 138.05, 137.18, 135.35, 132.66, 113.91, 113.54 (m), 111.09, 106.31, 102.87. ^{19}F NMR (564 MHz, CD_3CN, 20 °C): δ (ppm) –139.45 (dd, J = 23.7 and 6.8 Hz, 4F, Ar-F), –153.34 (t, J = 19.7 Hz, 2F, Ar-F), –162.91 (m, 4F, Ar-F). UV/vis (CH_2Cl_2, λ_{max}[nm] (ε, 10^5 $M^{-1}cm^{-1}$)): 393 (2.3). MALDI-TOF-MS: *m/z* (% intensity): 837.0 (100), 838.0 (35), 839.0 (9). Calcd for $C_{32}H_{10}AuF_{10}N_4$ ([M – PCCp]$^+$): 837.04. $PCCp^-$ (calcd: 190.02) was also detected as *m/z* = 190.0 (100), 191.0 (12) in the negative mode. Elemental analysis: C 48.88, H 0.99, N 12.13. Calcd (%) for

$C_{42}H_{10}AuF_{10}N_9$: C 49.09, H 0.98, Au 19.17, F 18.49, N 12.27. This compound was further characterized by single-crystal X-ray diffraction analysis.

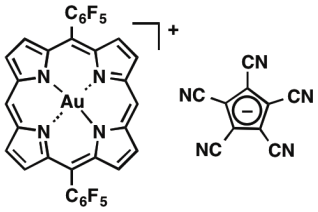

22^+ as a BF_4^- ion pair, 22^+-BF_4^-. $AgBF_4$ was used for anion exchange. After the workup, the residue was purified by chromatography over a silica gel column (Wakogel C-300, eluent: 10% MeOH/CH_2Cl_2) and was recrystallized from CH_2Cl_2/*n*-hexane to give **22**$^+$-BF_4^- (8.81 mg, 8.08 μmol, 87%) as a red solid. R_f = 0.50 (10% MeOH/CH_2Cl_2). ^{1}H NMR (600 MHz, CD_3CN, 20 °C): δ (ppm) 11.45 (s, 1H, *meso*-CH), 10.14 (d, J = 4.8 Hz, 2H, β-CH), 9.72 (d, J = 4.8 Hz, 2H, β-CH), 9.71 (d, J = 5.4 Hz, 2H, β-CH), 9.69 (d, J = 6.0 Hz, 2H, β-CH). ^{13}C{^{1}H} NMR (151 MHz, CD_3CN, 20 °C): δ (ppm) 147.68 (dm, $J_{C–F}$ = 247 Hz), 144.35 (dm, $J_{C–F}$ = 257 Hz), 139.42 (dm, $J_{C–F}$ = 250 Hz), 138.65, 137.98, 137.93, 137.84, 136.09, 133.73, 133.49, 133.16, 113.43 (m), 112.19, 107.62, 107.55. ^{19}F NMR (564 MHz, CD_3CN, 20 °C): δ (ppm) –139.44 (d, J = 17.5 Hz, 6F, Ar-F), –151.80 (s, $^{10}BF_4^-$), –151.85 (s, $^{11}BF_4^-$), –153.31 (m, 3F, Ar-F), –162.87 (m, 6F, Ar-F). UV/vis (CH_2Cl_2, λ_{max}[nm] (ε, 10^5 $M^{-1}cm^{-1}$)): 397 (3.0). MALDI-TOF-MS: *m/z* (% intensity): 1003.0 (100), 1004.0 (40), 1005.0 (9). Calcd for $C_{38}H_9AuF_{15}N_4$ ([M – BF_4]$^+$): 1003.02. BF_4^- (calcd: 87.00) was also detected as *m/z* = 87.0 (100), 86.0 (20) in the negative mode. Elemental analysis: C 41.61, H 1.04, N 5.11. Calcd (%) for $C_{38}H_9AuBF_{19}N_4$: C 41.86, H 0.83, Au 18.07, B 0.99, F 33.11, N 5.14.

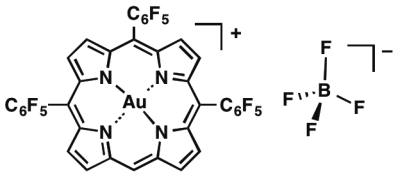

22^+ as a PF_6^- ion pair, 22^+-PF_6^-. $AgPF_6$ was used for anion exchange. After the workup, the residue was purified by chromatography over a silica gel column (Wakogel C-300, eluent: 10% MeOH/CH_2Cl_2) and was recrystallized from CH_2Cl_2/*n*-hexane to give **22**$^+$-PF_6^- (7.67 mg, 6.67 μmol, 71%) as a red solid. R_f = 0.66 (10% MeOH/CH_2Cl_2). ^{1}H NMR (600 MHz, CD_3CN, 20 °C): δ (ppm) 11.45 (s, 1H, *meso*-CH), 10.14 (d, J = 5.4 Hz, 2H, β-CH), 9.72 (d, J = 5.4 Hz, 2H, β-CH), 9.71 (d, J = 5.4 Hz, 2H, β-CH), 9.69 (d, J = 4.8 Hz, 2H, β-CH). ^{13}C{^{1}H} NMR (151 MHz, CD_3CN, 20 °C): δ (ppm) 147.72 (dm, $J_{C–F}$ = 246 Hz), 144.38 (dm, $J_{C–F}$ = 254

Hz), 139.44 (dm, $J_{C–F}$ = 249 Hz), 138.65, 138.01, 137.96, 137.87, 136.10, 133.75, 133.51, 133.18, 113.45 (m), 112.18, 107.66, 107.58. ^{19}F NMR (564 MHz, CD_3CN, 20 °C): δ (ppm) –72.97 (d, J = 705.6 Hz, 6F, PF_6^-), –139.44 (d, J = 17.5 Hz, 6F, Ar-F), –153.32 (m, 3F, Ar-F), –162.87 (m, 6F, Ar-F). UV/vis (CH_2Cl_2, λ_{max}[nm] (ε, 10^5 $M^{-1}cm^{-1}$)): 397 (3.2). MALDI-TOF-MS: *m/z* (% intensity): 1003.0 (100), 1004.0 (39), 1005.0 (7). Calcd for $C_{38}H_9AuF_{15}N_4$ ($[M – PF_6]^+$): 1003.02. PF_6^- (calcd: 144.96) was also detected as *m/z* = 145.0 (100) in the negative mode. Elemental analysis: C 39.50, H 0.91, N 4.80, F 34.62. Calcd (%) for $C_{38}H_9AuF_{21}N_4P$: C 39.74, H 0.79, Au 17.15, F 34.74, N 4.88, P 2.70. This compound was further characterized by single-crystal X-ray diffraction analysis.

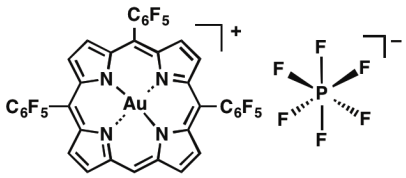

22^+ as a $PCCp^-$ ion pair, 22^+-$PCCp^-$. NaPCCp was used for anion exchange. After the workup, the residue was purified by chromatography over a silica gel column (Wakogel C-300, eluent: 10% MeOH/CH_2Cl_2) and was recrystallized from CH_2Cl_2/*n*-hexane to give **22^+**-$PCCp^-$ (4.92 mg, 4.12 μmol, 67%) as a pink solid. R_f = 0.58 (10% MeOH/CH_2Cl_2). ^{1}H NMR (600 MHz, CD_3CN, 20 °C): δ (ppm) 11.44 (s, 1H, *meso*-CH), 10.14 (d, J = 4.8 Hz, 2H, β-CH), 9.72 (d, J = 5.4 Hz, 2H, β-CH), 9.70 (d, J = 5.4 Hz, 2H, β-CH), 9.69 (d, J = 5.4 Hz, 2H, β-CH). ^{13}C{^{1}H} NMR (151 MHz, CD_3CN, 20 °C): δ (ppm) 147.63 (dm, $J_{C–F}$ = 247 Hz), 144.28 (dm, $J_{C–F}$ = 255 Hz), 139.35 (dm, $J_{C–F}$ = 248 Hz), 138.56, 137.91, 137.85, 137.76, 136.03, 133.68, 133.44, 133.12, 113.95, 113.38 (m), 112.15, 107.58, 107.50, 102.92. ^{19}F NMR (564 MHz, CD_3CN, 20 °C): δ (ppm) –139.33 (d, J = 13.0 Hz, 6F, Ar-F), –153.24 (m, 3F, Ar-F), –162.80 (m, 6F, Ar-F). UV/vis (CH_2Cl_2, λ_{max}[nm] (ε, 10^5 $M^{-1}cm^{-1}$)): 396 (3.8). MALDI-TOF-MS: *m/z* (% intensity): 1003.1 (100), 1004.0 (48), 1005.0 (13). Calcd for $C_{38}H_9AuF_{15}N_4$ ($[M – PCCp]^+$): 1003.02. $PCCp^-$ (calcd: 190.02) was also detected as *m/z* = 190.0 (100), 191.0 (12) in the negative mode. Elemental analysis: C 47.23, H 0.72, N 10.83. Calcd (%) for $C_{48}H_9AuF_{15}N_9 \cdot 0.7CH_3CN \cdot 0.5H_2O \cdot 0.4CH_2Cl_2$: C 47.27, H 1.03, Au 15.57, Cl 2.24, F 22.52, N 10.74, O 0.63.

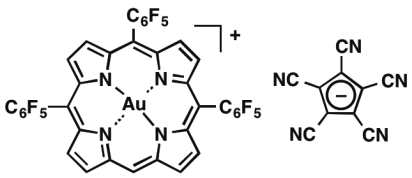

23^+ as a BF_4^- ion pair, 23^+-BF_4^-. $AgBF_4$ was used for anion exchange. After the workup, the residue was purified by chromatography over a silica gel column (Wakogel C-300, eluent: 5% MeOH/CH_2Cl_2) and was recrystallized from CH_2Cl_2/*n*-hexane to give **23**$^+$-BF_4^- (6.4 mg, 5.10 μmol, 61%) as a red solid. R_f = 0.29 (5% MeOH/CH_2Cl_2). ^{1}H NMR (600 MHz, CD_3CN, 20 °C): δ(ppm) 9.71 (s, 8H, β-H). $^{13}C\{^1H\}$ NMR (151 MHz, CD_3CN, 20 °C): δ(ppm) 147.91 (dm, J_{C-F} = 247 Hz), 144.66 (dm, J_{C-F} = 254 Hz), 139.64 (dm, J_{C-F} = 253 Hz), 138.76, 134.40, 113.40 (m), 108.92. ^{19}F NMR (564 MHz, CD_3CN, 20 °C): δ(ppm) –139.22 (d, J = 15.2 Hz, 8F, Ar-F), –154.75 (s, $^{10}BF_4^-$), –151.80 (s, $^{11}BF_4^-$), –153.02 (t, J = 19.5 Hz, 4F, Ar-F), –162.65 (tm, J = 19.5 Hz, 8F, Ar-F). UV/vis (CH_2Cl_2, λ_{max}[nm] (ε, 10^5 $M^{-1}cm^{-1}$)): 401 (4.0). MALDI-TOF-MS: *m/z* (% intensity): 1169.0 (100), 1170.0 (48), 1171.0 (13). Calcd for $C_{44}H_8AuF_{20}N_4$ ($[M - BF_4]^+$): 1169.01. BF_4^- (calcd: 87.00) was also detected as *m/z* = 87.0 (100), 86.0 (40) in the negative mode. Elemental analysis: C 41.70, H 0.65, N 4.83. Calcd (%) for $C_{44}H_8AuBF_{24}N_4$: C 42.07, H 0.64, Au 15.68, B 0.86, F 36.29, N 4.46. This compound was further characterized by single-crystal X-ray diffraction analysis.

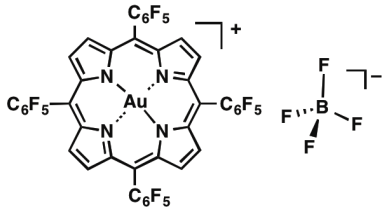

23^+ as a PF_6^- ion pair, 23^+-PF_6^-. $AgPF_6$ was used for anion exchange. After the workup, the residue was purified by chromatography over a silica gel column (Wakogel C-300, eluent: 5% MeOH/CH_2Cl_2) and was recrystallized from CH_2Cl_2/*n*-hexane to give **23**$^+$-PF_6^- (6.01 mg, 4.56 μmol, 55%) as a red solid. R_f = 0.37 (5% MeOH/CH_2Cl_2). ^{1}H NMR (600 MHz, CD_3CN, 20 °C): δ(ppm) 9.69 (s, 8H, β-H). $^{13}C\{^1H\}$ NMR (151 MHz, CD_3CN, 20 °C): δ(ppm) 147.68 (dm, J_{C-F} = 245.8 Hz), 144.44 (dm, J_{C-F} = 254.4 Hz), 139.42 (dm, J_{C-F} = 251.6 Hz), 138.53, 134.17, 113.20 (m), 108.70. ^{19}F NMR (564 MHz, CD_3CN, 20 °C): δ(ppm) –72.98 (d, J = 706.1 Hz, 6F, PF_6^-), –139.30 (d, J = 13.0 Hz, 8F, Ar-F), –153.10 (t, J = 21.4 Hz, 4F, Ar-F), –162.73 (t, J = 17.5 Hz, 8F, Ar-F). UV/vis (CH_2Cl_2, λ_{max}[nm] (ε, 10^5 $M^{-1}cm^{-1}$)): 401 (3.7). MALDI-TOF-MS: *m/z* (% intensity): 1169.0 (100), 1170.0 (38), 1171.0 (11). Calcd for $C_{44}H_8AuF_{20}N_4$ ($[M - PF_6]^+$): 1169.01. PF_6^- (calcd: 144.96) was also detected as *m/z* = 145.0 (100) in the negative mode. Elemental analysis: C 39.95, H 0.64, N 4.33, F 37.40. Calcd (%) for $C_{44}H_8AuF_{26}N_4P$: C 40.20, H 0.61, Au 14.98, F 37.58, N 4.26, P 2.36.

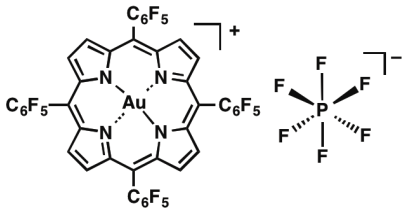

23^+ as a $PCCp^-$ ion pair, 23^+-$PCCp^-$. NaPCCp was used for anion exchange. After the workup, the residue was purified by chromatography over a silica gel column (Wakogel C-300, eluent: 10% MeOH/CH_2Cl_2) and was recrystallized from CH_2Cl_2/*n*-hexane to give **23^+**-$PCCp^-$ (7.31 mg, 5.36 μmol, 70%) as a red solid. R_f = 0.81 (10% MeOH/CH_2Cl_2). ^{1}H NMR (600 MHz, CD_3CN, 20 °C): δ (ppm) 9.71 (s, 8H, β-H). $^{13}C\{^1H\}$ NMR (151 MHz, CD_3CN, 20 °C): δ (ppm) 147.67 (dm, $J_{C–F}$ = 248.7 Hz), 144.40 (dm, $J_{C–F}$ = 251.6 Hz), 139.39 (dm, $J_{C–F}$ = 251.6 Hz), 138.52, 134.16, 114.79, 113.19 (m), 108.70, 102.80. ^{19}F NMR (564 MHz, CD_3CN, 20 °C): δ (ppm) –139.19 (d, J = 14.7 Hz, 8F, Ar-F), –153.03 (t, J = 19.7 Hz, 4F, Ar-F), –162.65 (m, 8F, Ar-F). UV/vis (CH_2Cl_2, λ_{max}[nm] (ε, 10^5 $M^{-1}cm^{-1}$)): 401 (3.7). MALDI-TOF-MS: *m/z* (% intensity): 1169.0 (100), 1170.0 (65), 1171.0 (23). Calcd for $C_{44}H_8AuF_{20}N_4$ ([M – PCCp]$^+$): 1169.01. $PCCp^-$ (calcd: 190.02) was also detected as *m/z* = 190.0 (100), 191.0 (13) in the negative mode. Elemental analysis: C 47.19, H 0.63, N 10.38. Calcd (%) for $C_{54}H_8AuF_{20}N_9 \cdot 1.6CH_3CN \cdot 0.5CH_2Cl_2$: C 47.22, H 0.95, Au 13.42, Cl 2.42, F 25.89, N 10.12. This compound was further characterized by single-crystal X-ray diffraction analysis.

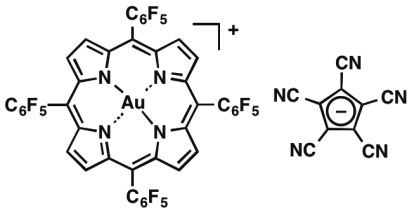

Ion pair of 16^+ and 35^-, 16^+-35^-. To a dry CH_2Cl_2 solution (9 mL) of **35** [51] (11.3 mg, 18.5 μmol) was added NaOH (500 mg, 12.5 mmol). After stirring for 2 h, the excess NaOH was removed. To the filtration was added **16^+**-Cl^- [39,65] (15.6 mg, 18.5 μmol) and the reaction mixture was washed with water to remove NaCl. The crude product was recrystallized from CH_2Cl_2/*n*-hexane to afford **16^+**-**35^-** (22.4 mg, 15.7 μmol, 85%) as a brown solid. ^{1}H NMR (600 MHz, DMSO-d_6, 20 °C): δ (ppm) 9.30 (s, 8H, **16^+**), 8.29 (d, J = 4.2 Hz, 2H, **35^-**), 8.27–8.26 (m, 8H, **16^+**), 7.99–7.92 (m, 12H, **16^+**), 7.73 (d, J = 4.8 Hz, 2H, **35^-**), 7.70–7.68 (m, 6H, **16^+**), 7.60 (d, J = 5.4 Hz, 2H, **35^-**), 7.59–7.52 (m, 9H, **35^-**), 7.46 (d, J = 4.2 Hz, 2H, **35^-**). $^{13}C\{^1H\}$ NMR (151 MHz, DMSO-d_6, 50 °C): δ (ppm) 145.50, 143.20, 141.26, 140.93, 138.35, 137.60, 136.41, 134.04, 132.97, 132.42, 132.27, 131.07, 129.42, 127.80, 127.30, 127.17, 127.03, 126.74, 123.05, 122.32, 121.98, 119.23, 108.18. UV/vis (CH_2Cl_2,

λ_{max}[nm] (ε, 10^5 $M^{-1}cm^{-1}$)): 409 (4.3), 522 (0.22), 670 (0.20). HRMS (ESI-TOF): *m/z*: calcd for $C_{44}H_{28}AuN_4$ ([M – **35**]$^+$): 809.1974; found 809.1975. Calcd for $C_{38}H_{23}N_4NiO$ ([M – **16**]$^-$): 609.1231; found 609.1230. This compound was further characterized by single-crystal X-ray diffraction analysis.

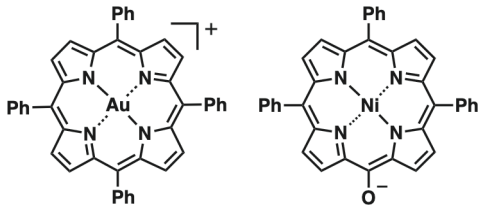

Ion pair of 16^+ and 19^-, 16^+-19^-. To a dry CH_2Cl_2 solution (5 mL) of **19** [55] (12.7 mg, 13.3 μmol) was treated with an excess amount of aqueous NaOH to yield porphyrin anion 19^- as a Na^+ ion pair in a CH_2Cl_2 phase. Then, 16^+-Cl^- [39,65] (9.20 mg, 8.88 μmol) was added to the solution and the reaction mixture was washed with water to remove NaCl. The CH_2Cl_2 phase was evaporated to dryness. The crude product was recrystallized from CH_2Cl_2/*n*-hexane to afford 16^+-19^- (15.2 mg, 8.61 μmol, 65%) as a brown solid. ^{1}H NMR (600 MHz, DMSO-d_6, 20 °C): δ (ppm) 9.28 (s, 8H, 16^+), 8.24 (dm, J = 6.6 Hz, 8H, 16^+), 8.21 (br, 2H, 19^-), 8.20 (br, 1H, 19^-), 8.02 (br, 2H, 19^-), 7.95 (tt, J = 7.2 and 1.8 Hz, 4H, 16^+), 7.92–7.89 (m, 8H, 16^+), 7.81 (br, 2H, 19^-), 7.70 (d, J = 7.2 Hz, 2H, 19^-), 7.33 (t, J = 7.2 Hz, 2H, 19^-), 7.26 (t, J = 7.2 Hz, 1H, 19^-). ^{13}C{^{1}H} NMR (151 MHz, DMSO-d_6, 20 °C): δ (ppm) 146.76, 145.73 (dm, $J_{13C–19F}$ = 243 Hz), 145.46, 145.30 (dm, $J_{13C–19F}$ = 241 Hz), 141.00 (dm, $J_{13C–19F}$ = 249 Hz), 138.54, 138.49, 138.32, 138.29, 137.23 (dm, $J_{13C–19F}$ = 249 Hz), 136.23, 136.19, 134.02, 132.40, 130.03, 129.99, 129.41, 127.81, 127.10, 127.06, 126.03, 123.05, 123.01, 114.13 (m), 103.47, 102.66, 91.73. ^{19}F NMR (564 MHz, DMSO-d_6, 20 °C): δ (ppm) –139.45 (dd, J = 26.5 and 6.8 Hz, 2F), –140.13 (d, J = 24.3 Hz, 4F), –155.23 (t, J = 109 Hz, 3F), –162.74– –162.91 (m, 6F). UV/vis (CH_2Cl_2, λ_{max}[nm] (ε, 10^5 $M^{-1}cm^{-1}$)): 409 (4.0), 439 (0.88), 523 (0.20), 682 (0.21). HRMS (ESI-TOF): *m/z*: calcd for $C_{44}H_{28}AuN_4$ ([M – **19**]$^+$): 809.1974; found 809.1974. Calcd for $C_{44}H_{12}F_{15}N_4NiO$ ([M – **16**]$^-$): 955.0131; found 955.0131.

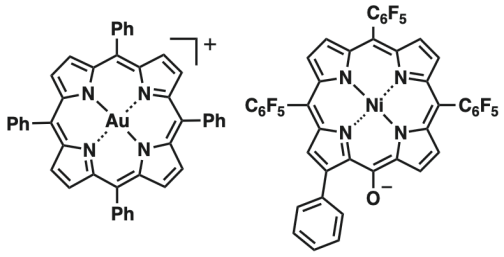

Ion pair of 22^+ and 35^-, 22^+-35^-. To a dry CH_2Cl_2 solution (1.6 mL) of **35** [51] (11.6 mg, 19.0 μmol) was added NaOH (500 mg, 12.5 mmol). After stirring for 2 h, the excess NaOH was removed. To the filtration was

added **22**$^{+}$-Cl^{-} (19.7 mg, 19.0 μmol) and the reaction mixture was washed with water to remove NaCl. The crude product was recrystallized from CH_2Cl_2/*n*-hexane to afford **22**$^{+}$-**35**$^{-}$ (21.1 mg, 13.1 μmol, 69%) as a brown solid. ^{1}H NMR (600 MHz, DMSO-d_6, 20 °C): δ (ppm) 11.60 (s, 1H, **22**$^{+}$), 10.28 (d, J = 4.8 Hz, 2H, **22**$^{+}$), 10.00 (d, J = 4.8 Hz, 2H, **22**$^{+}$), 9.98 (d, J = 5.4 Hz, 2H, **22**$^{+}$), 9.96 (d, J = 4.8 Hz, 2H, **22**$^{+}$), 8.45 (d, J = 4.2 Hz, 2H, **35**$^{-}$), 7.83 (d, J = 4.8 Hz, 2H, **35**$^{-}$), 7.73–7.70 (m, 8H, **35**$^{-}$), 7.62–7.54 (m, 11H, **35**$^{-}$). ^{13}C{^{1}H} NMR (151 MHz, DMSO-d_6, 20 °C): δ (ppm) 146.35 (dm, $J_{13C–19F}$ = 247 Hz), 145.17, 142.64 (dm, $J_{13C–19F}$ = 249 Hz), 142.46, 141.02, 140.74, 137.91 (dm, $J_{13C–19F}$ = 249 Hz), 137.82, 137.28, 136.84, 136.65, 136.53, 136.44, 135.42, 133.31, 133.06, 133.03, 132.54, 132.37, 131.35, 127.35, 127.31, 127.11, 126.97, 123.20, 122.81, 119.16, 112.24 (m), 111.24, 105.70. ^{19}F NMR (564 MHz, DMSO-d_6, 20 °C): δ (ppm) –138.69 (d, J = 19.7 Hz, 4F, Ar-F), –138.77 (d, J = 19.2 Hz, 2F, Ar-F), –152.30 (t, J = 23.7 Hz, 2F, Ar-F), –152.35 (t, J = 23.7 Hz, 1F, Ar-F), –161.40– –161.51 (m, 6F, Ar-F). UV/vis (CH_2Cl_2, λ_{max}[nm] (ε, 10^5 $M^{-1}cm^{-1}$)): 396 (3.1), 418 (1.3), 514 (0.16), 547 (0.14), 671 (0.20). HRMS (ESI-TOF): *m/z*: calcd for $C_{38}H_9AuF_{15}N_4$ ([M – **35**]$^{+}$): 1003.0248; found 1003.0248. Calcd for $C_{38}H_{23}N_4NiO$ ([M – **22**]$^{-}$): 609.1231; found 609.1231. This compound was further characterized by single-crystal X-ray diffraction analysis.

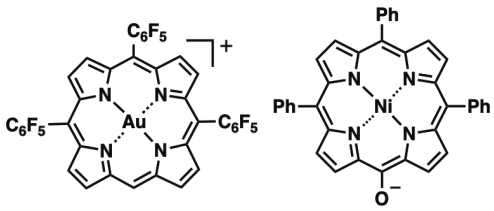

Ion pair of 22^{+} and 18^{-}, 22^{+}-18^{-}. To a CH_2Cl_2 solution (10 mL) of **18** [52,54] (20.0 mg, 19.3 μmol) was treated with an excess amount of aqueous NaOH to yield porphyrin anion **18**$^{-}$ as a Na^{+} ion pair in a CH_2Cl_2 phase. Then, **22**$^{+}$-Cl^{-} (17.0 mg, 19.3 μmol) was added to the solution and was washed with water to remove NaCl. The reaction mixture was evaporated to dryness. The crude product was recrystallized from CH_2Cl_2/*n*-hexane to afford **22**$^{+}$-**18**$^{-}$ (24.8 mg, 13.1 μmol, 68%) as a brown solid. ^{1}H NMR (600 MHz, $CDCl_3$, 20 °C): δ (ppm) 9.36 (d, J = 4.8 Hz, 2H, **22**$^{+}$), 9.28 (d, J = 4.2 Hz, 2H, **22**$^{+}$), 8.75 (s, 1H, **22**$^{+}$), 8.38 (d, J = 4.8 Hz, 2H, **22**$^{+}$), 8.07 (s, 4H, **18**$^{-}$), 7.33 (d, J = 4.8 Hz, 2H, **22**$^{+}$), 6.69 (d, J = 4.2 Hz, 2H, **18**$^{-}$), 5.79 (d, J = 4.2 Hz, 2H, **18**$^{-}$). ^{13}C{^{1}H} NMR (151 MHz, $CDCl_3$, 20 °C): δ (ppm) 161.05, 147.48, 146.46 (dm, $J_{13C–19F}$ = 244 Hz), 146.46 (dm, $J_{13C–19F}$ = 244 Hz), 145.85, 145.82 (dm, $J_{13C–19F}$ = 247 Hz), 143.33 (dm, $J_{13C–19F}$ = 252 Hz), 141.40 (dm, $J_{13C–19F}$ = 256 Hz), 141.27, 138.10 (dm, $J_{13C–19F}$ = 257 Hz), 137.95, 137.45 (dm, $J_{13C–19F}$ = 256 Hz), 136.19, 135.73, 134.66, 133.25, 131.73, 131.62, 131.49, 130.08, 127.21, 122.00, 115.97, 155.05, 113.17, 112.71, 109.59, 106.27, 105.83,

103.23, 92.07. ^{19}F NMR (564 MHz, $CDCl_3$, 20 °C): δ (ppm) –138.31 (d, J = 14.7 Hz, 2F, **22**$^+$), –138.59 (d, J = 17.5 Hz, 4F, **22**$^+$), –140.57 (d, J = 10.7 Hz, 2F, **18**$^–$), –141.55 (d, J = 10.7 Hz, 4F, **18**$^–$), –151.36 (t, J = 22.0 Hz, 1F, **22**$^+$), –151.57 (t, J = 21.4 Hz, 2F, **22**$^+$), –156.73 (t, J = 19.7 Hz, 1F, **18**$^–$), –156.85 (t, J = 22.0 Hz, 2F, **18**$^–$), –162.51 (m, 2F, **22**$^+$), –162.94 (m, 4F, **22**$^+$), –165.00 (m, 2F, **18**$^–$), –165.64 (m, 4F, **18**$^–$). UV/vis (CH_2Cl_2, λ_{max}[nm] (ε, 10^5 $M^{-1}cm^{-1}$)): 395 (3.1), 434 (0.92), 516 (0.15), 547 (0.14), 676 (0.19). HRMS (ESI-TOF): *m/z*: calcd for $C_{38}H_9AuF_{15}N_4$ ([M – **18**]$^+$): 1003.0248; found 1003.0248. Calcd for $C_{38}H_8F_{15}N_4NiO$ ([M – **22**]$^–$): 878.9818; found 878.9817. This compound was further characterized by single-crystal X-ray diffraction analysis.

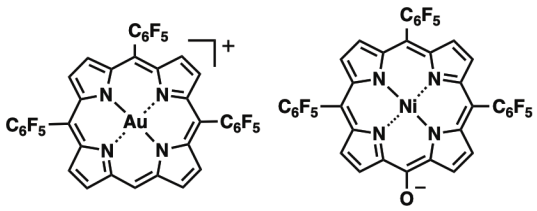

Ion pair of 22$^+$ and 19$^–$, 22$^+$-19$^–$. To a CH_2Cl_2 solution (10 mL) of **19** [55] (8.50 mg, 8.88 μmol) was treated with an excess amount of aqueous NaOH to yield porphyrin anion **19**$^–$ as a Na^+ ion pair in a CH_2Cl_2 phase. Then, **22**$^+$-$Cl^–$ (9.20 mg, 8.88 μmol) was added to the solution and was washed with water to remove NaCl. The reaction mixture was evaporated to dryness. The crude product was recrystallized from CH_2Cl_2/*n*-hexane to afford **22**$^+$-**19**$^–$ (10.3 mg, 5.26 μmol, 59%) as a brown solid. ^{1}H NMR (600 MHz, $CDCl_3$, 20 °C): δ (ppm) 9.29 (d, J = 4.2 Hz, 2H, **22**$^+$), 9.23 (d, J = 4.2 Hz, 2H, **22**$^+$), 8.82 (s, 1H, **22**$^+$), 8.36 (d, J = 4.8 Hz, 2H, **22**$^+$), 8.15 (br, 1H, **19**$^–$), 8.13 (br, 1H, **19**$^–$), 8.11 (br, 2H, **19**$^–$), 7.18 (d, J = 4.8 Hz, 2H, **19**$^–$), 6.88 (br, 1H, **19**$^–$), 6.83 (br, 1H, **19**$^–$), 6.76 (br, 1H, **19**$^–$), 6.59 (br, 2H, **19**$^–$), 5.97 (br, 1H, **19**$^–$), 5.49 (br, 2H, **19**$^–$). ^{13}C{^{1}H} NMR (151 MHz, $CDCl_3$, 20 °C): δ (ppm) 162.19, 146.64 (dm, $J_{13C–19F}$ = 233 Hz), 145.92 (dm, $J_{13C–19F}$ = 243 Hz), 145.55, 143.31 (dm, $J_{13C–19F}$ = 262 Hz), 143.29, 140.60, 138.69, 138.06 (dm, $J_{13C–19F}$ = 253 Hz), 137.71, 137.56, 137.49 (dm, $J_{13C–19F}$ = 254 Hz), 136.81, 136.25, 136.19, 135.70, 133.92, 132.86, 132.56 (dm, $J_{13C–19F}$ = 320 Hz), 131.66, 130.07, 128.47, 127.29, 127.09, 126.21, 125.47, 123.95, 122.93, 121.79, 115.95, 115.07, 110.01, 106.32, 103.63, 103.17, 91.74 (the signals of C_6F_5 units are overlapped). ^{19}F NMR (564 MHz, $CDCl_3$, 20 °C): δ (ppm) –138.21 (d, J = 17.5 Hz, 2F, **22**$^+$), –138.42 (d, J = 22.0 Hz, 4F, **22**$^+$), –140.54 (br, 2F, **19**$^–$), –141.59 (br, 2F, **19**$^–$), –141.77 (br, 2F, **19**$^–$), –151.32 (t, J = 17.5 Hz, 1F, **22**$^+$), –151.64 (t, J = 22.0 Hz, 2F, **22**$^+$), –156.93 (br, 2F, **19**$^–$), –157.09 (br, 1F, **19**$^–$), –162.56 (m, 2F, **22**$^+$), –162.96 (m, 4F, **22**$^+$), –165.07 (br, 2F, **19**$^–$), –165.55 (br, 2F, **19**$^–$), –165.74 (br, 2F, **19**$^–$). UV/vis (CH_2Cl_2, λ_{max}[nm] (ε, 10^5 $M^{-1}cm^{-1}$)): 396 (3.1), 420 (0.95), 441 (0.92), 516 (0.16), 546

(0.15), 682 (0.21). HRMS (ESI-TOF): *m/z*: calcd for $C_{38}H_9AuF_{15}N_4$ ([M – **19**]$^+$): 1003.0248; found 1003.0248. Calcd for $C_{44}H_{12}F_{15}N_4NiO$ ([M – **22**]$^-$): 955.0131; found 955.0129. This compound was further characterized by single-crystal X-ray diffraction analysis.

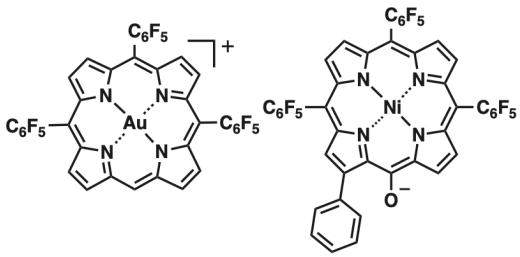

5,10,15-Tris(pentafluorophenyl)porphyrin Au^{II} complex, 22$^{\bullet}$. Following the reported procedure,[122] to a THF solution (10 mL) of **22**$^+$-BF_4^- (3.40 mg, 3.12 μmol) was treated with an excess amount of KC_8 to yield and the resulting solution was stirred for 15 min. After the reaction mixture was filtered, the solvent was removed under reduced pressure to afford **22**$^{\bullet}$ (2.81 mg, 2.81 μmol, 90%) as a brown solid. UV/vis (toluene, λ_{max}[nm] (ε, 10^5 $M^{-1}cm^{-1}$)): 412 (1.5), 604 (0.20), 790 (0.15). HRMS (ESI-TOF): *m/z*: calcd for $C_{38}H_9AuF_{15}N_4$ ([M]$^+$): 1003.0248; found 1003.0248.

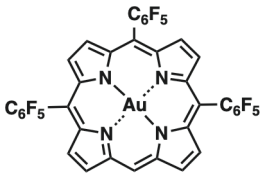

5-Oxy-10,15,20-triphenylporphyrin Ni^{II} complex, 35$^{\bullet}$. Following the reported procedure,[50] to a CH_2Cl_2 solution (5 mL) of **35** [51] (10.0 mg, 16.4 μmol) was treated with an excess amount of PbO_2 to yield and the resulting solution was stirred for 5 min. After the reaction mixture was filtered through a short Celite pad, the solvent was removed under reduced pressure. The crude product was recrystallized from CH_2Cl_2/*n*-hexane to afford **35**$^{\bullet}$ (9.80 mg, 16.1 μmol, 98%) as a brown solid. UV/vis (CH_2Cl_2, λ_{max}[nm] (ε, 10^5 $M^{-1}cm^{-1}$)): 345 (0.26), 443 (0.85), 497 (0.19), 810 (0.12). HRMS (ESI-TOF): *m/z*: calcd for $C_{38}H_{23}N_4NiO$ ([M]$^-$): 609.1231; found 609.1233. This compound was further characterized by single-crystal X-ray diffraction analysis.

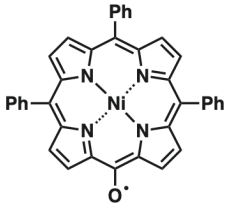

5,10,15-Triphenylporphyrin Au^{III} complex as a Cl$^-$ ion pair, 36$^+$-Cl$^-$. According to the literature procedure,[126] chloro(tetrahydrothiophene)gold(I)[135] (596 mg, 1.86 mmol) and tetrahydrothiophene (12 mL, 0.136 mol) were dissolved in CH_2Cl_2 (121 mL). To the solution, AgOTf (429 mg, 1.67 mmol) was added. After stirring for 1 h, the product was filtered and the solvent was removed. To the residue were added 5,10,15-triphenylporphyrin[125] (100 mg, 0.186 mmol) and $CHCl_3$ (135 mL). To the solution, 2,6-lutidine (144 μL, 1.24 mmol) was added and the mixture was stirred under reflux for 2 h. The reaction mixture passed through a short pad of silica (Wakogel C-300, eluent: 10% MeOH/CH_2Cl_2). After the removal of solvent by vacuum, the residue was chromatographed over ion-exchanged resin (Amberlite IRA402BL, eluent: 50% MeOH/CH_2Cl_2) and silica gel column (Wakogel C-300, eluent: 10% MeOH/CH_2Cl_2) and was recrystallized from CH_2Cl_2/*n*-hexane to give **36**$^+$-Cl$^-$ (26.1 mg, 33.9 μmol, 18%) as a red solid. R_f = 0.36 (10% MeOH/CH_2Cl_2). ^{1}H NMR (600 MHz, $CDCl_3$, 20 °C): δ (ppm) 11.83 (s, 1H, *meso*-H), 10.21 (d, J = 4.2 Hz, 2H, β-H), 9.41 (d, J = 4.2 Hz, 2H, β-H), 9.33 (d, J = 5.4 Hz, 2H, β-CH), 9.30 (d, J = 5.4 Hz, 2H, β-CH), 8.24–8.20 (m, 6H, Ph-H), 7.95–7.85 (m, 9H, Ph-H). ^{13}C{^{1}H} NMR (151 MHz, $CDCl_3$, 20 °C): δ (ppm) 138.58, 138.31, 137.11, 136.59, 136.54, 136.04, 134.15, 134.07, 134.04, 132.66, 131.98, 131.93, 129.49, 129.47, 127.78, 127.69, 123.47, 122.82, 110.61. UV/vis (CH_2Cl_2, λ_{max}[nm] (ε, 10^5 $M^{-1}cm^{-1}$)): 403 (4.0), 515 (0.18). HRMS (ESI-TOF): *m/z*: calcd for $C_{38}H_{24}N_4Au$ ([M – Cl]$^+$): 733.1661; found 733.1661. This compound was further characterized by single-crystal X-ray diffraction analysis.

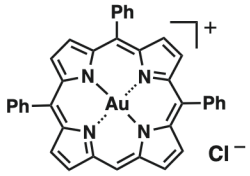

5,10,15-Triphenylporphyrin Au^{III} complex as a PF$_6^-$ ion pair, 36$^+$-PF$_6^-$. $AgPF_6$ (25.1 mg, 99.0 μmol) was added to a solution of **36**$^+$-Cl$^-$ (25.4 mg, 33.0 μmol) in 25% MeOH/CH_2Cl_2 and was stirred for 15 min. After removal of solvent by vacuum, the residue was chromatographed over silica gel column (Wakogel C-300, eluent: 5% MeOH/CH_2Cl_2) and was recrystallized from CH_2Cl_2/*n*-hexane to give **36**$^+$-PF_6^- (17.9 mg, 20.4 μmol, 62%) as a red solid. R_f = 0.33 (5% MeOH/CH_2Cl_2). ^{1}H NMR (600 MHz, CD_2Cl_2, 20 °C): δ (ppm) 11.10 (s, 1H, *meso*-H), 9.88 (d, J = 5.4 Hz, 2H, β-CH), 9.51 (d, J = 4.8 Hz, 2H, β-CH), 9.40 (d, J = 5.4 Hz, 2H, β-CH), 9.39 (d, J = 4.8 Hz, 2H, β-CH), 8.28–8.26 (m, 4H, Ph-H), 8.25–8.23 (m, 2H, Ph-H), 8.00–7.88 (m, 9H, Ph-H). ^{13}C{^{1}H} NMR (151 MHz, CD_2Cl_2, 20 °C): δ (ppm) 138.86, 138.66, 137.41, 137.13, 137.09, 136.91, 134.64, 134.58, 133.46, 133.06, 132.82, 132.65, 130.00, 129.97, 128.27, 128.17, 124.62, 123.77, 108.86. ^{19}F NMR

(564 MHz, CD_2Cl_2, 20 °C): δ (ppm) –73.54 (d, J = 709 Hz, 6F). UV/vis (CH_2Cl_2, λ_{max}[nm] (ε, 10^5 $M^{-1}cm^{-1}$)): 403 (3.7), 515 (0.17). HRMS (ESI-TOF): *m/z*: calcd for $C_{38}H_{24}N_4Au$ ($[M - PF_6]^+$): 733.1661; found 733.1661. This compound was further characterized by single-crystal X-ray diffraction analysis.

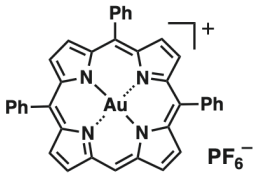

Ion pair of 36^+ and 35^-, 36^+-35^-. To a dry CH_2Cl_2 solution (10 mL) of **35** [51] (19.5 mg, 31.8 μmol) was added NaOH (500 mg, 12.5 mmol). After stirring for 1 h, the excess NaOH was removed. To the filtration was added $\mathbf{36}^+$-Cl^- (24.5 mg, 31.8 μmol) and the reaction mixture was washed with water to remove NaCl. The crude product was recrystallized from CH_2Cl_2/CH_3CN to afford $\mathbf{36}^+$-$\mathbf{35}^-$ (37.6 mg, 28.0 μmol, 88%) as a brown solid. ^{1}H NMR (600 MHz, CD_2Cl_2, 20 °C): δ (ppm) 9.16 (d, J = 5.4 Hz, 2H, $\mathbf{36}^+$), 9.09 (d, J = 4.8 Hz, 2H, $\mathbf{36}^+$), 8.99 (s, 1H, $\mathbf{36}^+$), 8.54 (d, J = 5.4 Hz, 2H, $\mathbf{36}^+$), 8.17–8.16 (m, 2H, $\mathbf{36}^+$), 8.04 (d, J = 4.8 Hz, 2H, $\mathbf{36}^+$), 7.96–7.94 (m, 4H, $\mathbf{36}^+$), 7.92–7.89 (m, 3H, $\mathbf{36}^+$), 7.84–7.80 (m, 6H, $\mathbf{36}^+$ and $\mathbf{35}^-$), 7.51–7.49 (m, 4H, $\mathbf{35}^-$), 7.39 (d, J = 6.0 Hz, 4H, $\mathbf{35}^-$), 6.93 (br, 2H, $\mathbf{35}^-$), 6.73 (br, 2H, $\mathbf{35}^-$). $^{13}C\{^1H\}$ NMR (151 MHz, CD_2Cl_2, 20 °C): δ (ppm) 139.62, 139.02, 136.42, 136.32, 135.62, 135.32, 134.79, 134.67, 134.07, 133.24, 131.78, 131.38, 131.28, 131.04, 130.75, 129.40, 129.27, 127.80, 127.50, 127.15, 127.02, 123.56, 122.11, 121.04, 106.78 (some of the signals of $\mathbf{35}^-$ were missing due to overlapping with other signals and broadening). UV/vis (CH_2Cl_2, λ_{max}[nm] (ε, 10^5 $M^{-1}cm^{-1}$)): 403 (3.7), 517 (0.18), 672 (0.23). HRMS (ESI-TOF): *m/z*: calcd for $C_{38}H_{24}N_4Au$ ($[M - \mathbf{35}]^+$): 733.1661; found 733.1661. Calcd for $C_{38}H_{23}N_4ONi$ ($[M - \mathbf{36}]^-$): 609.1231; found 609.1231.

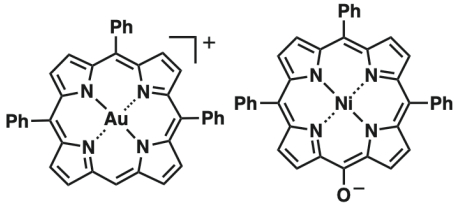

Ion pair of 36^+ and 18^-, 36^+-18^-. To a CH_2Cl_2 solution (10 mL) of **18** [54] (20.4 mg, 23.1 μmol) was treated with an excess amount of aqueous NaOH to yield porphyrin anion $\mathbf{18}^-$ as a Na^+ ion pair in a CH_2Cl_2 phase. Then, $\mathbf{36}^+$-Cl^- (17.8 mg, 23.1 μmol) was added to the solution and was washed with water to remove NaCl. The reaction mixture was evaporated to dryness. The crude product was recrystallized from CH_2Cl_2/*n*-hexane to afford $\mathbf{36}^+$-$\mathbf{18}^-$ (32.6 mg, 20.2 μmol, 87%) as a brown solid. ^{1}H NMR (600 MHz, CD_2Cl_2, 20 °C): δ (ppm) 9.76 (s, 1H, $\mathbf{36}^+$), 9.24 (d, J = 4.8 Hz, 2H, $\mathbf{36}^+$), 9.16 (d, J = 4.8 Hz, 2H, $\mathbf{36}^+$), 8.81 (d, J = 5.4 Hz, 2H, $\mathbf{36}^+$), 8.54

(d, J = 5.4 Hz, 2H, **36**$^+$), 8.29–8.27 (m, 2H, **36**$^+$), 7.97–7.96 (m, 4H, **36**$^+$), 7.94 (d, J = 4.8 Hz, 2H, **18**$^–$), 7.92–7.84 (m, 7H, **36**$^+$ and **18**$^–$), 7.80–7.78 (m, 4H, **36**$^+$), 6.80 (d, J = 4.8 Hz, 2H, **18**$^–$), 6.35 (d, J = 4.2 Hz, 2H, **18**$^–$). $^{13}C\{^1H\}$ NMR (151 MHz, CD_2Cl_2, 20 °C): δ (ppm) 162.77, 146.91 (dm, $J_{13C–19F}$ = 241 Hz), 146.72, 145.99 (dm, $J_{13C–19F}$ = 243 Hz), 142.05, 141.63 (dm, $J_{13C–19F}$ = 259 Hz), 139.54, 138.88, 138.37, 138.17 (dm, $J_{13C–19F}$ = 252 Hz), 137.74 (dm, $J_{13C–19F}$ = 253 Hz), 136.75, 136.58, 135.94, 135.83, 135.00, 134.64, 134.57, 131.95, 131.75, 131.68, 131.61, 131.33, 129.49, 129.34, 127.85, 127.70, 127.28, 123.92, 122.47, 121.61, 121.32, 115.53 (m), 107.04, 103.39, 92.41. ^{19}F NMR (564 MHz, CD_2Cl_2, 20 °C): δ (ppm) –137.87 (d, J = 19.7 Hz, 2F, **18**$^–$), –138.10 (d, J = 19.7 Hz, 4F, **18**$^–$), –155.10– –155.26 (m, 3F, **18**$^–$), –163.12– –163.31 (m, 6F, **18**$^–$). UV/vis (CH_2Cl_2, λ_{max}[nm] (ε, 10^5 $M^{-1}cm^{-1}$)): 403 (4.0), 435 (0.99), 517 (0.18), 676 (0.21). HRMS (ESI-TOF): *m/z*: calcd for $C_{38}H_{24}N_4Au$ ([M – **18**]$^+$): 733.1661; found 733.1660. Calcd for $C_{38}H_8N_4F_{15}ONi$ ([M – **36**]$^–$): 878.9818; found 878.9818.

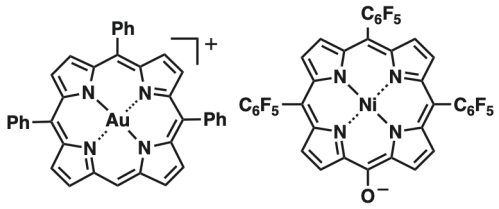

Method for single-crystal X-ray analysis (Chapter 2)

Crystallographic data are summarized in Table E1. A single crystal of **22**$^+$-Cl^- was obtained by vapor diffusion of *n*-hexane into a CH_2Cl_2 solution of **22**$^+$-Cl^-. The data crystal was a red prism of approximate dimensions 0.050 mm × 0.050 mm × 0.002 mm. A single crystal of **23**$^+$-Cl^- was obtained by vapor diffusion of $CHCl_3$ into a CH_2Cl_2 solution of **23**$^+$-Cl^-. The data crystal was a red prism of approximate dimensions 0.100 mm × 0.070 mm × 0.040 mm. A single crystal of **23**$^+$-BF_4^- was obtained by vapor diffusion of *n*-hexane into a CH_2ClCH_2Cl solution of **23**$^+$-BF_4^-. The data crystal was a red prism of approximate dimensions 0.020 mm × 0.020 mm × 0.020 mm. A single crystal of **21**$^+$-PF_6^- was obtained by vapor diffusion of cyclohexane into a CH_2ClCH_2Cl solution of **21**$^+$-PF_6^-. The data crystal was a red prism of approximate dimensions 0.100 mm × 0.020 mm × 0.010 mm. A single crystal of **22**$^+$-PF_6^- was obtained by vapor diffusion of *n*-hexane into a CH_2Cl_2 solution of **22**$^+$-PF_6^-. The data crystal was a red prism of approximate dimensions 0.030 mm × 0.010 mm × 0.005 mm. A single crystal of **21**$^+$-$PCCp^-$ was obtained by vapor diffusion of *n*-hexane into a THF solution of **21**$^+$-$PCCp^-$. The data crystal was a red prism of approximate dimensions 0.100 mm × 0.050 mm × 0.050 mm. A single crystal of **23**$^+$-$PCCp^-$ was obtained by vapor diffusion of *n*-hexane into a CH_2Cl_2 solution of **23**$^+$-$PCCp^-$. The data crystal was a red prism of approximate dimensions 0.010 mm × 0.010 mm × 0.005 mm. The data of **22**$^+$-Cl^-, **23**$^+$-BF_4^-, **22**$^+$-PF_6^-, **21**$^+$-$PCCp^-$, and **23**$^+$-$PCCp^-$ were collected at 90 K on a Rigaku Saturn 724 diffractometer with Si (111) monochromated synchrotron radiation (λ = 0.78228, 0.78255, and 0.78192 Å for **22**$^+$-Cl^-/**23**$^+$-$PCCp^-$, **23**$^+$-BF_4^-/**21**$^+$-$PCCp^-$, and **22**$^+$-PF_6^-, respectively) at BL40XU (SPring-8)[67,68] and those of **23**$^+$-Cl^- and **21**$^+$-PF_6^- were collected at 100 K on a DECTRIS PILATUS3 CdTe 1M diffractometer with Si (311) monochromated synchrotron radiation (λ = 0.4315 and 0.4403 Å for **23**$^+$-Cl^- and **21**$^+$-PF_6^-, respectively) at BL02B1 (SPring-8),[127] and structures were solved by dual-space method. The structures were refined by a full-matrix least-squares method by using a SHELXL 2014[136] (Yadokari-XG).[137,138] In each structure, the non-hydrogen atoms were refined anisotropically. Several disordered parts and solvent molecules were refined isotropically. CIF files (CCDC-1904174–1904180) can be obtained free of charge from the Cambridge Crystallographic Data Centre via www.ccdc.cam.ac.uk/data_request/cif.

Table E1 Summary of crystallographic data for Chapter 2.

	22^{+}-Cl^{-}	**23**$^{+}$-Cl^{-}	**23**$^{+}$-BF_4^{-}	**21**$^{+}$-PF_6^{-}	**22**$^{+}$-PF_6^{-}
formula	$C_{38}H_9AuF_{15}N_4 \cdot Cl \cdot CH_2Cl_2$	$C_{44}H_8AuF_{20}N_4 \cdot Cl \cdot 4CHCl_3$	$C_{44}H_8AuF_{20}N_4 \cdot BF_4 \cdot 0.607C_2H_4Cl_2$	$C_{32}H_{12}AuF_{10}N_4 \cdot F_6P \cdot 0.5C_2H_4Cl_2$	$C_{38}H_9AuF_{15}N_4 \cdot F_6P \cdot 1.455CH_2Cl_2$
fw	1123.83	1682.43	1316.37	1031.85	1318.28
crystal size, mm	0.050 × 0.050 × 0.002	0.100 × 0.070 × 0.040	0.020 × 0.020 × 0.020	0.100 × 0.020 × 0.010	0.030 × 0.010 × 0.005
crystal system	triclinic	monoclinic	monoclinic	triclinic	monoclinic
space group	*P*-1 (no. 2)	*C*2/*c* (no.15)	$P2_1/n$ (no. 14)	*P*-1 (no. 2)	$P2_1/c$ (no. 14)
a, Å	7.4641(2)	27.078(2)	22.598(5)	9.1552(7)	7.5597(3)
b, Å	16.2484(5)	15.4515(13)	16.471(3)	12.2080(10)	15.0303(6)
c, Å	16.5815(7)	14.0873(12)	23.477(5)	15.5409(13)	36.4416(13)
α, °	61.350(2)	90	90	111.547(8)	90
β, °	84.190(3)	108.053(8)	100.334(3)	91.837(7)	93.823(3)
γ, °	84.860(2)	90	90	101.828(7)	90
V, Å^3	1753.78(11)	5603.8(9)	8597(3)	1570.2(2)	4131.4(3)
ρ_{calcd}, gcm^{-3}	2.128	1.994	2.034	2.182	2.119
Z	2	4	8	2	4
T, K	90(2)	100(2)	90(2)	100(2)	90(2)
μ, mm^{-1}	5.769	0.903	4.629	1.435	5.069
no. of reflns	14377	51192	46884	47654	30983
no. of unique reflns	6142	6434	15651	7207	7040
variables	577	390	1366	505	642
λ, Å	0.78228	0.4315	0.78255	0.4403	0.78192
R_1 ($I > 2\sigma(I)$)	0.0374	0.0236	0.0857	0.0323	0.1083
wR_2 ($I > 2\sigma(I)$)	0.0857	0.0601	0.2248	0.0790	0.2555
GOF	1.122	1.064	1.027	1.077	0.981

	21^{+}-PCCp^{-}	**23**$^{+}$-PCCp^{-}
formula	$C_{32}H_{10}AuF_{10}N_4 \cdot C_{10}N_5 \cdot C_4H_8O$	$C_{44}H_8AuF_{20}N_4 \cdot C_{10}N_5$
fw	1099.66	1359.66
crystal size, mm	0.100 × 0.050 × 0.050	0.010 × 0.010 × 0.005
crystal system	monoclinic	triclinic
space group	*C*2/*c* (no. 15)	*P*-1 (no. 2)
a, Å	35.9738(6)	14.6498(3)
b, Å	6.96240(10)	17.8773(4)
c, Å	35.6473(6)	18.9784(4)
α, °	90	111.943(2)
β, °	117.7150(10)	96.1530(10)
γ, °	90	91.809(2)
V, Å^3	7904.0(2)	4569.94(18)
ρ_{calcd}, gcm^{-3}	1.848	1.976
Z	8	4
T, K	90(2)	90(2)
μ, mm^{-1}	4.850	4.254
no. of reflns	20589	38052
no. of unique reflns	7127	16199
variables	556	1513
λ, Å	0.78255	0.78228
R_1 ($I > 2\sigma(I)$)	0.0341	0.0371
wR_2 ($I > 2\sigma(I)$)	0.0765	0.0758
GOF	1.134	1.047

Method for single-crystal X-ray analysis (Chapter 3).

Crystallographic data are summarized in Table E2. A single crystal of **16**$^{+}$-**24**·Cl^{-} was obtained by vapor diffusion of *n*-hexane into a CH_2Cl_2 solution of the 1:1 mixture of the Cl^{-} ion pair of *meso*-tetraphenylporphyrin–Au^{III} complex **16**$^{+}$ [39] and dipyrrolyldiketone BF_2 complex **24**.[23] The data crystal was a red prism of approximate dimensions 0.130 mm × 0.090 mm × 0.010 mm. A single crystal of **16**$^{+}$-**25**·Cl^{-} was obtained by vapor diffusion of *n*-hexane into a $CHCl_3$ solution of the 1:1 mixture of **16**$^{+}$-Cl^{-} and β-tetramethyl-substituted dipyrrolyldiketone BF_2 complex **25**.[72] The data crystal was a red prism of approximate dimensions 0.160 mm × 0.160 mm × 0.010 mm. A single crystal of **16**$^{+}$-**26**·Cl^{-} was obtained by vapor diffusion of *n*-hexane into a CH_2Cl_2 solution of the 1:1 mixture of **16**$^{+}$-Cl^{-} and β-tetrafluorinated dipyrrolyldiketone BF_2 complex **26**.[73] The data crystal was a red prism of approximate dimensions 0.030 mm × 0.030 mm × 0.010 mm. A single crystal of **16**$^{+}$-**27**·Cl^{-} was obtained by vapor diffusion of *n*-hexane into a CH_2Cl_2 solution of the 1:1 mixture of **16**$^{+}$-Cl^{-} and α-di(4-fluorophenylethynyl)-substituted dipyrrolyldiketone BF_2 complex **27**.[74] The data crystal was a red prism of approximate dimensions 0.100 mm × 0.002 mm × 0.002 mm. A single crystal of **22**$^{+}$-**26**·Cl^{-} was obtained by vapor diffusion of 1,4-dioxane into a CH_2ClCH_2Cl solution of the 1:1 mixture of the Cl^{-} ion pair of 5,10,15-tris(pentafluorophenyl)porphyrin–Au^{III} complex **22**$^{+}$ and **26**.[73] The data crystal was a red plate of approximate dimensions 0.10 mm × 0.03 mm × 0.01 mm. The data of **16**$^{+}$-**24**·Cl^{-} and **16**$^{+}$-**25**·Cl^{-} were collected at 93 K on a Rigaku XtaLAB P200 diffractometer with graphite monochromatic CuKα radiation (λ = 1.54187 Å) and those of **16**$^{+}$-**26**·Cl^{-} and **16**$^{+}$-**27**·Cl^{-} were collected at 90 K on a DECTRIS EIGER X 1M diffractometer and at 100 K on a Rigaku Saturn 724 diffractometer, respectively, with Si (111) monochromated synchrotron radiation (λ = 0.81078 and 0.78229 Å, respectively) at BL40XU (SPring-8),[67,68] whereas the data of **22**$^{+}$-**26**·Cl^{-} was collected at 100 K on a DECTRIS PILATUS3 CdTe 1M diffractometer with Si (311) monochromated synchrotron radiation (λ = 0.4118 Å) at BL02B1 (SPring-8),[127] and structures were solved by dual-space method. The structures were refined by a full-matrix least-squares method by using a SHELXL 2014[136] (Yadokari-XG).[137,138] In each structure, the non-hydrogen atoms were refined anisotropically. CIF files (CCDC 1969168–1969172) can be obtained free of charge from the Cambridge Crystallographic Data Centre via www.ccdc.cam.ac.uk/data_request/cif.

Table E2 Summary of crystallographic data for Chapter 3.

	16^{+}**-24**·Cl^{-}	**16**$^{+}$**-25**·Cl^{-}	**16**$^{+}$**-26**·Cl^{-}	**16**$^{+}$**-27**·Cl^{-}	**22**$^{+}$**-26**·Cl^{-}
formula	$C_{44}H_{28}AuN_4$·$C_{11}H_9BClF_2N_2O_2$·$2CH_2Cl_2$	$C_{44}H_{28}AuN_4$·$C_{15}H_{17}BClF_2N_2O_2$·$3CHCl_3$	$C_{44}H_{28}AuN_4$·$C_{11}H_5BClF_6N_2O_2$·$3CH_2Cl_2$	$C_{44}H_{28}AuN_4$·$C_{35}H_{31}BClF_4N_2O_2$·$0.5C_6H_{14}$	$C_{38}H_9AuF_{15}N_4$·$C_{11}H_5BClF_6N_2O_2$
fw	1264.98	1509.34	1336.95	1486.63	1360.89
crystal size, mm	0.130 × 0.090 × 0.010	0.160 × 0.160 × 0.010	0.030 × 0.030 × 0.010	0.100 × 0.002 × 0.002	0.10 × 0.03 × 0.01
crystal system	monoclinic	monoclinic	monoclinic	triclinic	triclinic
space group	$P2_1/c$ (no. 14)	$P2_1/c$ (no. 14)	$P2_1/c$ (no. 14)	P-1 (no. 2)	P-1 (no. 2)
a, Å	14.472(4)	10.1907(11)	13.1977(5)	10.3456(5)	10.2403(6)
b, Å	20.503(8)	33.247(3)	14.0926(5)	14.6912(7)	13.9827(8)
c, Å	17.602(7)	18.5930(19)	27.6765(11)	24.2405(11)	16.8405(10)
α, °	90	90	90	98.390(3)	106.572(7)
β, °	105.554(13)	93.488(5)	98.8620(10)	92.663(4)	98.296(7)
γ, °	90	90	90	107.460(4)	103.213(7)
V, Å^3	5032(3)	6287.8(11)	5086.1(3)	3461.0(3)	2192.6(2)
ρ_{calcd}, gcm^{-3}	1.670	1.594	1.746	1.427	2.061
Z	4	4	4	2	2
T, K	93(2)	93(2)	90(2)	100(2)	100(2)
μ, mm^{-1}	8.422	8.753	4.495	2.779	0.875
no. of reflns	64456	39603	54010	26645	63345
no. of unique reflns	9243	11167	9300	12019	10038
variables	680	757	713	943	730
λ, Å	1.54187	1.54187	0.81078	0.78229	0.4118
R_1 ($I > 2\sigma(I)$)	0.0207	0.0791	0.0387	0.0553	0.0408
wR_2 ($I > 2\sigma(I)$)	0.0538	0.2020	0.0788	0.1342	0.1102
GOF	1.000	1.075	1.168	1.027	1.107

Method for single-crystal X-ray analysis (Chapter 4).

Crystallographic data are summarized in Table E3. A single crystal of **16**$^{+}$-**28**·Cl^{-} was obtained by vapor diffusion of *n*-hexane into a CH_2ClCH_2Cl solution of the 1:1 mixture of **16**$^{+}$-Cl^{-} and **28**. The data crystal was a red needle of approximate dimensions 0.05 mm × 0.01 mm × 0.01 mm. A single crystal of **16**$^{+}$-**29**·Cl^{-} was obtained by vapor diffusion of *n*-hexane into a CH_2ClCH_2Cl solution of the 1:1 mixture of **16**$^{+}$-Cl^{-} and **29**. The data crystal was a red plate of approximate dimensions 0.20 mm × 0.17 mm × 0.05 mm. The data of **16**$^{+}$-**28**·Cl^{-} was collected at 90 K on a DECTRIS EIGER X 1M diffractometer with Si (111) monochromated synchrotron radiation (λ = 0.81063 Å) at BL40XU (SPring-8)[67,68] and that of **16**$^{+}$-**29**·Cl^{-} was collected at 100 K on a DECTRIS PILATUS3 CdTe 1M diffractometer with Si (311) monochromated synchrotron radiation (λ = 0.4127 Å) at BL02B1 (SPring-8).[127] The structures were refined by a full-matrix least-squares method by using a SHELXL 2014[136] (Yadokari-XG).[137,138] In each structure, the non-hydrogen atoms were refined anisotropically. CIF files (CCDC-2217182–2217183) can be obtained free of charge from the Cambridge Crystallographic Data Centre *via* www.ccdc.cam.ac.uk/data_request/cif.

Table E3 Summary of crystallographic data for Chapter 4.

	16^{+}-**28**·Cl^{-}	**16**$^{+}$-**29**·Cl^{-}
formula	$C_{44}H_{52}B_2F_4N_4O_4Cl$· $C_{44}H_{28}AuN_4$	$C_{56}H_{60}B_2F_4N_4O_4Cl$· $C_{44}H_{28}AuN_4$·$C_2H_4Cl_2$
fw	1643.63	1894.77
crystal size, mm	0.05 × 0.01 × 0.01	0.20 × 0.17 × 0.05
crystal system	monoclinic	monoclinic
space group	$P2_1/c$ (no. 14)	$P2_1/c$ (no. 14)
a, Å	19.8907(5)	22.7418(8)
b, Å	12.0661(3)	17.5029(6)
c, Å	30.8480(7)	22.2910(7)
α, °	90	90
β, °	98.383(2)	102.364(7)
γ, °	90	90
V, Å^3	7324.5(3)	8667.1(6)
ρ_{calcd}, gcm^{-3}	1.491	1.452
Z	4	4
T, K	90(2)	100(2)
μ, mm^{-1}	2.933	0.464
no. of reflns	74302	248624
no. of unique reflns	13390	19885
variables	981	1162
λ, Å	0.81063	0.4127
R_1 ($I > 2\sigma(I)$)	0.0787	0.0361
wR_2 ($I > 2\sigma(I)$)	0.2093	0.1041
GOF	1.054	1.031

Method for single-crystal X-ray analysis (Chapter 6).

Crystallographic data are summarized in Table E4. A single crystal of **16**$^{+}$-**35**$^{-}$ was obtained by vapor diffusion of *n*-hexane into a $CHCl_3$ solution. The data crystal was a dark green plate of approximate dimensions 0.05 mm × 0.02 mm × 0.01 mm. A single crystal of **22**$^{+}$-**35**$^{-}$ was obtained by vapor diffusion of benzene into a CH_2Cl_2 solution. The data crystal was a dark brown block of approximate dimensions 0.20 mm × 0.12 mm × 0.05 mm. A single crystal of **22**$^{+}$-**18**$^{-}$ was obtained by vapor diffusion of H_2O into an CH_3CN solution. The data crystal was a green prism of approximate dimensions 0.34 mm × 0.07 mm × 0.01 mm. A single crystal of **22**$^{+}$-**19**$^{-}$ was obtained by vapor diffusion of *n*-hexane into a CH_2Cl_2 solution. The data crystal was a red prism of approximate dimensions 0.12 mm × 0.04 mm × 0.01 mm. A single crystal of **35**$^{\bullet}$ was obtained by vapor diffusion of *n*-hexane into a CH_2Cl_2 solution. The data crystal was a dark brown prism of approximate dimensions 0.15 mm × 0.15 mm × 0.02 mm. The data of **16**$^{+}$-**35**$^{-}$ was collected at 100 K on a DECTRIS PILATUS3 CdTe 1M diffractometer with Si (311) monochromated synchrotron radiation (λ = 0.4132 Å) at BL02B1 (SPring-8),[127] and those of **22**$^{+}$-**35**$^{-}$, **22**$^{+}$-**19**$^{-}$, and **35**$^{\bullet}$ were collected at 90 K on a DECTRIS EIGER X 1M diffractometer with Si (111) monochromated synchrotron radiation (λ = 0.81106, 0.81078, and 0.81082 Å, respectively) at BL40XU (SPring-8),[67,68] whereas the data of **22**$^{+}$-**18**$^{-}$ was collected at 93 K on a Rigaku XtaLAB P200 diffractometer with graphite monochromatic CuKα radiation (λ = 1.54184 Å). All the structures were solved by dual-space method. The structures were refined by a full-matrix least-squares method by using a SHELXL 2014[136] (Yadokari-XG).[137,138] In each structure, the non-hydrogen atoms were refined anisotropically. CIF files (CCDC-2201074–2201078) can be obtained free of charge from the Cambridge Crystallographic Data Centre via www.ccdc.cam.ac.uk/data_request/cif.

Table E4 Summary of crystallographic data for Chapter 6.

	16^{+}**-35**$^{-}$	**22**$^{+}$**-35**$^{-}$	**22**$^{+}$**-18**$^{-}$	**22**$^{+}$**-19**$^{-}$	**35**$^{\bullet}$
formula	$C_{44}H_{28}AuN_4$· $C_{38}H_{23}N_4NiO$·2.1$CHCl_3$	$C_{38}H_9AuF_{15}N_4$· $C_{38}H_{23}N_4NiO$·4C_6H_6	$C_{38}H_9AuF_{15}N_4$· $C_{38}H_8F_{15}N_4NiO$· 2.7CH_3CN	$C_{38}H_9AuF_{15}N_4$· $C_{44}H_{12}F_{15}N_4NiO$	$C_{38}H_{23}N_4NiO$· 0.787CH_2Cl_2
fw	1670.86	1926.20	1994.55	1959.74	677.16
crystal size, mm	0.05 × 0.02 × 0.01	0.20 × 0.12 × 0.05	0.34 × 0.07 × 0.01	0.12 × 0.04 × 0.01	0.15 × 0.15 × 0.02
crystal system	monoclinic	monoclinic	tetragonal	triclinic	triclinic
space group	$P2_1/c$ (no. 14)	$P2_1/n$ (no. 14)	$I4_1/a$ (no. 88)	$P\bar{1}$ (no. 1)	$P\bar{1}$ (no. 2)
a, Å	9.8586(6)	13.6663(3)	31.55790(10)	7.8505(5)	10.0948(4)
b, Å	26.4691(16)	24.8072(4)	31.55790(10)	14.4756(9)	12.2142(5)
c, Å	26.8400(17)	23.3642(4)	27.93260(10)	15.5707(11)	13.8996(7)
α, °	90	90	90	90.252(2)	65.751(3)
β, °	99.581(7)	92.3350(10)	90	99.032(2)	79.994(4)
γ, °	90	90	90	97.615(2)	72.615(3)
V, Å^3	6906.2(7)	7914.4(3)	27818.1(2)	1731.5(2)	1488.66(12)
ρ_{calcd}, gcm^{-3}	1.607	1.617	1.905	1.879	1.511
Z	4	4	16	1	2
T, K	100(2)	90(2)	93(2)	90(2)	90(2)
μ, mm^{-1}	0.656	3.041	5.527	3.518	1.187
no. of reflns	202597	83909	187600	18527	15396
no. of unique reflns	15827	14468	13851	11182	5426
variables	935	1135	1154	1102	435
λ, Å	0.4132	0.81106	1.54184	0.81078	0.81082
R_1 ($I > 2\sigma(I)$)	0.0392	0.0400	0.0284	0.0507	0.0966
wR_2 ($I > 2\sigma(I)$)	0.0875	0.0873	0.0772	0.1007	0.2453
GOF	1.115	1.151	1.029	1.012	1.095

Method for single-crystal X-ray analysis (Chapter 7).

Crystallographic data are summarized in Table E5. A single crystal of **36**$^+$-Cl^- was obtained by vapor diffusion of *n*-hexane into a CH_2ClCH_2Cl solution. The data crystal was a red prism of approximate dimensions 0.140 mm × 0.054 mm × 0.050 mm. A single crystal of **36**$^+$-PF_6^- was obtained by vapor diffusion of *n*-hexane into a CH_2ClCH_2Cl solution. The data crystal was a red prism of approximate dimensions 0.22 mm × 0.15 mm × 0.10 mm. The data of **36**$^+$-Cl^- was collected at 100 K on a DECTRIS PILATUS3 CdTe 1M diffractometer with Si (311) monochromated synchrotron radiation (λ = 0.4127 Å) at BL02B1 (SPring-8),[127] whereas that of **36**$^+$-PF_6^- was collected at 90 K on a Bruker D8 Venture diffractometer with Mo-Kα radiation (λ = 0.71073 Å) focused by multilayer confocal mirror. All the structures were solved by dual-space method. The structures were refined by a full-matrix least-squares method by using a SHELXL 2014[136] (Yadokari-XG).[137,138] In each structure, the non-hydrogen atoms were refined anisotropically. The contribution to the scattering arising from the presence of disordered solvents in the crystal of **36**$^+$-Cl^- was removed by use of the utility SQUEEZE in the PLATON software package.[139,140] CIF files (CCDC-2226630–2226631) can be obtained free of charge from the Cambridge Crystallographic Data Centre via www.ccdc.cam.ac.uk/data_request/cif.

Table E5 Summary of crystallographic data for Chapter 7.

	36$^+$-Cl^-	**36**$^+$-PF_6^-
formula	$C_{38}H_{28}AuN_4 \cdot Cl \cdot C_2H_4Cl_2$	$C_{38}H_{24}AuN_4 \cdot F_6P \cdot 2C_2H_4Cl_2$
fw	867.98	1076.45
crystal size, mm	0.140 × 0.054 × 0.050	0.22 × 0.15 × 0.10
crystal system	triclinic	triclinic
space group	*P*-1 (no. 2)	*P*-1 (no. 2)
a, Å	9.226(5)	11.0492(8)
b, Å	13.732(7)	12.6993(11)
c, Å	14.409(15)	14.8836(12)
α, °	66.996(19)	95.369(3)
β, °	76.46(2)	107.589(3)
γ, °	81.05(2)	97.545(3)
V, Å^3	1629(2)	1953.8(3)
ρ_{calcd}, gcm^{-3}	1.769	1.830
Z	2	2
T, K	100(2)	90(2)
μ, mm^{-1}	1.173	4.147
no. of reflns	47965	38434
no. of unique reflns	7444	8642
variables	407	538
λ, Å	0.4127	0.71073
R_1 ($I > 2\sigma(I)$)	0.0206	0.0282
wR_2 ($I > 2\sigma(I)$)	0.0544	0.0763
GOF	1.091	1.071

Method for DFT calculations.

DFT calculations were carried out using the *Gaussian 09* and *Gaussian 16* programs. EDA calculations were carried out by using *GAMESS* program.[108,109,141]

Method for steady-state absorption measurements of single crystals.

An inverted optical microscope (IX71, Olympus) was used for steady-state absorption measurements of single crystals. The halogen lamp placed above the sample stage was employed as the incident light, and focused on the sample microcrystal with the objective lens (×40, NA 0.40). The transmitted light was collected with the objective lens (×60, NA 0.70), and then passed through a confocal pinhole (1 μm in diameter) to select the monitoring position which was the same in the femtosecond pump-probe measurement. The intensity was detected with another CCD camera (DU970P, Andor) coupled with another polychrometer (250is, Chromex). The absorption spectra were calculated by using reference light which was transmitted through only coverslip.

Method for femtosecond transient absorption measurements of single crystals.

Femtosecond transient absorption measurements of crystals were carried out using 100-fs pulses (800 nm) from a Ti:Sapphire chirped pulse amplified system (Tsunami and Spitfire-ACE, Spectra-Physics) operating at 1 kHz repetition rate under the microscope.[142,143] The output beam of the amplified system was divided into two using a beam splitter (80% – 20%). The stronger beam was guided into optical parametric oscillator and amplifier (OPA-800, Spectra-Physics), where the excitation wavelength was tuned to 650 nm and the pulse duration was ca. 150 fs in fwhm. These excitation pulses were chopped at a 500 Hz repetition rate with an optical chopper (S2000, Thorlabs) and were circularly polarized by Berek compensator (Newport). After passing through the concave and convex lenses to change the beam diameter at sample position, the excitation pulses were guided into an inverted optical microscope (IX71, Olympus), and focused at the sample with an objective lens (×60, NA 0.70). The excitation intensity was set to be ca. 0.1 mJ/cm^2 with a neutral density filter to avoid the photodecomposition. A small portion of the weaker fundamental beam was focused into a CaF_2 window (3-mm thickness) to generate the white-light continuum in the wavelength range of 380 to 860 nm, which was used as probe light. The probe pulses were guided into the microscope co-linearly with the pump pulses, and focused into the sample with the same ×60 objective lens. The transmitted light of the probe was collected with an objective lens (×40, NA 0.40), and then the intensity was detected with a CCD camera (BU-54DUV, Bitran) coupled with a polychrometer (250is, Chromex). The time delay between pump and probe pulses was

carefully varied from –10 ps to 600 ps by a computer controlled translation stage (STM-150, SIGMA Koki). The temporal cross correlation of the pump and probe pulses at the sample position was 350 fs in fwhm. The chirping of the monitoring white light continuum was corrected for transient absorption spectra. The diameter of the pump beams was about 1.2 mm in fwhm at the focusing point, which was larger than that of the probe. The smooth and flat area of single microcrystal was selected.

Electrochemical analysis.

CVs were measured under Ar atmosphere in solutions containing the sample and $TBAPF_6$ (0.1 M) as a supporting electrolyte using an ALS/CH Instruments 619E electrochemical analyzer with a glassy-carbon disk working electrode (3-mm diameter), an $Ag/AgNO_3$ (0.010 M) reference electrode, and a Pt counter electrode. Spectroelectrochemical analyses were conducted using an ALS/CH Instruments 720 electrochemical analyzer and a JASCO V-670 spectrometer with a thin layer quartz glass cell (path length: 1.0 mm), a Pt mesh working electrode, an $Ag/AgNO_3$ (0.010 M) reference electrode, and a Pt counter electrode.

ESR measurements and simulations.

ESR measurements were performed by a JEOL JES-FA200 spectrometer equipped with an OXFROD ESR900 cryostat. The measurements temperature was controlled by OXFORD mercuryITC temperature controller in the temperature range from 4 K to 140 K. The ESR spectral simulation was performed with the MATLAB subroutine package EasySpin.[124]

Method for transient absorption measurements.

Transient absorption measurements on the sub-picosecond to nanosecond timescale were conducted by a home-made pump-probe system. An amplified femtosecond laser, Spirit One 1040-8 (Spectra-Physics, 1040 nm, the pulse width: ~270 fs), was split into two beams with a ratio of 1:9. The stronger beam was directed to a noncollinear optical parametric amplifier (NOPA), Spirit-NOPA-3H (Spectra-Physics) to generate the 680-nm femtosecond laser pulse for the pump beam. The pump beam was chopped prior to the sample at 500 Hz for signal differencing. The other weaker beam was focused on deuterated water placed in a 10-mm quartz cuvette to generate the white light continuum for the probe beam. Both pump and probe beams were focused on the sample solution placed in the 2-mm quartz cuvette. The polarization between the pump and probe pulses was set at the magic angle. The intensity of the pump pulse was set to 60 and 80 nJ/pulse. The transmitted probe beam was detected with multichannel detection system, PK120-C-RK (UNISOKU), composed of a CMOS

linear image sensor and a polychromator. The instrumental response function was shorter than approximately 100 fs. The sample solution was stirred with a stirrer during the experiments. All the measurements were performed at r.t. The obtained transient absorption spectra were globally analyzed using the four-state sequential decay kinetic models convolved with a Gaussian pulse using the Glotaran program.[114]

References

(1) *Supramolecular Chemistry: From Molecules to Nanomaterials*; Gale, P. A.; Steed, J. W., Eds.; Wiley, 2012.

(2) Meyer, E. A.; Castellano, R. K.; Diederich, F. *Angew. Chem. Int. Ed.* **2003**, *42*, 1210.

(3) Riley, K. E.; Hobza, P. *Acc. Chem. Res.* **2013**, *46*, 927.

(4) Stone, A. J. *The Theory of Intermolecular Forces*; Oxford University Press, 2013.

(5) Magnus, G. *Ann. Phys.* **1828**, *90*, 239.

(6) Magnus, G. *Ann. Chim. Phys.* **1829**, *40*, 110.

(7) Atoji, M.; Richardson, J. W.; Rundle, R. E. *J. Am. Chem. Soc.* **1957**, *79*, 3017.

(8) Hunter, C. A.; Lawson, K. R.; Perkins, J.; Urch, C. J. *J. Chem. Soc., Perkin Trans. 2* **2001**, 651.

(9) Martinez, C. R.; Iverson, B. L. *Chem. Sci.* **2012**, *3*, 2191.

(10) Chen, T.; Li, M.; Liu, J. *Cryst. Growth Des.* **2018**, *18*, 2765.

(11) Thakuria, R.; Nath, N. K.; Saha, B. K. *Cryst. Growth Des.* **2019**, *19*, 523.

(12) Grimme, S. *Angew. Chem. Int. Ed.* **2008**, *47*, 3430.

(13) Wheeler, S. E. *Acc. Chem. Res.* **2013**, *46*, 1029.

(14) *Supramolecular Materials for Opto-Electronics*; Koch, N., Ed.; RSC, 2014.

(15) Wu, D.; Zhi, L.; Bodwell, G. J.; Cui, G.; Tsao, N.; Müllen, K. *Angew. Chem. Int. Ed.* **2007**, *46*, 5417.

(16) Wu, D.; Feng, X.; Takase, M.; Haberecht, M. C.; Müllen, K. *Tetrahedron* **2008**, *64*, 11379.

(17) Wu, D.; Pisula, W.; Haberecht, M. C.; Feng, X.; Müllen, K. *Org. Lett.* **2009**, *11*, 5686.

(18) Wu, D.; Pisula, W.; Enkelmann, V.; Feng, X.; Müllen, K. *J. Am. Chem. Soc.* **2009**, *131*, 9620.

(19) Wu, D.; Liu, R.; Pisula, W.; Feng, X.; Müllen, K. *Angew. Chem. Int. Ed.* **2011**, *50*, 2791.

(20) Laursen, B. W.; Krebs, F. C. *Angew. Chem. Int. Ed.* **2000**, *39*, 3432.

(21) Laursen, B. W.; Krebs, F. C. *Chem. Eur. J.* **2001**, *7*, 1773.

(22) Shi, D.; Schwall, C.; Sfintes, G.; Thyrhaug, E.; Hammershøj, P.; Cárdenas, M.; Simonsen, J. B.; Laursen, B. W. *Chem. Eur. J* **2014**, *20*, 6853.

(23) Maeda, H.; Kusunose, Y. *Chem. Eur. J.* **2005**, *11*, 5661.

(24) Haketa, Y.; Sasaki, S.; Ohta, N.; Masunaga, H.; Ogawa, H.; Mizuno, N.; Araoka, F.; Takezoe, H.; Maeda, H. *Angew. Chem. Int. Ed.* **2010**, *49*, 10079.

(25) Haketa, Y.; Honsho, Y.; Seki, S.; Maeda, H. *Chem. Eur. J.* **2012**, *18*, 7016.

(26) Webster, O. W. *J. Am. Chem. Soc.* **1965**, *87*, 1820.

(27) Sakai, T.; Seo, S.; Matsuoka, J.; Mori, Y. *J. Org. Chem.* **2013**, *78*, 10978.

(28) Bando, Y.; Haketa, Y.; Sakurai, T.; Matsuda, W.; Seki, S.; Takaya, H.; Maeda, H. *Chem. Eur. J.* **2016**, *22*, 7843.

(29) *The Porphyrin Handbook*; Kadish, K. M.; Smith, K. M.; Guilard, R., Eds.; Academic Press, 1999.

(30) *Handbook of Porphyrin Science*; Kadish, K. M.; Smith, K. M.; Guilard, R., Eds.; World Scientific, 2010.

(31) Fang, M.; Wilson, S. R.; Suslick, K. S. *J. Am. Chem. Soc.* **2008**, *130*, 1134.

(32) Inokuma, Y.; Kwon, J. H.; Ahn, T. K.; Yoo, M.-C.; Kim, D.; Osuka, A. *Angew. Chem. Int. Ed.* **2006**, *45*, 961.

(33) Tsurumaki, E.; Hayashi, S.-Y.; Tham, F. S.; Reed, C. A.; Osuka, A. *J. Am. Chem. Soc.* **2011**, *133*, 11956.

(34) Fleischer, E. B.; Laszlo, A. *Inorg. Nucl. Chem. Lett.* **1969**, *5*, 373.

(35) Brun, A. M.; Harriman, A.; Heitz, V.; Sauvage, J. P. *J. Am. Chem. Soc.* **1991**, *113*, 8657.

(36) Fukuzumi, S.; Ohkubo, K.; Wenbo, E.; Ou, Z.; Shao, J.; Kadish, K. M.; Hutchison, J. A.; Ghiggino, K. P.; Sintic, P. J.; Crossley, M. J. *J. Am. Chem. Soc.* **2003**, *125*, 14984.

(37) Fortage, J.; Boixel, J.; Blart, E.; Hammarström, L.; Becker, H. C.; Odobel, F. *Chem. Eur. J.* **2008**, *14*, 3467.

(38) Che, C.-M.; Sun, R. W.-Y.; Yu, W.-Y.; Ko, C.-B.; Zhu, N.; Sun, H. *Chem. Commun.* **2003**, 1718.

(39) Haketa, Y.; Bando, Y.; Sasano, Y.; Tanaka, H.; Yasuda, N.; Hisaki, I.; Maeda, H. *iScience* **2019**, *14*, 241.

(40) Maeda, H.; Fukui, A.; Yamakado, R.; Yasuda, N. *Chem. Commun.* **2015**, *51*, 17572.

(41) Maeda, H.; Takeda, Y.; Haketa, Y.; Morimoto, Y.; Yasuda, N. *Chem. Eur. J.* **2018**, *24*, 8910.

(42) Fumoto, N.; Haketa, Y.; Tanaka, H.; Yasuda, N.; Maeda, H. *Org. Lett.* **2021**, *23*, 3897.

(43) Balch, A. L. *Coord. Chem. Rev.* **2000**, *200–202*, 349.

(44) Falk, H. *The Chemistry of Linear Oligopyrroles and Bile Pigments*; Springer, 1989.

(45) Jackson, A. H.; Kenner, G. W.; Smith, K. M. *J. Am. Chem. Soc.* **1966**, *88*, 4539.

(46) Bonnett, R.; Dimsdale, M. J.; Sales, K. D. *J. Chem. Soc. D* **1970**, 962.

(47) Fuhrhop, J.-H.; Besecke, S.; Subramanian, J. *J. Chem. Soc., Chem. Commun.* **1973**, *160*, 1.

(48) Balch, A. L.; Noll, B. C.; Phillips, S. L.; Reid, S. M.; Zovinka, E. P. *Inorg. Chem.* **1993**, *32*, 4730.

(49) Esdaile, L. J.; Senge, M. O.; Arnold, D. P. *Chem. Commun.* **2006**, *2*, 4192.

(50) Shimizu, D.; Oh, J.; Furukawa, K.; Kim, D.; Osuka, A. *J. Am. Chem. Soc.* **2015**, *137*, 15584.

(51) Esdaile, L. J.; Rintoul, L.; Goh, M. S.; Merahi, K.; Parizel, N.; Wellard, R. M.; Choua, S.; Arnold, D. P. *Chem. Eur. J.* **2016**, *22*, 3430.

(52) Stähler, C.; Shimizu, D.; Yoshida, K.; Furukawa, K.; Herges, R.; Osuka, A. *Chem. Eur. J.* **2017**, *23*, 7217.

(53) Jun-i, Y.; Fukui, N.; Furukawa, K.; Osuka, A. *Chem. Eur. J.* **2018**, *24*, 1528.

(54) Sasano, Y.; Yasuda, N.; Maeda, H. *Dalton Trans.* **2017**, *46*, 8924.

(55) Sasano, Y.; Haketa, Y.; Tanaka, H.; Yasuda, N.; Hisaki, I.; Maeda, H. *Chem. Eur. J.* **2019**, *25*, 6712.

(56) Tanaka, H.; Haketa, Y.; Yasuda, N.; Maeda, H. *Chem. Asian J.* **2019**, *14*, 2129.

(57) Tanaka, H.; Haketa, Y.; Bando, Y.; Yamakado, R.; Yasuda, N.; Maeda, H. *Chem. Asian J.* **2020**, *15*, 494.

(58) Tanaka, H.; Haketa, Y.; Maeda, H. *J. Porphyrin Phthalocyanines* **2023**, in press.

(59) Sasano, Y.; Tanaka, H.; Haketa, Y.; Kobayashi, Y.; Ishibashi, Y.; Morimoto, T.; Sato, R.; Shigeta, Y.; Yasuda, N.; Asahi, T.; Maeda, H. *Chem. Sci.* **2021**, *12*, 9645.

(60) Tanaka, H.; Kobayashi, Y.; Furukawa, K.; Okayasu, Y.; Akine, S.; Yasuda, N.; Maeda, H. *J. Am. Chem. Soc.* **2022**, *144*, 21710.

(61) Tanaka, H.; Okayasu, Y.; Kobayashi, Y.; Maeda, H. *Chem. Eur. J.* **2023**, *29*, in press.

(62) Lahaye, D.; Muthukumaran, K.; Hung, C.-H.; Gryko, D.; Rebouças, J. S.; Spasojević, I.; Batinić-Haberle, I.;

Lindsey, J. S. *Bioorg. Med. Chem.* **2007**, *15*, 7066.

(63) Frost, J. R.; Huber, S. M.; Breitenlechner, S.; Bannwarth, C.; Bach, T. *Angew. Chem. Int. Ed.* **2014**, *54*, 691.

(64) Lindsey, J. S.; Wagner, R. W. *J. Org. Chem.* **1989**, *54*, 828.

(65) Lv, H.; Yang, B.; Jing, J.; Yu, Y.; Zhang, J.; Zhang, J. L. *Dalton Trans.* **2012**, *41*, 3116.

(66) Frisch, M. J.; Trucks, G. W.; Schlegel, H. B.; Scuseria, G. E.; Robb, M. A.; Cheeseman, J. R.; Scalmani, G.; Barone, V.; Men-nucci, B.; Petersson, G. A.; Nakatsuji, H.; Caricato, M.; Li, X.; Hratchian, H. P.; Izmaylov, A. F.; Bloino, J.; Zheng, G.; Sonnen-berg, J. L.; Hada, M.; Ehara, M.; Toyo-ta, K.; Fukuda, R.; Hasegawa, J.; Ishida, M.; Nakajima, T.; Honda, Y.; Kitao, O.; Nakai, H.; Vreven, T.; Montgomery, J. A., Jr; Peralta, J. E.; Ogliaro, F.; Bearpark, M.; Heyd, J. J.; Brothers, E.; Kudin, K. N.; Staroverov, V. N.; Keith, T.; Kobayashi, R.; Normand, J.; Raghavachari, K.; Rendell, A.; Burant, J. C.; Iyengar, S. S.; Tomasi, J.; Cossi, M.; Rega, N.; Millam, J. M.; Klene, M.; Knox, J. E.; Cross, J. B.; Bakken, V.; Adamo, C.; Jaramillo, J.; Gomperts, R.; Stratmann, R. E.; Yazyev, O.; Austin, A. J.; Cammi, R.; Pomelli, C.; Ochterski, J. W.; Martin, R. L.; Morokuma, K.; Zakrzewski, V. G.; Voth, G. A.; Salvador, P.; Dannenberg, J. J.; Dap-prich, S.; Daniels, A. D.; Far-kas, Ö.; Foresman, J. B.; Ortiz, J. V.; Cioslowski, J.; Fox, D. J. *Gaussian 09 (Revision D.01)*; Gaussian, Inc.: Wallingford CT, 2013.

(67) Yasuda, N.; Murayama, H.; Fukuyama, Y.; Kim, J.; Kimura, S.; Toriumi, K.; Tanaka, Y.; Moritomo, Y.; Kuroiwa, Y.; Kato, K.; Tanaka, H.; Takata, M. *J. Synchrotron Radiat.* **2009**, *16*, 352.

(68) Yasuda, N.; Fukuyama, Y.; Toriumi, K.; Kimura, S.; Takata, M.; Garrett, R.; Gentle, I.; Nugent, K.; Wilkins, S. *AIP Conf. Proc.* **2010**, *1234*, 147.

(69) Kawahara, S.-I.; Tsuzuki, S.; Uchimaru, T. *J. Phys. Chem. A* **2004**, *108*, 6744.

(70) Xu, X.; Pooi, B.; Hirao, H.; Hong, S. H. *Angew. Chem. Int. Ed.* **2014**, *53*, 1283.

(71) Li, P.; Maier, J. M.; Vik, E. C.; Yehl, C. J.; Dial, B. E.; Rickher, A. E.; Smith, M. D.; Pellechia, P. J.; Shimizu, K. D. *Angew. Chem. Int. Ed.* **2017**, *56*, 7209.

(72) Maeda, H.; Haketa, Y.; Bando, Y.; Sakamoto, S. *Synth. Met.* **2009**, *159*, 792.

(73) Maeda, H.; Ito, Y. *Inorg. Chem.* **2006**, *45*, 8205.

(74) Yamakado, R.; Sakurai, T.; Matsuda, W.; Seki, S.; Yasuda, N.; Akine, S.; Maeda, H. *Chem. Eur. J.* **2016**, *22*, 626.

(75) Dong, B.; Sakurai, T.; Honsho, Y.; Seki, S.; Maeda, H. *J. Am. Chem. Soc.* **2013**, *135*, 1284.

(76) Dong, B.; Sakurai, T.; Bando, Y.; Seki, S.; Takaishi, K.; Uchiyama, M.; Muranaka, A.; Maeda, H. *J. Am. Chem. Soc.* **2013**, *135*, 14797.

(77) Haketa, Y.; Takayama, M.; Maeda, H. *Org. Biomol. Chem.* **2012**, *10*, 2603.

(78) Spackman, P. R.; Turner, M. J.; McKinnon, J. J.; Wolff, S. K.; Grimwood, D. J.; Jayatilaka, D.; Spackman, M. A. *J. Appl. Crystallogr.* **2021**, *54*, 1006.

(79) McKinnon, J. J.; Spackman, M. A.; Mitchell, A. S. *Acta Crystallogr. B* **2004**, *60*, 627.

(80) Spackman, M. A.; Jayatilaka, D. *CrystEngComm* **2009**, *11*, 19.

(81) Tan, S. L.; Jotani, M. M.; Tiekink, E. R. T. *Acta Crystallogr. E* **2019**, *75*, 308.

(82) Haketa, Y.; Maeda, H. *Bull. Chem. Soc. Jpn.* **2018**, *91*, 420.

(83) Haketa, Y.; Urakawa, K.; Maeda, H. *Mol. Syst. Des. Eng.* **2020**, *5*, 757.

(84) Yamasumi, K.; Maeda, H. *Bull. Chem. Soc. Jpn.* **2021**, *94*, 2252.

(85) John, E. A.; Massena, C. J.; Berryman, O. B. *Chem. Rev.* **2020**, *120*, 2759.

(86) Sánchez-Quesada, J.; Seel, C.; Prados, P.; de Mendoza, J.; Dalcol, I.; Giralt, E. *J. Am. Chem. Soc.* **1996**, *118*, 277.

(87) Coles, S. J.; Frey, J. G.; Gale, P. A.; Hursthouse, M. B.; Light, M. E.; Navakhun, K.; Thomas, G. L. *Chem. Commun.* **2003**, 568.

(88) Juwarker, H.; Lenhardt, J. M.; Pham, D. M.; Craig, S. L. *Angew. Chem. Int. Ed.* **2008**, *47*, 3740.

(89) Li, S.; Jia, C.; Wu, B.; Luo, Q.; Huang, X.; Yang, Z.; Li, Q.-S.; Yang, X.-J. *Angew. Chem. Int. Ed.* **2011**, *50*, 5721.

(90) Suk, J.-M.; Naidu, V. R.; Liu, X.; Lah, M. S.; Jeong, K.-S. *J. Am. Chem. Soc.* **2011**, *133*, 13938.

(91) Wang, Y.; Xiang, J.; Jiang, H. *Chem. Eur. J.* **2011**, *17*, 613.

(92) Selvakumar, P. M.; Yowan Jebaraj, P.; Sahoo, J.; Suresh, E.; Jeya Prathap, K.; Kureshy, R. I.; Subramanian, P. S. *RSC Adv.* **2012**, *2*, 7689.

(93) Hua, Y.; Liu, Y.; Chen, C.-H.; Flood, A. H. *J. Am. Chem. Soc.* **2013**, *135*, 14401.

(94) Massena, C. J.; Wageling, N. B.; Decato, D. A.; Martin Rodriguez, E.; Rose, A. M.; Berryman, O. B. *Angew. Chem. Int. Ed.* **2016**, *55*, 12398.

(95) Liu, Y.; Parks, F. C.; Zhao, W.; Flood, A. H. *J. Am. Chem. Soc.* **2018**, *140*, 15477.

(96) Parks, F. C.; Liu, Y.; Debnath, S.; Stutsman, S. R.; Raghavachari, K.; Flood, A. H. *J. Am. Chem. Soc.* **2018**, *140*, 17711.

(97) Maeda, H.; Haketa, Y. *Org. Biomol. Chem.* **2008**, *6*, 3091.

(98) Haketa, Y.; Maeda, H. *Chem. Eur. J.* **2011**, *17*, 1485.

(99) Haketa, Y.; Bando, Y.; Takaishi, K.; Uchiyama, M.; Muranaka, A.; Naito, M.; Shibaguchi, H.; Kawai, T.; Maeda, H. *Angew. Chem. Int. Ed.* **2012**, *51*, 7967.

(100) Kinoshita, T.; Haketa, Y.; Maeda, H.; Fukuhara, G. *Chem. Sci.* **2021**, *12*, 6691.

(101) Haketa, Y.; Naganawa, A.; Sugiura, S.; Yasuda, N.; Maeda, H. *Eur. J. Org. Chem.* **2020**, 3491.

(102) Frisch, M. J.; Trucks, G. W.; Schlegel, H. B.; Scuseria, G. E.; Robb, M. A.; Cheeseman, J. R.; Scalmani, G.; Barone, V.; Petersson, G. A.; Nakatsuji, H.; Li, X.; Caricato, M.; Marenich, A. V.; Bloino, J.; Janesko, B. G.; Gomperts, R.; Mennucci, B.; Hratchian, H. P.; Ortiz, J. V.; Izmaylov, A. F.; Sonnenberg, J. L.; Williams-Young, D.; Ding, F.; Lipparini, F.; Egidi, F.; Goings, J.; Peng, B.; Petrone, A.; Henderson, T.; Ranasinghe, D.; Zakrzewski, V. G.; Gao, J.; Rega, N.; Zheng, G.; Liang, W.; Hada, M.; Ehara, M.; Toyota, K.; Fukuda, R.; Hasegawa, J.; Ishida, M.; Nakajima, T.; Honda, Y.; Kitao, O.; Nakai, H.; Vreven, T.; Throssell, K.; Montgomery, J. A., Jr; Peralta, J. E.; Ogliaro, F.; Bearpark, M. J.; Heyd, J. J.; Brothers, E. N.; Kudin, K. N.;

Staroverov, V. N.; Keith, T. A.; Kobayashi, R.; Normand, J.; Raghavachari, K.; Rendell, A. P.; Burant, J. C.; Iyengar, S. S.; Tomasi, J.; Cossi, M.; Millam, J. M.; Klene, M.; Adamo, C.; Cammi, R.; Ochterski, J. W.; Martin, R. L.; Morokuma, K.; Farkas, O.; Foresman, J. B.; Fox, D. J. *Gaussian 16 (Revision C.01)*; Gaussian, Inc.: Wallingford CT, 2016.

(103) Phipps, M. J. S.; Fox, T.; Tautermann, C. S.; Skylaris, C.-K. *Chem. Soc. Rev.* **2015**, *44*, 3177.

(104) Kitaura, K.; Ikeo, E.; Asada, T.; Nakano, T.; Uebayasi, M. *Chem. Phys. Lett.* **1999**, *313*, 701.

(105) Fedorov, D. G.; Kitaura, K. *J. Comput. Chem.* **2007**, *28*, 222.

(106) Desiraju, G. R. *J. Am. Chem. Soc.* **2013**, *135*, 9952.

(107) Yu, P.; Zhen, Y.; Dong, H.; Hu, W. *Chem* **2019**, *5*, 2814.

(108) Schmidt, M. W.; Baldridge, K. K.; Boatz, J. A.; Elbert, S. T.; Gordon, M. S.; Jensen, J. H.; Koseki, S.; Matsunaga, N.; Nguyen, K. A.; Su, S.; Windus, T. L.; Dupuis, M.; Montgomery, J. A. *J. Comput. Chem.* **1993**, *14*, 1347.

(109) Gordon, M. S.; Schmidt, M. W. In *Theory and Applications of Computational Chemistry*; Dykstra, C. E.; Frenking, G.; Kim, K. S.; Scuseria, G. E., Eds.; Elsevier, 2005; pp. 1167–1189.

(110) Sasano, Y. Ion-Pairing Assemblies Based on Non-Complexing π-Electronic Anions. Ph.D. Dissertation, Ritsumeikan University, 2019.

(111) Kasha, M.; Rawls, H. R.; El-Bayoumi, M. A. *Pure Appl. Chem.* **1965**, *11*, 371.

(112) Takahashi, Y.; Sankararaman, S.; Kochi, J. K. *J. Am. Chem. Soc.* **1989**, *111*, 2954.

(113) Gueret, R.; Poulard, L.; Oshinowo, M.; Chauvin, J.; Dahmane, M.; Dupeyre, G.; Lainé, P. P.; Fortage, J.; Collomb, M. N. *ACS Catal.* **2018**, *8*, 3792.

(114) Snellenburg, J. J.; Laptenok, S. P.; Seger, R.; Mullen, K. M.; van Stokkum, I. H. M. *J. Stat. Softw.* **2012**, *49*, 1.

(115) Marcus, Y.; Hefter, G. *Chem. Rev.* **2006**, *106*, 4585.

(116) Billing, R.; Rehorek, D.; Hennig, H. In *Photoinduced Electron Transfer II, Topics in Current Chemistry*; Mattay, J., Ed.; Springer, 1990; Vol. 22, pp. 151–199.

(117) Kochi, J. K.; Michael Bockman, T. In *Advances in Organometallic Chemistry*; Stone, F. G. A.; West, R., Eds.; Academic Press, 1991; Vol. 33, pp. 51–124.

(118) Arnett, E. M.; Troughton, E. B.; McPhail, A. T.; Molter, K. E. *J. Am. Chem. Soc.* **1983**, *105*, 6172.

(119) Arnett, E. M.; Molter, K. E.; Marchot, E. C.; Donovan, W. H.; Smith, P. *J. Am. Chem. Soc.* **1987**, *109*, 3788.

(120) Arnett, E. M.; Amarnath, K.; Harvey, N. G.; Cheng, J.-P. *J. Am. Chem. Soc.* **1990**, *112*, 344.

(121) Komatsu, K.; Kitagawa, T. *Chem. Rev.* **2003**, *103*, 1371.

(122) Preiß, S.; Förster, C.; Otto, S.; Bauer, M.; Müller, P.; Hinderberger, D.; Hashemi Haeri, H.; Carella, L.; Heinze, K. *Nat. Chem.* **2017**, *9*, 1249.

(123) Weller, A. *Z. Phys. Chem.* **1982**, *133*, 93.

(124) Stoll, S.; Schweiger, A. *J. Magn. Reson.* **2006**, *178*, 42.

(125) Senge, M. O.; Feng, X. *J. Chem. Soc., Perkin Trans. 1* **2000**, 3615.

(126) Chambron, J. C.; Heitz, V.; Sauvage, J. P. *New J. Chem.* **1997**, *21*, 237.

(127) Sugimoto, K.; Ohsumi, H.; Aoyagi, S.; Nishibori, E.; Moriyoshi, C.; Kuroiwa, Y.; Sawa, H.; Takata, M. *AIP Conf. Proc.* **2010**, *1234*, 887.

(128) Pearson, R. G. *J. Am. Chem. Soc.* **1963**, *85*, 3533.

(129) Takiguchi, A.; Tanaka, H.; Maeda, H.; Shinokubo, H. *Bull. Chem. Soc. Jpn.* **2022**, *95*, 796.

(130) Fujita, M.; Haketa, Y.; Tanaka, H.; Yasuda, N.; Maeda, H. *Chem. Commun.* **2022**, *58*, 9870.

(131) Gotoh, H.; Nakatsuka, S.; Tanaka, H.; Yasuda, N.; Haketa, Y.; Maeda, H.; Hatakeyama, T. *Angew. Chem. Int. Ed.* **2021**, *60*, 12835.

(132) Maeda, H.; Nishimura, T.; Haketa, Y.; Tanaka, H.; Fujita, M.; Yasuda, N. *J. Org. Chem.* **2022**, *87*, 7818.

(133) Kuno, A.; Hirata, G.; Tanaka, H.; Kobayashi, Y.; Yasuda, N.; Maeda, H. *Chem. Eur. J.* **2021**, *27*, 10068.

(134) Rosenau, C. P.; Jelier, B. J.; Gossert, A. D.; Togni, A. *Angew. Chem. Int. Ed.* **2018**, *57*, 9528.

(135) Uson, R.; Laguna, A.; Laguna, M.; Briggs, D. A.; Murray, H. H.; Fackler, J. P., Jr In *Inorganic Syntheses*; Kaesz, H. D., Ed.; Wiley, 1989; Vol. 26, pp. 85–91.

(136) Sheldrick, G. M. *Acta Crystallogr. A* **2008**, *64*, 112.

(137) *Yadokari-XG, Software for Crystal Structure Analyses*; Wakita, K. 2001.

(138) Kabuto, C.; Akine, S.; Nemoto, T.; Kwon, E. *J. Cryst. Soc. Jpn.* **2009**, *51*, 218.

(139) Spek, A. L. *PLATON, A Multipurpose Crystallographic Tool*; Utrecht University: Utrecht, The Netherlands, 2005.

(140) van der Sluis, P.; Spek, A. L. *Acta Crystallogr. A* **1990**, *46*, 194.

(141) Barca, G. M. J.; Bertoni, C.; Carrington, L.; Datta, D.; De Silva, N.; Deustua, J. E.; Fedorov, D. G.; Gour, J. R.; Gunina, A. O.; Guidez, E.; Harville, T.; Irle, S.; Ivanic, J.; Kowalski, K.; Leang, S. S.; Li, H.; Li, W.; Lutz, J. J.; Magoulas, I.; Mato, J.; Mironov, V.; Nakata, H.; Pham, B. Q.; Piecuch, P.; Poole, D.; Pruitt, S. R.; Rendell, A. P.; Roskop, L. B.; Ruedenberg, K.; Sattasathuchana, T.; Schmidt, M. W.; Shen, J.; Slipchenko, L.; Sosonkina, M.; Sundriyal, V.; Tiwari, A.; Galvez Vallejo, J. L.; Westheimer, B.; Włoch, M.; Xu, P.; Zahariev, F.; Gordon, M. S. *J. Chem. Phys.* **2020**, *152*, 154102.

(142) Ishibashi, Y.; Inoue, Y.; Asahi, T. *Photochem. Photobiol. Sci.* **2016**, *15*, 1304.

(143) Ishibashi, Y.; Murakami, M.; Araki, K.; Mutai, T.; Asahi, T. *J. Phys. Chem. C* **2019**, *123*, 11224.

List of Publications

(1) Tanaka, H.; Haketa, Y.; Yasuda, N.; Maeda, H. "Substitution-Pattern- and Counteranion-Depending Ion-Pairing Assemblies Based on Electron-Deficient Porphyrin–Au^{III} Complexes" *Chem. Asian J.* **2019**, *14*, 2129.
(Chapter 2 includes the contents of this report and is reproduced with permission from Wiley)

(2) Tanaka, H.; Haketa, Y.; Bando, Y.; Yamakado, R.; Yasuda, N.; Maeda, H. "Ion-Pairing Assemblies of Porphyrin–Au^{III} Complexes in Combination with π-Electronic Receptor–Anion Complexes" *Chem. Asian J.* **2020**, *15*, 494.
(Chapter 3 includes the contents of this report and is reproduced with permission from Wiley)

(3) Sasano, Y.; Tanaka, H.; Haketa, Y.; Kobayashi, Y.; Ishibashi, Y.; Morimoto, T.; Sato, R.; Shigeta, Y.; Yasuda, N.; Asahi, T.; Maeda, H. "Ion-pairing π-electronic systems: ordered arrangement and noncovalent interactions of negatively charged porphyrins" *Chem. Sci.* **2021**, *12*, 9645.
(Chapter 5 includes the contents of this report and is reproduced with permission from the Royal Society of Chemistry)

(4) Tanaka, H.; Kobayashi, Y.; Furukawa, K.; Okayasu, Y.; Akine, S.; Yasuda, N.; Maeda, H. "π-Stacked Ion Pairs: Tightly Associated Charged Porphyrins in Ordered Arrangement Enabling Radical-Pair Formation" *J. Am. Chem. Soc.* **2022**, *144*, 21710.
(Chapter 6 includes the contents of this report and is reproduced with permission from the American Chemical Society)

(5) Tanaka, H.; Haketa, Y.; Maeda, H. "Ion-pairing assemblies comprising porphyrin–Au^{III} complexes and helical π-system–anion complexes" *J. Porphyrins Phthalocyanines* **2023**, *27*, in press (DOI: 10.1142/S1088424622500973).
(Chapter 4 includes the contents of this report and is reproduced with permission from the World Scientific)

(6) Tanaka, H.; Okayasu, Y.; Kobayashi, Y.; Maeda, H. "Substituent-Dependent Photoexcitation Processes of π-Stacked Ion Pairs" *Chem. Eur. J.* **2023**, *29*, in press (DOI: 10.1002/chem.202203957).
(Chapter 7 includes the contents of this report and is reproduced with permission from Wiley)

The contents of the following reports are not included in this dissertation.

(7) Haketa, Y.; Bando, Y.; Sasano, Y.; Tanaka, H.; Yasuda, N.; Hisaki, I.; Maeda, H. "Liquid Crystals Comprising π-Electronic Ions from Porphyrin–Au^{III} Complexes" *iScience* **2019**, *14*, 241.

(8) Sasano, Y.; Haketa, Y.; Tanaka, H.; Yasuda, N.; Hisaki, I.; Maeda, H. "Peripheral Modifications of *meso*-Hydroxyporphyrins: Formation of π-Electronic Anions and Ion-Pairing Assemblies" *Chem. Eur. J.* **2019**, *25*, 6712.

(9) Gotoh, H.; Nakatsuka, S.; Tanaka, H.; Yasuda, N.; Haketa, Y.; Maeda, H.; Hatakeyama, T. "Syntheses and Physical Properties of Cationic BN-Embedded Polycyclic Aromatic Hydrocarbons" *Angew. Chem. Int. Ed.* **2021**, *60*, 12835.

(10) Fumoto, N.; Haketa, Y.; Tanaka, H.; Yasuda, N.; Maeda, H. "π-Electronic Ion-Pairing Assemblies of Deprotonation-Induced Anions" *Org. Lett.* **2021**, *23*, 3897.

(11) Kuno, A.; Hirata, G.; Tanaka, H.; Kobayashi, Y.; Yasuda, N.; Maeda, H. "Dipyrrolyldiketone Pt^{II} Complexes: Ion-Pairing π-Electronic Systems with Various Anion-Binding Modes" *Chem. Eur. J.* **2021**, *27*, 10068.

(12) Yamasumi, K.; Sugiura, S.; Tanaka, H.; Maeda, H. "Charged π-Electronic Systems That Provide Assembled Structures" *J. Synth. Org. Chem. Jpn.* **2022**, *80* (3), 232.

(13) Takiguchi, A.; Tanaka, H.; Maeda, H.; Shinokubo, H. "Diverse Crystal Structures of Ion Pairs Consisting of Oxaporphyrinium Cations and Pentacyanocyclopentadienide" *Bull. Chem. Soc. Jpn.* **2022**, *95*, 796.

(14) Maeda, H.; Nishimura, T.; Haketa, Y.; Tanaka, H.; Fujita, M.; Yasuda, N. "Ion-Pairing Assemblies of Anion-Responsive π-Electronic Systems Bearing Triazole Moieties Introduced by Click Chemistry" *J. Org. Chem.* **2022**, *87*, 7818.

(15) Fujita, M.; Haketa, Y.; Tanaka, H.; Yasuda, N.; Maeda, H. "Ion-pairing assemblies of heteroporphyrin-based π-electronic cation with various counteranions" *Chem. Commun.* **2022**, *58*, 9870.

Acknowledgements

The author wishes to express his gratitude to Prof. Dr. Hiromitsu Maeda, Ritsumeikan University, for his invaluable guidance and encouragement throughout this study. The author desires to express his sincere thanks to Dr. Yohei Haketa, Ritsumeikan University, for active discussions and the synchrotron-radiation single-crystal X-ray analyses (BL40XU and BL02B1 at SPring-8). The author would like to show his greatest appreciation to Prof. Dr. Yoichi Kobayashi and Dr. Yoshinori Okayasu, Ritsumeikan University, for the help of transient absorption spectra and helpful discussions. The author owes a very important dept to Dr. Nobuhiro Yasuda, Diffraction and Scattering Division, JASRI and Prof. Dr. Kunihisa Sugimoto, Kindai University, for synchrotron radiation single-crystal X-ray analysis (BL40XU and BL02B1/SPring-8). The author desires to express his sincere thanks to Prof. Dr. Atsuhiro Osuka, Prof. Dr. Takayuki Tanaka, Dr. Hirotaka Mori, Dr. Koji Naoda, Dr. Shinichiro Ishida, Dr. Takanori Soya, Dr. Koki Kise, and Mr. Akito Nakai, Kyoto University, for single-crystal X-ray analysis. The author is deeply grateful to Prof. Dr. Ko Furukawa, Niigata University, for ESR measurement. The author would like to thank Dr. Yukihide Ishibashi and Prof. Dr. Tsuyoshi Asahi, Ehime University, for solid-state absorption and transient absorption measurements. The author is grateful to Prof. Dr. Yasuteru Shigeta, University of Tsukuba, and Dr. Ryuma Sato, RIKEN Center for Biosystems Dyanamics Research (BDR), for the help of theoretical studies. The author gratefully acknowledges to Prof. Dr. Shigehisa Akine, Kanazawa University, for analysis of heterodimerization model. The author owes my deepest gratitude to Prof. Dr. Tatsuki Morimoto, Tokyo University of Technology, for electrochemical analysis. The author thanks to Dr. Ryosuke Miyake, Ochanomizu University, for ^{13}C NMR measurement with a Prodigy cryo probe head. The author thanks Research Center for Computational Sciences, Okazaki, Japan, for the help of theoretical studies. The author expresses his appreciation to Prof. Dr. Hitoshi Tamiaki, Ritsumeikan University, for various measurements, including NMR, UV/vis absorption, and ESI-TOF-MS. The author wishes to thank the Japan Society for the Promotion of Science (JSPS) for three years since April 2020 for financial support.

Finally, the author is deeply grateful to the current and former group members in Ritsumeikan University.

Hiroki Tanaka